RICHARD TAUBERT

# FROM NEAR-FIELD TO FAR-FIELD:

## PLASMONIC COUPLING IN THREE-DIMENSIONAL NANOSTRUCTURES

# From Near-Field to Far-Field:

## Plasmonic Coupling in
## Three-Dimensional Nanostructures

Von der Fakultät Mathematik und Physik
der Universität Stuttgart zur Erlangung der Würde
eines Doktors der Naturwissenschaften (Dr. rer. nat.)
genehmigte Abhandlung

vorgelegt von

**Richard Taubert**

aus Singen (Htwl.)

Seht ihr den Mond dort stehen?
Er ist nur halb zu sehen
Und ist doch rund und schön!
So sind wohl manche Sachen,
Die wir getrost belachen,
Weil unsre Augen sie nicht sehn.

— *Matthias Claudius*

# PUBLICATIONS

PARTS OF THIS THESIS HAVE ALREADY BEEN PUBLISHED

IN SCIENTIFIC JOURNALS:

[1]  R. Taubert, R. Ameling, T. Weiss, A. Christ, and H. Giessen: *From near-field to far-field coupling in the third dimension: Retarded interaction of particle plasmons*, Nano Lett. **11**, 4421–4424, (2011), DOI 10.1021/nl202606g.

[2]  R. Taubert, D. Dregely, T. Stroucken, A. Christ, and H. Giessen: *Octave-wide photonic band gap in three-dimensional plasmonic Bragg structures and limitations of radiative coupling*, Nat. Commun. **3**, 691, (2012), DOI 10.1038/ncomms1694.

[3]  R. Taubert, M. Hentschel, J. Kästel, and H. Giessen: *Classical analog of electromagnetically induced absorption in plasmonics*, Nano Lett. **12**, 1367–1371, (2012), DOI 10.1021/nl2039748.

AT INTERNATIONAL CONFERENCES:

[4]  R. Taubert and H. Giessen: *From near-field to far-field coupling: Towards three-dimensional Bragg plasmonics*, Metamaterials (Karlsruhe, Germany), Sept. 16, 2010.

[5]  R. Taubert, R. Ameling, T. Weiss, A. Christ, and H. Giessen: *From near-field to far-field: Radiative coupling of particle plasmon resonances in three-dimensional geometries*, NanoMeta (Seefeld, Austria), Jan. 6, 2011.

[6]  R. Taubert and H. Giessen: *Octave-wide photonic band gap in three-dimensional plasmonic Bragg structures*, Conference on Lasers and Electrooptics/Quantum Electronics and Laser Science (CLEO / QELS) (Baltimore, USA), Invited Talk, May 6, 2011.

[7]  R. Taubert, R. Ameling, T. Weiss, A. Christ, and H. Giessen: *From near-field to far-field: Radiative coupling of particle plasmon resonances in three-dimensional geometries*, CLEO/Europe: European Quantum Electronics Conference 2011 (Munich, Germany), May 22, 2011.

[8]  R. Taubert and H. Giessen: *From near-field to far-field: Radiative coupling of particle plasmon resonances in three-dimensional geometries*, XXX. General Assembly and Scientific Symposium of the International Union of Radio Science (URSI GASS) (Istanbul, Turkey), Aug. 17, 2011.

[9]  R. Taubert, M. Hentschel, J. Kästel, and H. Giessen: *Classical analog of electromagnetically induced absorption in plasmonics*, 3rd International Conference on Metamaterials, Photonic Crystals, and Plasmonics, META'12 (Paris, France), Apr. 19, 2012.

OTHER SCIENTIFIC CONTRIBUTIONS WHICH ARE NOT PART OF THIS THESIS:

[10]  D. Dregely, R. Taubert, J. Dorfmüller, R. Vogelgesang, K. Kern, and H. Giessen: *3D optical Yagi-Uda nanoantenna array*, Nat. Commun. **2**, 271, (2011), DOI 10.1038/ncomms1268, (cit. on p. 143).

[11]  T. Weiss, N. A. Gippius, G. Granet, S. G. Tikhodeev, R. Taubert, L. Fu, H. Schweizer, and H. Giessen: *Strong resonant mode coupling of Fabry-Pérot and grating resonances in stacked two-layer systems*, Photonics Nanostruct. **9**, 390–397, (2011), DOI 10.1016/j.photonics.2011.03.007, (cit. on p. 79).

[12]  A. Tittl, P. Mai, R. Taubert, D. Dregely, N. Liu, and H. Giessen: *Palladium-based plasmonic perfect absorber in the visible and its applications to hydrogen sensing*, Nano Lett. **11**, 4366–4369, (2011), DOI 10.1021/nl202489g.

[13]  M. Gentile, M. Hentschel, R. Taubert, H. Guo, H. Giessen, and M. Fiebig: *Investigation of the nonlinear optical properties of metamaterials by second harmonic generation*, Appl. Phys. B **105**, 149–162, (2011), DOI 10.1007/s00340-011-4766-y.

# CONTENTS

## GLOSSARY

| | |
|---|---|
| $A$ | absorbance, $1 - T - R$ |
| $\alpha$ | polarizability |
| $\mathbf{B}$ | magnetic flux density |
| $c$ | speed of light in vacuum, $299\,792\,458$ m/s |
| $\chi$ | electric susceptibility |
| $\mathbf{D}$ | electric displacement field |
| $\delta$ | energetic detuning |
| $d_x$ | lateral periodicity |
| $d_z$ | vertical spacing distance |
| $\mathbf{E}$ | electric field |
| $e$ | electron charge, $1.602 \times 10^{-19}$ C |
| $E_{\mathrm{PPR}}$ | particle plasmon resonance energy |
| $\varepsilon$ | electric permittivity |
| $\varepsilon_0$ | electric field constant, $8.854 \times 10^{-12}$ F/m |
| $\varepsilon_{\mathrm{D}}$ | free electron susceptibility in the Drude model |
| $\Gamma$ | nonradiative width |
| $\gamma$ | harmonic oscillator damping constant |
| $\Gamma_0$ | radiative width |
| $\gamma_{\mathrm{D}}$ | damping frequency in the Drude model |
| $H$ | wire height |

| | |
|---|---|
| **H** | magnetic field |
| $\mathcal{I}$ | unit matrix |
| **J** | electric current density |
| $k$ | angular wave number, $|\mathbf{k}|^2$ |
| **k** | wave vector |
| $\kappa$ | harmonic oscillator coupling constant |
| $L$ | wire length |
| $\lambda$ | vacuum wavelength |
| $\lambda_{\text{PPR}}$ | particle plasmon resonance wavelength |
| $m_{\text{e}}$ | electron mass, $9.109 \times 10^{-31}$ kg |
| $\mu$ | magnetic permeability |
| $\mu_{\text{o}}$ | magnetic field constant, $4\pi \times 10^{-7}$ N/A$^2$ |
| $N$ | layer number |
| $n$ | (complex) refractive index |
| $n_{\text{Sp}}$ | refractive index of the spacer layer |
| $n_{\text{Sub}}$ | refractive index of the substrate |
| $\omega$ | angular frequency |
| $\omega_{\text{p}}$ | (bulk) plasma frequency |
| $\omega_{\text{PPR}}$ | particle plasmon resonance frequency |
| **P** | electric polarization |
| **p** | dipole moment |
| $\varphi$ | phase |
| $R$ | reflectance, $|\mathfrak{r}|^2$ |
| $\mathfrak{r}$ | reflection amplitude |
| $S$ | lateral shift |
| $T$ | transmittance, $|\mathfrak{t}|^2$ |
| $\mathfrak{t}$ | transmission amplitude |
| $W$ | wire width |

# ACRONYMS

| | |
|---|---|
| EBL | electron beam lithography |
| EIA | electromagnetically induced absorption |
| EIT | electromagnetically induced transparency |
| FDTD | finite difference time domain |
| FFT | fast Fourier transform |
| FIB | focused ion beam |
| FIT | finite integration technique |
| FMM | Fourier modal method |
| FP | Fabry-Pérot |
| FTIR | Fourier-transform infrared spectrometer |
| FWHM | full width at half maximum |
| LHS | left hand side |
| LSPR | localized surface plasmon resonance |
| MCT | Mercury Cadmium Telluride |
| MIBK | Methylisobutylketone |
| NIM | negative index material |
| NMP | N-methylpyrrolidone |
| PBG | photonic band gap |
| PC | photonic crystal |
| PH | plasmon hybridization |
| PMMA | Polymethylmethacrylat |
| PPR | particle plasmon resonance |
| QD | quantum dot |
| QW | quantum well |
| RCWA | rigorously coupled wave approximation |
| RHS | right hand side |
| SEM | scanning electron microscope |

| SERS | surface-enhanced Raman scattering |
|------|-----------------------------------|
| SMM | scattering matrix method |
| SOD | spin-on dielectric |
| SPP | surface plasmon polariton |
| SRR | split ring resonator |

## LIST OF FIGURES

## LIST OF TABLES

# ABSTRACT

This thesis provides a comprehensive study of the coupling phenomena that occur in plasmonic nanostructures. Electromagnetic coupling between metallic nanoparticles leads to strong spectral modifications in the structures, which are determined using linear optical spectroscopy in the visible and infrared wavelength range. In contrast to previous investigations, the key aspect here are the properties of plasmonic far-field coupling in three-dimensionally arranged structures. These are fabricated by electron beam lithography in a multilayer process, which allows for a three-dimensional arrangement of plasmonic particles.

We study coupling in a plasmonic dimer for different arrangements. In order to address the transition from the near-field to the far-field regime, we investigate a structure consisting of two nanowires stacked on top of each other for a wide range of interparticle spacings, and thus are able to examine near- as well as far-field coupling effects. In case of near-field coupling, only the quasistatic near fields of the plasmonic structures are important and the plasmon hybridization scheme gives an excellent qualitative description of all the observed phenomena. In contrast, the far-field regime is characterized by the occurrence of Fabry-Pérot modes due to the large vertical spacing between the particles. These couple to the particle plasmon resonances, forming new coupled modes which are extensively discussed.

A situation of particular interest occurs whenever the interparticle distance fulfills the Bragg criterion, i. e., the vertical distance equals a multiple of half the particle plasmon resonance wavelength: then the coupled mode which spectrally approaches the single layer particle plasmon resonance becomes dark and a broad region of high reflectance forms. Increasing the number of oscillators stacked at this particular distance leads to the increase of the spectral width of the plasmonic response and the formation of a broad photonic band gap, which spans about one octave in the optical wavelength regime. In contrast to previous similar investigations which were carried out with semiconductor quantum well structures or atoms in optical lattices, the plasmonic particles exhibit an extraordinarily strong coupling to the light field. Therefore, we are able to explore the regime where the coupling between

the oscillators is limited by their large radiative decay rate, rather than nonradiative decay channels.

Finally, we address the intermediate coupling regime by investigating a structure which utilizes properties of both, near- and far-field coupling. A dipolar cut-wire is placed on top of a quadrupolar cut-wire pair. As long as the spacing between both, quadrupolar and dipolar oscillator is sufficiently small (near-field regime), the coupling leads to a transmittance peak in the spectra due to a destructive interference between the coupled modes. Hence, this effect is described as the plasmonic analog of electromagnetically induced transparency. On increasing distance, the relative phase of the oscillators changes and constructive instead of destructive interference is achieved. As a consequence, a sub-dipolar linewidth peak in the absorbance spectrum is observed. The phenomenon can thus be termed the plasmonic analog of electromagnetically induced absorption. In the pure near-field regime, the plasmonic fields exhibit no retardation phase due to their quasistatic nature. In the far-field regime, however, a coupling to the quadrupolar oscillator would not be possible. Hence, the occurrence of this effect relies on the intermediate regime, where properties of both, near- and far-field regime are present.

## ZUSAMMENFASSUNG

Die vorliegende Arbeit befasst sich eingehend mit Wechselwirkungseffekten in plasmonischen Nanostrukturen. Elektromagnetische Wechselwirkung zwischen metallischen Nanopartikeln führt zu ausgeprägten Änderungen in deren Spektren. Mittels linearer optischer Spektroskopie im sichtbaren und infraroten Spektralbereich werden diese untersucht. Im Gegensatz zu früheren Arbeiten liegt der Schwerpunkt hier auf plasmonischen Fernfeldeffekten in dreidimensional angeordneten Strukturen. Diese werden mittels Elektronenstrahllithographie in einem Mehrschichtverfahren, welches eine dreidimensionale Anordnung der plasmonischen Partikel ermöglicht, hergestellt.

Zunächst wird die Kopplung in einer Struktur bestehend aus zwei Partikeln in verschiedenen räumlichen Anordnungen untersucht. Um den Übergang vom Nahfeld- in den Fernfeldbereich zu untersuchen, wird der Abstand zweier vertikal übereinander angeordneter Partikel über

einen großen Bereich variiert, so dass Nah- wie auch Fernfeldeffekte beobachtet werden können. Für den Nahfeldbereich ist es ausreichend, die quasistatischen Nahfelder der plasmonischen Strukturen zu berücksichtigen. In diesem Fall liefert das Konzept der Plasmon-Hybridisierung sehr gute qualitative Erklärungen für die beobachteten Effekte. Im Gegensatz dazu treten im Fernfeldbereich Fabry-Pérot-Resonanzen auf, welche zusammen mit den Plasmonresonanzen der Partikel gekoppelte Moden ausbilden. Die Eigenschaften dieser neuen Moden werden ausführlich diskutiert.

Eine interessante Situation ergibt sich, wenn der Abstand zwischen den Partikeln die Bragg-Bedingung für die Resonanzwellenlänge der Partikelplasmonen erfüllt, d.h. der vertikale Abstand einem Vielfachen der Plasmon-Resonanzwellenlänge entspricht: In diesem Fall ist die gekoppelte Mode, die sich spektral der Partikelplasmonresonanz eines einzelnen Partikels annähert, nur noch sehr schwach durch das externe Lichtfeld anregbar, was zu einem sehr breiten Spektralbereich mit hoher Reflektion führt. Erhöht man die Anzahl der Oszillatoren in dieser speziellen Geometrie, so erhöht sich die spektrale Breite des gekoppelten Systems stark, und es bildet sich eine breite photonische Bandlücke aus, die ungefähr eine Oktave im optischen Spektralbereich umfasst. Im Gegensatz zu ähnlichen vorherigen Experimenten, die mit Halbleiter-Quantenfilm-Strukturen oder Atomen in Lichtgittern durchgeführt wurden, zeichnen sich plasmonische Partikel durch eine besonders starke Kopplung an das Lichtfeld aus. Dadurch ist es möglich, das Regime, in dem die Kopplung zwischen Oszillatoren durch deren schnellen radiativen Zerfall statt durch nicht-radiative Zerfallsmechanismen begrenzt wird, zu untersuchen.

Schließlich wird der Übergangsbereich zwischen Nahfeld- und Fernfeldkopplung anhand einer Struktur, in der Eigenschaften beider Bereiche eine Rolle spielen, untersucht. Ein Nanodraht, welcher die Eigenschaften eines Dipols aufweist wird über einem Nanodraht-Paar, welches als Quadrupol fungiert, angeordnet. Bei kleinen Abständen (im Nahfeldbereich) zwischen Dipol- und Quadrupoloszillator führt die Wechselwirkung zu einem Transmissionsfenster im Spektrum, da die Moden der gekoppelten Struktur destruktiv interferieren. Dieser Effekt wird daher auch als das plasmonische Analogon zur elektromagnetisch induzierten Transparenz bezeichnet. Vergrößert man den Abstand, so ändert sich die relative Phase zwischen den Oszillatoren, so dass eine konstruktive statt einer destruktiven Interferenz erreicht werden kann. Dies führt zu einem schmalen Absorptionspeak, dessen spektrale Brei-

te kleiner als die der Dipol-Absorption ist. Dieser Effekt wird als das plasmonische Analogon zur elektromagnetisch induzierten Absorption bezeichnet. Im reinen Nahfeldbereich sind die Felder quasistatischer Natur weshalb eine Retardationsphase nicht definierbar ist. Im Fernfeldbereich wäre hingegen eine Kopplung an den Quadrupol-Oszillator nicht möglich. Das Auftreten dieses Effekts erfordert daher den Übergangsbereich, in dem Eigenschaften beider Grenzfälle, Nahfeld und Fernfeld, eine Rolle spielen.

# 1

## INTRODUCTION

Shaping the interaction of light and matter has been one of the most essential, yet also fundamental subjects of physics during the last 150 years. In many cases "matter" referred to materials composed of naturally occurring building blocks such as atoms or molecules. During the last decades the availability of mesoscopic artificial functional nanostructures has widely expanded the range of possibilities. Among those are quantum wells (QWs) and quantum dots (QDs), as well as plasmonic nanoparticles. While the former two are examples of artificial quantum systems with a focus on quantum mechanical properties, plasmonic nanoparticles are classical oscillators, despite their mesoscopic dimensions. This fact arises from the high number of free electrons which proves the classical description to be valid down to feature sizes well below 10 nm [14, 15].

Already in ancient times metallic nanoparticles have been utilized—the Romans used metal oxides to fabricate stained glass. From time to time the fabrication process accidentally lead to the formation of metallic nanoparticles which resulted in glass with extraordinary optical properties, for example dichroism [16]. Similar techniques were used in medieval ages to pigment the colorful glass windows of churches and cathedrals. Due to the unique long-term stability of the nanoparticle coloring compared to organic dye molecules, these windows still exhibit their vivid colors centuries later.

The first scientific investigation of the optical properties of metallic nanoparticles dates back to the 19th century and was carried out by Michael Faraday, who gave a phenomenological description of the different color effects which arise from metallic particles [17]. The observations of anomalous effects on metallic gratings made by Robert Wood [18] are of equal importance. For both of these, Lord Rayleigh provided substantial theoretical contributions [19–21]. A full theoretical treatment of light scattering and absorption by spherical nanoparticles was later given by Gustav Mie [22].

Almost half a decade later, the concept of surface plasma oscillations was proposed [23–25], terming the resulting quasiparticle as "plasmons" for the first time [26]. The corresponding concept of a bound wave on

a conducting surface had, however, already been given before in the radio wave regime. Explicit derivations were carried out by Arnold Sommerfeld [27] for the propagation along metallic wires, as well as by Jonathan Zenneck [28] for waves bound to a (sea) water surface. These waves therefore are known as Sommerfeld-Zenneck waves. In the pioneering works on surface plasmon polaritons (SPPs) the excitation was performed via a local electron beam, schemes for the optical excitation were proposed later by Andreas Otto [29] as well as Erwin Kretschmann and Heinz Raether [30].

In the late 1990s the interest in plasmonic oscillations of metallic nanoparticles emerged due to the broad availability of reliable nanofabrication techniques. Many of the early experiments approached the subject from a fundamental, solid state physics perspective, i. e., to understand the elementary excitations of matter [31–38]. In the mean time the focus has shifted towards the utilization of the plasmonic oscillators as building blocks themselves.

The motivation to particularly investigate plasmonic coupling has emerged from various different areas of research:

Quite early, the possibility of using plasmonic particle chains as *plasmonic waveguides* was investigated [39–49]. In contrast to conventional copper wiring, these plasmonic waveguides consisting of a row of near-field coupled plasmonic particles were expected to allow for a higher bandwidth for optical on-chip interconnects [50]. However, in long chains substantial losses inhibit a signal transport over long distances.

*Metamaterials* are materials consisting of artificial building blocks which act as effective media for waves with a substantially larger wavelength. Still, their building blocks are considerably larger than atoms and thus can be shaped to achieve specific optical properties. The most prominent prospect of metamaterials was the realization of media with negative refractive index, which has led to a re-emerging interest in linear optical effects. Initially proposed by Victor Veselago in 1968 [51], these materials would exhibit unusual physical properties, might be used for the realization of a perfect lens which overcomes the diffraction limit [52], or allow for the design of cloaking devices [53, 54], utilizing similar concepts to those in General Relativity.

Many of the designs have been proposed for and first realized in the microwave regime [55–58]. Their operation principle in the visible wavelength range is tightly connected to particle plasmons in the metals [59]. However, the miniaturization to optical wavelengths [60–67] is hampered by the fact that, even though Maxwell's equations are scale-

invariant, the optical properties of the constituent materials are not. This imposes some fundamental constraints [68] on the realization.

In almost exact analogy to radio frequency antennas, plasmonic structures can act as *optical nanoantennas* [69–71] mediating electromagnetic energy transfer from the far field to the near field and vice versa [72]. Therefore, they improve the mismatch between light wavelengths and the size of nanoscale objects [73]. This enables the possibility to interface them to quantum emitters which are themselves weakly emitting and to enhance their emission efficiency [74–76] as well as their spatial emission pattern [77, 78]. In this case, the quantum emitter is equivalent to the feed current in a classical radiowave antenna [79, 80].

The nanoantenna converts incoming radiation into localized fields allowing for the possibility to focus light energy into deeply subwavelength volumes. In connection with the resonant field enhancement due to the plasmonic oscillation several exciting possibilities arise:

First, while using SPPs and particle plasmon resonances (PPRs) for *refractive index sensing* [81–83], has become a standard technique, the strong field enhancement is particularly useful. It can be utilized to enhance weak molecular signals, such as vibrational bands [84] or Raman signals in surface-enhanced Raman scattering (SERS), where enhancement factors exceeding $10^5$ were reported [85, 86].

Second, the field concentration allows for a confinement of the sensing volume to subwavelength dimensions, which is important for detection on a few-particle [87] or even single-molecule level [88, 89].

Third, field enhancement effects can be utilized to increase the efficiency of nonlinear processes such as second-harmonic generation [90, 91] or potentially even high-harmonic generation [92–94].

In all of these areas it has become apparent, that the understanding of a single building block is not sufficient, therefore, the understanding of coupling effects is *vital.* For *metamaterials*, this is equivalent to the transition from atomic to solid state physics. As the fundamental property of *nanoantennas* is to mediate between near- and far fields, it is necessary not only to include near-field coupling effects, which have been largely investigated throughout the past decade, but also to include far-field coupling. For *plasmonic sensing*, the design of complex coupled building blocks yields a tremendous increase in the figure of merit compared to single plasmonic oscillators [95, 96]. In case of SERS, finding a geometry which allows for a controlled enhancement is still a subject of active research and coupling effects might play an important

role in the enhancement process [97]. Finally, it has been suggested to use direct radiative plasmonic coupling instead of *plasmonic waveguides* for optical interconnects, which has the potential to drastically reduce the losses [98].

From these considerations it has become apparent, that a thorough understanding of plasmonic coupling in the near- as well as the far-field regime is an elementary prerequisite for all the areas of research introduced above. This thesis is devoted to the investigation of plasmonic coupling effects with a special emphasis on far-field coupling in three-dimensionally arranged plasmonic particle geometries.

Chapter 2 will introduce the fundamental concepts. After introducing the basic equations, we will discuss the optical properties of metals, particularly those of gold, which is exclusively used throughout this work. The optical interaction of (metallic) nanoparticles with radiation will be reviewed. Furthermore, the concept of Fano resonances will be introduced.

Chapter 3 will give a short review of the methods used for the experimental realization of the nanostructured samples. In particular, the layer-by-layer fabrication method will be introduced which is vital for the three-dimensional arrangement of the plasmonic particles. Beyond this, a brief description of the utilized calculation methods will be given.

Subsequently, chapter 4 will discuss the basic building block that will be used for many of the investigations. Then, their coupling in different arrangements and regimes will be discussed, exclusively restricted to dimer structures. In order to give a comprehensive description of the coupling effects, this chapter will also refer to previous work on plasmonic coupling, and then extend its scope to the far-field coupling domain in three-dimensional arrangements. Up to now, only calculations for these geometries had been available [99]. Experimental results will be presented and in addition the coupling mechanism will be investigated, alongside with an intuitive model for the coupling. Furthermore, Bragg spacing will be introduced. This corresponds to an arrangement of the particles such that their interparticle distance matches a multiple of half their plasmonic resonance wavelength, giving rise to interesting optical features.

Chapter 5 will then extend the scope to structures with multiple particles stacked on top of each other along the light propagation direction, yet their vertical spacing will be restricted to Bragg spacing. This plasmonic multilayer arrangement will be compared to conventional passive photonic crystal structures [100] which exhibit photonic band gaps

due to a refractive index variation. In the plasmonic Bragg structures, a very broad photonic band gap emerges due to the radiative coupling of the plasmonic oscillators.

Finally, chapter 6 will provide a perspective onto the coupling in the regime between near- and far field. It will discuss a structure, in which properties of both domains are present. This will allow to implement a classical analog to an effect known from atomic physics, namely the classical analog of electromagnetically induced absorption.

∼

# 2

# NANOSCALE OPTICS USING METALLIC NANOPARTICLES

## 2.1 BASIC EQUATIONS OF ELECTRODYNAMICS

### 2.1.1 *Maxwell's Equations*

The basis of all electromagnetic and therefore also optical phenomena are Maxwell's equations, which in a general way are expressed as [101]

$$\nabla \times \mathbf{E} + \frac{\partial}{\partial t}\mathbf{B} = 0 \tag{2.1}$$

$$\nabla \times \mathbf{H} - \frac{\partial}{\partial t}\mathbf{D} = \mathbf{J} \tag{2.2}$$

$$\nabla \cdot \mathbf{D} = \rho \tag{2.3}$$

$$\nabla \cdot \mathbf{B} = 0. \tag{2.4}$$

Here $\mathbf{E}$, $\mathbf{H}$, $\mathbf{D}$, and $\mathbf{B}$ are the vectorial magnitudes of electric and magnetic field as well as the electric displacement and magnetic flux density, $\mathbf{J}$ is the current density and $\rho$ the electric charge density. A great deal of the physics involved in a specific problem of electrodynamics is the choice of relations between $\mathbf{E}$ and $\mathbf{D}$, $\mathbf{B}$ and $\mathbf{H}$ and the dependence of $\rho$ and $\mathbf{J}$ upon those. In most general form these constitutive relations can be written as [102]

$$\mathbf{D} = \varepsilon_0 \bar{\varepsilon}\, \mathbf{E} + \bar{\bar{\xi}}\, \mathbf{H}$$

$$\mathbf{B} = \mu_0 \bar{\mu}\, \mathbf{H} + \bar{\zeta}\, \mathbf{E},$$

where the tensors $\bar{\varepsilon}$, $\bar{\bar{\xi}}$, $\bar{\mu}$, and $\bar{\zeta}$ describe the relation between all the different field components. However, as long as only isotropic media are involved, all the tensors reduce to scalars and $\bar{\bar{\xi}}$ and $\bar{\zeta}$ vanish. This leads to the simplified constitutive relations

$$\mathbf{D} = \varepsilon_0 \varepsilon \mathbf{E}$$
$$\mathbf{B} = \mu_0 \mu \mathbf{H}. \tag{2.5}$$

These can also be derived from a microscopic point of view, which yields

$$\mathbf{D} = \varepsilon_0 \mathbf{E} + \mathbf{P}$$
$$\mathbf{B} = \mu_0 \mathbf{H} + \mathbf{M},$$
(2.6)

where $\mathbf{P}$ is the microscopic electric polarization and $\mathbf{M}$ the microscopic magnetization in the medium. For common materials $\mathbf{M}$ is negligible at optical frequencies and $\mu = 1$. The treatment of $\mathbf{P}$ deserves some more attention. In its most general case it might be an arbitrary function of $\mathbf{r}, \mathbf{r}', t$, and $t'$, however, with the fundamental assumptions of linearity, locality, and time dependence only on $(t - t')$, the polarization can be expressed in frequency space as

$$\mathbf{P}(\mathbf{r}, \omega) = \varepsilon_0 \chi(\mathbf{r}, \omega) \, \mathbf{E}(\mathbf{r}, \omega),$$
(2.7)

where $\chi(\mathbf{r}, \omega)$ is the electric susceptibility. For homogeneous media additionally the dependence on $\mathbf{r}$ can be omitted. Inserting eq. 2.7 into eq. 2.6 and comparing to eq. 2.5 yields a connection between dielectric function $\varepsilon$ and susceptibility $\chi$:

$$\varepsilon(\omega) = 1 + \chi(\omega).$$
(2.8)

### 2.1.2  *Electromagnetic Wave Propagation in Media*

From Maxwell's equations, an electromagnetic wave equation can be derived. Assuming $\rho = 0$ and $\mathbf{J} = 0$, taking the rotation[i] of eq. 2.1 and combining with eq. 2.2, eq. 2.3, and eq. 2.5 leads to

$$\Delta \mathbf{E} - \varepsilon_0 \mu_0 \, \varepsilon \mu \, \frac{\partial^2}{\partial t^2} \mathbf{E} = 0.$$
(2.9)

The wave equation for the magnetic field is obtained analogously. This is the fundamental equation expressing the propagation of electromagnetic waves in homogeneous media. The phase velocity of the electromagnetic wave is conferred from this to be $1/\sqrt{\varepsilon_0 \mu_0 \, \varepsilon \mu}$, which can be divided into the vacuum velocity $c = 1/\sqrt{\varepsilon_0 \mu_0}$ and the refractive index of the medium $n = \sqrt{\varepsilon \mu}$. The phase velocity in a medium is therefore connected to its refractive index by $c_{\text{medium}} = c/n$, which for usual materials with $n > 1$ is below the vacuum velocity.

---

i  making use of $\nabla \times \nabla \times \mathbf{E} = \nabla(\nabla \cdot \mathbf{E}) - \Delta \mathbf{E}$

With a plane wave ansatz further consequences follow. Inserting

$$\mathbf{E}(\mathbf{r}, t) = \mathbf{E_o}\, e^{i(\mathbf{kr} - \omega t)} \tag{2.10}$$

into eq. 2.9 gives the dispersion relation for electromagnetic waves

$$|\mathbf{k}|^2 = \left(\frac{\omega n}{c}\right)^2. \tag{2.11}$$

The absolute value of $\mathbf{k}$ is defined as the angular wave number and can be expressed in terms of the wavelength $\lambda$,

$$k = |\mathbf{k}| = \frac{2\pi n}{\lambda}.$$

Here $\lambda$ is the vacuum wavelength, but it is also possible to introduce the effective wavelength in the medium $\lambda_{\mathrm{medium}} = \lambda/n$. For usual materials, $n > 1$, it is smaller than the vacuum wavelength.

From Maxwell's equations additional characteristics of electromagnetic waves can be derived. Inserting eq. 2.10 into eq. 2.1 yields

$$\mathbf{B}(\mathbf{r}, t) = \frac{1}{\omega}\left(\mathbf{k} \times \mathbf{E}(\mathbf{r}, t)\right) = \mathbf{B_o}\, e^{i(\mathbf{kr} - \omega t)},$$

which means that $\mathbf{B}$ is perpendicular to $\mathbf{k}$ and $\mathbf{E}$, whereas eq. 2.3 gives $\mathbf{E} \perp \mathbf{k}$, hence all the vectors are perpendicular to each other, forming a right-handed trihedron[ii].

### 2.1.3  Boundary Conditions at Interfaces

Finally, it is necessary to treat boundaries between media. To derive these, the integral representation of Maxwell's equation is more suited, which are obtained from the differential form by application of Gauss' and Stokes' theorem [101]:

$$\oint_S \mathbf{D} \cdot d\mathbf{a} = \int_V \rho\, d^3x \tag{2.12}$$

$$\oint_S \mathbf{B} \cdot d\mathbf{a} = 0 \tag{2.13}$$

$$\oint_C \mathbf{H} \cdot d\mathbf{l} = \int_{S'} \left(\mathbf{J} + \dot{\mathbf{D}}\right) \cdot d\mathbf{a}' \tag{2.14}$$

$$\oint_C \mathbf{E} \cdot d\mathbf{l} = \int_{S'} \dot{\mathbf{B}} \cdot d\mathbf{a}', \tag{2.15}$$

---

ii  This is true as long as $\mathbf{D} = \varepsilon_0 \varepsilon \mathbf{E}$ holds. For anisotropic media $\mathbf{D}$ remains perpendicular to $\mathbf{k}$ and $\mathbf{B}$, but not necessarily $\mathbf{E}$.

where the volume $V$ is enclosed by the surface $S$ with normal vector $\mathbf{n} = \mathbf{a}/a$, and the surface $S'$ is surrounded by the path $C$ with tangential vector $\mathbf{l}$.

Performing the integration of eqs. 2.12 and 2.13 for an infinitely small cylinder across the boundary plane, with one capping surface in each medium yields [101]

$$(\mathbf{D_2} - \mathbf{D_1}) \cdot \mathbf{n} = \sigma \tag{2.16}$$

$$(\mathbf{B_2} - \mathbf{B_1}) \cdot \mathbf{n} = 0. \tag{2.17}$$

Therefore, the normal component of $\mathbf{B}$ is continuous across the boundary, while the normal component of $\mathbf{D}$ is discontinuous due to the surface charge $\sigma$.

Similarly, the integration of eqs. 2.14 and 2.15 around an infinitely small surface whose normal vector lies in the boundary plane results in

$$\mathbf{n} \times (\mathbf{E_2} - \mathbf{E_1}) = 0 \tag{2.18}$$

$$\mathbf{n} \times (\mathbf{H_2} - \mathbf{H_1}) = \mathbf{K}, \tag{2.19}$$

which means that the tangential component of $\mathbf{E}$ is continuous across the boundary, while the tangential component of $\mathbf{H}$ jumps by the amount of the surface current $\mathbf{K}$.

A large part of linear optics is based only on these continuity conditions and many important laws follow as a direct consequence, most importantly Snell's law of refraction at an interface of two media with refractive indices $n_1$ and $n_2$:

$$\frac{\sin \alpha}{\sin \beta} = \frac{n_2}{n_1}, \tag{2.20}$$

where $\alpha$ and $\beta$ are the angles between surface normal and incoming respectively outgoing $\mathbf{k}$ vector of plane waves.

Furthermore, Fresnel's equations are contained, which describe the intensities of reflected and transmitted light at an interface [101]:

$$r^{\perp} = \frac{n_1 \cos \alpha - n_2 \cos \beta}{n_1 \cos \alpha + n_2 \cos \beta} \qquad t^{\perp} = \frac{2 n_1 \cos \alpha}{n_1 \cos \alpha + n_2 \cos \beta}$$

$$r^{\parallel} = \frac{n_2 \cos \alpha - n_1 \cos \beta}{n_2 \cos \alpha + n_1 \cos \beta} \qquad t^{\parallel} = \frac{2 n_1 \cos \alpha}{n_2 \cos \alpha + n_1 \cos \beta}.$$

Here the $r^{\perp/\parallel}$ and $t^{\perp/\parallel}$ are the reflection and transmission amplitudes for the $\mathbf{E}$ field component perpendicular and parallel to the the plane of incidence.

### 2.1.4 *The Hertzian Dipole*

In the previous section, only the propagation of electromagnetic radiation was treated, regardless of its sources. A powerful theoretical concept is the Hertzian dipole, which describes the electromagnetic fields generated by an infinitely small oscillating dipole moment.

The radiation generated by a harmonic oscillation of a charge distribution can be derived from the vector potential [101]

$$\mathbf{A}(\mathbf{x}, t) = \frac{\mu_0}{4\pi} \int d^3x' \mathbf{J}(\mathbf{x'}) \frac{e^{ik|\mathbf{x}-\mathbf{x'}|}}{|\mathbf{x} - \mathbf{x'}|}, \tag{2.21}$$

from which the fields can be calculated using

$$\mathbf{H} = \frac{1}{\mu_0} \nabla \times \mathbf{A} \qquad\qquad \mathbf{E} = \frac{i}{k} \sqrt{\frac{\varepsilon_0}{\mu_0}} \nabla \times \nabla \times \mathbf{A}. \tag{2.22}$$

If the source is infinitely small, only the lowest order in eq. 2.21 has to be considered. Furthermore, the current is transformed to a charge distribution, which leads to

$$\mathbf{A}(\mathbf{x}) = -\frac{i\mu_0 \omega \, \mathbf{p}}{4\pi} \frac{e^{ikr}}{r},$$

where $\mathbf{p}$ is the electric dipole moment vector and $r$ is the distance from the dipole. Inserting this into eq. 2.22 gives the explicit expressions for the electromagnetic fields:

$$\mathbf{E} = \frac{k^3}{4\pi\varepsilon_0} \left[ (\mathbf{n} \times \mathbf{p}) \times \mathbf{n} \, \frac{e^{ikr}}{kr} \right. \tag{2.23}$$

$$\left. + \left( 3\mathbf{n} \left( \mathbf{n} \cdot \mathbf{p} \right) - \mathbf{p} \right) \left( \frac{1}{(kr)^3} - \frac{i}{(kr)^2} \right) e^{ikr} \right]$$

$$\mathbf{H} = \frac{ck^2}{4\pi} (\mathbf{n} \times \mathbf{p}) \frac{e^{ikr}}{r} \left( 1 - \frac{1}{ikr} \right) \tag{2.24}$$

with the unit vector $\mathbf{n} = \mathbf{r}/|\mathbf{r}|$.

Here, we will only evaluate the electric field. It can be divided into three contributions according to the power of $(kr)$ in the denominator.

For small $(kr) \ll 1$, which means $r \ll \lambda$, the second term dominates and the field is approximated as

$$\mathbf{E} = \frac{1}{4\pi\varepsilon_0} \frac{e^{ikr}}{r^3} \left( 3\mathbf{n} \left( \mathbf{n} \cdot \mathbf{p} \right) - \mathbf{p} \right). \tag{2.25}$$

This exactly corresponds to the solution for a static electric dipole, apart from the oscillation term $\exp(ikr)$. As a consequence, considering only the dipolar near fields is equivalent to solving an electrostatic problem and modulating the solution at optical frequency.

On the other hand, for large distances compared to the wavelength, and thus $kr \gg 1$, the $1/(kr)$ term dominates which yields the oscillating far field of the dipole

$$\mathbf{E} = \frac{1}{4\pi\varepsilon_0} \left( \mathbf{n} \times \mathbf{p} \right) \times \mathbf{n} \, \frac{k^2 \, e^{ikr}}{r}. \tag{2.26}$$

In the intermediate regime, all three terms of eq. 2.23 have to be included and no further simplification is possible.

To visualize the dipole fields, Fig. 2.1 shows the calculated absolute electric fields $|\mathbf{E}|$ in two planes, one perpendicular and one parallel to $\mathbf{p}$. The near field (Fig. 2.1 (a),(d)) exhibits the typical behavior of a quasistatic dipole field, with a maximum field strength along the dipole axis. The falloff for increasing radius is very strong such that almost no oscillation pattern is found in this near field. Therefore the exponential function can be approximated as $e^{ikr} \approx 1$ in the near-field limit. The strongest field is located along the dipole direction, as can be seen from Fig. 2.1 (a).

This is different for the far field (b), where along the $z$ direction the field intensity vanishes completely. Instead, the electric field is maximum in the $xy$ plane, perpendicular to the dipole. The far-field plot furthermore shows a pronounced oscillation behavior indicating the emission of electromagnetic spherical waves, which is especially obvious from the $xy$ plane plot (e).

Finally, Fig. 2.1 (c) and (f) show the full electric field as given by eq. 2.23. Besides the superposition of near- and far field this also contains the additional $-i/(kr)^2$ term which oscillates at opposite phase with respect to both other terms. Its contribution is observed best along the $z$ direction in (c) because of the vanishing far-field term. Along this direction a wave pattern with a $\pi$ phase shift with respect to the far-field term is present, which exactly corresponds to the intermediate term.
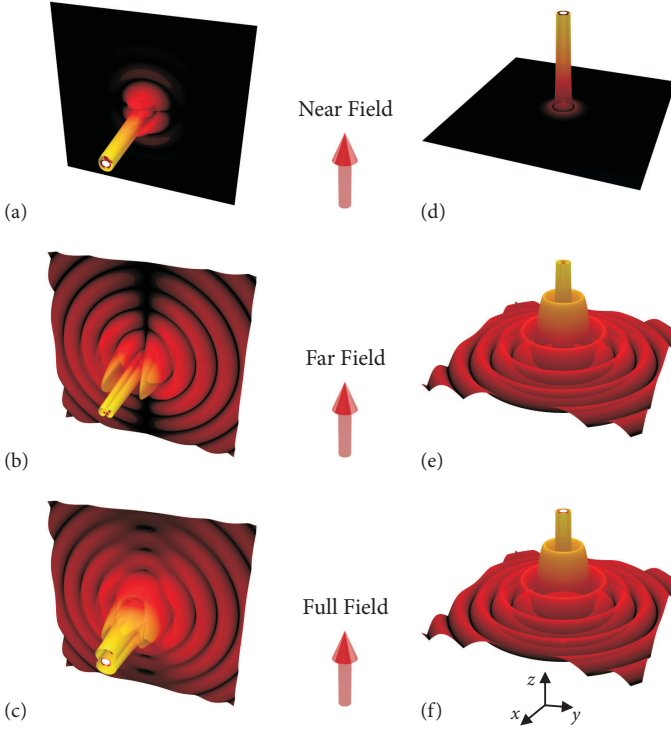
FIGURE 2.1. Near-, far-, and full absolute electric field $|\mathbf{E}|$ of a Hertzian dipole calculated by eqs. 2.23, 2.25 and 2.26. The dipole is located at the origin and oriented along $z$ direction. (a-c) Field in the $yz$ plane ($x = 0$), parallel to the dipole. (d-f) Field in the $xy$ plane ($z = 0$), perpendicular to the dipole.

Based on these considerations, it is possible to make a clear distinction between the regimes of plasmonic coupling which will be discussed in the upcoming chapters: in the near-field regime the coupling is mediated by the near fields. This means that a quasistatic approximation is sufficient in order to describe the effects. For the far-field regime, however, the oscillating properties of the fields will be crucial. Finally, chapter 6 will deal with the special case of coupling in the intermediate regime.

## 2.2   THE HARMONIC OSCILLATOR

The essence of light-matter interaction is the description of the inter-play between electromagnetic waves and the electrons confined in a medium, no matter whether it is a gas, a fluid or a solid. In a solid, the electrons are either bound or can move freely, leading to many different effects and phenomena. Nonetheless, many of those can be captured—at least qualitatively—within a very simple, yet universal model which despite its simplicity succeeds in describing them correctly. This model is the harmonic oscillator, which is well-known throughout and beyond physics.

In this classical model, which is known as the Lorentz oscillator model, the electrons are bound by harmonic forces to the atomic cores. These exert a restoring force on the electrons, therefore they undergo harmonic oscillations when driven by a periodic, external (light) field. This is captured by the basic differential equation [103, 104]

$$m_e \frac{\partial^2}{\partial t^2}\mathbf{x} + 2m_e\gamma \frac{\partial}{\partial t}\mathbf{x} + m_e\omega_o'^2\mathbf{x} = -e\mathbf{E}(t), \tag{2.27}$$

where $m_e$ is the electron mass, $x$ the particle displacement from equi-librium, $\gamma$ a damping constant, $\omega_o'$ the oscillation frequency of the free, undamped oscillator, $e$ the elementary charge, and $E(t)$ the external light field. We solve it by using the harmonic ansatz

$$\mathbf{E}(t) = \mathbf{E_o}\, e^{-i\omega t}$$
$$\mathbf{x}(t) = \mathbf{x}(\omega)\, e^{-i\omega t}.$$

Inserting this into eq. 2.27, we obtain a frequency-dependent solution for the oscillation amplitude

$$\mathbf{x}(\omega) = \frac{e}{m_e} \frac{1}{\omega^2 - \omega_o'^2 + 2i\gamma\omega}\mathbf{E_o}.$$

This expression can be used to derive the microscopic electric polar-ization as

$$\mathbf{P}(\omega) = -N_e e\mathbf{x}(\omega) = -\frac{N_e e^2}{m_e} \frac{1}{\omega^2 - \omega_o'^2 + 2i\gamma\omega}\mathbf{E_o}, \tag{2.28}$$

where $N_e$ denotes the number of electrons interacting with the light field. Using the definition of **P**, eq. 2.7, we find an expression for the electric susceptibility in the oscillator model,

$$\chi(\omega) = -\frac{\omega_p^2}{\omega^2 - \omega_o'^2 + 2i\gamma\omega}, \tag{2.29}$$

where the plasma frequency $\omega_p^2 = (N_e e^2)/(m_e \varepsilon_o)$ has been introduced. It is possible to decompose this fraction into

$$\chi(\omega) = -\frac{\omega_p^2}{2\omega_o} \left( \frac{1}{\omega - \omega_o + i\gamma} - \frac{1}{\omega + \omega_o + i\gamma} \right),$$

with $\omega_o^2 = \omega_o'^2 - \gamma^2$. The resonance can therefore be parametrized by two poles in the complex frequency plane located at $\omega_{1,2} = \pm\omega_o - i\gamma$. From a physical point of view, the additional assumption $\gamma \ll \omega_o$ is reasonable. Therefore, it is a good approximation to neglect the pole at negative frequency and the final form of the susceptibility is

$$\chi(\omega) \approx -\frac{\omega_p^2}{2\omega_o} \frac{1}{\omega - \omega_o + i\gamma}. \tag{2.30}$$

To construct the complex dielectric function of a material it may be necessary to consider several elementary excitations so that the general result incorporates a summation over all possible oscillator terms,

$$\varepsilon(\omega) = 1 - \sum_n \frac{f_n}{\omega - \omega_{o,n} + i\gamma_n}, \tag{2.31}$$

where $f_n$ is an oscillator strength which has to be obtained by additional considerations.

## 2.3 OPTICS OF METALS

### 2.3.1 *Bulk Optical Properties of Noble Metals*

The peculiar physical properties of metals arise predominantly from the presence of free electrons, which is owed to the specific electronic configuration of the constituent atoms. In a simple picture, the free electrons emerge in the transition from a single atom to a crystal lattice from the electrons located in the partially populated outer shells.

While this is true for many elements in the periodic table, those with one electron located in the outer shell form metals with very high free carrier density and conductivity compared to their direct neighbors. The most prominent of these are the elements in group Ib, namely the noble metals copper, silver and gold. This group is characterized by fully populated d-bands with a single s-electron in the outer shell, thus the members of this group exhibit the highest conductivity of all elemental compositions, even at high frequencies, where they possess only little absorption up to visible wavelengths.

The free electrons dominate the linear optical properties of metals. In order to describe these, it is possible to utilize the Lorentz oscillator model derived above, with a small modification: as no restoring force acts on free electrons, the resonance frequency is set to $\omega'_\mathrm{o} = 0$ in eq. 2.29. This description is known as the Drude model for the optical properties of metals. The free electron permittivity yields

$$\varepsilon_\mathrm{D}(\omega) = 1 - \frac{\omega_\mathrm{p}^2}{\omega^2 + i\gamma_\mathrm{D}\omega}, \tag{2.32}$$

which can be split into a real and an imaginary part:

$$\varepsilon_\mathrm{D,1}(\omega) = 1 - \frac{\omega_\mathrm{p}^2}{\gamma_\mathrm{D}^2 + \omega^2}$$

$$\varepsilon_\mathrm{D,2}(\omega) = \frac{\omega_\mathrm{p}^2 \gamma_\mathrm{D}}{\omega\gamma_\mathrm{D}^2 + \omega^3}. \tag{2.33}$$

Here, $\omega_\mathrm{p}$ denotes the bulk plasma frequency as defined above and $\gamma_\mathrm{D}$ is the damping or collision frequency. The plasma frequency $\omega_\mathrm{p}$ is the characteristic parameter for the description of bulk plasma oscillations. For frequencies below $\omega_\mathrm{p}$ the electrons reconfigure as a response to the external field and compensate it. Therefore, only an evanescent wave can penetrate the metal and $\varepsilon_1(\omega)$ is negative. Above the bulk plasma frequency $\varepsilon_1(\omega > \omega_\mathrm{p}) > 0$, electromagnetic waves can propagate in the metal—it becomes transparent.

In general, a correction to $\omega_\mathrm{p}$ is necessary to account for the specific band structure of the considered metal. Therefore, an effective mass $m^*$ is used to obtain correct results. However, due to the specialty of gold and silver in terms of electron configuration, their effective mass is almost exactly 1.

The phenomenological parameter $\gamma_\mathrm{D}$ is introduced into the classical model to describe collisions of electrons with the lattice and therefore a

damping of the electron motion which leads to the material resistivity. This is not true from a quantum mechanical point of view, and the parameter $\gamma_D$ has to be interpreted as a damping constant which occurs due to collisions with deviations from the periodic structure of the crystal such as phonons or impurities.

The Drude model gives a good parametrization of $\varepsilon(\omega)$ for noble metals, as long as no interband transitions are involved. The lowest-energy interband transition for the noble metals considered here is the d-band transition. For silver it occurs in the UV-regime, at approximately 920 THz ($\lambda \approx 320$ nm) [15]. This is the reason for the excellent flat reflectivity and low absorption of silver throughout the whole optical regime.

For gold, this transition already occurs around 580 THz ($\lambda \approx 510$ nm), leading to substantial absorption above this frequency [15]. Even at lower frequencies down to 500 THz (wavelengths up to $\lambda = 600$ nm), its influence on $\varepsilon(\omega)$ can be observed in terms of a deviation from perfect Drude-like behavior. This accounts for the typical yellow-reddish color of gold and causes absorption which makes gold less usable for the visible wavelength range, at least for the blue side of the spectrum.

The optical properties of gold in the infrared and visible region have been determined by a multitude of researchers using different methods [105–115] and are extensively tabulated [116, 117]. Fig. 2.2 (a) gives an overview over the measured permittivity obtained from various experiments in the relevant frequency range. The overall consistency is quite good, given the fact that different measurement methods and sample preparation techniques have been used. Only $\varepsilon_2$ in data set I [114] shows substantial deviation from the other measurements.

As a great variety of different values for $\omega_p$ and especially $\gamma_D$ have been reported, we thoroughly reexamine these with respect to the experimental data. For example, Ordal et al. [117] report $\gamma_D = 6.5$ THz, however, this value does not show a good parametrization of the experimental $\varepsilon(\omega)$ at least in the near-infrared region considered here.

We use a nonlinear curve fitting approach to retrieve $\omega_p$ and $\gamma_D$ from different experimental data sets using eq. 2.33. Only the spectral range below 480 THz ($\approx 2$ eV, 620 nm) is considered to avoid any contribution from the interband transition. In the first iteration step the initial values $\omega_p = 2000$ THz and $\gamma_D = 1$ THz are used to fit $\varepsilon_{D,1}$. The obtained value for $\omega_p$ fits quite reliable, as $\varepsilon_{D,1}$ is rather robust against changes of $\gamma_D$. The retrieved values are then used as initial parameters for the fit
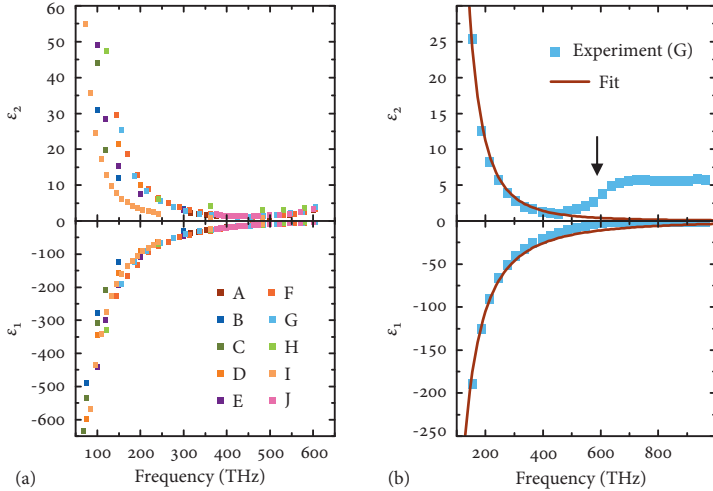
FIGURE 2.2.    (a) Overview of different measurements of $\varepsilon(\omega)$ of gold, obtained by different methods: Schulz (A) [105], Padalka and Shkliarevskii (B) [106], Bolotin et al. (C) [107], Dold and Mecke (D) [108], Motulevich and Shubin (E) [109], Thèye (F) [111], Johnson and Christy (G) [112], Hagemann et al. (H) [113], Weaver et al. (I) [114] and Innes and Sambles (J) [115].    (b) Experimental data of Johnson and Christy (G) [112]. The red line denotes a Drude model fit with $\omega_p$ = 2073 THz and $\gamma_D$ = 21.1 THz. In the frequency range below the interband transition, the optical properties show a very good agreement with the Drude model. The interband transition frequency located slightly below 600 THz is denoted by the black arrow. Already at 500 THz a pronounced deviation from Drude behavior is observed.

of $\varepsilon_{D,2}$. In this second step, $\omega_p$ is kept fixed. The procedure is repeated until the fits to both curves converge and yield similar values.

The retrieved parameters are collected in table 2.1. Apart from data sets D and H, a simultaneous fit of both curves with one set of parameters is not possible. The fit of $\varepsilon_{D,1}$ tends to overestimate $\gamma_D$ while $\omega_p$ often has to be kept fixed in the fit of $\varepsilon_{D,2}$. This is particularly true for the data sets in the infrared and visible frequency range, F and G. In this case, it is reasonable to obtain the value for $\omega_p$ from the $\varepsilon_{D,1}$ data and the value for $\gamma_D$ from the $\varepsilon_{D,2}$ data.

Examining the values of table 2.1, one finds, that the values for $\omega_p$ are more or less consistent, only data set B deviates. In contrast, there is

| DATA SET | SPECTRAL RANGE | FIT OF $\varepsilon_1$ | | FIT OF $\varepsilon_2$ | |
|---|---|---|---|---|---|
| | | $\omega_p$ | $\gamma_D$ | $\omega_p$ | $\gamma_D$ |
| | THz | THz | THz | THz | THz |
| B [106] | 27–300 | 1680 | 10.3 | 1680F | 8.2 |
| C [107] | 31–120 | 1808 | 18.9 | 1826 | 12.4 |
| D [108] | 30–240 | 1933 | 20.0 | 1933F | 11.8 |
| E [109] | 25–300 | 2089 | 8.8 | 2089F | 10.6 |
| F [111] | 145–600 | 2158 | 0.0 | 2158F | 19.8 |
| G [112] | 155–600 | 2073 | 0.0 | 2073F | 21.1 |
| H [113] | 1–580 | 1801 | 11.9 | 1802 | 11.3 |
| I [114] | 24–480 | 2021 | 4.0 | 2021F | 4.9 |
| J [115] | 370–430 | 1859 | 0.0 | 1859F | 28.6 |
| K [110] | 9–100 | 2173 | 6.3 | 2189 | 6.4 |

TABLE 2.1. Fitted Drude parameters for gold retrieved from the different experimental determinations of the optical constants. Values that were kept fixed in an iteration are marked by "F".

a huge spread in the values of $\gamma_D$. Data set J has to be treated separately, here a strong deviation of the retrieved values from those originally reported in the paper itself is found. This is attributed to the selection of the data range, which is restricted to frequencies above 370 THz. Therefore, almost no information in the infrared region is contained in the numerical data, which makes a reliable fit impossible. The other values reported for $\gamma_D$ are consistently lower, with the lowest values obtained from data sets I and K. Apparently low values for $\gamma_D$ are predominantly found in measurements which incorporate the far-infrared regime well below 100 THz, while data sets in the near infrared yield substantially higher values around $\gamma_D \approx 20$ THz.

The experimental data of Johnson and Christy [112] (data set G) is usually considered as authoritative for the optical properties of gold in the near-infrared and visible regime and is well confirmed by the measurement of Thèye [111] (data set F). The data set of Johnson and Christy is shown in Fig. 2.2 (b) alongside with the fitting result. The parameters are $\omega_p$ = 2073 THz and $\gamma_D$ = 21.1 THz, which are similar to those retrieved from the data of Thèye. Furthermore, the graph clearly shows the deviation from Drude-like behavior when approaching the interband transition, which is marked by a black arrow. For the optical and near-infrared range, the two data sets, F and G, give a reasonable agreement to experiments and confirm each other.

It is apparent from these considerations, that a retrieval of the Drude parameters always has to account for the respective spectral range. The assumption of a frequency-independent parameter $\gamma_D$ does not reflect physical reality. The electrons in a real metal behave more complex than suggested by the free-electron assumption. For example, electron-electron interaction effects are present which lead to a frequency-dependence in $\gamma_D$ [111, 118]. Therefore, the Drude model should be utilized as no more than an easy possibility to parametrize the optical properties of metals by only two parameters, without a physical over-interpretation of the obtained constants [117]. In order to give a more precise description it is of course possible to use the tabulated experimental values directly. Furthermore, a more detailed parametrization using additional resonant terms to account for the interband transitions can be implemented as well [119, 120].

### 2.3.2   *Surface Plasmons*

Besides the excitation of volume plasmons in bulk metal, which has been described in the previous section, it is also possible to excite electron oscillations on metallic surfaces and thin films [26]. These surface modes consist of light waves traveling along the surface in conjunction with electron oscillations in the metal, thus they are termed surface plasmon polaritons (SPPs) [121]. Their **k** vector lies in the surface plane, while their electric fields decay evanescently with increasing distance from the surface.

From the continuity relations (eqs. 2.16 to 2.19) their dispersion relation can be derived, assuming one dielectric and one metallic half-space. This results in

$$k_\parallel = k_{in}\sqrt{\frac{\varepsilon_m \varepsilon_d}{\varepsilon_m + \varepsilon_d}}, \tag{2.34}$$

where $k_\parallel$ is the angular wavenumber of the excited SPP, $k_{in}$ the angular wavenumber of the exciting light, and $\varepsilon_{m,d}$ are the permittivity of the metal and the dielectric. To obtain a propagating SPP, $k_\parallel$ has to be real, and because of $\varepsilon_m < 0$, the additional requirement $|\varepsilon_m| > \varepsilon_d$ has to be fulfilled.

One can infer from eq. 2.34 that their spectral position is very sensitive to the optical properties of the metal and the dielectric, which makes them useful for the determination of $\varepsilon(\omega)$ of the metal [30], but also for a multitude of sensing applications [122]. However, as their dispersion curve does not cross the light cone, they do not directly couple to the light field. This is on the one hand of advantage, because their spectral width is quite narrow, which further benefits the sensing applications. On the other hand it requires quite some effort to excite them, which usually is accomplished by applying special excitation geometries [29, 30] to match the **k** vectors of light and SPP.

This problem is overcome when the lateral uniformity of the film is broken, for example by the transformation from a film to a structured array of metallic nanoparticles. Then the so-called localized surface plasmon resonance (LSPR) is excited which corresponds to a SPP restricted to the finite surface of the nanoparticle. These localized resonances are the subject of the remainder of this thesis and therefore will be discussed in detail in the upcoming section.

## 2.4    NANOPARTICLE OPTICS

### 2.4.1    *Mie Theory*

The description of electronic resonances in metallic nanoparticles in terms of SPPs traveling on their surface is one point of view. It is also possible to regard them as eigenmodes in a confined geometry. This point of view is subject to Mie theory.

In 1908, Mie was able to derive an analytical solution to the scattering of a spherical particle with distinct permittivity and permeability without using any further assumptions [22]. Therefore, the theory is able to give analytical results over the whole spectrum and for arbitrarily sized spheres. It was extended to ellipsoidal particles later [123].

Mie theory is among a set of only very few examples of an exact analytical solution to a physical problem. Here we review its basic ideas and then proceed to the limit of particles small compared to the wavelength, which is the most interesting case for the description of plasmonic nanoparticles.

The basic geometry is given in Fig. 2.3. Light polarized along the $x$ direction impinges on a spherical particle with radius $a$. Its permittivity and permeability are $\varepsilon_1$ and $\mu_1$, and it is embedded into a medium with $\varepsilon_2$ and $\mu_2$.
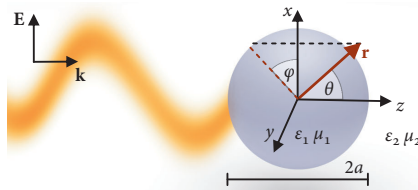


FIGURE 2.3. Schematic geometry for the calculation of Mie scattering by a sphere.

To solve the problem of scattering by the spherical particle it is necessary to find a solution to the Helmholtz equation for the electric and magnetic field: $\mathbf{E}$ and $\mathbf{H}$ in spherical polar coordinates:

$$\nabla^2 \mathbf{E} + k^2 \mathbf{E} = 0$$
$$\nabla^2 \mathbf{H} + k^2 \mathbf{H} = 0.$$

(2.35)

This problem can be transformed to the solution of a scalar Helmholtz equation by constructing the so-called vector spherical harmonic functions.

These can be found by considering

$$\mathbf{M} = \nabla \times (\mathbf{r}\psi)$$
$$\mathbf{N} = \frac{1}{k}\nabla \times \mathbf{M},$$

(2.36)

where $\mathbf{r}$ is the position vector. It can be shown [124] that $\mathbf{M}$ and $\mathbf{N}$ not only are a solution to eq. 2.35 as soon as $\psi$ solves the scalar Helmholtz equation $\nabla^2\psi + k^2\psi = 0$, additionally $\nabla \cdot \mathbf{M} = \nabla \cdot \mathbf{N} = 0$ as well as $\nabla \times \mathbf{N} = k\mathbf{M}$ and $\nabla \times \mathbf{M} = k\mathbf{N}$, properties which closely resemble the relation of electric and magnetic fields in Maxwell's equations.

Solutions to the scalar Helmholtz equation are of the form

$$\psi_{emn} = \cos m\varphi \, P_n^m(\cos\theta) \, z_n(kr)$$
$$\psi_{omn} = \sin m\varphi \, P_n^m(\cos\theta) \, z_n(kr),$$

(2.37)

where $P_n^m(\cos\theta)$ denotes the associated Legendre polynomials and $z_n(kr)$ is a wild card for any of the spherical Bessel- or Hankel functions $j_n$, $y_n$, $h_n^{(1)}$ or $h_n^{(2)\,\text{iii}}$.

The major step of solving the problem is the expansion of a linearly polarized plane wave $\mathbf{E} = E_0\hat{\mathbf{e}}_x \exp(ikr\cos\theta)$ in the basis of vector spherical harmonics introduced above. A lengthy calculation [124] yields the expansion

$$\mathbf{E} = E_0 \sum_{n=1}^{\infty} i^n \frac{2n+1}{n(n+1)} \left(\mathbf{M}_{o1n}^j - i\mathbf{N}_{e1n}^j\right),$$

(2.38)

where only two of the several possible vector spherical harmonic functions are needed, namely[iv]

$$\mathbf{M}_{o1n}^z = \nabla \times \left(\mathbf{r}\sin\varphi \, P_n^1(\cos\theta) \, z_n(kr)\right)$$
$$\mathbf{N}_{e1n}^z = \frac{1}{k}\left[\nabla \times \left(\nabla \times \left(\mathbf{r}\cos\varphi \, P_n^1(\cos\theta) \, z_n(kr)\right)\right)\right].$$

(2.39)

---

iii see appendix A.1 for the definitions

iv The superscript $z$ in $\mathbf{M}_{o1n}^z$ and $\mathbf{N}_{e1n}^z$ denotes which Bessel or Hankel function has to be inserted for $z_n$. Possibilities are $j$, $y$ or $h$, the latter indicates $h_n^{(1)}$.

Using the coefficient $E_n = E_0 i^n (2n+1)/(n(n+1))$, the internal and scattered fields of the sphere then can be written in the following way:

$$\mathbf{E}_{\text{int}} = \sum_{n=1}^{\infty} E_n \left( c_n \mathbf{M}_{o1n}^j - i d_n \mathbf{N}_{e1n}^j \right)$$

$$\mathbf{H}_{\text{int}} = \frac{-k_1}{\omega \mu_1} \sum_{n=1}^{\infty} E_n \left( d_n \mathbf{M}_{e1n}^j + i c_n \mathbf{N}_{o1n}^j \right)$$

$$\mathbf{E}_{\text{sca}} = \sum_{n=1}^{\infty} E_n \left( i a_n \mathbf{N}_{e1n}^h - b_n \mathbf{M}_{o1n}^h \right)$$

$$\mathbf{H}_{\text{sca}} = \frac{k_2}{\omega \mu_2} \sum_{n=1}^{\infty} E_n \left( i b_n \mathbf{N}_{o1n}^h + a_n \mathbf{M}_{e1n}^h \right).$$

(2.40)

Here, $k_1$ and $\mu_1$ are the wavenumber and magnetic permeability inside the sphere, and $k_2$, $\mu_2$ those of the surrounding. According to these results, the electric and magnetic field inside the sphere can be written as a linear combination of Bessel functions, outside the sphere the scattered fields are given as linear combinations of Hankel functions $h_n^{(1)}$. This result is quite general, as up to now only the spherical symmetry of the system and the material parameters of sphere and surrounding have been used. The size dependence, however, is completely contained in the coefficients $a_n$, $b_n$, $c_n$, and $d_n$. In our case, the internal field is not of interest, hence we will only pursue the calculation of the external coefficients $a_n$ and $b_n$. These are derived from the boundary conditions, eqs. 2.16 to 2.19, namely the continuity of the tangential component of the electric and magnetic field on the surface of the sphere, thus

$$\left( \mathbf{E}_{\text{int}}(r = a) + \mathbf{E}_{\text{ext}}(r = a) - \mathbf{E}(r = a) \right)_{\parallel} = 0$$

$$\left( \mathbf{H}_{\text{int}}(r = a) + \mathbf{H}_{\text{ext}}(r = a) - \mathbf{H}(r = a) \right)_{\parallel} = 0.$$

(2.41)

These are evaluated component-wise for the $\theta$ and $\varphi$ component, which yields the scattering parameters

$$a_n = \frac{v \Psi_n(vx) \Psi_n'(x) - \Psi_n(x) \Psi_n'(vx)}{v \Psi_n(vx) \Xi_n'(x) - \Xi_n(x) \Psi_n'(vx)}$$

$$b_n = \frac{\Psi_n(vx) \Psi_n'(x) - v \Psi_n(x) \Psi_n'(vx)}{\Psi_n(vx) \Xi_n'(x) - v \Xi_n(x) \Psi_n'(vx)}.$$

(2.42)

Here for simplicity $\mu_1 = \mu_2 = 1$ is assumed, the relative refractive index is $v = \sqrt{(\varepsilon_1/\varepsilon_2)} = n_1/n_2$, $x = k_2 a = 2\pi n_2 a/\lambda$ is the size parameter, the

prime indicates a derivative with respect to the given argument, and the Riccati-Bessel functions have been introduced:

$$\Psi_n(X) = Xj_n(X)$$
$$\Xi_n(X) = Xh_n^{(1)}(X). \tag{2.43}$$

Considering the energy fluxes allows for the computation of absorption as well as scattering cross section of the sphere [124]:

$$C_{\text{sca}} = \frac{2\pi}{k_2^2} \sum_{n=1}^{\infty} (2n+1)\left(|a_n|^2 + |b_n|^2\right)$$
$$C_{\text{abs}} = \frac{2\pi}{k_2^2} \sum_{n=1}^{\infty} (2n+1)\,\mathfrak{Re}\left(a_n + b_n\right). \tag{2.44}$$
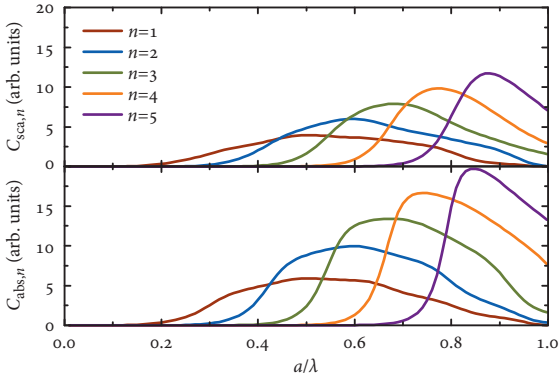


FIGURE 2.4. Calculated Mie scattering (top panel) and absorption (bottom panel) coefficients for a sphere with $n_1 = 1.5$ embedded into vacuum ($n_2 = 1$). The summands of eq. 2.44 are shown in dependence of the ratio of sphere radius $a$ and wavelength $\lambda$. For small particles it is appropriate to neglect the higher order modes and only consider $a_1$ and $b_1$.

Fig. 2.4 shows the summation coefficients up to $n = 5$ for $C_{\text{sca}}$ as well as $C_{\text{abs}}$. It is obvious that for small particles contributions of $n > 1$ can be neglected and only $a_1$ and $b_1$ are of importance. As an additional simplification, it is sufficient to expand $\Psi_1$ and $\Xi_1$ into a series for small $x$ instead of considering the exact function. Doing so and taking only the lowest possible order terms, only $a_1$ remains and is given by

$$a_1 = -i\frac{2x^3}{3}\frac{v^2-1}{v^2+2}. \tag{2.45}$$

Inserting this into eq. 2.44 yields the absolute scattering and absorption cross sections for a small sphere

$$
\begin{aligned}
C_{\text{sca}} &\propto \frac{a^6}{\lambda^4} \left| \frac{v^2 - 1}{v^2 + 2} \right|^2 \\
C_{\text{abs}} &\propto \frac{a^3}{\lambda} \Im \left( \frac{v^2 - 1}{v^2 + 2} \right).
\end{aligned}
\tag{2.46}
$$

From these equations, several fundamental conclusions can be drawn. First, the scattering of a small sphere shows a pronounced dependence on the wavelength to the fourth power. The $1/\lambda^4$ dependence of the scattering cross section has been derived by Lord Rayleigh [19, 20] in his explanation of the color of the sky and is hence commonly referred to as Rayleigh scattering. Scattering by small particles is more efficient for shorter light wavelengths, therefore predominantly blue light is scattered in the atmosphere leading to a blue colored sky.

Second, the relative fraction of scattered and absorbed light is of interest: scattering is proportional to $a^6$ and absorption to $a^3$. For particles very small compared to the wavelength, absorption always surpasses scattering. For larger particles scattering is increasingly important and finally dominates over absorption.

Finally, the quotient containing the material dependence has to be investigated. For identical materials and thus vanishing material contrast this factor is 0 and neither extinction nor scattering take place, which is in accordance with common sense. For dielectric, non-absorbing media, the factor is purely real and $C_{\text{abs}}$ vanishes. However, the refractive index contrast leads to a finite scattering. In this limit, the dispersion usually can be neglected and the fraction yields a constant factor between $-1/2$ and 1, depending on the refractive indices. For more complicated materials with complex and frequency-dependent $\varepsilon$ it is convenient to rewrite the fraction to read

$$
\frac{\varepsilon_1 - \varepsilon_2}{\varepsilon_1 + 2\varepsilon_2}.
\tag{2.47}
$$

This form will appear again below, where it is obtained from another point of view.

### 2.4.2 Electrostatic Approximation

As elaborated above, the beauty of Mie theory is to deliver an exact theory for the interaction of light with a spherical particle. However, it

is apparent that the description is rather complicated and even in the most simple cases exact expressions are lengthy.

The electrostatic approximation is a different approach. While Mie theory gives the description for arbitrary sized spheres, the electrostatic approximation is only valid for small particles. One benefit is the applicability to more complex structures, which is at least possible for ellipsoidal particles.

In the electrostatic approach the spherical particle is assumed to be sufficiently small to describe the external electromagnetic wave as a constant static electric field across the extent of the nanoparticle. This implies a simplification of the considered problem from the solution of the Helmholtz equation (eq. 2.35) to the solution of the Laplace equation for the electrostatic potential:

$$\nabla^2 \Phi = 0. \tag{2.48}$$

The electric field is assumed to be constant and pointing into $z$ direction: $\mathbf{E}_0 = E_0 \hat{\mathbf{e}}_z$. This problem exhibits a cylindrical symmetry, therefore a series expansion in terms of Legendre polynomials inside and outside the sphere is feasible [101]:

$$
\begin{aligned}
\Phi_{\text{in}} &= \sum_{n=0}^{\infty} u_n r^n P_n(\cos\theta) \\
\Phi_{\text{out}} &= \sum_{n=0}^{\infty} \left( v_n r^n + w_n^{-l-1} \right) P_n(\cos\theta).
\end{aligned}
\tag{2.49}
$$

Here $\Phi_{\text{in}}$ and $\Phi_{\text{out}}$ denote the potential inside and outside the sphere, and $P_n(\cos\theta)$ are the Legendre polynomials[v]. The other parameters follow the definitions in Fig. 2.3.

The expansion coefficients $u_n$, $v_n$, and $w_n$ are determined from the boundary conditions at the surface of the sphere, where $E_\parallel$ and $D_\perp$ have to be continuous, as well as for $r \to \infty$, where the influence of the sphere has to vanish, and only the applied external field remains. This yields the internal and external potential:

$$
\begin{aligned}
\Phi_{\text{in}} &= -\frac{3\varepsilon_2}{\varepsilon_1 + 2\varepsilon_2} E_0 r \cos\theta \\
\Phi_{\text{out}} &= -E_0 r \cos\theta + \frac{\varepsilon_1 - \varepsilon_2}{\varepsilon_1 + 2\varepsilon_2} E_0 a^3 \frac{\cos\theta}{r^2}.
\end{aligned}
\tag{2.50}
$$

v  see appendix A.1 for definitions

The internal potential corresponds to the potential of the external field modified by the dielectric properties of the sphere. The potential outside the sphere is way more interesting and its expression can be simplified by introducing a point dipole potential

$$p = 4\pi\varepsilon_0\varepsilon_1 a^3 \frac{\varepsilon_1 - \varepsilon_2}{\varepsilon_1 + 2\varepsilon_2} E_0 \cos\theta \tag{2.51}$$

so that $\Phi_{\text{out}}$ is the sum of the external static field potential and that of an electrostatic point dipole located at the center of the sphere.

From this, the electric field can be calculated, which yields

$$\mathbf{E}_{\text{out}} = -\nabla\Phi_{\text{out}} = \mathbf{E}_0 + \frac{3\mathbf{n}(\mathbf{n}\cdot\mathbf{p}) - \mathbf{p}}{4\pi\varepsilon_0\varepsilon_2}\frac{1}{r^3} \tag{2.52}$$

with the dipole moment

$$\mathbf{p} = 4\pi\varepsilon_0\varepsilon_2 a^3 \frac{\varepsilon_1 - \varepsilon_2}{\varepsilon_1 + 2\varepsilon_2}\mathbf{E}_0. \tag{2.53}$$

This allows to derive the polarizability of the sphere, given the definition [125]

$$\mathbf{p} = \varepsilon_0\varepsilon_2\alpha\mathbf{E}_0$$
$$\Rightarrow \alpha = 4\pi a^3 \frac{\varepsilon_1 - \varepsilon_2}{\varepsilon_1 + 2\varepsilon_2}. \tag{2.54}$$

This factor strongly resembles the $a_1$ coefficient obtained from Mie theory for a small particle (eq. 2.45), apart from a constant factor and the absence of a dependence on $\lambda$, which is not surprising, as it results from an electrostatic calculation.

### 2.4.3  Ellipsoid Particles

The electrostatic approximation can also be carried out for ellipsoid particles with semiaxes $a_1 \leqslant a_2 \leqslant a_3$. In spite of rather complicated math, the resulting polarizability is quite similar:

$$\alpha_j = 4\pi a_1 a_2 a_3 \frac{\varepsilon_1 - \varepsilon_2}{3\varepsilon_2 + 3L_j(\varepsilon_1 - \varepsilon_2)}. \tag{2.55}$$

Here $\alpha_j$ denotes the polarizability along the $j$th axis. The $L_j$ are given by the expression

$$L_j = \frac{a_1 a_2 a_3}{2}\int_0^\infty \frac{dq}{\left(a_j^2 + q\right)\sqrt{\left(a_1^2 + q\right)\left(a_2^2 + q\right)\left(a_3^2 + q\right)}}. \tag{2.56}$$

For the special case of a spherical particle, $a_1 = a_2 = a_3$, the factor $L_j = 1/3$ and the result is reduced to that of eq. 2.54. For more complicated cases it is usually necessary to evaluate $\alpha_j$ numerically. This will be done in the following paragraph for special cases.

### 2.4.4  Metallic Nanoparticles: Particle Plasmons

The use of the electrostatic approach described in the previous paragraph has been applied to nanoparticle optics with an enormous success. The transition to optics is accomplished by reinterpreting the DC permittivities $\varepsilon_i$ as their frequency-dependent counterparts[vi] $\varepsilon_i(\omega)$. As long as the particle dimensions are well below the wavelength, this approach is quite reasonable and the obtained results are in quite good agreement with the experiments.

As stated before, the permittivity of dielectric materials is varying only slowly with frequency in the spectral region of interest and the quotient $(\varepsilon_1 - \varepsilon_2)/(\varepsilon_1 + 2\varepsilon_2)$ is a constant factor for dielectric particles. In this case, the polarizability shows no strong dependence on the wavelength and is mainly dominated by the particle size.

This changes drastically for metallic particles. For these, the real part of the dielectric constant is negative and the denominator approaches 0 whenever the condition

$$\mathfrak{Re}\ \varepsilon_1 = -2\varepsilon_2 \tag{2.57}$$

is fulfilled. This means that resonances in the particle polarizability $\alpha$ occur. These arise due to the excitation of electronic oscillations inside the particle and thus are termed particle plasmon resonance (PPR)[vii].

Assuming a Drude model (eq. 2.32) for $\varepsilon_1$, the PPR for a spherical particle in vacuum according to eq. 2.57 is located at $\omega_{PPR}^2 = 1/3\omega_p^2$, when neglecting losses in the metal. Surprisingly, the resonance position only depends on the material properties and not on size [126]. However, this is only true for very small particles, with dimensions on the order of the skin depth. For larger particles one has to include corrections leading to a size dependence.

---

vi  For simplicity the indication of $\omega$-dependence will be skipped in the following. However, the appearance of $\varepsilon$ will imply the frequency-dependent quantity $\varepsilon(\omega)$.

vii  As stated in the previous chapter, from the viewpoint of propagating SPPs on the particle surface, often the term localized surface plasmon resonance (LSPR) is used. However, for consistency and to avoid confusion with propagating SPPs we will only use the term PPR in the following.
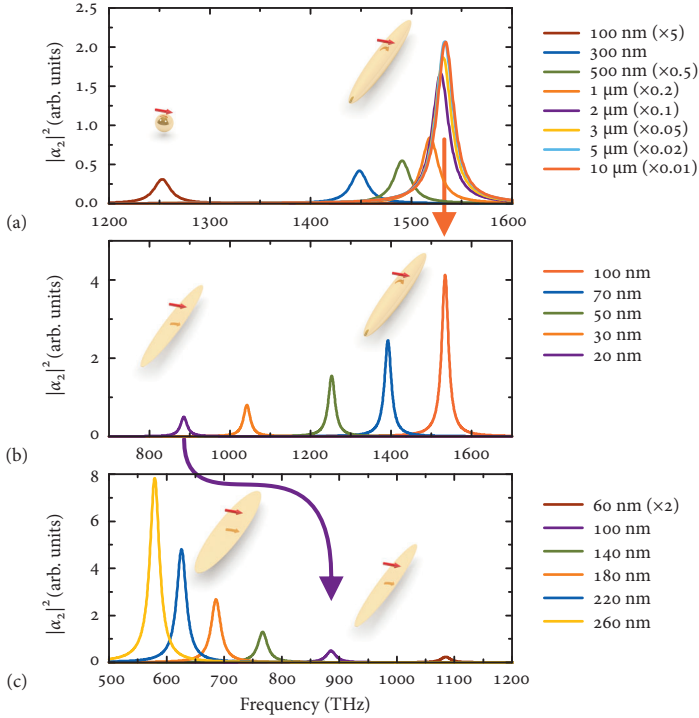
FIGURE 2.5. Analytically calculated spectra for metallic ellipsoid particles with varying parameters $a_1$, $a_2$, and $a_3$. The graphs show the absolute square value of polarizability along the second axis, $|\alpha_2|^2$. (a) Variation of $a_1$ from 100 nm to 10 µm for constant $a_2 = a_3 = 100$ nm. The spectral change upon transformation from a sphere to a strongly elongated particle with extreme aspect ratio is shown. The spectra have to be scaled due to the large increase of polarizability. Additionally, a pronounced blue shift is observed. (b) Spectra for a decrease of $a_3$ for the 10 µm long particle with $a_2 = 100$ nm. On decreasing height the spectra shift to the red. (c) Tuning of the ellipsoid width $a_2$ for constant $a_1 = 10$ µm and $a_3 = 20$ nm. Along the axis of considered polarizability a size increase leads to a red shift of the resonance.

Using eq. 2.55 it is possible to calculate spectra of non-spherical metallic ellipsoids. As can be seen from the equation, the factor $L_j$ directly affects the resonance condition which in this case reads

$$\mathfrak{Re}\, \varepsilon_1 = \varepsilon_2 \left(1 - \frac{1}{L_j}\right). \tag{2.58}$$

Consequently, the spectral position of the PPR strongly depends on the $L_j$ coefficients and thus on the exact geometry of the particle.

This is demonstrated in Fig. 2.5, where the spectral changes for the transformation from a spherical metallic particle to an elongated, nano-wire-like ellipsoid are shown. These analytical calculations are performed using eq. 2.55 and Drude model optical constants (eq. 2.32 with $\omega_p$ = 2170 THz and $\gamma$ = 20 THz) for the particle. The polarizability $\alpha_2$ of the ellipsoid is investigated, as this will be the relevant case for the following chapters. The graphs show the absolute square value of $\alpha_2$, which is proportional to the scattering cross section of the particle. The evaluation of extinction yields spectrally similar results but different absolute numbers. In general, a strong dependence of the absolute value of $\alpha_2$ on the particle size is observed. This is attributed to the fact of $\alpha \propto (a_1 a_2 a_3)$, which is approximately the volume of the particle.

Starting from a spherical particle, Fig. 2.5 (a) shows the spectral dependence on elongation along the first axis. $a_1$ is increased by a factor of 100. This results in a substantial increase in scattering strength, so that the individual spectra have been scaled in order to fit the graph. At the same time the spectra exhibit a pronounced blue shift which starts to saturate above an aspect ratio of approximately 10. The final particle with a length of 10 μm is taken as a basis for the variation of the ellipsoid height in Fig. 2.5 (b). The particle is squeezed along the third axis by lowering the $a_3$ parameter from 100 nm, which corresponds to a cylindrically symmetric ellipsoid to a completely deformed ellipsoid with $a_3$ = 20 nm. The height reduction shifts the PPR to the red, accompanied by a reduction in scattering strength. Finally, the particle dimension along the axis of the external field, $a_2$, is changed. Starting from the particle with $a_1$ = 10 μm and $a_3$ = 20 nm the width of the ellipsoid is changed from 60 to 260 nm. In contrast to the other directions, a size increase along this direction results in a red shift instead of a blue shift. This can be intuitively understood, as the particle dimensions along the light polarization axis can be interpreted in terms of a resonator length for the oscillating electrons [127–129].

Even though these spectra originate from an analytical calculation for ellipsoid particles, they qualitatively reproduce all the essential features of the fundamental particle plasmon modes in metallic nanowires that are about to be treated in the upcoming chapters and thus provide an analytical model for their description.

## 2.5    RESONANT COUPLED OSCILLATOR MODEL

Even though full-Maxwell calculations are very helpful in the design and prediction of the spectra of systems under consideration, they suffer from the huge disadvantage of not being able to provide adequate understanding of the underlying physics of the coupling processes. Therefore we need a simple model which captures the essence of the physics that is contained in the radiative coupling of plasmonic structures.

This model has already been derived in semiconductor physics for the radiative coupling of excitons in multilayer quantum well (QW) structures [130, 131]. Even though being targeted at completely different structures, the model can be transferred without greater effort to the description of plasmonic structures. This is possible because the particle plasmon as well as the exciton can be regarded as a resonant response arising from electronic excitations in in a thin sheet of material. Thus, at least for the linear optical properties both behave similarly, even though they strongly differ in terms of their optical parameters. This will be discussed later in context of the experimental findings.
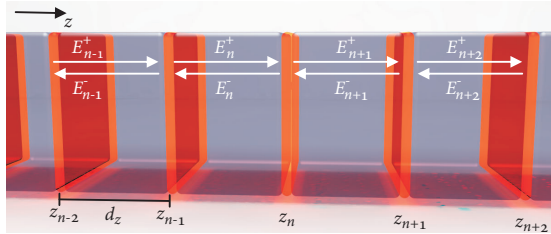


FIGURE 2.6. Schematic of the model system for the calculation of a structure of multilayered, radiatively coupled resonant sheets.

Fig. 2.6 displays a principal sketch of this coupled oscillator model. The system consists of a number $N$ of thin layers which are stacked along $z$ direction and are homogeneous in the plane perpendicular to it. They are separated by dielectric layers of a certain thickness $d_z$. The thickness of these spacer layers is large enough, such that on the one hand near-field coupling effects between the sheets can be safely neglected. On the other hand the thickness of the resonant sheets is sufficiently small compared to $d_z$ such that they can be considered as infinitely thin.

The wave equation derived from eqs. 2.1 to 2.4 for one polarization direction in the quasi-one-dimensional geometry then reads

$$\left(\frac{\partial^2}{\partial z^2} - \frac{1}{c^2}\frac{\partial^2}{\partial t^2}\right)E(z,t) = \frac{1}{\varepsilon_0 c^2}\frac{\partial^2}{\partial t^2}P(z,t). \tag{2.59}$$

The non-resonant polarization within the spacer layers is described in terms of a background refractive index, therefore, only the resonant polarization located in the infinitely thin resonant layers has to be included. This is

$$P(z,t) \approx \sum_{n=1}^{N} P_n(t)\delta(z-z_n),$$

where $\delta(z)$ is the Dirac delta distribution. For the electric field in the spacer between two resonant layers two counter-propagating waves are assumed, as depicted in Fig. 2.6:

$$E(z,t) = E_n^+(t - z/c) + E_n^-(t + z/c). \tag{2.60}$$

This model consequently only includes the radiative fields, and therefore, as already stated above, will not be able to describe near-field effects for small spacings.

The fields in the individual layers now have to be connected to each other by the appropriate boundary conditions. As an abbreviation we introduce

$$\mathcal{E}_n(z,t) = E_n^+(t - z/c) + E_n^-(t + z/c)$$

as the field in the $n$th layer. First, the tangential component of the electric field has to be continuous, therefore

$$\mathcal{E}_n(z_n,t) = \mathcal{E}_{n+1}(z_n,t). \tag{2.61}$$

Second, from eq. 2.59 one obtains

$$\begin{aligned}
\frac{\partial}{\partial z}\left(\mathcal{E}_{n+1}(z,t) - \mathcal{E}_n(z,t)\right)\Big|_{z=z_n} &= -\frac{1}{c}\frac{\partial}{\partial t}\left(\mathcal{E}_{n+1}(z_n,t) - \mathcal{E}_n(z_n,t)\right) \\
&= \frac{1}{\varepsilon_0 \varepsilon_{\mathrm{Sp}} c^2}\frac{\partial^2}{\partial t^2}P_n(t),
\end{aligned}$$

$$\tag{2.62}$$

where $\varepsilon_{Sp}$ is the permittivity of the spacer layer. From these boundary conditions one obtains

$$E_n^+(t - z/c) = E_1^+(t - z/c) - \frac{1}{2\varepsilon_0\varepsilon_{Sp}c} \sum_{m=1}^{n-1} \frac{\partial}{\partial t} P_m\left(t - \frac{z - z_m}{c}\right)$$

$$E_n^-(t - z/c) = E_{N+1}^-(t - z/c) - \frac{1}{2\varepsilon_0\varepsilon_{Sp}c} \sum_{m=n}^{N} \frac{\partial}{\partial t} P_m\left(t + \frac{z - z_m}{c}\right). \tag{2.63}$$

Here, $E_1^+$ and $E_{N+1}^-$ denote the incoming wave from the left and right side. Furthermore, one can make a harmonic ansatz for the fields and the polarizability

$$E_n^\pm = E_{n,o}^\pm \, e^{-i\omega t}$$
$$P_n = P_{n,o} \, e^{-i\omega t}. \tag{2.64}$$

The polarizability of one layer is given by

$$P_n(t) = \varepsilon_0 \int dt' \chi(t, t') \mathcal{E}_n(z_n, t'), \tag{2.65}$$

introducing the linear susceptibility $\chi(t, t')$ of the resonant layer. Inserting eq. 2.64 and eq. 2.65 into eq. 2.63, the solution is found by Fourier transformation into the frequency domain and matrix inversion. By defining the matrix $\mathcal{D}_{mn}$ and column vector $\mathcal{U}_n$ as

$$\mathcal{D}_{mn} = e^{ik|z_m - z_n|}$$
$$\mathcal{U}_n = e^{ikz_n}$$

and assuming illumination only from the left side ($E_{N+1}^- = 0$), the outgoing fields $E_{N+1}^+(\omega)$ and $E_1^-(\omega)$ can be expressed as[viii]

$$E_{N+1}^+(\omega) = E_1^+(\omega)\left(1 + i\frac{k}{2\varepsilon_{Sp}}\mathcal{U}^\dagger\left(\mathcal{I} - i\frac{k}{2\varepsilon_{Sp}}\chi(\omega)\mathcal{D}\right)^{-1}\chi(\omega)\mathcal{U}\right)$$

$$E_1^-(\omega) = E_1^+(\omega)i\frac{k}{2\varepsilon_{Sp}}\mathcal{U}^T\left(\mathcal{I} - i\frac{k}{2\varepsilon_{Sp}}\chi(\omega)\mathcal{D}\right)^{-1}\chi(\omega)\mathcal{U}. \tag{2.66}$$

---

viii $\mathcal{Y}^{-1}$ denotes the inverse, $\mathcal{Y}^T$ the transpose and $\mathcal{Y}^\dagger$ the Hermitian adjoint of matrix or vector $\mathcal{Y}$. $\mathcal{I}$ denotes the identity matrix of appropriate dimension.

From these fields transmission and reflection amplitude can be computed using

$$\mathfrak{t} = \frac{E_{N+1}^{+}(\omega)}{E_{1}^{+}(\omega)}$$
$$\mathfrak{r} = \frac{E_{1}^{-}(\omega)}{E_{1}^{+}(\omega)},$$

(2.67)

which then allows to calculate the linear transmittance, reflectance and absorbance

$$T = |\mathfrak{t}|^2$$
$$R = |\mathfrak{r}|^2$$
$$A = 1 - T - R.$$

## 2.6 FANO RESONANCES

In optical spectra, often asymmetric resonance features instead of symmetric Lorentzian lineshapes are observed. This effect is quite general and can be found in a multitude of different contexts [132]. The explanation for the emergence of these asymmetric features has first been given by Fano [133], who derived it in the context of atomic autoionization spectra.

The asymmetry originates from an interference effect, namely the interference of a discrete transition with that of a transition to a continuum. It can be expressed as [132]

$$\sigma = \frac{(F + q)^2}{F^2 + 1}.$$

(2.68)

Here, $\sigma$ is the cross section, $F$ is a dimensionless frequency, $F = 2(\omega - \omega_o)/\gamma$, with resonance frequency $w_o$ and spectral width $\gamma$. The asymmetry of the Fano resonance feature is controlled by the parameter $q$, as can be seen in Fig. 2.7, where normalized Fano lineshapes are shown for different $q$.

For $q = 0$, a symmetric resonance dip within the continuum is observed. For increasing $q$ the typical asymmetric shape is present. A special situation is the case of $q = 1$ where the shape is antisymmetric with respect to the resonance frequency. For larger values, the lineshape becomes more symmetric again, however the Fano character is
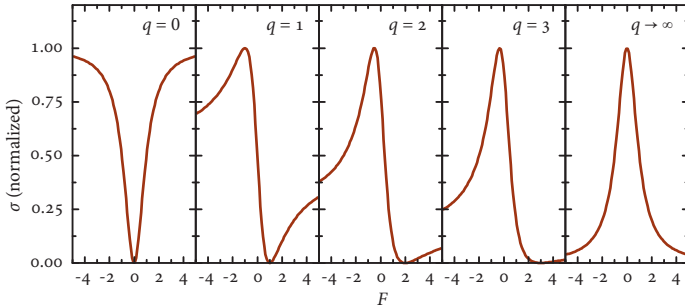
FIGURE 2.7. Normalized Fano resonance profiles for different values of the asymmetry parameter $q$. For negative $q$ the resonance profile is mirrored along the ordinate.

still present and can be identified by the local minimum which still exists on one side of the resonance peak. Only for $q \to \infty$ the asymmetry is lost completely. In this case the excitation path to the continuum becomes negligible and only the discrete narrow state is excited, thus the shape approaches that of a usual Lorentzian line.

In plasmonic and metamaterial systems Fano resonances occur and have been investigated for quite different structures [134], such as stacked dimers [135–137], ring-disk dimer structures [138–140], plasmonic oligomers [95, 141–145], hybrid material dimers [146], and other structures [147–151]. Furthermore, several theoretical investigations have been performed [152–156]. Strictly speaking, in these systems there is no continuum in the spirit of eq. 2.68. Instead, structures which exhibit resonant features with strongly different spectral widths, yet similar resonance frequencies are investigated. Then the broad resonance acts as a quasi-constant continuum and the narrow resonance shows the characteristic asymmetric shape.

Besides this, the Fano mechanism is closely connected to the occurrence of electromagnetically induced transparency (EIT) which is a special limiting case of a Fano resonance and will be discussed in detail in chapter 6.

$\sim$

# METHODS

## 3.1 EXPERIMENTAL TECHNIQUES

### 3.1.1 *Sample Fabrication*

All the structures investigated throughout this thesis were fabricated by electron beam lithography (EBL) using a multilayer technique. EBL is the premier technique for nanofabrication when it comes to flexibility and reproducibility. An electron beam of several ten kV and typically around 100 pA is focused onto a substrate with a resulting spot size < 10 nm, which allows for the exposure of very small and well-defined regions. Additionally, it is possible to control the beam: on the one hand it can be switched on and off by an electrostatic beam blanker, on the other hand two electrostatic deflectors scan the beam position over a write field of approximately 100 μm × 100 μm. In order to structure a surface, an electron beam sensitive resist is applied to the substrate surface. The electron beam introduces local modifications in this resist layer, which are subsequently transformed into a resist pattern by developing the sample. Depending on resist type, two different fabrication procedures can be applied.

In a negative tone resist the exposed areas become insensitive to the developer, therefore they remain while all the unexposed areas are removed.

As a negative resist, AR-N 7500[i] was used. The main functional component is a resin composed of phenol-formaldehyde polymers [157], to which a photo-active compound is added. On exposure to the electron beam, crosslinks are formed between different chains so that the resulting polymer network is not soluble in the developer (AR-300-47[i]), which mainly consists of the solvent 2-methoxy-1-methylethylacetat (PGMEA).

The positive tone resist works exactly opposite to the negative one: The exposed areas become soluble in the developer, while the unexposed areas remain, therefore using the same exposure pattern, the

---

i  Allresist GmbH, Am Biotop 14, D-15344 Strausberg, Germany, www.allresist.de

positive resist yields the inverse pattern compared to the negative resist process.

As a positive photoresist, Polymethylmethacrylat (PMMA) is used (AR-P 631, AR-P 641, AR-P 671[i]), which is diluted to a fraction of typically 1 % to 2.5 % in chlorobenzene. Different chain lengths of PMMA are utilized with molecular weights of 50K up to 950K. By electron beam irradiation the chains are split into smaller parts and then can be removed by a molecular weight selective developer, which is Methylisobutylketone (MIBK).

By applying multilayers of different chain lengths it is possible to fabricate an undercut in the resist layer due to the different development rate. An approximately 200 nm thick PMMA 200K layer is applied, followed by a thin PMMA 950K layer. In the bottom layer the development speed is faster, which leads to a larger void compared to the top layer. This is advantageous for the fabrication process, as the structure size is mainly defined by the aperture in the top resist layer, while the undercut created in the bottom resist layer facilitates the subsequent resist removal step (lift off).

As a substrate, quartz glass with an improved infrared transparency (Infrasil302[ii]) is used. The substrate is prepared by cleaning in a 55 °C acetone ultrasound bath for more than 15 min, followed by rinsing in acetone and 1-propanol and nitrogen drying. Then the further processing depends on the type of resist used. The fabrication sequences for both types are displayed in Fig. 3.1 (a) and (b).

For a negative resist, first a gold layer with appropriate thickness is evaporated onto the substrate surface by electron beam evaporation. For this, the sample is placed, substrate surface facing down, into a vacuum chamber. At the bottom of the chamber a gold crucible is placed which is heated by an electron beam. For a sufficiently low pressure in the chamber (approximately $10^{-6}$ mbar) the mean free path for the gold atoms is sufficiently long such that they reach the substrate surface and form a smooth film there. The whole process is controlled by a quartz microbalance, which is used to monitor the overall thickness of the film as well as the evaporation speed. The latter is kept constant at around 1 Å/s to 2 Å/s by a feedback loop. In order to improve the adhesion between gold and substrate surface, a thin layer of about 2 nm of chromium is evaporated directly before gold evaporation.
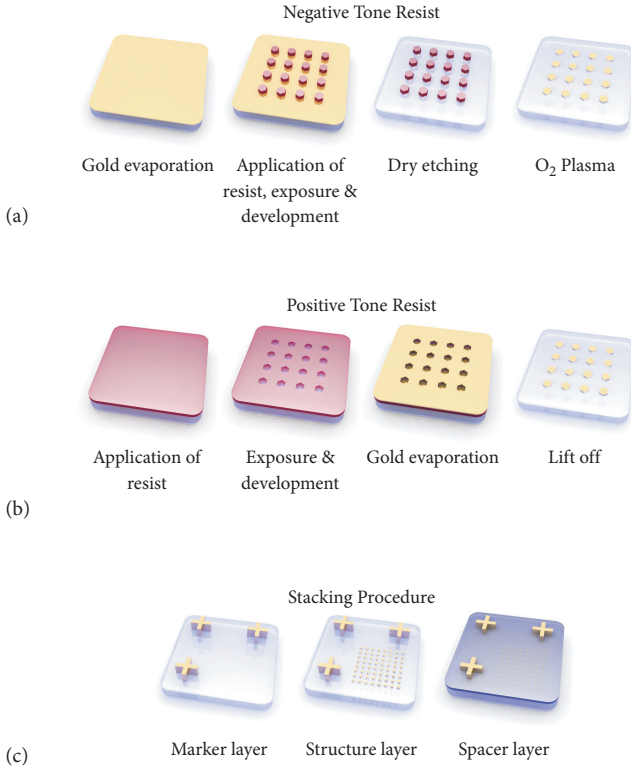
FIGURE 3.1.    (a) Processing steps for structuring with negative tone resist. (b) Fabrication sequence for positive resist.   (c) Stacking technique.

Next, the resist layer with a thickness of around 80 nm is spin coated onto the sample, followed by a soft baking step of 60 s at 90 °C. Then the pattern is exposed by EBL and developed for 20 s in AR-300-47 with gentle movement. The development process is stopped in deionized water, where the sample is also thoroughly rinsed for 60 s.

At this point only the resist pattern remains on the gold film, which has to be transferred to the gold by dry etching. This is accomplished by  Ar  ion beam etching, which is an anisotropic etching process. It is performed in a reactive ion beam etching machine, where an argon ion beam of typically 100 mA is accelerated by a 500 V voltage in a Kaufman source and then impinges onto the sample for 90 s. The  Ar

ions physically remove the gold film, while the resist masks the areas which should not be removed. To increase the homogeneity and prevent a redeposition of the removed material the sample is rotated and tilted by 20° with respect to the ion beam axis.

Finally, the remaining resist is removed by a cleaning step in a $O_2$ plasma, which leaves only the gold structure on the sample surface.

The method is different for a positive tone resist (Fig. 3.1 (b)). Here, first the PMMA resist layer is spin coated onto the substrate, followed by a 2 min soft baking step at 165 °C for each of the two resist layers. Then, a conductive polymer (ESPACER 300Z[iii]) is spin coated on top of the resist layer.

After this, the pattern is exposed by EBL, the conductive layer is removed and the resist is developed in a 1:3 dilution of MIBK in 1-propanol for 180 s to 240 s and 60 s in pure 1-propanol to stop the developing process. Next, a cleaning step of 18 s in $O_2$ plasma is applied to remove residual resist in the exposed areas. This is followed by the evaporation of the gold layer as described above. Finally, a lift off process for 2 h in 55 °C hot acetone or N-methylpyrrolidone (NMP) removes the remaining resist with the unnecessary gold film on top, leaving only the gold pattern on the surface of the substrate.

In order to be able to fabricate multiple exposure layers stacked on top of each other, one has to apply a layer-by-layer stacking technique [158, 159]. This is described in Fig. 3.1 (c). As a first step, a marker layer is applied to the substrate which is later used by the EBL machine to align its coordinate system. The marker layer is patterned by using a thick PMMA resist layer with lift off. Processing the markers in a separate step introduces the freedom to make them very thick (about 200 nm), which is advantageous for the marker detection routine.

After marker fabrication the first layer is processed with either negative or positive resist. The EBL machine has to align its coordinate system with respect to the given markers. Apart from this, the fabrication process for an individual layer is exactly identical to the procedures described above. In addition, a spacer layer has to be applied after the completion of each layer. As a spacer material, a spin-on dielectric (SOD) is utilized (Futurrex IC1-200[iv]), which can be applied to the sample by spin coating.

---

iii  Showa Denko Europe GmbH, Konrad-Zuse-Platz 4, D-81829 München, Germany, www.showa-denko.de

iv  Futurrex Inc., 12 Cork Hill Road, Franklin, NJ 07416, USA, www.futurrex.com

For the most samples under investigation, an exact spacing is crucial. Therefore, the thickness of the spacer layer has to be controlled thoroughly. This is done by varying the dilution of the SOD as well as the rotation speed. A combination of several coating runs with different dilutions allows to process a great variation of spacer layers with a set of three to five different dilutions of SOD. A phenomenological formula for the spin coating layer thickness is given by [160]

$$d_z = \kappa \frac{c_o^2}{f^{1/2}},$$ (3.1)

where $d_z$ denotes the resulting layer height, $c_o$ is the solvent concentration and $f$ is the rotation frequency. $\kappa$ is a constant which depends on the resist and substrate used and might also vary with the equipment used. Even though eq. 3.1 is not exact, it provides a good starting point for the design of a spacer layer. After each SOD spin coating run, a baking step for 2 min at 200 °C is necessary to remove the remaining solvents from the layer. Then it is possible to process the next structure layer on the sample. Owing to the spin coating process, the sample surface is very smooth, with a remaining roughness well below 10 nm.

As shown in Fig. 3.1, processing of thick crosses is advantageous for the alignment accuracy. However, even being completely buried under several layers of SOD, the electron backscattering from the gold provides enough signal to ensure a proper alignment of the layers. Alternatively, it is possible to process new alignment marks in each layer, which renders the first process step of marker fabrication unnecessary. This is a simplification of the technique, however, their layer thickness is much smaller in this case (equal to that of the structure layer) and therefore the backscattering signal is strongly decreased. Additionally, the experimental errors in marker detection add up from layer to layer so that substantial deviations might build up in structures with increasing number of layers.

In the realization of nanostructures using EBL, several well-known experimental errors occur which have to be minimized in order to get good results. These are drift, proximity effect, as well as overlay and stitching errors.

First, drift errors occur due to a distortion of the write field and result in deformed and misplaced structures. The distortion originates from local charges which are incorporated into the substrate due to the electron beam. These local charges lead to an additional displacement of the electron beam. This problem occurs only for EBL on non-conductive

substrates such as quartz. To prevent the effect, a conductive layer has to be applied to the substrate which ensures the distribution of the excess charges. One can either evaporate a thin 2 nm thick Cr layer or use a conductive polymer, where the latter is substantially faster to apply and also easier to remove.

The second source of error is the proximity effect. As soon as the electrons enter the resist layer and the substrate, scattering on the atomic lattice occurs, so that the exposure dose is spread within a small area around the exposed point with a Gaussian distribution. The proximity effect strongly depends on electron energy and resist/substrate material combination. The scattering cross section for an electron from an ionic core can be estimated from the Rutherford cross section, which is proportional to the square of the ion charge. Therefore, scattering from a gold layer ($Z = 79$) is much more severe than scattering from the resist layer, which predominantly contains hydrogen, carbon, or oxygen atoms with a $Z$ on the order of 1 to 10. There are several ways to account for the proximity effect. One approach is to use relatively high energy electrons with accelerating voltages of up to 100 kV. Then the Gaussian function around the exposure spot becomes broad and can be treated as a constant background over the whole exposure area. Another way is to measure the point spread function of the exposure process and apply an algorithm which optimizes the writing pattern to achieve a desired exposure pattern. Several commercial programs are available to do this. In many cases it is already sufficient to do a proper dose test study to determine the correct exposure conditions in conjunction with a reasonable structure design.

The last two errors are stitching and overlay inaccuracies, which are tightly connected. Stitching errors are present when several fields are exposed next to each other to form a large array. Going from one field to the next involves a movement of the sample stage. If the coordinate system of the stage is not properly aligned to that of the electron column, the subsequent fields are not written at the correct position, but slightly displaced. To compensate this, EBL machines possess internal routines to align both coordinate systems. This is done by driving the stage to different positions and scanning a specific marker with the electron beam. The resulting discrepancy then automatically can be compensated by the exposure algorithm. Overlay errors are similar, but refer to a misalignment of several layers in a multilayer exposure. Large overlay errors indicate problems in marker detection—if the marker detection works properly, the overlay error should be of approximately same mag-

nitude as the stitching error, as it is then governed by the remaining uncertainty in marker detection by the electron optical system. With an accurate EBL machine, very low values of typically less than 20 nm of overlay and stitching accuracy can be achieved.

### 3.1.2   *Measurement*

All spectral measurements were performed using a Fourier-transform infrared spectrometer (FTIR) spectrometer (Bruker Vertex 80$^\text{v}$). To acquire spectra from small sample areas, an attached microscope (Bruker Hyperion$^\text{v}$) was used. The main component of the spectrometer is a Michelson interferometer with one moving mirror. This mirror is scanned at kHz frequency while time transients are recorded on the detector. Applying a numerical fast Fourier transform (FFT) yields the measured spectrum.

Using FTIR spectroscopy is of advantage because of the very broad spectral range from 600 nm to 25 μm, which is achieved by using different light sources, beam splitters, polarizers and detectors.

As a light source, a tungsten lamp with a spectral range from the visible up to 3.3 μm and a $CaF_2$ beamsplitter with a spectral range from the UV up to 2.5 μm were used in all measurements. Depending on the considered spectral range, either a Si photodiode (400 nm to 1100 nm), an InGaAs photodiode (800 nm to 1700 nm), or a liquid-nitrogen-cooled Mercury Cadmium Telluride (MCT) detector (1.4 μm to 16.7 μm) were utilized.

A linear polarizer covering the visible and near-infrared spectral range was inserted into the beam path. As for all the structures under investigation no polarization conversion is expected, no analyzer was necessary in the measurement.

In the microscope, the light is focused onto the sample surface by a 15× Cassegrain objective with a numerical aperture of 0.4. In the reflectance measurement, the light is focused and collected by the same objective, while in the transmittance measurement, a second, identical Cassegrain object is present for the illumination of the sample. Focusing onto the arrays is performed by using visible light and the attached CCD camera. To obtain measurements for defined spatial areas, two knife-edge apertures are attached within the beam path, which allow

---

to restrict the beam to a rectangular area. This aperture was set to a slightly smaller area than the actual array size in order to suppress edge effects. As reference measurement, an area next to the arrays of nanostructures was utilized for transmittance, for reflectance, a 200 nm thick Au mirror was used.

## 3.2    SIMULATION TECHNIQUES

For a numerical evaluation of electrodynamic problems, Maxwell's equations have to be evaluated numerically. For these calculations two different methods were used. On the one hand, the commercially available CST Studio Suite[vi], on the other hand a home-made code running on Matlab, which uses the scattering matrix method (SMM) [161], also known as Fourier modal method (FMM) or rigorously coupled wave approximation (RCWA). These are described in the following sections.

### 3.2.1    CST Microwave Studio

CST Microwave Studio uses the finite integration technique (FIT) which solves Maxwell's equations in their integral form [162] (eqs. 2.12 to 2.15) instead of the differential form used by many other algorithms. The structure can be defined using a graphical editor. The program then performs an automated mesh generation and also an automated adaptive meshing routine in order to increase the simulation accuracy. The application of Maxwell's equations on this mesh grid transforms the problem from a continuous one to a discretized matrix problem which can be solved numerically. The accuracy of the solution is given by the resolution of the mesh and can also be strongly influenced by a reasonable meshing strategy, for example with a higher density on edges.

CST Microwave Studio provides a set of different solvers for versatile applications ranging from electrostatic all the way to optical problems. For the calculation of spectra and field distributions of plasmonic structures, the frequency domain solver is most suited. It allows to apply "unit cell" boundary conditions, which assume the calculation domain to be one unit cell of an infinite array. Therefore it is straightforward to calculate plasmonic particle arrays. For the frequency domain solver time-harmonic electromagnetic fields are assumed, which is well suited for the calculation of spectra in the optical frequency domain. The

---

vi  CST AG, Bad Nauheimer Str. 19, D-64289 Darmstadt, Germany, www.cst.com

solver automatically chooses frequencies in order to sample the whole required spectral range. Frequency samples are then calculated until the convergence criterion is reached.

An advantage of the FIT over the more common finite difference time domain (FDTD) technique is that the formulation is also valid on non-cubic grids. A tetrahedral grid is of particular advantage for the parametrization of curved surfaces. The cubic meshing is known to fail under these circumstances as the cubic parametrization of a curved surface leads to a staircase effect. Here, sharp edges are introduced due to the modeling which leads to unphysical calculation results.

All the CST calculations shown in chapter 6 were performed using the frequency domain solver of CST Microwave Studio with a tetrahedral mesh as discretization grid.

### 3.2.2 *Scattering Matrix Method*

The scattering matrix method represents a suitable alternative to calculations using CST, as it is a method specifically suited to light propagation problems in stratified and periodic media [161, 163]. In order to be able to calculate a problem in SMM, a structure generally has to be stratified along the light propagation axis and periodic along the other two directions.

To solve the problem, the structure is decomposed into several layers. As these individual layers are now laterally periodic in both directions, Maxwell's equations can be rigorously solved as an infinite-dimensional linear eigenvalue problem. Assuring proper convergence, the calculation is truncated for a certain number of harmonics $N_G$ yielding the scattering matrix of a single layer. Subsequently, all scattering matrices of the individual layers are combined by considering the appropriate boundary conditions. The method allows for a very high accuracy, and for $N_G \rightarrow \infty$ even an asymptotically exact solution.

Calculation of metallodielectric structures within this method is hampered by the strong permittivity differences at the interfaces between metallic and dielectric components in the structure. In order to achieve good convergence, large numbers of harmonics have to be considered, which is a major problem, as the computation time scales with $N_G^3$. Alternatively, optimization methods such as adaptive spatial resolution and correct factorization rules allow for substantially decreased calculation times [164].

The SMM has been applied to the calculation of all nanowire spectra throughout this thesis. The advantage over CST in this case is, that the dimension of the problem can be restricted easily, which leads to a huge computation acceleration while the accuracy along the other direction is not affected.

In the calculations, the nanowire structures are placed on top of a quartz substrate ($n_{\text{Sub}}^2$ = 2.13) and each layer is embedded into a spacer layer ($n_{\text{Sp}}^2$ = 2.13). The top layer is also capped by a spacer layer in order to maintain a homogeneous environment. All dielectrics are assumed dispersion-free. If not stated otherwise, the experimental values of Johnson and Christy [112] are used to model the gold. For all calculations $N_{\text{G}}$ = 51 was used.

$\sim$

# COUPLING IN PLASMONIC DIMERS

## 4.1 INTRODUCTION

This chapter will introduce the basics of plasmonic coupling, discussing exclusively the two-particle system. Considering the dimer system is crucial for the basic understanding of the coupling mechanisms, and a generalization to multi-particle structures mainly requires an extension of the phenomena already present for two particles.

As a first point, it is vital to examine the basic properties of the building block itself. Then, the lateral near- as well as far-field coupling of these building blocks in planar arrays of particles is investigated. Subsequently, this will be extended to stacked geometries, with an alignment of the constituents along the light propagation axis. In this particular geometry, only near-field coupling has been investigated up to now. Here, we will present experimental as well as numerical results from the near-field up to the far-field regime, and also provide an intuitive model to understand the coupling in the radiative regime.

Already at an early stage, it has been recognized that the response of ensembles of particle plasmon oscillators exhibits strong deviations from those of single ones [165–170]. This is owed to their sensitivity to the direct environment, where already the plasmonic oscillation taking place in a neighboring particle suffices to disturb the resonance.

Plasmonic coupling in planar geometries has been addressed in a multitude of contexts. Numerous investigations have focused on near-field coupling in dimer structures, in theory [168, 171–173] as well as experiment [166, 167, 174–176]. Investigations have not been restricted to simple systems of identical particles, also coupling in dimers with complex particles such as split ring resonators (SRRs) [177, 178] or rings [179], dimers in complex arrangements [180, 181], under special excitation geometries [182–184], for very small spacings [14], or heterodimers consisting of different particles, either from a materials perspective [146, 185, 186] or building block perspective [187–190] have been studied.

Others have experimentally investigated regular arrays of particles and studied near-field coupling [165, 169, 191, 192] or planar radiative coupling [170, 193–196], and developed theoretical models for the ef-

fects observed [197–200]. Beyond this, the coupling in arrays of complex building blocks has been examined [201, 202]. A special case is the investigation of waveguide-coupled structures, where the coupling between the particles is not mediated by the particle fields themselves, nor the radiative field but by the collective coupling to another photonic mode such as a waveguide mode [99, 203–209].

Another aspect of plasmonic coupling is the design of complex plasmonic building blocks [210], where special properties are tailored harnessing the near-field coupling within a single complex unit cell. Here, a multitude of different structures such as ring-disk dimer structures [138–140, 211], dolmen structures [147, 150, 212–216], nanocrosses [148], asymmetric SRR dimers [151], trimers [149, 217–219], and furthermore oligomers [95, 141–145, 220] and hetero-oligomers [150] have been investigated.

## 4.2 THE MODEL SYSTEM: PLASMONIC NANOWIRES

The major building block that will be used throughout the following chapters is a metallic nanowire made of gold. This system has already been investigated before in a plethora of different aspects [99, 134–136, 203–207, 221–232], mainly in connection with coupling of particle plasmon resonance (PPR) modes to waveguide modes in a planar dielectric slab. Therefore, many aspects of this building block are already well understood. Fig. 4.1 shows a schematic of the plasmonic gold nanowire. It is characterized by a width $W$, a height $H$ and is assumed to be infinitely elongated along the $y$-direction, with the incoming light being polarized perpendicular to the wire.

This building block has several advantages. First of all, the parameter space is small due to its simple geometry. This is further supported by the reduced dimensionality: even though the wires can be arranged three-dimensionally by stacking, the infinite extent along the $y$ axis leads to a quasi-two-dimensional problem, which particularly improves calculation speed. Furthermore, for the relevant parameter combinations the three structural dimensions differ by more than one order of magnitude, which leads to a strong spectral separation of the eigenmodes[i]. Hence, in most cases only one PPR mode can be excited by visible or infrared light. A last advantage of this system is its spec-

---

i see chapter 2, eq. 2.58. A large difference in structural dimensions and hence $L_j$ in the three directions leads to a pronounced spectral separation of the resonance positions.
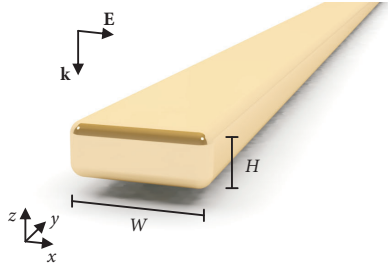
FIGURE 4.1. Schematic of a single gold nanowire. The spectral position and radiative width strongly depend on the exact wire geometry. Typical wire dimensions are a few tens of nanometers for the height $H$ and a few hundreds of nanometers for the width $W$. Along the $y$ axis the wire is assumed infinite in the calculations. In the experiments the wire length is limited by the array size which is on the order of 100 μm side length.

tral range. The PPR wavelengths can be tuned to the visible and near-infrared regime with wavelengths between 600 nm and 1 μm without great efforts, while for cut-wires and other plasmonic building blocks most designs with dimensions suitable for electron beam lithography (EBL) yield a PPR wavelength $\lambda_{\mathrm{PPR}}$ well above 1 μm.

To investigate the influence of the fundamental geometry parameters $W$ and $H$ on the resulting spectra of the wires, Fig. 4.2 shows calculated spectra[ii] for different wire geometries. In the following calculations, the wires will be placed on a quartz substrate with $n_{\mathrm{Sub}}$ = 1.46. To maintain a homogeneous dielectric environment, also a capping layer with $n_{\mathrm{Sp}}$ = 1.46 is placed on top of the wires. For the gold, the experimentally acquired optical properties of Johnson and Christy [112] are used.

In a first step, Fig. 4.2 (a), the wire width $W$ is varied, keeping the wire height fixed to $H$ = 20 nm. For the narrow wires, the PPR is spectrally located around $E_{\mathrm{PPR}}$ = 2 eV. Its exhibits a relatively narrow spectral width and high absorbance of 57 %. Increasing $W$ leads to a pronounced change in the spectra: a red-shift and spectral broadening of the PPR is observed. This effect is accompanied by a slight change in the spectral shape: while for narrow wires the spectrum exhibits an almost symmetric Lorentzian lineshape, the larger wires exhibit an asymmetry in their

---

ii  It has to be noted that, as the scattering matrix method (SMM) technique is used, these calculations are still performed for periodic arrays. However, the period ($d_x$ = 360 nm) is chosen such that coupling effects are weak (compare Fig. 4.6 and Fig. 4.7).
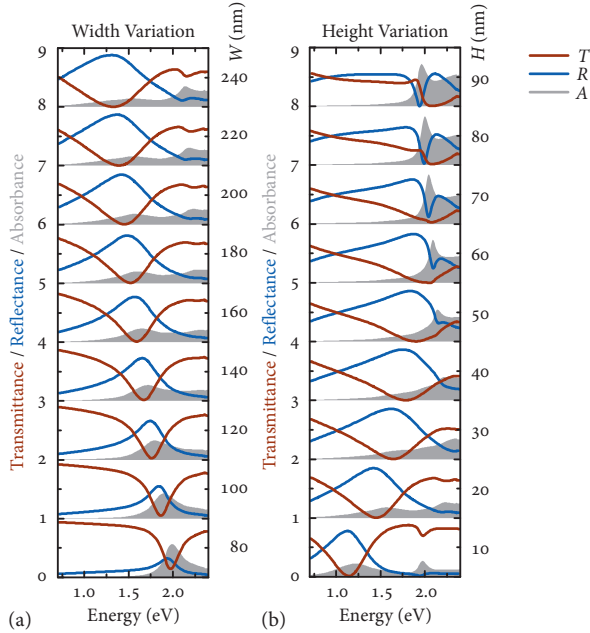
FIGURE 4.2. Calculated transmittance, reflectance, and absorbance spectra for different widths $W$ and heights $H$ of a gold nanowire.    (a) Variation of $W$ for fixed $H$ = 20 nm. For increasing width, the PPR shifts to lower energy. (b) Variation of $H$ for $W$ = 200 nm. Increasing the wire height leads to a blue shift of the PPR. Additionally, a pronounced asymmetry of the spectral shape is observed. For large $H$, higher PPR modes spectrally approach the fundamental PPR and a Fano-type lineshape is observed starting from $H \approx 50$ nm. In both cases an increased particle volume leads to a higher oscillator strength of the PPR and therefore to a linewidth increase as well as a decrease in absorption. Both effects are clearly observed in the spectra. The spectra are shifted up for clarity.

spectral shape: the slope on the blue side is steeper than the one on the red side of the resonance.

In a second step, Fig. 4.2 (b), the height is varied, keeping the wire width fixed at $W$ = 200 nm. In this case, the low wires exhibit a PPR at approximately 1.1 eV and increasing the height leads to a pronounced blue shift to approximately 2 eV, which is, as in the case of (a), accompanied by a strong increase of the spectral width.

In both cases one observes that the balance between absorbance and reflectance pronouncedly changes on increasing wire size, whereas the modulation depth of the transmittance varies only weakly. The large wires show very low absorbance at the PPR, instead the reflectance peaks to more than 90 %, for the small wires this is exactly opposite, with dominating absorbance and low reflectance.

All these effects are included in the theory considerations of section 2.4.4. The red- and blue shifts for width and height variation as well as the increasing and decreasing oscillator strengths are qualitatively predicted by the quasistatic polarizability of a metallic ellipsoid as described by eq. 2.55. The distribution of intensities between absorbance and reflectance can be deduced from eq. 2.46, where extinction dominates for small particles, therefore leading to a large contribution to absorbance while for larger particles, the scattering outweighs extinction and thus reflectance is stronger.

Another aspect of Fig. 4.2 has not been considered yet. For increasing width or height of the wire, additional spectral features are observed. This is especially the case for the height variation spectra starting from $H$ = 50 nm, where an additional PPR mode is present. It shifts to the red and increases in strength for increasing height. Similarly, a weak feature around 2 eV appears in (a) for large widths. These features arise due to the excitation of higher-order modes which spectrally approach each other as the ratio of width and height of the wires approaches unity. The overlap between the fundamental dipolar mode and the higher mode results in a complicated Fano-type spectral shape, which is most clearly observed in the case of height variation (panel (b)). As the charge distributions of these modes are more complicated than that of the fundamental dipolar mode they only couple weakly to the light field and thus exhibit smaller linewidths and a more distinct feature in absorbance compared to the fundamental dipole mode.

Their appearance is rather distracting for a study of the interaction of the fundamental modes of different particles. Therefore, it is advantageous to choose designs which do not feature higher order modes in the considered spectral range.

Finally, we introduce a different display style for the calculation results. Fig. 4.2 depicts the conventional spectra. In this representation, it is sometimes difficult to precisely observe the spectral changes on variation of a parameter. Therefore, in the following a colormap representation will be used. This is exemplarily shown in Fig. 4.3, where transmittance, reflectance, and absorbance are plotted color coded. In
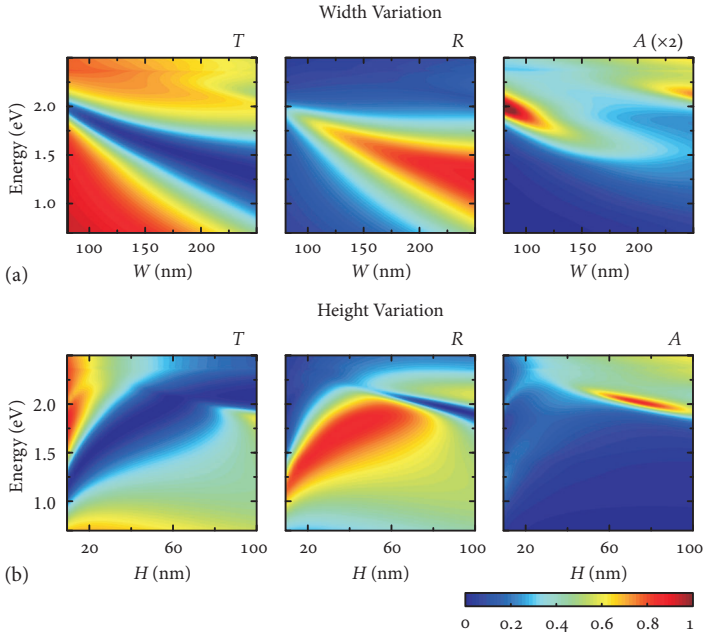
FIGURE 4.3. Color-coded representation of the calculation results shown in Fig. 4.2. In these more detailed graphs the spectra are plotted color-coded over the energy on the vertical axis and the parameter of interest on the horizontal axis. The spectral changes on variation of the respective parameter can be observed much clearer compared to Fig. 4.2. (a) Variation of the wire width. The increase in spectral width and the red shift for increasing width is obvious here. (b) Variation of the wire height $H$. This leads to a blue shift of the spectra. For large heights, the influence of the higher order mode is clearly visible.

this representation, the ordinate consistently displays the spectral parameter, energy, frequency, or wavelength, while the abscissa displays the varying parameter—in this case $W$ or $H$. Hence, spectra for one specific parameter value are easily recognized as a vertical cross section in the graph.

This representation has several advantages. On the one hand, a huge amount of information is included. In contrast to Fig. 4.2, the colormaps of Fig. 4.3 contain calculated spectra with a step size of 2 nm for $H$ and 5 nm for $W$. The information density is higher by a factor of 4 or 5. On the other hand, it is easier to observe trends such as the

interchange of intensities between reflectance and absorbance in case of width variation (Fig. 4.3 (a)) as well as the functional dependence of the spectra on the varied parameter.

Altogether, the spectra shown in Fig. 4.3 facilitate the observation of relevant spectral effects such as all the red- and blue shifts and changing spectral widths, not only for the fundamental but also for the higher order modes. Hence, in the following this representation will predominantly be used.

## 4.3   THE PLASMON HYBRIDIZATION MODEL

In 2003, the concept of plasmon hybridization was introduced by Prodan et al. [233]. This concept draws an analogy between a coupled plasmonic structure and hybridization of electronic orbitals in molecular physics. This proves to be a very helpful tool in the intuitive understanding of the response of complex coupled plasmonic structures.

In molecular physics the electronic orbitals of the $H_2^+$ molecule ion are found by assuming the solutions to be a linear combination of the respective atomic orbitals. The latter are known, as the corresponding problem for the H atom can be solved analytically. To compute the actual coefficients of the linear combination, the appropriate boundary conditions, namely the unity of the norm of the wavefunction, have to be applied. As a result, two new eigenstates are found, one of which possesses an increased total energy and the other a decreased total energy. Thus, these states are termed the antibonding and the bonding state, respectively. Due to the increased energy, the antibonding state is not stable and only the bonding state forms a stable configuration. The resulting wavefunctions are classified with respect to their symmetry: the bonding one is symmetric, the antibonding one antisymmetric.

This concept of hybridized states has successfully been applied to plasmonic systems: Prodan et al. [233] have shown that the spectra of complex plasmonic structures can be understood in terms of a hybridization of the plasmon modes of their building blocks. In case of a spherical core-shell-particle consisting of a metallic shell around a dielectric core, the problem can be decomposed to a hybridization of the plasmonic oscillation of a spherical metallic particle and a "void" plasmon of a dielectric sphere inside a metallic environment. Subsequently, the concept has successfully been applied to a multitude of different systems [234] such as the coupling of a spherical metallic particle to a metallic surface [235] and a film [236], as well as to coupling

in plasmonic oligomers [95, 142–145], coupling of modes of different order in a single particle [237], and, most importantly, as in our case, to plasmonic dimers [238, 239].
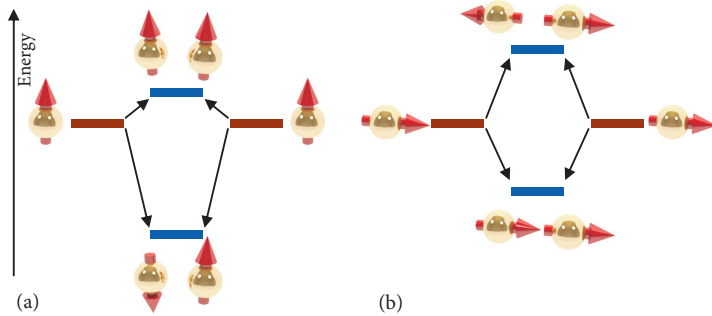


FIGURE 4.4. Plasmon hybridization scheme for a dimer structure. The coupled system exhibits two new resonances which can be classified by their symmetry. Antisymmetric and symmetric modes are characterized by antisymmetric respectively symmetric charge oscillations. The new energies and thus frequencies of the modes have to be deduced from the specific coupling situation,   (a) for polarization perpendicular to the interparticle axis, the symmetric mode is shifted to higher energy and the antisymmetric mode to lower energy. This situation is reversed for   (b) polarization parallel to the interparticle axis.

In the plasmon hybridization concept the atoms are replaced by the plasmonic particles and the quantum mechanical wavefunction by the deformation field of the electron liquid inside the particles. As shown in Fig. 4.4 an isolated particle exhibits a certain PPR energy. Coupling two particles leads—in full analogy to the $H_2^+$ system—to two new PPR modes of the coupled system. Just as in the case of electron wavefunctions, these are characterized by their symmetry.  For one mode the charge oscillations are parallel, thus this is called the symmetric mode, the other one shows antisymmetric charge oscillations and is referred to as the antisymmetric mode.  In contrast to the molecular system, there is no stability criterion in the plasmonic case and both modes occur.  However, they do not necessarily couple to the radiation field and therefore might not be excited by the incoming light field.

As depicted in Fig. 4.4, the resonance energy shift is determined by the specific geometry and also excitation condition, i. e., the polarization of the incoming light with respect to the interparticle axis. The resonance shifts can be understood by fundamental electrostatic consid-

erations, namely by calculating the influence of the momentary charge distribution of the neighboring particle. The electrostatic interaction energy of two dipoles with dipole moment $\mathbf{p}_1$ and $\mathbf{p}_2$ is given by [101]

$$W_{12} = \frac{\mathbf{p}_1 \cdot \mathbf{p}_2 - 3(\mathbf{c} \cdot \mathbf{p}_1)(\mathbf{c} \cdot \mathbf{p}_2)}{4\pi\varepsilon_0 d^3} \tag{4.1}$$

with a spacing $d$ between the dipoles, and the unit vector $\mathbf{c}$ pointing along the interparticle axis. Depending on the light polarization with respect to the interparticle axis, different shifts occur. For perpendicular light polarization ($\mathbf{p}_1, \mathbf{p}_2 \perp \mathbf{c}$, Fig. 4.4 (a)), the energy is increased for the symmetric oscillation and thus a blue shift is observed while the resonance energy is decreased for the antisymmetric mode. The situation is opposite for parallel light polarization (($\mathbf{p}_1, \mathbf{p}_2 \parallel \mathbf{c}$, Fig. 4.4 (b)). In this case, the PPR energy is increased for the antisymmetric mode and decreased for the symmetric mode. This is in accordance with the observations in laterally coupled dimer structures [166, 174, 176].

This hybridization concept is not restricted to plasmonics. It already occurs in simple mechanical systems such as two coupled harmonic oscillators, where two eigenmodes with symmetric and antisymmetric oscillation exist as well. Furthermore, it is notable that the correct description of plasmon hybridization was already given as early as in 1991 in the context of fast-electron scattering from spherical metal particle pairs by Schmeits and Dambly [240].

In the following, the plasmon hybridization scheme will provide a useful tool in the description of the near-field coupling properties of plasmonic systems and give a straightforward interpretation of the coupling effects in plasmonic dimer systems and regular arrays. However, it only allows for a qualitative interpretation and does not provide quantitative results. These have to be acquired differently.

## 4.4 LATERAL COUPLING IN PLANAR ARRAYS OF PLASMONIC PARTICLES

Throughout this thesis, all plasmonic particles will be arranged in periodic arrays with field dimensions on the order of $100\,\mu m \times 100\,\mu m$. Even though single particle spectroscopy is feasible, the fabrication technique allows for a reproducible patterning over large areas and therefore the measurement of large fields with higher light intensities and thus a better signal-to-noise ratio. Apart from this, for the investigation of coupling, arrays are the most straightforward choice. Therefore, plasmonic

coupling in planar arrays, i. e., structures where the plasmonic particles are confined to a single layer, is reviewed in this section. An example of such a planar array of nanowires is displayed in Fig. 4.5. Apart from the single particle geometry the lateral period $d_x$ is important. Furthermore, the dielectric environment, represented by the refractive indices of the substrate $n_{Sub}$ and the spacer or capping layer $n_{Sp}$, is crucial.
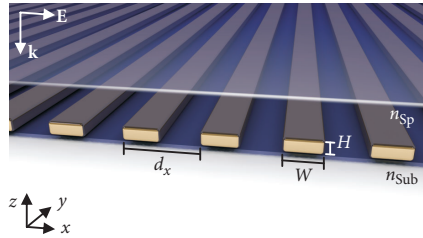


FIGURE 4.5. Schematic of a planar periodic array of nanowires. Besides the single wire properties, essential parameters are the periodicity $d_x$ as well as the environment refractive indices, $n_{Sub}$ (for the substrate) and $n_{Sp}$ (for the spacer or capping layer).

The influence of near-field coupling on the particle spectra in a planar array of nanowires is shown in Fig. 4.6. The spectra are shown color coded over the lateral periodicity of the wires $d_x$. As the wire width itself is 200 nm, the leftmost region shows spectra for gaps between the particles as low as 20 nm up to a spacing of 150 nm between individual wires. For increased periodicity the coupling to the neighboring particles seems to vanish. Indeed, the main influence of coupling effects on the spectra can be observed for gaps below 50 nm ($d_x$ = 250 nm), although for larger periodicities a change in the linewidth still is present. Decreasing the distance between the nanowires obviously leads to a strong red-shift and pronounced broadening of the PPR.

This can be explained in a straightforward manner by utilizing the plasmon hybridization scheme: in principle the planar wire array is a system of $N$ coupled oscillators with $N$ being the number of wires in the array. Therefore, there are $N$ possible modes supported by the system. However, due to symmetry it is only possible to excite the completely symmetric mode, where all plasmons in the wires oscillate in phase. For decreasing periodicity the interaction with the neighboring particles becomes significant and the situation corresponds to $\mathbf{c} \parallel \mathbf{p_1}, \mathbf{p_2}$ in eq. 4.1. Consequently, a red shift is observed.
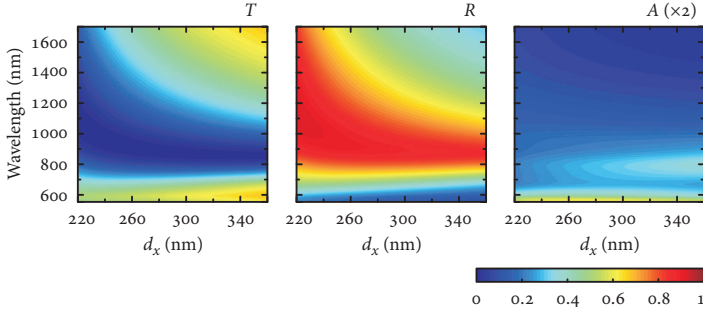
FIGURE 4.6. Calculated spectra for a single layer nanowire array with $W = 200$ nm and $H = 20$ nm and varying lateral periodicity $d_x$. For small lateral spacings between the wires the spectra exhibit a red shift as well as an increased linewidth.

The modification of the PPR linewidth is quite straightforward to explain as well. On decreasing periodicity and constant wire geometry, the fraction of gold and therefore the oscillator strength of the nanowire layer is increased, as the bare number of electrons increases. Therefore, the PPR spectral width is substantially increased.

If only near-field interaction of the dipolar oscillators would be present, we would expect the coupling to vanish upon further increase of $d_x$ beyond the range depicted in Fig. 4.6 and to show no dependence on $d_x$ any more. This is not the case, as Fig. 4.7 (a) demonstrates. Here, the calculation domain is extended to lateral distances as high as $d_x = 1200$ nm. For large distances, new, narrow spectral features appear which strongly depend on the periodicity $d_x$, which leads to a strong modification of the PPR lineshapes. To explain this behavior it is important to recognize, that the plasmonic nanowire array can also be considered as a surface with a periodic modulation. This is especially important as soon as the lateral periodicity approaches the considered wavelength regime. The appearance of anomalies in the diffraction patterns of metallic gratings was first observed by Wood [18], hence they are termed Wood anomalies. Rayleigh gave an explanation of one special case of Wood's anomalies by considering the occurrence of new diffraction orders in the grating [21]. Consequently, these anomalies are termed Rayleigh anomalies and their spectral positions Rayleigh wavelengths, $\lambda_R$. These can be deduced from grating diffraction theory, as depicted in Fig. 4.7 (b): light

with wavelength $\lambda$ impinging onto a periodically corrugated surface with wave vector $\mathbf{k}_{\text{in}}$ is diffracted according to [241]

$$d_x \left( \sin \theta_M - \sin \theta_{\text{in}} \right) = \frac{M\lambda}{n}, \tag{4.2}$$

where $\theta_{\text{in}}$ is the angle between surface normal and $\mathbf{k}_{\text{in}}$, $M$ an integer number, $\theta_M$ the angle between $\mathbf{k}_M$ of the $M$th diffraction order and the surface normal, and $n$ the refractive index of the medium it propagates in. For a subwavelength grating only the zeroth order can propagate. As soon as $\lambda$ approaches $d_x$, the first diffraction order opens, associated with a redistribution of energies between the possible diffraction orders [242]. Exactly at the transition, the newly opened diffraction order is characterized by a $\mathbf{k}_M$ which lies in the surface plane and therefore propagates along the surface. Using this, the Rayleigh wavelengths can be calculated from eq. 4.2 using $\theta_M = 90°$. For the special case of normal incidence, $\theta_{\text{in}} = 0°$, we obtain the criterion

$$\lambda_{\text{R},n,M} = \frac{n}{M} d_x. \tag{4.3}$$

The Rayleigh wavelengths calculated according to this equation are displayed as dashed white lines in Fig. 4.7 (a). As the plasmonic grating is located at the interface between substrate and superstrate, there are two branches of Rayleigh anomalies, one for the propagation in air ($\lambda_{\text{R,air},M}$) and in the substrate ($\lambda_{\text{R,quartz},M}$). Both beautifully match the numerical calculations.

As $\mathbf{k}_M$ lies in the substrate plane, it is possible to interpret the Rayleigh anomalies as surface waves supported by the periodic surface [243–245]. In these terms, two types of modes are present in the system, the particle plasmonic oscillator modes and the photonic surface mode due to the periodicity. The PPRs interact with the photonic modes leading to a characteristic Fano lineshape [246]. An equivalent point of view is the description of the system as an array of dipoles which are coupled via their radiative fields [165, 195, 199, 201, 202]. In both cases the description leads to remarkably narrow resonance features of the coupled PPR-surface mode system which arise due to their radiatively coupled, collective nature [194, 196, 198, 206, 247].

## 4.5    NEAR-FIELD COUPLING IN STACKED DIMERS

The arrangement of plasmonic building blocks in a single layer on a surface imposes geometric limitations on the tuning capabilities of the
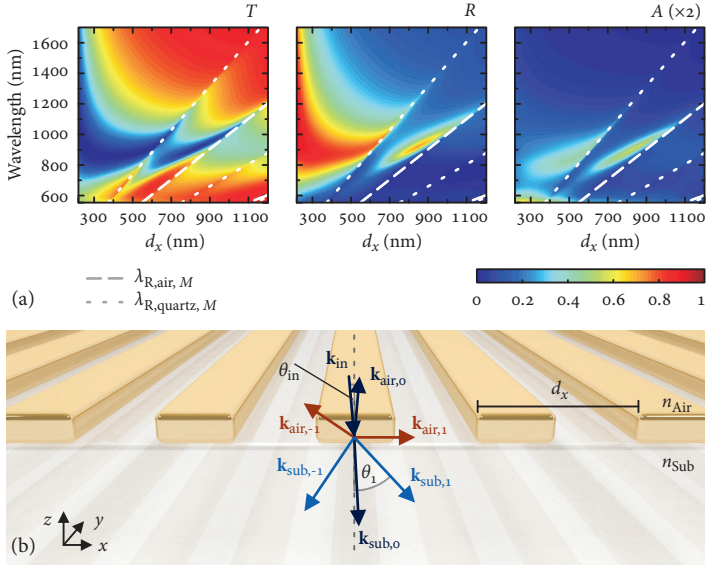
FIGURE 4.7.    (a) Calculated spectra for a single layer structure with larger periods $d_x$. As soon as $d_x$ becomes comparable to the wavelength, Rayleigh anomalies, indicated by the dashed white lines (eq. 4.3) occur.    (b) Schematic of diffraction orders on a planar periodic structure. Light impinges onto the structure along direction $\mathbf{k}_{in}$. In addition to the directly reflected ($\mathbf{k}_{air,o}$) and transmitted ($\mathbf{k}_{sub,o}$) waves, diffraction orders into the substrate as well as the superstrate may be open. Rayleigh anomalies occur whenever $\mathbf{k}_M$ for a diffraction order lies in the substrate plane, as this is the case for $\mathbf{k}_{air,1}$ in the graph.

system. The ability to arrange them in a truly three-dimensional fashion constitutes an improvement in several ways.

First, it opens up several new free design parameters. Greater freedom is possible in the arrangement of the building blocks, especially with respect to the illumination direction. For example, a placement of more than one plasmonic particle in the direction of the traveling light wave is possible, although some sophisticated schemes have been proposed to achieve this in a planar arrangement [183].

Second, the three-dimensional arrangement induces a symmetry breaking due to retardation in the excitation of the PPRs. This allows for an excitation of modes in the structure, which would be dark in planar geometries. This is particularly true for the antisymmetric mode in the

dimer system: for a planar arrangement under normal incidence, an excitation of the antisymmetric mode is not possible due to the symmetry of the system. Vertical stacking of the oscillators yields a finite dipole moment for the antisymmetric mode and thus it couples to the radiation field and can be observed by far-field spectroscopy.

The interest in stacked plasmonic structures has been fueled by the quest for truly three-dimensional metamaterials. While early investigations on metamaterials only considered so-called metasurfaces consisting of planar arrangements of building blocks on a surface, a real material should have a bulk character and thus would have to be three-dimensional [68, 158]. One particular motivation was the fact, that the antisymmetric mode is similar to a ring current in a coil and therefore an optical magnetic moment could be induced in the spacing between the wires [248–251]. This would then lead to a modified magnetic response to the light field and potentially allow for a negative $\mu$, which would make it a promising candidate for a negative index material (NIM).

To investigate near-field coupling in stacked nanowire structures Fig. 4.8 displays calculations of a stacked two layer gold nanowire structure. The wire geometry is kept constant with respect to the previous section[iii].

In these and the following calculations it is important to minimize the effect of lateral coupling. As elaborated in the paragraphs above, this is not simply accomplished by choosing large lateral periodicities, but rather a trade-off between vanishing near-field coupling and suppressed far-field coupling has to be made. Therefore we use the maximum lateral periodicity $d_x$ where no Rayleigh wavelength resides inside the considered spectral region. For $d_x$ = 400 nm, the longest Rayleigh wavelength is $\lambda_{R,\text{quartz},1}$ = 584 nm, which is sufficiently outside the spectral region of interest. For this particular lateral periodicity in this geometry, the single layer PPR peaks around 850 nm[iv].

The spectra are displayed depending on the vertical spacing $d_z$. As expected, they exhibit pronounced differences compared to Fig. 4.6. Two modes are observed, one is broader and located on the blue side

---

iii  $W$ = 200 nm, $H$ = 20 nm

iv  To be more specific, the transmittance minimum is located at $\lambda$ = 854 nm, the reflectance maximum at $\lambda$ = 873 nm and the absorbance maximum at $\lambda$ = 800 nm. As the PPR is considerably broad, a localization of the resonance with an accuracy of 1 nm or even 10 nm is sufficient in most cases. We do not intend to discuss the "true" resonance position with respect to the numbers given above.

of the single layer PPR, the other is rather narrow and located on the red side. In contrast to the lateral arrangement discussed before, the dipole vectors of the particle plasmon oscillations are perpendicular to the interparticle axis for a stacked arrangement. Consequently, it corresponds to the situation of Fig. 4.4 (a), so that the red shifted mode can be identified to be the antisymmetric mode, while the blue shifted mode corresponds to the symmetric oscillation of the PPRs.
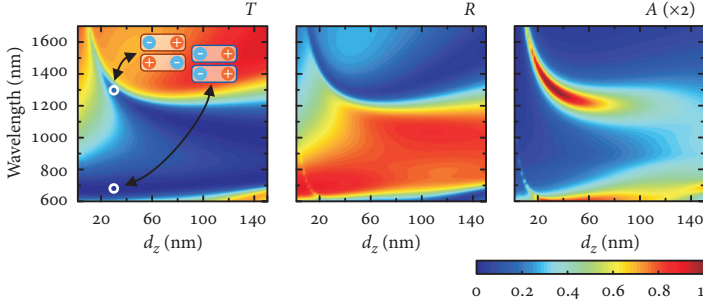


FIGURE 4.8. Calculated transmittance, reflectance, and absorbance for the stacked dimer structure depending on the vertical distance. White circles indicate the positions at which electric field plots are displayed (see Fig. 4.9). For decreasing $d_z$ the splitting between symmetric and antisymmetric mode increases due to an increased electrostatic interaction strength. At the same time, the coupling to the far field decreases for the antisymmetric mode and increases for the symmetric mode.

The spectral width of the symmetric mode is significantly larger than that of the antisymmetric mode. The net dipole moment of the latter is small due to the antisymmetric oscillation of the individual dipoles which are very close to each other. Therefore, it exhibits a narrow linewidth which decreases further on decreasing vertical spacing $d_z$ and, as can be seen from the absorbance graph, also experiences a significant amount of nonradiative decay.

As expected, the splitting of the modes is increased on decreasing spacing $d_z$ and thus increasing coupling strength. However, this splitting is not symmetric, as one would confer from eq. 4.1. This indicates that, even though the plasmon hybridization scheme provides excellent qualitative predictions by simple electrostatic considerations, reality is more complex and additional considerations are necessary. One can think of several possibilities why this asymmetry occurs, for example

(a)                                     $d_z = 30$ nm, $\lambda = 1298$ nm



(b)                                     $d_z = 30$ nm, $\lambda = 681$ nm
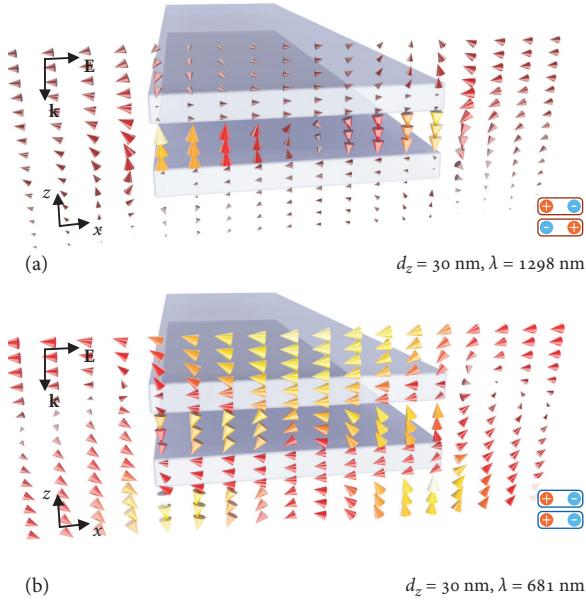
FIGURE 4.9. Normalized logarithmic electric field intensity for a stacked dimer structure with a vertical distance of $d_z = 30$ nm. (a) Field distribution of the antisymmetric mode ($\lambda = 1298$ nm). The plasmons oscillate antiparallel, leading to a vortex-like field distribution, with strong field enhancement between the wires. (b) Field distribution of the symmetric mode ($\lambda = 681$ nm). In this case, the particle plasmons oscillate parallel, therefore the dipole moment of this mode is much larger than that of the antisymmetric mode.

the onset of absorption in the gold for wavelengths below 600 nm or the different dipole moments and therefore radiative damping rates of the modes.

In addition, the excitation of a higher order mode can be observed in the simulations for a spacing below $d_z = 20$ nm. This higher order mode manifests itself in the reflectance as well as absorbance spectra (at the bottom of Fig. 4.8) and shows a strong red shift for decreased $d_z$. However, this mode is difficult to observe in experiment, as it occurs for very small spacings and is spectrally very narrow, thus it will be hidden in inhomogeneous broadening.

In order to confirm the interpretation given above, Fig. 4.9 displays the calculated electric field distribution in the system with a spacing of 30 nm at two different spectral positions, indicated as white circles in the spectra of Fig. 4.8. These field graphs show the normalized logarithmic electric field strength in the $xz$ plane. Temporally, the fields are plotted for the moment of maximum field intensity in an oscillation cycle.

In Fig. 4.9 (a) the antisymmetric mode is observed very well. As already discussed before, the antiparallel charge oscillations resemble a circular current such that a magnetic field in $y$ direction is induced in the structure. This circular pattern is pronouncedly present in the electric field plot. Furthermore the proximity of opposite charges leads to a strong field enhancement close to the borders of the wires.

In contrast, the electric field of the symmetric mode, displayed in Fig. 4.9 (b) is characterized by a symmetric charge oscillation. The overall field distribution in this case is quite uniform and directed along the $x$ axis. Comparing this to the situation in (a) it is becomes clear, that the symmetric mode exhibits a substantially stronger coupling to the incoming light field. This is in agreement with the linewidths of the modes observed in the spectrum.

## 4.6 INVERSION OF THE HYBRIDIZATION SCHEME BY LATERAL DISPLACEMENT

Up to now, we have only considered nanowires with a direct vertical alignment. By dropping this restriction interesting new coupling schemes can be found. According to eq. 4.1, the spectral shifts of the hybridized modes are strongly dependent on the exact electrostatic interaction energy and thus to the arrangement of the oscillators with respect to each other as well as to the polarization direction. Therefore, any change in the relative orientation of the wires should have a significant influence on their optical spectra.

To accomplish this, we introduce a lateral shift $S$ between upper and lower layer. Similar investigations have already been carried out on nanowire geometries [135, 136] as well as on cut wire pairs in stacked [137] and planar [150] arrangements. The wires arranged directly on top of each other display a behavior according to Fig. 4.4 (a) while the situation of full displacement closely resembles an end-to-end alignment as shown in Fig. 4.4 (b), with reversed energy shift. Thus, for a continuous

increase of lateral shift, it should be possible to observe the interchange in spectral positions of the modes.

Calculations for Au wires with $W$ = 200 nm and $H$ = 20 nm with a periodicity of $d_x$ = 400 nm and a vertical spacing of $d_z$ = 30 nm are shown in Fig. 4.10 (a). The non-shifted system exactly corresponds to the one investigated in the previous section, except for a now fixed vertical spacing. Due to limitations in the calculation algorithm, the maximum lateral shift that can be calculated is $S$ = 190 nm, even though $S$ = 200 nm corresponds to the completely displaced case.

Already in case of top-on-top arrangement without shift, the antisymmetric mode exhibits a characteristic Fano lineshape with asymmetric, dispersive profile due to the spectral overlap of the modes. This is most pronounced in the reflectance spectrum. For increasing $S$ the antisymmetric mode shifts to the blue and the symmetric mode undergoes a spectral shift to the red from 700 nm to slightly above 900 nm, accompanied by a strong increase in spectral width[v].

Different Fano profiles are present in the spectra for different $S$. At small displacements, the lineshape of the antisymmetric mode is rather asymmetric. For approaching resonance wavelengths, the behavior changes to a characteristic narrow dip on a broad peak, which is similar to that of $q$ = 0 in Fig. 2.7.

Fig. 4.10 (c) shows a more detailed colormap graph, where especially the shift of the antisymmetric mode and thus the inversion of the plasmon hybridization scheme is beautifully observed. The shift of the

---

v  The observation of the spectral shift of the antisymmetric mode is facilitated due to the narrower and more or less constant spectral width.

---

FIGURE 4.10 (*FACING PAGE*). Calculated spectra for a lateral shift of the top layer in the stacked dimer structure. (a) Schematic of the structure and calculated spectra. The displacement $S$ is increased from 0 nm to 190 nm. (b) Schematic for the mode inversion. In the structure with full lateral displacement, the energy shifts are reversed compared to the non-displaced case. (c) This inversion of the hybridization scheme is beautifully observed in the color-coded plots, especially for the antisymmetric mode. Below 700 nm wavelength an interaction of higher-order modes takes place. White circles in the transmittance graph indicate positions at which the electric fields are displayed in Fig. 4.11. (d) The same calculation as in (c) but for a spacing of $d_z$ = 80 nm. For larger spacing the near-field interaction is substantially reduced and the inversion is not observed any more.

(a)

(b)

(c)

(d)
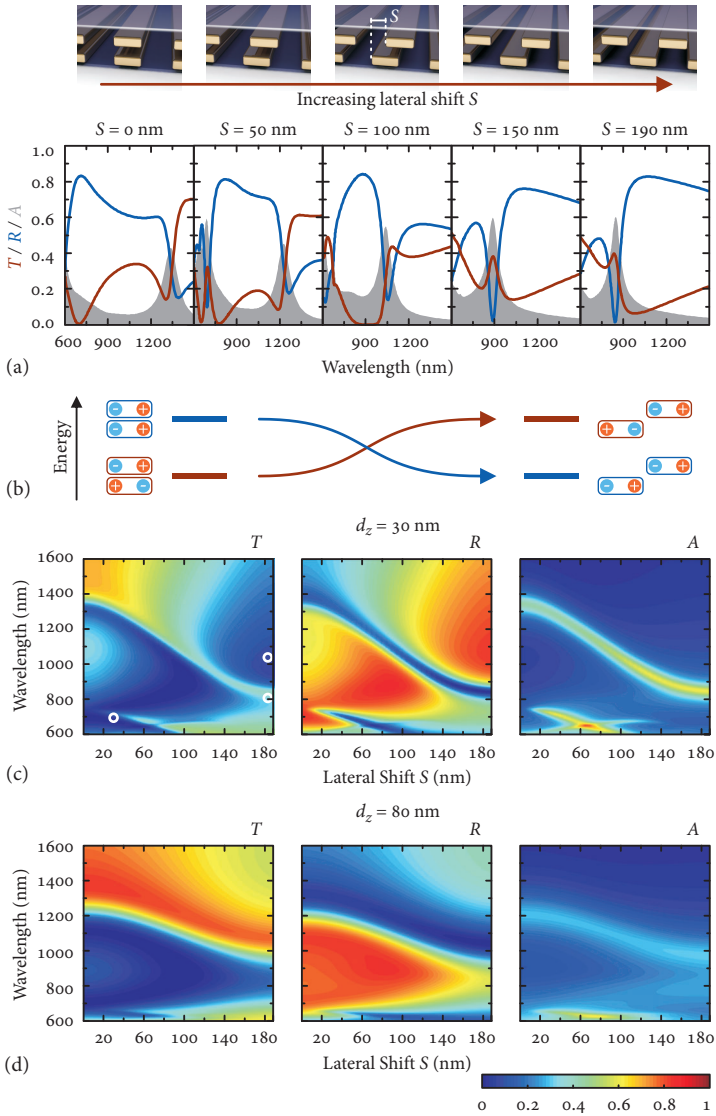
symmetric mode is most pronounced in the reflectance graph, where the broad peak of high reflectance is first observed on the blue side of the antisymmetric mode and on increasing $S$ shifts to its red side.

For small $S$ another mode can be identified in the spectra at approximately $\lambda$ = 700 nm. This very narrow mode is also visible in the calculated spectra in Fig. 4.10 (a) for $S$ = 50 nm at a wavelength slightly below 800 nm. It corresponds to a higher order mode of the coupled system, which arises due to the slight symmetry breaking introduced in the structure and then blue shifts out of the calculation domain for higher $S$. This mode can be seen as a second-order antisymmetric mode. In both wires second order PPR modes are excited, their respective charge oscillations are opposite, leading to the induction of two separate, counter-oriented magnetic moments in the structure [135] (see Fig. 4.11 (c)).

To verify the interpretation given above, Fig. 4.11 shows field calculations for the shifted wire structure. The displacements and spectral positions of these field calculations are indicated as white circles in the transmittance graph of Fig. 4.10 (c). Fig. 4.11 (a) and (b) display the electric fields for the symmetric and antisymmetric mode in case of full displacement ($S$ = 190 nm). The modes exhibit different characteristics compared to those in Fig. 4.9. Now, for the symmetric mode the ends of the wires with opposite charge are close to each other, leading to a field enhancement in the gap. This spatial proximity of opposite charges leads to the pronounced red shift of this mode. The electric field distribution of the antisymmetric mode for this geometry reveals the reason for the weak coupling of this mode to the light field: the opposite plasmonic oscillation of comparable strength in both wires yields almost no net dipole moment, which can be almost intuitively observed in this graph. Finally, the higher order antisymmetric mode is displayed in Fig. 4.11 (c) in the structure with $S$ = 30 nm. As stated above, this

FIGURE 4.11 *(FACING PAGE)*. Normalized logarithmic electric field intensity for a stacked dimer structure with a lateral shift and a vertical distance of $d_z$ = 30 nm. (a) Field distribution of the symmetric mode ($\lambda$ = 1069 nm). (b) Field distribution of the antisymmetric mode ($\lambda$ = 846 nm). The plasmons oscillate antiparallel, which in the shifted arrangement is the (slightly) blue-shifted case. (c) Field distribution of the higher order antisymmetric mode that can be excited at small lateral displacement ($S$ = 30 nm) at a wavelength of 725 nm. In this case two counter-oriented electric field vortices are present, which leads to the excitation of two magnetic moments with opposite direction.

(a)                    $d_z$ = 30 nm, $S$ = 190 nm, $\lambda$ = 1069 nm

(b)                    $d_z$ = 30 nm, $S$ = 190 nm, $\lambda$ = 846 nm

(c)                    $d_z$ = 30 nm, $S$ = 30 nm, $\lambda$ = 725 nm
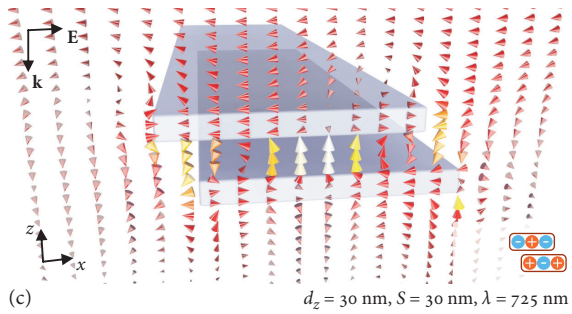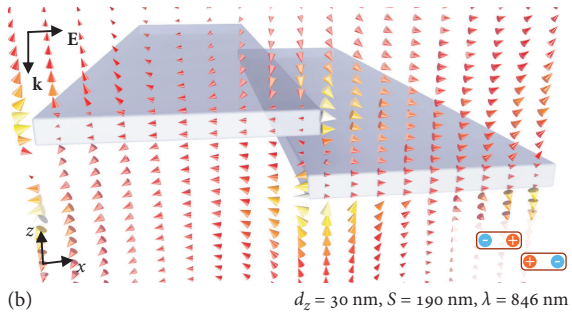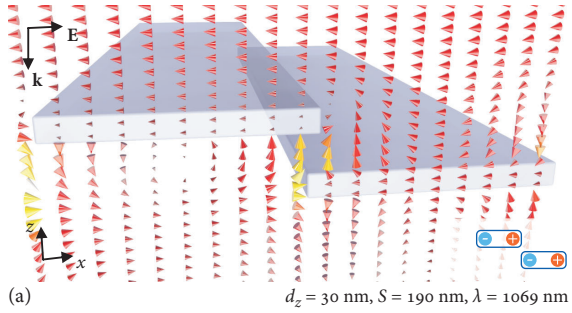
electric field distribution can be considered as an antisymmetric higher order mode. It is similar to the antisymmetric mode in Fig. 4.9 (a), but shows two counter-oriented vortices of the electric field. Therefore, an excitation of this mode principally leads to the induction of two oppositely aligned magnetic moments in $y$ direction.

The electric field distributions qualitatively confirm the findings so that we can conclude by stating that the plasmon hybridization scheme again allows to qualitatively understand the observations in the dimer system, even for a more complex spatial arrangement. However, a calculation of the actual shifts using eq. 4.1 does not yield quantitatively correct values, just as it was the case in the previous section for the non-shifted vertical dimer arrangement.

The experimental observation of the mode inversion in a stacked arrangement of laterally shifted wires is quite challenging due to fabrication issues. This can be conferred from Fig. 4.10 (d). In this graph, the same calculation as in Fig. 4.10 (c) is shown for an increased vertical spacing of $d_z$ = 80 nm. No inversion is observed any more owing to the strongly decreased interaction due to the larger spacer layer. To observe a strong effect it is therefore necessary to fabricate very thin spacer layers. For these, however, the planarization using a spin-on dielectric (SOD) is not sufficient any more. This leads to a strong surface modulation for the second layer and the expected spectra are not observed in the experiments.

## 4.7    RADIATIVE COUPLING IN STACKED DIMERS

The results on lateral near- and far-field interaction in planar as well as near-field interaction in stacked geometries constitute the state of the art. No investigations on radiative coupling have been carried out so far. This stems mainly from the fact, that conventional fabrication techniques did not allow for a three-dimensional arrangement of the building blocks at large vertical distances, only a spacing of several ten nanometers could be accomplished without the benefits afforded by a sophisticated stacking technique. Using the layer-by-layer stacking technique described in section 3.1.1, a vertical arrangement even at large distances is possible.

The investigations in the planar arrays indicate that it is vital to consider far-field coupling effects as well. A vertical arrangement, however, has several advantages. Apart from the placement of several oscillators along the propagation direction of incoming light and the other advan-

tages of a stacked configuration mentioned in the section above, the orientation of the dipoles is favorable in the stacked geometry: dipolar emission is most efficient in the plane perpendicular to the dipolar orientation. In the stacked geometry the dipoles are therefore arranged along their strongest emission direction. Consequently, we expect substantially stronger coupling effects in the stacked arrangement compared to those in lateral geometries.

To investigate the basic properties of radiative coupling in stacked structures, we increase the vertical distance $d_z$ in the stacked nanowire dimer structure beyond the near-field coupling regime as indicated in Fig. 4.12. Doing so, we will examine coupling over the whole range of vertical spacings, from as low as $d_z = 30$ nm, which is well in the near-field regime, up to spacings of more than 1 µm, where the spacer layer is substantially larger than one wavelength.
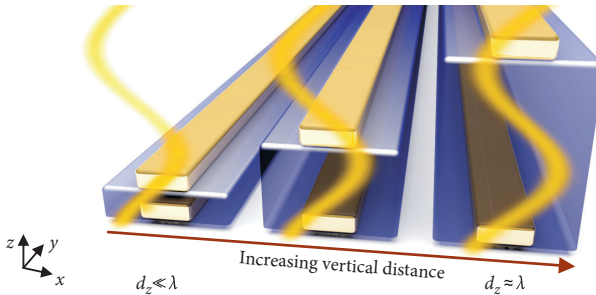


FIGURE 4.12. Schematic of the transition from the near-field to the far-field regime. The vertical spacing is substantially increased such that $d_z \approx \lambda$.

### 4.7.1   *Mirror Microcavities*

In case of a large vertical spacing, the overall dimensions of the system are comparable to the wavelength and retardation plays a key role. An idealized resonance phenomenon which is connected to retardation effects is the Fabry-Pérot (FP) resonance. As it will be important to consider these, we first review their basic properties in Fig. 4.13.

Illuminating a thin metallic film with broadband white light yields a spectrally almost flat reflectance. Besides some absorption in the metal only a small fraction of light is transmitted. As soon as a second, identical metallic film is placed at a distance $d_z$ below the first one,
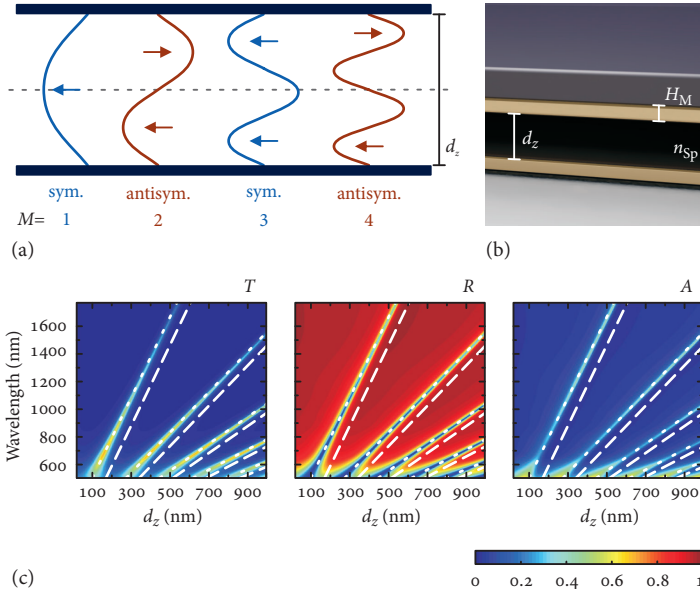
FIGURE 4.13.    (a) Schematic of FP modes in a cavity. The mode symmetry is characterized by the electric field distribution inside the resonator. The odd modes (odd multiples of $\lambda/2$) are symmetric while the even modes (multiples of $\lambda$) exhibit an antisymmetric field distribution.    (b) Schematic for the calculated system. The distance between the mirror layers is filled with a dielectric spacer. For symmetry reasons a capping layer is also applied on top of the upper mirror. (c) Calculated transmittance, reflectance, and absorbance spectra for a micro-cavity consisting of two $H_M$ = 20 nm thick Au mirrors and quartz ($n_{Sp}$ = 1.46) as a spacer material. Long-dashed white lines indicate the calculation using the basic FP formula (eq. 4.4). The dotted white lines indicate the calculations which include an apparent length increase of $d_{ALI}$ = 100 nm (eq. 4.5).

interference phenomena occur and have to be taken into account. Sharp dips appear in the previously flat reflectance spectra, while concurrently peaks are observed in transmittance. These sharp features are associated with multiple interference of the waves in the resonator and thus are very sensitive to the exact spacing between the metallic films.

The spectral positions associated with these modes are determined by the condition, that a multiple of the wavelength exactly matches one round trip of light in the cavity. Thus, the total phase shift is $\Delta\varphi_{tot}$ =

$M \cdot 2\pi$ with a natural number $M$. In case of ideal reflectors only the retardation phase $\Delta\varphi_{\mathrm{ret}} = 2\pi \cdot 2n_{\mathrm{Sp}}d_z/\lambda$ is of importance. Here, $n_{\mathrm{Sp}}$ is the refractive index of the spacer layer. This yields the resonance condition

$$\lambda_M = \frac{2n_{\mathrm{Sp}}d_z}{M},\tag{4.4}$$

where the FP resonance wavelength linearly depends on $d_z$.

For FP modes symmetry considerations are crucial as well. The modes can be classified by their symmetry, however, the criterion in this case is the electromagnetic field distribution between the mirrors. This is depicted in Fig. 4.13 (a). The modes with odd $M$ exhibit a symmetric electric field distribution with respect to the symmetry axis between the mirrors. In contrast, the even modes display an antisymmetric electric field distribution.

Fig. 4.13 (c) shows spectra which were obtained by SMM calculations for a microcavity consisting of two Au films of 20 nm thickness completely embedded into quartz (see Fig. 4.13 (b)). As already mentioned, the FP modes can be observed as dips in reflectance or peaks in transmittance. The calculated FP resonance positions using eq. 4.4 are indicated in the spectra of Fig. 4.13 (c) as long-dashed white lines. Obviously, this does not describe the FP mode positions correctly.

The reason is the assumption of perfectly reflecting mirrors in eq. 4.4, which is not true for a 20 nm thin metal film. One has to account for this by adding an apparent length increase $d_{\mathrm{ALI}}$ which arises from the fact that the cavity mirrors are no perfect reflectors, hence the field penetrates into the boundaries of the cavity [252]. The dotted white lines indicate the corrected resonance positions

$$\lambda_{\mathrm{corr},M} = \frac{2\left(n_{\mathrm{Sp}}d_z + d_{\mathrm{ALI}}\right)}{M},\tag{4.5}$$

where for the plot $d_{\mathrm{ALI}} = 100$ nm has been assumed. This value leads to a good agreement with the SMM calculations. From the magnitude of $d_{\mathrm{ALI}}$ it is obvious, that it cannot be interpreted in terms of a penetration depth but rather has to be seen as an additional phase term which incorporates the reflection from a non-perfect boundary into the model.

### 4.7.2    *From Near- to Far-Field Coupling in the Nanowire Dimer*

The symmetry considerations for cavities above can be transferred to the radiatively coupled dimer system. This transition is illustrated in Fig. 4.14. As in the near-field coupled case, the symmetry of the plasmonic oscillations in the wires has to be taken into account, but in addition, it is also necessary to consider the symmetry of the electric field between both wires, just as in the case of the cavities shown above. Therefore, the symmetric mode in the far-field regime comprises a symmetric plasmon oscillation *and* a symmetric electric field distribution in the spacing between the wires. The opposite is true for the antisymmetric mode, as shown in the bottom row of Fig. 4.14.
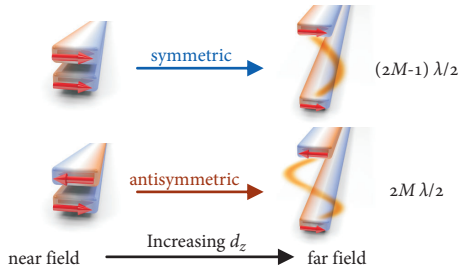


FIGURE 4.14. Schematic of the transition of the dimer modes from the near-field to the far-field coupling regime. In the far-field case (right), retardation plays a crucial role and the system exhibits coupled FP-PPR modes. The symmetries of the charge oscillations *and* the electric field have to be taken into account. Just as for mirror cavities, odd modes are symmetric and even modes are antisymmetric in both, electric field distribution and plasmon oscillation. The mode index $M$ is a natural number.

Just as for the plain cavities, a mode order can be assigned, connecting the vertical spacing between the wires and the wavelength of the mode: the symmetric modes are found for vertical distances which match an odd multiple of $\lambda/2$ while for the antisymmetric mode, an even multiple of $\lambda/2$ is required. However, this is only true for frequencies far away from the single layer PPR, for wavelengths close to it, the particle plasmon phase varies strongly and additional considerations are required, which we will discuss below.

In order to investigate the radiative coupling properties of the dimer structure systematically, Fig. 4.15 displays spectra acquired from SMM
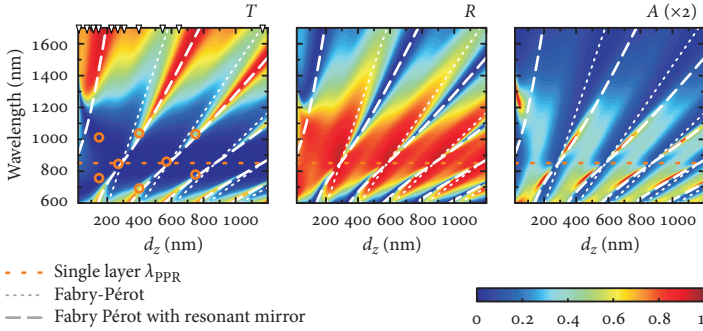
FIGURE 4.15. Calculated $d_z$-dependent transmittance, reflectance, and absorbance spectra for the near- as well as the far-field coupling regime of the stacked dimer structure. The single layer PPR is denoted by the orange line. Unperturbed FP modes are indicated by the dotted white lines, modes calculated by the analytical resonant mirror model are shown as long-dashed white lines. Orange circles indicate positions, where electric field calculations have been performed (see Figs. 4.16, 4.17 and 4.23). White triangles at the top of the transmittance graph indicate the position of experimentally realized samples (section 4.9). Absorbance is increased by a factor of 2 for clarity.

calculations for the same geometry as investigated in section 4.5[vi] but now for a substantially increased vertical spacing. Therefore, the region up to $d_z = 150$ nm in Fig. 4.15 corresponds to the spectra displayed in Fig. 4.8. At large vertical spacing strongly $d_z$-dependent spectral features are observed. These features strongly resemble FP modes, however, the spectral position for a pure FP mode depends linearly on the vertical distance $d_z$ (see Fig. 4.13), which is obviously not the case here. Second, their spectral width is strongly modified, depending on their spectral position. Especially when approaching the single layer PPR wavelength $\lambda_{\text{PPR}}$, indicated by an orange horizontal line in Fig. 4.15, their width strongly narrows and almost vanishes close to $\lambda_{\text{PPR}}$.

Therefore, it has to be concluded that the PPR modes in the wires couple to the FP modes which arise due to the arrangement of the wires. This results in a modification of the spectral position as well as linewidth of the new, coupled FP-PPR modes.

To confirm these findings and to give a straightforward explanation for this coupling of two particle plasmonic modes to a FP mode, we

_____

vi  $W = 200$ nm, $H = 20$ nm, embedded into quartz environment

(a)      $d_z = 150$ nm, $\lambda = 1012$ nm     (b)      $d_z = 150$ nm, $\lambda = 757$ nm
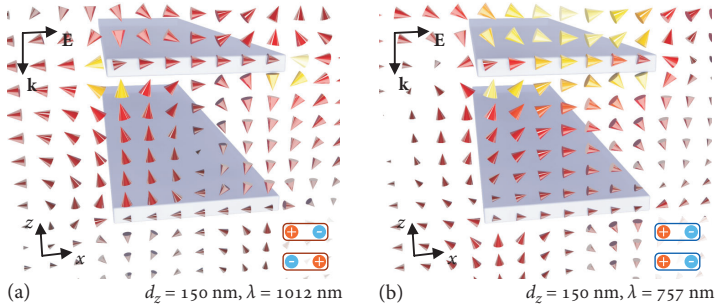
FIGURE 4.16. Normalized logarithmic electric field intensity for a stacked dimer structure with a vertical distance of $d_z = 150$ nm.   (a) Field distribution of the antisymmetric mode ($\lambda = 1012$ nm).   (b) Field distribution of the symmetric mode ($\lambda = 757$ nm).  Despite the increased vertical spacing, both fields still exhibit the typical behavior already observed in Fig. 4.9. The strong field enhancement that was visible in Fig. 4.9 (a) is less pronounced due to the larger spacing.

describe the new spectral positions of the coupled modes in an analytical resonant mirror cavity model, which will be given in the following section 4.8.

Before, we examine the electric field distribution at selected spacing distances and wavelengths. The field graphs show the normalized logarithmic electric field strength in the $xz$ plane at the time of maximum electric field intensity. The vertical spacings as well as spectral positions of the calculations are indicated in the transmittance graph of Fig. 4.15 as orange circles.

For a spacing of $d_z = 150$ nm, the electric field distribution shown in Fig. 4.16 still exhibit the characteristics of the near-field coupled system, as can be seen by comparing Fig. 4.16 to Fig. 4.9. This finding is consistent with the observations in the spectra (Fig. 4.15) where the splitting

FIGURE 4.17 (FACING PAGE). Normalized logarithmic electric field intensity for a stacked dimer structure with a vertical distance of $d_z = 400$ nm and $d_z = 750$ nm. Field distribution of the   (a) first,   (b,c) second and   (d) third coupled FP-PPR modes. The symmetric (a,d) and antisymmetric (b,c) field distribution as well as plasmon oscillations are pronouncedly visible. For the second (third) mode one (two) field nodes are present between the wires.

(a)    $d_z = 400$ nm, $\lambda = 1038$ nm

(b)    $d_z = 400$ nm, $\lambda = 692$ nm

(c)    $d_z = 750$ nm, $\lambda = 1033$ nm

(d)    $d_z = 750$ nm, $\lambda = 779$ nm
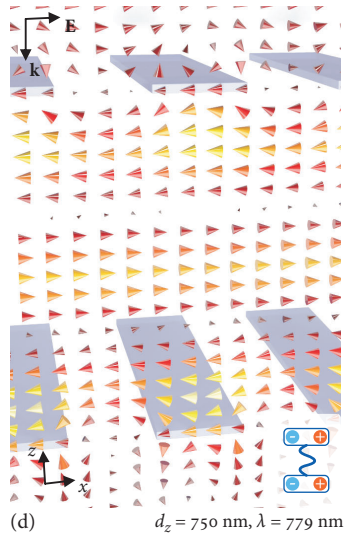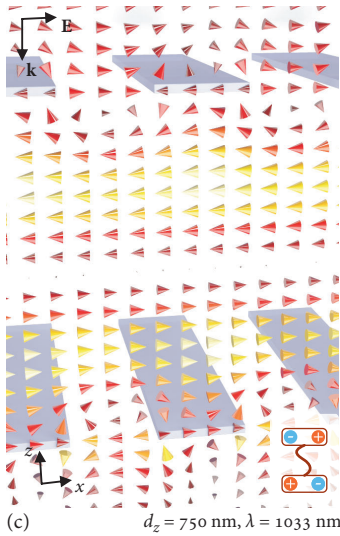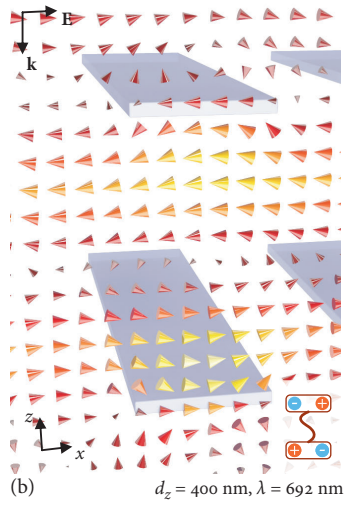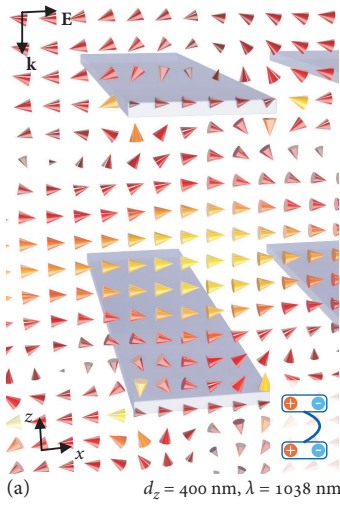
into symmetric and antisymmetric mode is still present, but with substantially lower spectral separation. Owing to the reduced coupling strength, the field enhancement for the antisymmetric mode is much lower compared to the structure with $d_z$ = 30 nm (Fig. 4.9 (a)).

The electric field distributions for vertical distances larger than $d_z$ = 150 nm are shown in Fig. 4.17. These agree well with the interpretation of the far-field regime dimer modes shown in Fig. 4.14. Besides the symmetry of the plasmonic oscillations, the graphs display the importance of considering the electromagnetic field in between the wires for far-field interaction. Panel (a) of Fig. 4.17 shows a symmetric electric field with one field antinode in the middle between the wires, accompanied by symmetric charge oscillations. The situation is changed for the second mode, which is observed in two panels, once for a wavelength below the single particle PPR wavelength (b) and once above $\lambda_{PPR}$ (c), at different vertical spacings $d_z$. Here antisymmetric charge oscillations are accompanied by a field distribution similar to the second FP mode with one field node in the middle, which is pronouncedly visible in both graphs. Finally, the next higher mode is observed in panel (d), which corresponds to a symmetric mode again and exhibits two field nodes in between the wires.

## 4.8   ANALYTICAL COUPLING MODELS

Apart from the full numerical description of the system which was provided above, it is desirable to find a simple analytic model which captures the core features of the physics involved. Here, we will check the validity of an analytical model already introduced before for coupled excitons. Afterwards we introduce the resonant mirror model, which describes a possibility to derive the spectral positions of the coupled modes from straightforward phase considerations.

### 4.8.1   *Eigenmode Coupling Model*

In the context of radiatively coupled excitons in multi-quantum well (QW) structures a model has been developed to describe the modulation of spectral position as well as width of the coupled modes in radiatively coupled multilayer structures [253–255] with $N$ identical resonant layers separated by a vertical distance $d_z$. Within this model the resonance energy shift $\Delta E_o$ and the modified spectral width $\Gamma_{o,c}$ are found by

determination of the complex eigenvalues of a $N \times N$ coupling matrix $\mathcal{A}$ which describes the interaction between the single excitons. Therefore, the solutions of

$$\det(\mathcal{A} - \mathcal{I}(\Delta E_o - i\Gamma_{o,c})) = 0$$

have to be found, where the elements of $\mathcal{A}$ are given by

$$\mathcal{A}_{i,j} = -i\Gamma_o \, e^{ik|i-j|d_z}. \tag{4.6}$$

Here, $\Gamma_o$ is the radiative width of the single layer. Nonradiative decay is neglected within this model in order to obtain simple analytical results. For a two layer system the solution is straightforward and yields

$$\begin{aligned} \Delta E_o^{\pm} &= \pm\Gamma_o \sin kd_z \\ \Gamma_{o,c}^{\pm} &= \Gamma_o(1 \pm \cos kd_z), \end{aligned} \tag{4.7}$$

where "+" and "-" denote the symmetric and antisymmetric mode respectively. These are shown in Fig. 4.18 (a), where additionally $k \approx k_{\text{PPR}} = 2\pi/\lambda_{\text{PPR}}$ is assumed. Their spectral position and width are oscillatory functions of $d_z/\lambda_{\text{PPR}}$. The energy shift is zero whenever $d_z$ equals a multiple of $\lambda_{\text{PPR}}/2$ and maximum for odd multiples of $\lambda_{\text{PPR}}/4$. In contrast, $\Gamma_{o,c}$ oscillates between $2\Gamma_o$ and zero and reaches its extremal values whenever $\Delta E_o = 0$. For $d_z$ being an odd multiple of $\lambda_{\text{PPR}}/2$, the antisymmetric linewidth is twice the single oscillator linewidth and the symmetric mode vanishes. This situation is reversed when $d_z$ is a multiple of $\lambda_{\text{PPR}}$. Then the symmetric mode exhibits maximum width and the antisymmetric mode vanishes. This behavior has been attributed to excitonic superradiance.

Despite the fact that this model is straightforward, it obviously fails to describe our findings in a plasmonic system. Overall, the oscillatory behavior suggested by Fig. 4.18 is not observed in the calculations of Fig. 4.15, even though it seems to capture some of the basic features, for example the fact that one mode becomes dark for $d_z = \lambda_{\text{PPR}}/2$.

This does not arise from the approximation $k \approx k_{\text{PPR}}$. An inclusion of the frequency dependence in $k$ would lead to a transcendental equation which then would have to be solved numerically. However, this frequency dependence in $k$ would only lead to a distorted sine and cosine shape, whereas the basic properties of the model would retain.

There are several reasons for the failure of the model: First, Fig. 4.18 (a) is suggestive in terms of its display style. According to the figure one
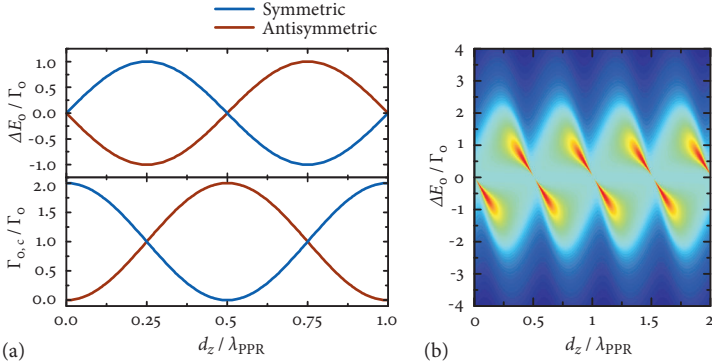
FIGURE 4.18.    (a) Energy shift $\Delta E_o$ (top panel) and linewidth $\Gamma_{o,c}$ (bottom panel) depending on the spacing in a simple two-oscillator coupling model [253]. Both quantities are given in units of the radiative decay rate of a single oscillator $\Gamma_o$. This model suggests a $\lambda_{PPR}$-periodic variation of the spectra. The maximum resonance position deviation is achieved for $d_z = (2M - 1)\lambda_{PPR}/4$. For $d_z = M\lambda_{PPR}/2$ the resonance shift is zero and the linewidths are extremal.    (b) Sum of two Lorentzians with width and height determined by the model shown in (a) (eq. 4.7). As this graph only sums up two resonances, it does not exactly describe the real spectra. The color scale is given in arbitrary units.

would expect two distinct peaks which oscillate in the spectrum on a change of $d_z$. This is not the case, as the total oscillation amplitude of the energy shift is less than the total linewidth itself. As concurrently the linewidths undergo strong changes, the behavior is not obvious. For this reason, panel (b) of Fig. 4.18 shows the sum of two Lorentzian lineshapes whose widths and spectral positions are determined by the results of eq. 4.7 (see panel (a)). It has to be noted, that this calculation does not provide a physically correct result. The modes are simply added without taking oscillator strengths or interference phases into account. Thus it cannot be related in a direct manner to an observable quantity such as transmittance or reflectance. The only purpose is to visualize the principal behavior predicted by eq. 4.7. There is a certain similarity between both graphs[vii], especially regarding the vanishing of one mode for $d_z/\lambda_{PPR} = M/2$.

vii For a comparison of the graphs it has to be noted, that Fig. 4.18 (b) is plotted over energy, while Fig. 4.15 is shown over the wavelength

Second, there is a more fundamental reason why the model does not describe the spectra correctly. The strong coupling to the light field gives rise to FP modes which have to be included into a coupled eigenmode model. Then the PPRs are able to couple to them, which yields the characteristic behavior observed in Fig. 4.15 [11, 256]. As this is not the case in eq. 4.7, the model necessarily fails to describe the coupled FP-PPR modes correctly.

Finally, it is furthermore doubtful, if this model can be used to describe the coupling in QW structures as well. One major simplification in the derivation of eq. 4.7 is to neglect the nonradiative contribution to the linewidth. For QW structures, this nonradiative contribution is usually about one order of magnitude stronger than the radiative contribution, which leads to substantially different spectral effects.

Therefore it has to be concluded that this model fails to describe the radiative coupling of oscillators in real systems. For oscillators which are strongly damped by nonradiative effects, neglecting those is not appropriate. For oscillators where this would be possible, the coupling to the light field gives rise to the presence of FP modes which have to be included into the coupling model. This causes the model to fail for this situation as well.

### 4.8.2   *Resonant Mirror Model*

To calculate the coupled FP-PPR resonance positions we consider the phases the phases in the system. On the one hand, there are phases due to the propagation between both layers, on the other hand the oscillators which are present at the boundaries behave more complex than ordinary cavity mirrors. Taking into account both effects leads to an easy model, which is termed the resonant mirror model [257–259].

In a first step, the two PPR layers are described as an ideal cavity. Using eq. 4.4 yields the dotted white lines in Fig. 4.15, which correspond to the unperturbed FP modes. These give a very rough approximation for the mode position. In a similar manner to the apparent length increase in a non-ideal cavity (eq. 4.5), the plasmonic layers have to be included. Here we deal with *resonant* mirrors, i. e., the boundary layers of the cavity exhibit resonances of their own. These resonances do not only alter the amplitude of the reflection coefficients at the boundaries but also impose an additional phase which has to be taken into account in

the resonance condition. Therefore a resonant phase $\varphi_{\mathrm{r,res}}(\lambda)$ has to be included into the total phase shift, which then reads

$$\Delta\varphi_{\mathrm{tot}} = 2\pi M = 2\pi\frac{2n_{\mathrm{Sp}}d_z}{\lambda} + 2\varphi_{\mathrm{r,res}}(\lambda). \qquad (4.8)$$
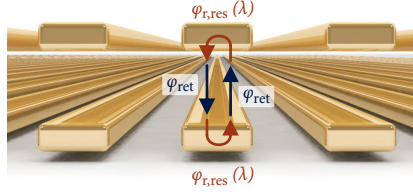


FIGURE 4.19. Schematic of the resonant mirror model. In addition to the retardation phase $\varphi_{\mathrm{ret}}$ the phase upon reflection from the nanowire layers, $\varphi_{\mathrm{r,res}}(\lambda)$, has to be considered. As the wires exhibit a plasmonic resonance, this phase shows a strong dependence on the wavelength of the light.

To obtain the resonant contribution $\varphi_{\mathrm{r,res}}(\lambda)$ we calculate the reflection phase for a resonant layer using the considerations of section 2.5. For a single resonant layer located at the origin ($z_n = 0$), the reflection amplitude described by eqs. 2.66 and 2.67 is strongly simplified and reads

$$\mathfrak{r} = \frac{i\frac{k}{2\varepsilon_{\mathrm{Sp}}}\chi(\omega)}{1 - i\frac{k}{2\varepsilon_{\mathrm{Sp}}}\chi(\omega)}. \qquad (4.9)$$

Using the susceptibility derived from the harmonic oscillator model, eq. 2.30 yields the reflection amplitude for a single resonant layer

$$\mathfrak{r} = -\frac{i\Gamma_{\mathrm{o}}(\omega)}{\omega - \omega_{\mathrm{PPR}} + i(\Gamma + \Gamma_{\mathrm{o}}(\omega))}. \qquad (4.10)$$

Here, $\omega_{\mathrm{PPR}}$ is the PPR frequency and $\Gamma$ the nonradiative damping rate. The expression $\Gamma_{\mathrm{o}}(\omega)$ contains all the constants and describes the coupling to the light field. Due to the inclusion of the $k/(2\varepsilon_{\mathrm{Sp}})$ factor into $\Gamma_{\mathrm{o}}(\omega)$, it depends on the frequency itself. This dependence can be expressed as

$$\Gamma_{\mathrm{o}}(\omega) = \Gamma_{\mathrm{o}}(\omega_{\mathrm{PPR}}) \cdot \frac{\omega}{\omega_{\mathrm{PPR}}}. \qquad (4.11)$$

As a consequence, the lineshape of the resonance is slightly asymmetric. However, it is often appropriate, especially for narrow resonances, to neglect this dependence and assume $\Gamma_o(\omega) \approx \Gamma_o(\omega_{PPR})$[viii].

The coupling to the light field leads to the modification of the spectral width of the oscillator observed in the reflection spectra. This is obvious from the denominator of eq. 4.10, where $\Gamma_o(\omega)$ adds up to the nonradiative contribution of the linewidth. Therefore $\Gamma_o(\omega_{PPR})$ is identified as the radiative linewidth of the oscillator.

To calculate the resonant phase contribution finally the phase of the reflection amplitude given in eq. 4.10 has to be evaluated:

$$\varphi_{r,res}(\omega) = \arctan\left(\frac{\mathfrak{Im}(\mathfrak{r})}{\mathfrak{Re}(\mathfrak{r})}\right) = \arctan\left(\frac{\omega - \omega_{PPR}}{\Gamma + \Gamma_o}\right). \qquad (4.12)$$

Converting this to the wavelength scale using $\omega = 2\pi c/\lambda$, $\omega_{PPR} = 2\pi c/\lambda_{PPR}$ and $\Gamma_{tot}^\lambda = 2\pi c/(\Gamma + \Gamma_o)$ yields

$$\varphi_{r,res}(\lambda) = \arctan\left(\frac{\Gamma_{tot}^\lambda(\lambda_{PPR} - \lambda)}{\lambda \lambda_{PPR}}\right). \qquad (4.13)$$

This can be rewritten[ix] to

$$\varphi_{r,res} = \frac{\pi}{2} + \arctan\frac{\lambda \lambda_{PPR}}{\Gamma_{tot}^\lambda(\lambda - \lambda_{PPR})}. \qquad (4.14)$$

Inserting this into eq. 4.8 accurately reproduces the resonance positions in the radiative coupling domain ($d_z > 150\,\text{nm}$), which is indicated by the white long-dashed lines in Fig. 4.15. Despite its simplicity, the resonant mirror model shows very good agreement with the numerical calculations and therefore provides a straightforward explanation of the physics involved.

## 4.9 EXPERIMENTAL RESULTS

To experimentally confirm the findings, a series of samples was fabricated using EBL in a two layer process. In the experiment, only one specific $d_z$ can be fabricated for each sample, therefore eleven different samples were realized with spacer thicknesses as low as 30 nm up to

---

viii For simplicity this will be denoted by using $\Gamma_o$ without any additions.

ix see appendix A.2 for details.

more than 1 μm. The measured linear spectrum of each sample corresponds to a vertical cross section in Fig. 4.15. The white arrows at the top of the transmittance graph in that figure indicate the realized $d_z$ values.

The nominal sample geometry was chosen according to the calculations[x]. The structures were defined in negative resist on top of a 20 nm thick gold film, with subsequent Ar ion beam etching. As a spacer, a SOD layer was utilized. The varying spacer thickness was realized by multiple coating runs utilizing different dilutions of the SOD. The resulting spacer thickness was subsequently verified by a profilometer with a height resolution of about 10 nm.

This independent measurement is crucial, as it provides an external verification of the spacer thickness, which otherwise would have to be conferred from a comparison of calculated and measured spectra.



| 500 nm | | |
|---|---|---|
| $d_z = 80$ nm | $d_z = 270$ nm | $d_z = 650$ nm |
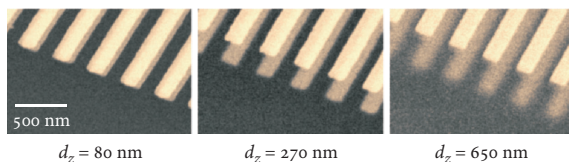
FIGURE 4.20. SEM micrographs of the fabricated structures width different vertical spacings $d_z$ =80 nm, 270 nm, and 650 nm.

Fig. 4.20 shows representative scanning electron microscope (SEM) images of three of the eleven samples with different spacer thicknesses of 80 nm, 270 nm, and 650 nm. The distance between both layers is pronouncedly observed in case of the higher distances. At the same time, the image of the bottom layer becomes increasingly blurred due to higher electron scattering in the spacer material. The images demonstrate a good lateral alignment of the layers with respect to each other, with deviations on the order of 20 nm.

For all fabricated samples, linear transmittance as well as reflectance spectra were measured in a Fourier-transform infrared spectrometer (FTIR) microscope. Owing to the broad spectral range of the samples, two measurements are necessary. These were acquired using a Si and an InGaAs photodiode. Some spectral overlap is provided, which is then used to match both measurements.

---

x  $W = 200$ nm, $H = 20$ nm, and $d_x = 400$ nm
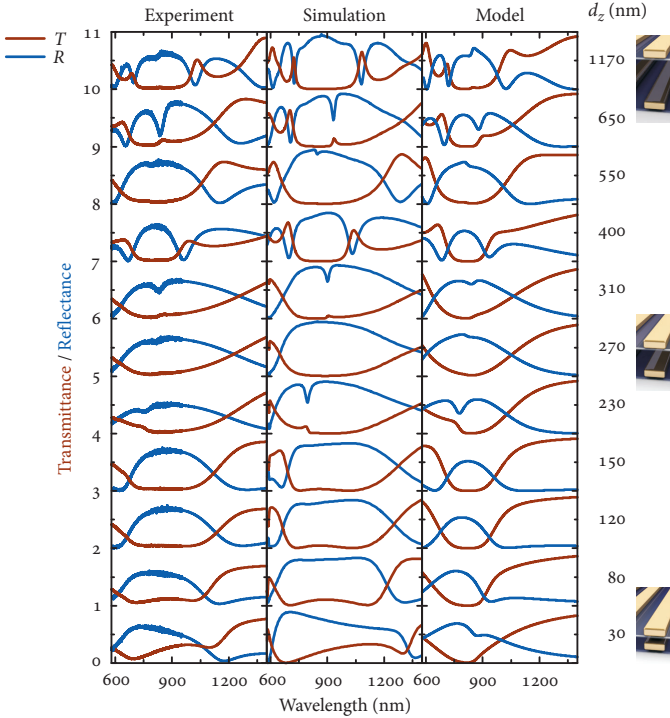
FIGURE 4.21. Transmittance and reflectance spectra for plasmonic dimers at different vertical distances $d_z$. The left panel shows the measured spectra. The middle panel displays the calculated transmittance and reflectance for the corresponding spacer thicknesses. For comparison, the spectra calculated by the resonant mirror model (eqs. 2.66 and 2.67) are shown. As this model does not incorporate near-field coupling effects, the agreement for small $d_z$ is bad.

The acquired spectra are displayed in the left panel of Fig. 4.21 for all eleven samples. For comparison, the calculated results are shown in the right panel. It is noteworthy, that no free parameters are used in the calculations due to the additional determination of spacer thickness.

For small distances the near-field splitting is clearly observed. It is present up to approximately $d_z \approx 150\,\mathrm{nm} \approx \lambda_{\mathrm{PPR}}/(5 n_{\mathrm{Sp}})$. At larger distances, the spectra are dominated by far-field effects. The spectrum for $d_z = 270\,\mathrm{nm}$ shows only one broad feature, a situation which is repeated at $d_z = 550\,\mathrm{nm}$. These vertical distances correspond to the

cases where the coupled FP-PPR modes spectrally approach the single layer $\lambda_{PPR}$. This situation will be discussed in detail in section 4.10. For larger distances more and more modes are present, leading to an increased number of resonant features in the spectra.

As a last point of this section the deviations between calculation and experiment have to be discussed. The overall agreement between calculations and experiment is very good. Mainly three types of deviations are observed in Fig. 4.21: First, a deviation of the spectral position is present for some spectral features. This is attributed to the accuracy of the stylus profilometer measurement. Especially in the near-field coupled case a small deviation already results in substantial spectral shifts (see leftmost region of Fig. 4.15), so that an error of only 10 nm in the determination of the layer thickness already yields strong spectral shifts.

Second, sharp features are attenuated in the spectra. This can partially be attributed to inhomogeneous broadening, as arrays of particles were investigated. Additionally, the measurement method using a high-NA-Cassegrain objective leads to an averaging over a cone of incident **k** vectors. This averaging is not accounted for in the calculations, where an incoming plane wave strictly normal to the sample is assumed. Therefore the measurement technique could partially also contribute to this type of deviation.

Finally, the reflectance measurements show substantially lower absolute values compared to calculation. While in the latter, values of 90 % are obtained, the experiment does not keep up to these high values. Several potential reasons for this deviation exist. It might partially stem from imperfections and inhomogeneities in the structure, such as rough surfaces which scatter light. Additionally, for a perfect reflectance measurement all light has to be collected, which is much harder in reflectance compared to transmittance measurements.

As we do not intend to provide quantitative measurements, but rather investigate the basic properties of coupling in the structure none of the above effects is serious in the sense of altering the interpretation of the data.

## 4.10   BRAGG SPACING

It has already become apparent that a special vertical distance has to be investigated in detail. Namely the one, where the FP modes spectrally approach the single layer PPR. This happens at the intersections of the

dotted white lines and the orange line in Fig. 4.15. For the given geometry, the first three of these are approximately $d_z$ = 270 nm, 540 nm, and 820 nm.

For these $d_z$ the the Bragg criterion for the single layer resonance wavelength is fulfilled:

$$d_z = M \frac{\lambda_{PPR}}{2n_{Sp}}, \tag{4.15}$$

where $M$ denotes an integer number. Therefore, they will be referred to as the $M$th Bragg distance.

Fulfilling the Bragg criterion at the single layer PPR can be regarded as a matched spatial arrangement of the oscillators with respect to their resonance wavelength. Around the $\lambda_{PPR}$, the resonant part of eq. 4.13 undergoes a strong variation. The phase difference of the oscillators with respect to their off-resonant phase is exactly $\pi/2$ at $\lambda = \lambda_{PPR}$. Therefore the coupled FP-PPR mode which spectrally approaches the single layer resonance becomes close to optically inactive, which is shown in detail in Fig. 4.22 for the first Bragg spacing.
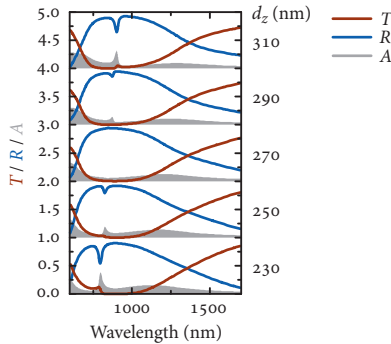


FIGURE 4.22. Transmittance, reflectance, and absorbance spectra around the first Bragg spacing ($d_z$ =270 nm) extracted from Fig. 4.15. When approaching $\lambda_{PPR}$, the linewidth of the coupled FP-PPR modes becomes very narrow and almost vanishes exactly at Bragg spacing. In this case only one very broad spectral feature remains in the spectrum.

This has two immediate consequences. First, the PPR radiative fields add up destructively in forward direction and constructively in backward direction, leading to high reflectance and low transmittance of the

structure. This is typical for periodic Bragg structures such as Bragg mirrors, where multilayer interference in backward direction leads to high reflectance. This can be observed in the electric field distributions which are shown for the first and second Bragg distance in Fig. 4.23. A high electric field strength is observed above the structure, indicating its high reflectance.



| (a) | $d_z$ = 270 nm, $\lambda$ = 846 nm | (b) | $d_z$ = 570 nm, $\lambda$ = 860 nm |
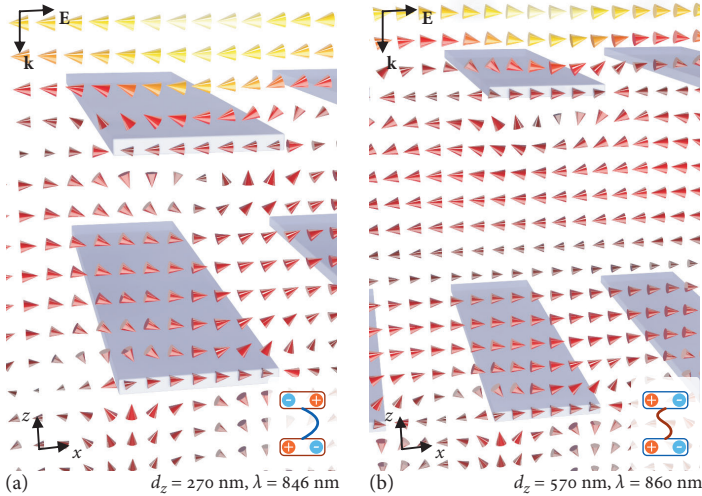
FIGURE 4.23. Normalized logarithmic electric field intensity for a stacked dimer structure at (a) first ($d_z$ = 270 nm) and (b) second ($d_z$ = 570 nm) Bragg distance. For these special situations, the mode which is spectrally close to $\lambda_{PPR}$ becomes optically almost inactive and the field distribution is governed by the neighboring modes. In this case, field distribution and plasmon oscillation exhibit a different symmetry: a symmetric field distribution is accompanied by an antisymmetric plasmon oscillation in (a) and vice versa in (b).

Second, as the corresponding coupled mode vanishes, the spectra are dominated by the neighboring coupled modes. These possess opposite symmetry. Therefore, in this case the field distribution between the wires exhibits a different symmetry than the plasmon oscillation. At first Bragg distance, a symmetric field between the wires is observed, yet the plasmons in the wires show an antisymmetric oscillation. At second Bragg distance, this situation is reversed, the electric field in between is antisymmetric with a symmetric plasmon oscillation, as can be observed in the field calculations of Fig. 4.23.

It is also possible to explain this intuitively in the resonant mirror model. Shifting one oscillator by $\pi/2$ and the other by $-\pi/2$, their oscillation symmetry is effectively reversed and thus the symmetry of the plasmon oscillation does not correspond to the field symmetry in between any more.

For exact Bragg spacing ($d_z$ = 270 nm) only one feature can be observed in the transmittance and reflectance spectrum of Fig. 4.22. Its width is strongly enhanced compared to the single layer PPR width. Due to the matched spatial arrangement the system now acts as if it consisted of only a single oscillator with substantially increased oscillator strength. This is similar to a superradiant mode in a system of coupled quantum emitters. In those systems, all modes but one become dark, or subradiant, with only one superradiant mode carrying all the oscillator strength of the system. The situation is slightly different in our case as we deal with classical oscillators and measure linear transmittance and reflectance instead of monitoring the spontaneous decay of two-level quantum systems. However, it has already been pointed out by Rehler and Eberly in the context of superradiance that a broadening of the radiative width in a coupled system also occurs in classical ensembles of oscillators and is not an inherently quantum-mechanical effect [260].

## 4.11 CONNECTION TO CAVITY-COUPLED OSCILLATORS

To complete the description of the dimer structure, we finally investigate the correspondence of the far-field coupled dimer system to a system where an oscillator is placed inside a cavity, and therefore can interact with the cavity modes. When using a quantum emitter as oscillator, this scheme is one of the fundamental experiments of quantum electrodynamics, as it describes the interaction between the fundamental quanta of the elementary excitations in matter with the fundamental quantized modes of the light field in the cavity. It has been experimentally realized using atomic ensembles [261, 262], single atoms [263] or single quantum dots (QDs) [264] as quantum oscillators. Besides the quantum optical interpretation it has been shown, that the mode splitting which arises in the strong coupling regime can also be understood as a linear-optical effect of the resonant dispersion of a medium placed inside the cavity [265]. Thus, it is also feasible to implement this in a classical plasmonic oscillator geometry, which has been realized by Ameling et al. for cut-wire pairs [259] as well as surface plasmon resonances [221].

(a)

(b)
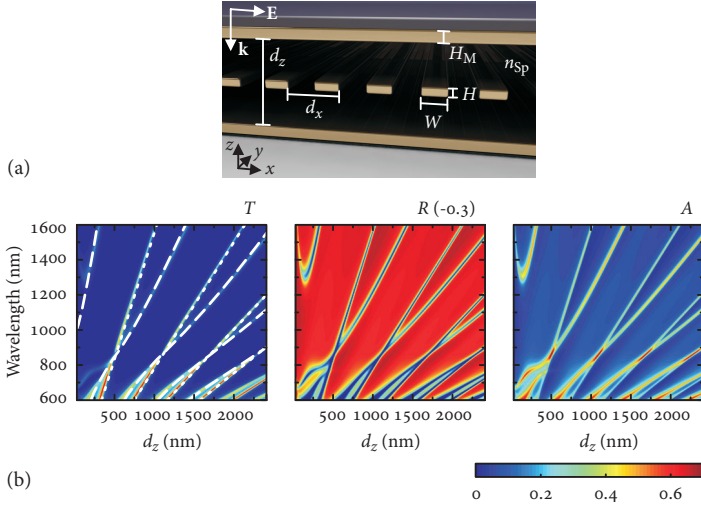
FIGURE 4.24.   (a) Schematic of a plasmonic nanowire layer inside a microcavity. (b) Calculated transmittance, reflectance and absorbance spectra for the system depicted in (a). The thickness of the  Au  mirrors is 20 nm, the wire geometry is $W = 200$ nm and $H = 20$ nm. This system exhibits a strong correspondence to the far-field coupled plasmonic dimer structure. The resonance positions of the coupled modes can be modeled in exact analogy to the nanowire dimer. However, an additional phenomenologic correction has to be introduced.

In analogy to the derivation of the phase upon reflection from a resonant layer (eq. 4.13) it is also possible to calculate the phase upon transmission from the same equations, eqs. 2.66 and 2.67. In doing so, one obtains the resonant transmission phase which is

$$\varphi_{\mathrm{t,res}}(\omega) = \arctan \frac{\Gamma_{\mathrm{o}}}{\omega_{\mathrm{PPR}} - \omega}$$
$$\Rightarrow \varphi_{\mathrm{t,res}}(\lambda) = \arctan \frac{\lambda \lambda_{\mathrm{PPR}}}{\Gamma_{\mathrm{tot}}^{\lambda}(\lambda - \lambda_{\mathrm{PPR}})}, \tag{4.16}$$

where all the quantities are analogous to those in eq. 4.13. It is noteworthy, that the resonant transmission phase almost exactly corresponds to the reflection phase (eq. 4.13) apart from an additional $\pi/2$ term in

the latter. The condition for constructive interference in the resonant mirror model then is

$$\varphi_{\text{tot}} = 2\pi M = 2nkd_z + 2\varphi_{\text{t,res}}(\lambda) + 2\varphi_{\text{ALI}}, \tag{4.17}$$

where $\varphi_{\text{ALI}}$ is the phase due to the reflection from the thin gold mirror, as derived in eq. 4.5.

Calculations of a single layer of nanowires placed in the center between two thin metallic mirror layers are displayed in Fig. 4.24. The wire geometry exactly corresponds to that of the dimer structure, the mirror thickness is set to $H_{\text{M}} = 20\,\text{nm}$. Owing to the high $Q$ factor of the microcavity compared to the relatively low and frequency-dependent $Q$ factor of the dimer system, the spectral widths of the coupled resonances observed in Fig. 4.24 are strongly reduced. Furthermore, their spectral width is rather constant over the whole spectral range in contrast to the observations in the dimer system.

Despite these differences, the resonance positions calculated from eq. 4.17 show a very good agreement. In particular, no modification of the single oscillator properties is necessary. The same oscillator parameters as in Fig. 4.15 are used, namely $\lambda_{\text{PPR}} = 854\,\text{nm}$ and $\Gamma_{\text{tot}}^{\lambda} = 3000\,\text{nm}$. Also the apparent length increase obtained in Fig. 4.13 for an empty cavity ($d_{\text{ALI}} = 100\,\text{nm}$) is appropriate to describe the additional reflection phase from the mirrors.

However, in order to achieve an agreement between model and calculated results, one modification has to be introduced into eq. 4.17. An additional phenomenologic factor for the resonant phase is necessary so that the equation reads

$$\varphi_{\text{tot}} = 2\pi M = 2nkd_z + \Xi \cdot \left(2\varphi_{\text{t,res}}(\lambda)\right) + 2\varphi_{\text{ALI}}. \tag{4.18}$$

This correction factor is

$$\Xi = \begin{cases} 0 & M \text{ even} \\ 2 & M \text{ odd} \end{cases}. \tag{4.19}$$

The even modes are not influenced by the resonant layer in the middle of the cavity, while the odd modes experience twice the phase shift expected. This correction factor arises from the fact that in the resonant mirror model the resonance position is only calculated from a simple phase approach and does not take into account the actual fields. The even FP modes exhibit a field node in the center, therefore the electric

field strength at the oscillators is close to zero and no interaction is possible [259]. For the odd modes, the transmittance phase $\varphi_{\text{t,res}}$ are taken to be equal and independent of each other, however, in the real system they occur on transmission from both sides through the same resonant layer, which interacts with both counter-propagating waves and thus has to adopt a self-consistent state in accordance with Maxwell's equations.

As this section has shown, the resonant mirror model discloses a peculiar correspondence between both, the stacked dimer structure, which constitutes its own cavity due to the arrangement of the oscillators, and an oscillator placed into an external cavity. Both share the common concept of multi-beam interference with the incorporation of resonant oscillators.

## 4.12    CONCLUSION

In summary, this chapter has provided a thorough study of the plasmonic dimer geometry in different arrangements. Near- and far-field coupling in planar and stacked geometries have been discussed.

In the near-field regime, the plasmon hybridization concept is a valuable tool for the qualitative description of the observed coupling effects. In general, the coupled dimer system supports two modes which are characterized by their symmetry. The frequency of these with respect to the original single particle resonance has to be determined by the specific geometry of the structure and is very sensitive to a modification of the particle arrangement. This has been observed by displacing one of the oscillators which leads to a sign change in the interaction energy and therefore to an inversion of the plasmon hybridization scheme.

In the stacked arrangement, an increase of the vertical distance between the plasmonic oscillators leads to the emergence of multi-beam interference effects, namely Fabry-Pérot modes. These modes, which only exist due to the specific spatial arrangement of the oscillators interact with the bare particle plasmon resonances giving rise to new, coupled modes.

Numerous different arrangements of the building blocks could be investigated by means of scattering matrix method calculations. For an experimental verification, a set of eleven samples consisting of plasmonic dimers with different vertical distances $d_z$ was fabricated. The experimental measurements on this set of samples agree well with the numerical calculations and support these. In the experiment, $d_z$ was

varied from very small spacings of approximately 30 nm up to spacings of more than 1 μm,where more than one wavelength fits into the spacer layer. Thus the range from near-field interaction all the way to far-field interaction is covered by the experimental data.

In order to provide an intuitive understanding of the far-field coupled dimer structure, we have introduced the resonant mirror model, which is able to predict the resonance position of the coupled modes. This model includes the retardation between the layers as well as the phase behavior of the plasmon resonances. Even though all calculations and findings have been implemented using elongated gold nanowires which are extended quasi-infinitely into one direction, a transfer to other building blocks such as nanorods, nanodiscs, or even more complicated structures should be straightforward.

It has been the purpose of this chapter to dwell on the description of the coupling effects particularly in the dimer system. The situation of Bragg spacing has only been addressed in brief. This will be investigated in detail in the upcoming chapter, where systems consisting of more than two oscillators stacked in Bragg fashion are subject of study.

∼

# PLASMONIC BRAGG STRUCTURES

## 5.1 INTRODUCTION

While the previous chapter has been dedicated to the investigation of spacing dependence in a plasmonic dimer structure, this chapter will change the perspective to a different aspect of radiative coupling.

Already in the dimer structure it has become apparent that a special situation occurs, whenever the oscillators are arranged such that the vertical (i. e., in the direction of light propagation) distance $d_z$ exactly matches a multiple of half the oscillator wavelength. Therefore, vertical distances with $d_z = M\lambda_{\mathrm{PPR}}/(2n_{\mathrm{Sp}})$, where $\lambda_{\mathrm{PPR}}$ is the light wavelength at the oscillator eigenfrequency, $n_{\mathrm{Sp}}$ is the refractive index of the surrounding, and $M$ is an integer number, are of particular interest.

This chapter will be devoted to the investigation of these so-called Bragg structures. The spacing between resonant layers will mostly be fixed to the first Bragg distance ($M = 1$). Under these circumstances an increase of oscillator number will yield peculiar effects such as the emergence of an ultra-broad photonic band gap in multilayered structures.
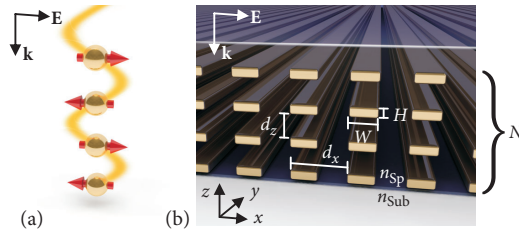


FIGURE 5.1. (a) Schematic of four radiatively coupled resonant oscillators. (b) Schematic of a Bragg stacked plasmonic structure consisting of four layers and embedded into a dielectric spacer material with refractive index $n_{\mathrm{Sp}} = 1.46$. The gold nanowires have a width $W = 180\,\mathrm{nm}$ and height $H = 20\,\mathrm{nm}$, and are arranged at a lateral periodicity $d_x = 360\,\mathrm{nm}$ and vertical distance $d_z = 260\,\mathrm{nm}$. The lateral spacing $d_x$ is chosen such that lateral near-field coupling as well as higher diffraction orders are negligible.

The radiative coupling of optical oscillators is one of the most fundamental optical problems and has already been investigated in different fields of optics, especially for a Bragg-type arrangement. Fig. 5.1 (a) schematically depicts the situation of four oscillators at Bragg distance. On the one hand, each oscillator is excited with a certain phase retardation due to the large spacing between them, on the other hand, the arrangement leads to a coherent superposition of the re-radiated fields of the oscillators, as the spacing matches the oscillator resonance wavelength. In semiconductor physics, radiative coupling of excitons in quantum wells (QWs) [131, 266–273] at Bragg distance has been investigated. In atomic physics this arrangement is important for light propagation through atoms arranged in an optical lattice [274–277]. On a very large length scale metallo-dielectric photonic crystals with unit cells of several mm to cm are a subject of research for GHz applications.

In all cases the observation of photonic band gaps (PBGs) is possible: for coupled QWs the emergence of a PBG with a width of approximately 5 meV was observed for 100 coupled oscillators [272]. In optical lattices PBGs of several MHz to GHz spectral width should be possible [277]. In the macroscopic GHz metallo-dielectric photonic crystals PBGs of several GHz have been found [278, 279] which corresponds to approximately one octave at those frequencies.

We will transfer this concept to plasmonic structures. Fig. 5.1 (b) shows a schematic of the structure. Plasmonic nanowires with dimensions similar to those in the previous chapter are stacked on top of each other using a spin-on dielectric (SOD) spacer layer. The lateral periodicity $d_x$ is chosen such that near-field coupling is negligible and no Rayleigh anomalies are present in the considered spectral region. For this geometry, the single oscillator particle plasmon resonance (PPR) is located at around 1.5 eV, thus the nominal Bragg spacing is approximately $d_z$ = 260 nm. As before, the structure is illuminated from above with light polarized perpendicular to the wires.

## 5.2   NON-RESONANT AND RESONANT STRUCTURES

A system of coupled oscillators with a spacing on the order of the wavelength possesses analogies to passive photonic crystal (PC) structures [100]. These usually exhibit a spatial periodic refractive index modulation on the order of the wavelength of light which is accomplished by a multilayer structure made of different dielectric materials [280–282]. However, the incorporation of mutually coupled plasmonic oscillators

leads to new phenomena compared to purely passive, non-resonant structures.

The difference between the non-resonant passive PC structure and a resonant, stacked plasmonic multilayer structure is demonstrated in Fig. 5.2. There, calculated spectra for a stack of eight 20 nm thick Au layers separated by a dielectric spacer material of $n_{Sp}$ = 1.46 to an eight layer nanowire structure with the same spacer material and thickness are shown.

The bare metal multilayer structure (Fig. 5.2 (a)) mainly exhibits high reflectance. A small amount of transmittance is possible at the Fabry-Pérot (FP) modes [283], just as this was shown in Fig. 4.13. Due to the fact that the $N$ layers constitute $N-1$ coupled cavities [284, 285], the FP modes are hybridized into seven branches[i]. For a purely dielectric structure, these hybridized modes would eventually yield the bands of the PC structure for very large layer numbers, however, the incorporation of metallic layers substantially increases the absorbance, therefore the emergence of pass bands cannot be observed in the metallic structure.

Replacing the metal layers by resonant nanowire structures yields a strong change in the observed spectra, as can be seen in Fig. 5.2 (b). First, the off-resonant behavior changes: the metal film exhibits a high reflectivity over the whole spectral region, consequently showing high reflectance and very low transmittance. In contrast to this, the reflectance of the nanowire structure is very low for wavelengths far away from $\lambda_{PPR}$, thus it is almost transparent. Second, the incorporation of the PPR oscillators qualitatively changes the response of the system as the interaction of FP and PPR modes leads to the formation of coupled FP-PPR modes as discussed in section 4.7. This opens up new possibilities to tune the response of the system.

A peculiar situation occurs especially for Bragg spacing. As in the case of the dimer structure, the coupled FP-PPR modes which are spectrally close to the single layer PPR can barely be excited by the light field and therefore almost vanish in the spectra. This leads to the emergence of a broad region of high reflectance which is accompanied by low absorbance. The spectral width of this region, as indicated by the white solid line in the spectra of Fig. 5.2 (b), is considerably larger than in case of the passive structure.

To examine this in greater detail we first consider the off-Bragg situation. Fig. 5.3 displays a comparison of the spectra for the passive as well

---

i  This can be observed with greater clarity in Fig. 5.3.
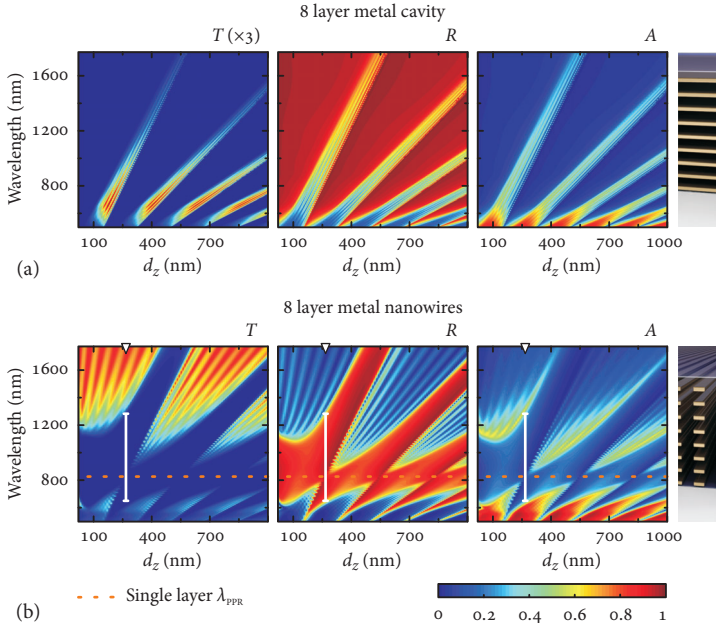
FIGURE 5.2.    (a) Color-coded calculated transmittance, reflectance, and absorbance spectra for eight stacked 20 nm thick continuous Au layers. The spacer thickness $d_z$ is varied to the right. Transmittance is scaled by a factor of 3 for clarity.    (b) Color-coded calculated transmittance, reflectance and absorbance spectra for an eight layer plasmonic nanowire stack with $\lambda_{PPR}$ = 820 nm (indicated by the orange dashed line). The first Bragg spacing is indicated by a white arrow at the top of the graphs. White solid lines indicate the width of the stop band at Bragg distance.

as resonant structure stacked at a vertical spacing of $d_z$ = 350 nm for one to ten layers. In the left panel the FP modes are observed as dips in reflectance upon the highly reflecting background of the metal layers. In case of uncoupled cavities the FP modes would be degenerate and only one peak would be visible in the spectrum regardless of the number of layers. This is obviously not the case. The individual cavities are coupled and due to this interaction the mode energies are slightly detuned, which leads to $N - 1$ hybridized FP modes in the spectrum [284].
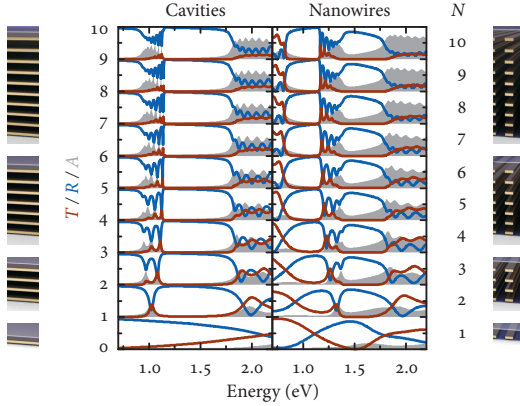
FIGURE 5.3. Calculated transmittance, reflectance, and absorbance spectra for a one- to ten layer structure consisting of 20 nm thick Au layers (left) and plasmonic nanowires (right) each stacked at a vertical distance of $d_z$ = 350 nm.

The same situation is also observed in case of the nanowire structure in the right panel. Here the dips in reflectance are observed on top of the plasmonic resonance reflectance.

Overall, it has to be noted that the *non-Bragg* arrangement of nanowires and the passive multilayer cavity structure exhibit strong similarities with only two differences: First, the stacked nanowires exhibit a spectral shift compared to the cavities, which can be straightforwardly explained by the resonant mirror model. Second, the modulation depth of the modes is reversed, which may be connected to the frequency-dependent, strongly varying reflection amplitude in case of the nanowires.

## 5.3    BRAGG SPACING

The situation changes whenever the coupled FP-PPR modes spectrally approach $\lambda_{PPR}$. Then a distinct Fano-type lineshape of the corresponding mode on the plasmonic background is observed. This is demonstrated in Fig. 5.4 where a detail of the reflectance spectra for a structure consisting of two and eight layers for stacking distances very close to Bragg spacing is shown.
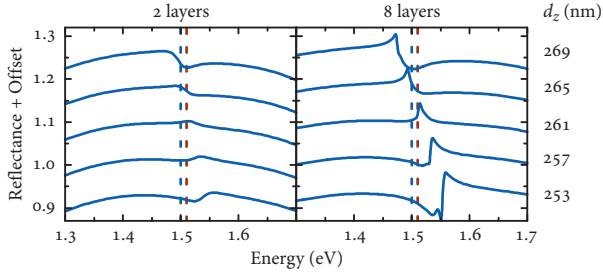
FIGURE 5.4. Detailed calculation of the spectral shape of the reflectance around Bragg spacing for a two and eight layer nanowire structure. Around Bragg spacing the FP-PPR mode exhibits a Fano lineshape. The spectra are shifted upwards for clarity. The red and blue dashed lines denote the transmittance minimum, respectively reflectance maximum of the single layer structure.

In case of the two layer nanowire structure (left panel of Fig. 5.4) a typical Fano shape is observed. Starting from $d_z$ values below and shifting it to values above Bragg distance, the coupled mode spectrally shifts over the single layer $\lambda_{PPR}$, changing its asymmetry. In case of minimal feature size, which occurs for $d_z = 261$ nm, the shape is almost symmetric. It is not exactly located at the reflectance maximum of the single layer structure (blue dashed line in Fig. 5.4), but slightly blue shifted to it ($\approx 10$ meV). The position of the transmittance minimum (red dashed line in Fig. 5.4) is spectrally closer to the peak position but also does not perfectly agree. Given the fact that the total width of the PPR is more than one order of magnitude larger, this spectral displacement is negligible.

For the eight layer nanowire structure (right panel of Fig. 5.4), the situation is similar, however, more modes are involved and the spectra are more complex. Still, they qualitatively exhibit the same behavior as in the two layer case. Additionally, the peak height of the remaining feature at $d_z = 261$ nm is higher than for the two layer structure.

The vertical distance at which the coupled FP-PPR mode becomes almost dark coincides very well with the calculated distance using eq. 4.15, as long as one takes the additional height $H$ of the plasmonic wires into account. Nevertheless, $d_z$ will be optimized by minimizing the height of the FP-PPR mode in the following.

The influence of an increasing layer number $N$ in case of Bragg spacing is shown in the calculated spectra of Fig. 5.5 for one to ten layers.
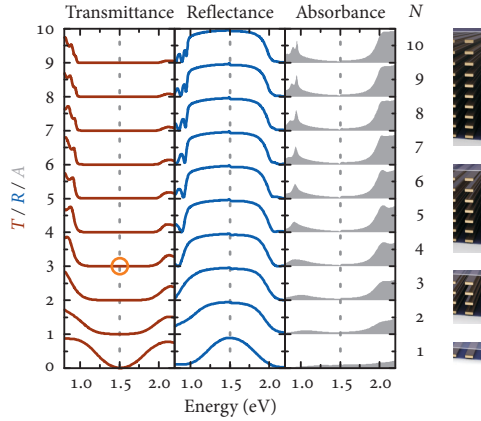
FIGURE 5.5. Calculated transmittance, reflectance, and absorbance spectra for the Bragg stacked ($d_z = 265\,\mathrm{nm}$) multilayer structures with increasing layer number $N$. The single oscillator resonance energy $E_{\mathrm{PPR}}$ is indicated by a dashed gray line as a guide to the eye. The orange circle denotes the spectral position and layer number at which an electric field calculation is performed (see Fig. 5.6).

These display distinct differences to those for a non-Bragg arrangement (see Fig. 5.3). Due to the absence of one branch of coupled FP-PPR modes a very broad region with low transmittance and high reflectance is observed. It is accompanied by low absorbance, which is only substantial at the borders. The coupled system resembles a single oscillator whose oscillator strength and thus radiative linewidth increases with increasing layer number $N$. This stems from the fact that the spatial arrangement of the oscillators is exactly matched to their resonance wavelength and therefore on the one hand, the oscillators are excited with a matched phase retardation and on the other hand their re-emitted fields exhibit a matched phase relationship.

Beyond this, the spectral shape of this feature changes for increasing layer number, from a typical Lorentzian-like shape in case of one layer to a rectangular, PBG-type shape. Its spectral width of approximately $1\,\mathrm{eV}$ is quite remarkable—it spans about one octave in the optical frequency range.

The reason for this exceptionally broad band gap is the efficient coupling of the PPRs to the light field and hence their large spectral width.

This comprises a major difference to the atomic or excitonic oscillators which have been investigated before. Also, in comparison to purely dielectric structures, the PBG is very broad. The maximum achievable width in dielectric structures is governed by the dielectric refractive index contrast of the constituents. This has to be kept quite low, as materials with high refractive index contrasts mostly exhibit high absorption as well. This problem is circumvented by using the structured resonant plasmonic nanowire arrays instead of plain films.

Finally, we investigate the electric field distribution in a Bragg stacked multilayer structure. Fig. 5.6 shows the normalized logarithmic electric field calculated for a four layer structure stacked at Bragg distance ($d_z$ = 265 nm) at the single layer PPR wavelength ($\lambda_{PPR}$ = 826 nm). The corresponding spectral position is indicated in the transmittance spectra of Fig. 5.5. Similar to the findings in section 4.10, the matching of the vertical spacing to the wavelength is observed. The field distribution in the spacer layers is similar to that of a $\lambda/2$ FP mode. Furthermore, the plasmonic oscillations are opposite in neighboring wires. Both of these effects agree with the observations in the two layer case for the first Bragg distance (Fig. 4.23 (a)).

The superposition of the re-emitted fields of the oscillators is constructive in backward and destructive in forward direction. Therefore, the electric field amplitude gradually decreases with increasing penetration depth. This leads to the observation of high reflectance and low transmittance. Neglecting this decay of electric field intensity across the structure, the symmetry considerations of the dimer structure can be transferred to the multilayer structure. With respect to the symmetry plane in the middle of the structure the electric field distribution in the spacer layers is symmetric. In contrast, the charge oscillations in neighboring wires are opposite and thus antisymmetric. This is in accordance with the observations in the dimer structure, where at Bragg spacing plasmon oscillation and electric field distribution possess opposite symmetry as well.

FIGURE 5.6 (*FACING PAGE*). Normalized logarithmic electric field intensity for a stacked four layer Bragg structure with a vertical distance of $d_z$ = 265 nm at the single layer PPR wavelength. . The vertical spacing between the wires exactly matches half the PPR wavelength. This leads to a suppression of transmittance (low field intensity below the structure) and a high reflectance of the structure (high field intensity above).

$d_z = 265$ nm, $N = 4$, $\lambda = 826$ nm
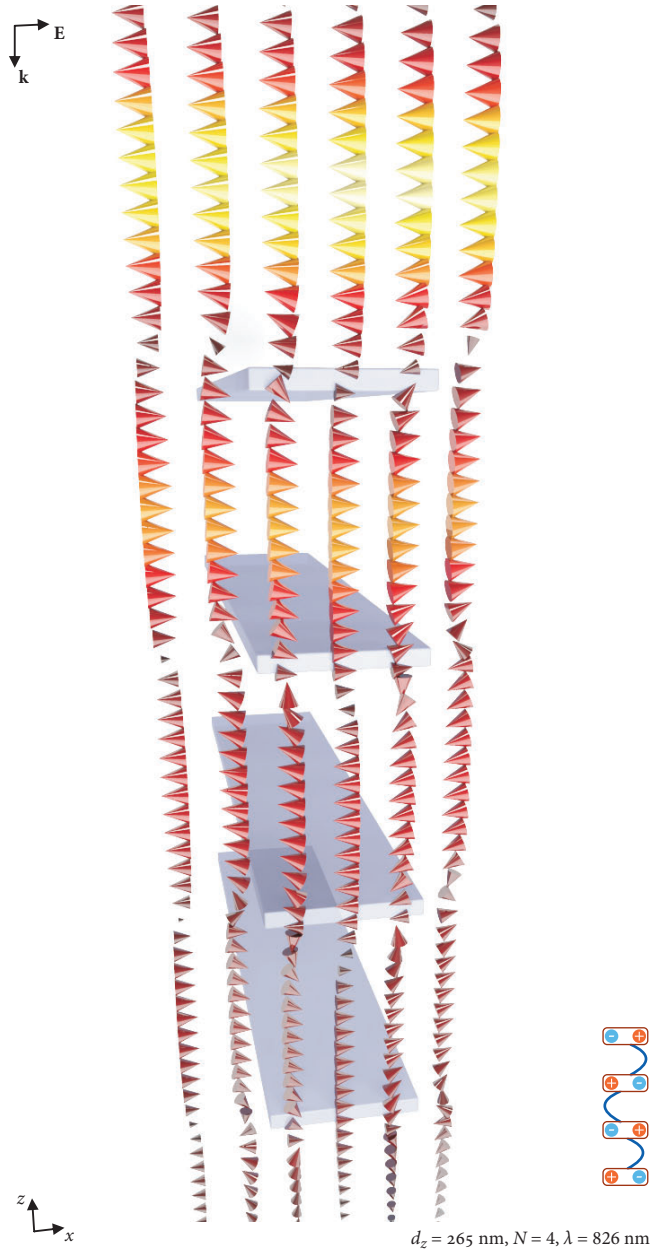
## 5.4   EXPERIMENTAL RESULTS

The experimental implementation of multilayer structures with high layer numbers is quite challenging, as the accuracy of the sample geometry due to fabrication tolerances as well as contamination of the sample increases with each processed layer. Therefore, a trade-off has to be made. From Fig. 5.5 it is obvious that the strongest modifications in the spectra occur for layer numbers $N$ of up to four. Beyond this, no substantial changes can be observed and only the steepness of the slopes at the border of the PBG is increased.

We fabricated a sample consisting of up to four layers, each stacked at Bragg distance. Each layer was exposed in a Polymethylmethacrylat (PMMA) resist layer with subsequent development and evaporation of 2 nm Cr and 20 nm Au. After lift-off a SOD layer was applied. The thickness of this spacer layer was controlled by using different solvent fractions of the SOD as well as a variation of spin speed and multiple coating runs. An identical spacer layer was also applied to the top layer in order to provide a homogeneous environment for all plasmonic nanowires. The nominal sample geometry was chosen to match the calculations above, with $W = 180$ nm, $H = 20$ nm, $d_x = 360$ nm and $d_z = 260$ nm. Of these parameters, $d_z$ is most critical, yet as well hardest to control. However, the experimental accuracy is sufficient for the realization of a multilayer Bragg structure.
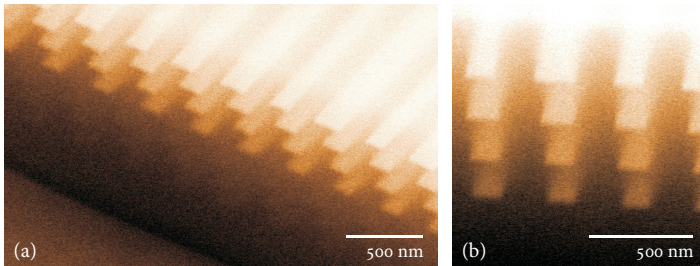


FIGURE 5.7. Scanning electron micrographs of a four layer plasmonic Bragg structure. To reveal the three-dimensional arrangement the images show a groove cut by a FIB. (a) Inclined incidence perspective. (b) Image at grazing incidence looking along the wire direction.

Scanning electron microscope (SEM) images of the sample are displayed in Fig. 5.7. To obtain these micrographs, a groove of more than 1 μm depth was cut by a focused ion beam (FIB) close to the border of the structure. This is necessary to reveal the underlying layers, which otherwise would be not accessible due to a huge amount of scattered electrons from the upper gold layers and the spacer material. Fig. 5.7 (a) shows the structure from an oblique incidence perspective. Panel (b) is recorded under grazing incidence perspective, looking almost in direction of the wires. From this perspective the uniformity of the layer spacing is well observed.

Transmittance as well as reflectance spectra were recorded in a Fourier-transform infrared spectrometer (FTIR) microscope. Due to the large spectral range of the samples, these were acquired using a Si and an InGaAs photodiode as described in section 4.9.
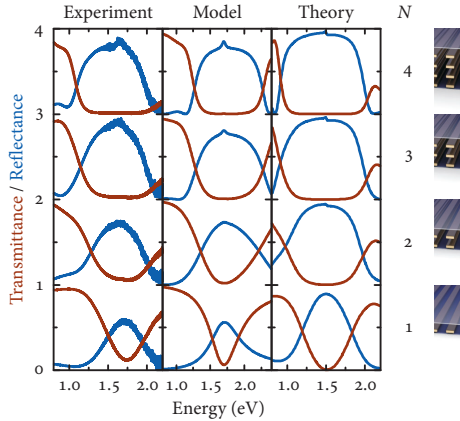


FIGURE 5.8. Left: Experimental transmittance (red) and reflectance (blue) spectra for one to four layers. Middle: Spectra calculated using the analytical coupling model [131]. The oscillator parameters extracted from the single layer experimental data were used as calculation input. Right: SMM calculation. The small peak in reflectance at 1.5 eV is a remainder of the coupled FP-PPR mode whose linewidth almost vanishes at Bragg distance.

To investigate the evolution of the spectra on increasing layer number, spectra were acquired after the completion of each layer. These are shown in the left panel of Fig. 5.8. To compare these results with calculations, the middle panel of the figure shows spectra calculated by

the analytical coupling model of eqs. 2.29, 2.66 and 2.67 [131], and the right panel shows the full scattering matrix method (SMM) results.

The transformation of the spectral shape from a Lorentzian lineshape in the single layer case to a rectangular band-gap-type lineshape for a Bragg multilayer stack is pronouncedly observed. The photonic band gap in the four layer structure, extracted from the reflectance measurement exhibits a spectral width of 815 meV, whereas the single PPR width is only 530 meV. Both of these values are slightly below the values obtained from the SMM calculations, which yield 1025 meV for four layers and 640 meV for a single layer, respectively. In the gap region, the structure exhibits a very high reflectivity of around 80 % experimentally, while the reflectance in the SMM calculation peaks to almost 100 %. The analytical results in the middle panel seemingly supply a much better agreement with the experimental spectra in terms of absolute values. This stems from the fact that for this calculation $E_{\mathrm{PPR}}$ as well as $\Gamma_{\mathrm{o}}$ and $\Gamma$ are extracted[ii] from the experimental single layer spectra and used as calculation input. Deviations between the results obtained from SMM and experiment predominantly originate from fabrication imperfections, and the measurement technique using a high-NA Cassegrain objective, as discussed in the previous chapter.

## 5.5    ANALYTICAL MODELING: LIMITATIONS OF RADIATIVE COUPLING

### 5.5.1    *Spectral Broadening*

Strikingly, we observe a broad, saturating PBG for already four layers in the plasmonic structure, while in excitonic structures around 100 oscillators are necessary. Both, the broad spectral width of the PBG and fast saturation arise from the large dipole moment of the PPR, which results in a radiative coupling strength exceeding that of a typical excitonic resonances by about 4 orders of magnitude. Additionally, this efficient coupling makes the emergence of a PBG in our plasmonic structures far more robust against nonradiative contributions to the linewidth.

To gain insight into the mechanisms that lead to the formation of broad PBGs, we study the influence of the coupling strength on band gap formation within the single oscillator model introduced in eqs. 2.66 and 2.67. At Bragg spacing, the layers are sufficiently separated so that

---

ii  see appendix A.3 for details

near-field coupling effects can safely be neglected and the model is applicable.

The evaluation of eq. 2.66 requires more effort in case of a $N$-oscillator system, compared to the dimer system considered before. However, the fact that only Bragg spacing is investigated leads to a simplification of the results. The analytical calculation of the reflection amplitude[iii] for the $N$ oscillator system requires a solution of the equation

$$\mathfrak{r}(E) = \frac{E_1^-}{E_1^+} = \mathcal{U}^T \frac{ik}{2\varepsilon_{Sp}} \chi(E) \left( \mathcal{I} - \frac{ik}{2\varepsilon_{Sp}} \chi(E) \mathcal{D} \right)^{-1} \mathcal{U}. \tag{5.1}$$

In case of Bragg spacing $kz_n$ always evaluates[iv] to a multiple of $\pi$, therefore the matrix $\mathcal{D}$ and the vector $\mathcal{U}$ are strongly simplified:

$$\begin{aligned} \mathcal{D}_{mn} &= e^{i\pi|m-n|} &= (-1)^{|m-n|} \\ \mathcal{U}_n &= e^{i\pi(n-1)} &= (-1)^{n-1}, \end{aligned} \tag{5.2}$$

where for the second equation the first oscillator has been assumed to be located at position $z_1 = 0$. The major task in order to solve eq. 5.1 is the inversion of the matrix

$$\mathcal{A} = \left( \mathcal{I} - \frac{ik}{2\varepsilon_{Sp}} \chi(E) \mathcal{D} \right) = \begin{pmatrix} 1-\eta & \eta & -\eta & \cdots \\ \eta & 1-\eta & \eta & \cdots \\ -\eta & \eta & 1-\eta & \cdots \\ \vdots & \vdots & \vdots & \ddots \end{pmatrix}, \tag{5.3}$$

where the abbreviation $\eta = ik\chi(E)/(2\varepsilon_{Sp})$ has been utilized. Finding a general symbolic expression for $\mathcal{A}^{-1}$ requires some effort, as $\mathcal{A}$ has a finite but variable dimensionality $N$. However, its special structure facilitates the solution. The calculation[v] yields

$$\mathcal{A}_{mn}^{-1} = \delta_{mn} + (-1)^{m+n} \frac{\eta}{1-N\eta} \tag{5.4}$$

---

iii  the derivation for transmission amplitude is analogous
iv  implicitly assuming $k \approx k_{PPR}$
v  see appendix A.4 for details

in component notation. Using this, it is possible to evaluate $\mathcal{U}^T \mathcal{A}^{-1} \mathcal{U}$ which yields

$$
\begin{aligned}
\mathcal{U}^T \mathcal{A}^{-1} \mathcal{U} &= \sum_{m=1}^{N} \sum_{n=1}^{N} (-1)^{m-1} \left( \delta_{mn} + (-1)^{m+n} \frac{\eta}{1 - N\eta} \right) (-1)^{n-1} \\
&= N + N^2 \frac{\eta}{1 - N\eta} \\
&= \frac{N}{1 - N\eta}.
\end{aligned}
\tag{5.5}
$$

Inserting this result into eq. 5.1 leads to

$$
\mathfrak{r}(E) = \frac{N \frac{ik}{2\varepsilon_{\mathrm{Sp}}} \chi(E)}{1 - N \frac{ik}{2\varepsilon_{\mathrm{Sp}}} \chi(E)}.
$$

Now it is possible to insert the harmonic oscillator susceptibility (eq. 2.30) which finally gives[vi]

$$
\mathfrak{r}(E) = - \frac{-iN\Gamma_{\mathrm{o}}}{E - E_{\mathrm{PPR}} + i(\Gamma + N\Gamma_{\mathrm{o}})}.
\tag{5.6}
$$

The result of this evaluation is quite straightforward: the reflectance as well as transmittance amplitude of the $N$ oscillator system at Bragg spacing corresponds to that of a single oscillator with an $N$ times enhanced radiative width [131, 270–273]. Therefore the observed linewidth of the coupled system strongly increases on an increase of oscillator number.

In semiconductor QW structures this behavior has been attributed to a superradiant coupling of the quantum oscillators [271, 272]. While the term superradiance denotes an enhancement of the spontaneous decay rate of quantum oscillators [286], it has been pointed out by Rehler and Eberly [260] that the lifetime of a system of $N$ coupled classical dipolar oscillators is decreased by a factor of $1/N$ compared to a single oscillator, which exactly corresponds to an increase of radiative linewidth.

### 5.5.2   *Dephasing Limit to the PBG*

The result of eq. 5.6 implies an unlimited growth of the radiative width with increasing oscillator number $N$, which obviously cannot be true

---

vi  As in section 4.8 the $k/(2\varepsilon_{\mathrm{Sp}})$ factor is included into $\Gamma_{\mathrm{o}}(\omega)$ and for ease of calculation the $\omega$-dependence is neglected.

and hence at some point has to become unphysical[vii]. Indeed, it relies on an exact phase coherence of the excitations in different layers. The total linewidth $\Gamma_{\text{tot}}(N) = N\Gamma_{\text{o}} + \Gamma$ does not only represent the spectral width of the radiation, but also governs its spatial extent. Consequently, a growth in spectral linewidth imposes a limit due to dephasing onto the re-radiated field, which eventually can become smaller than the sample dimensions. Thus, the number of oscillators that can be coupled by the radiation field is limited by the dephasing length

$$l_{\text{d}} = \frac{c}{n_{\text{Sp}}} \cdot \frac{\hbar}{\Gamma_{\text{tot}}(N)} = \frac{c}{n_{\text{Sp}}} \cdot \frac{\hbar}{N\Gamma_{\text{o}} + \Gamma}, \qquad (5.7)$$

where in the latter equality the total linewidth obtained from eq. 5.6 has been used.

From this, a criterion for the maximum number of oscillators that still yield a Lorentzian lineshape can be derived. The overall structure dimension, which is approximately $Nd_z$, has to be smaller than $l_{\text{d}}$. Utilizing the Bragg criterion

$$d_z = \frac{\hbar c \pi}{n_{\text{Sp}} E_{\text{PPR}}}$$

leads to

$$N < \frac{1}{\pi} \frac{E_{\text{PPR}}}{N\Gamma_{\text{o}} + \Gamma}. \qquad (5.8)$$

In case of plasmonic oscillators, the radiative linewidth is the major contribution, thus $\Gamma$ can be neglected and one can estimate the limiting number of layers at which still a Lorentzian lineshape is achieved as

$$N_{\text{lim}} = \sqrt{\frac{E_{\text{PPR}}}{\pi \Gamma_{\text{o}}}}, \qquad (5.9)$$

and the limiting linewidth is

$$\Gamma_{\text{lim}} = N_{\text{lim}}\Gamma_{\text{o}} = \sqrt{\frac{E_{\text{PPR}}\Gamma_{\text{o}}}{\pi}}. \qquad (5.10)$$

vii The assumption $k \approx k_{\text{PPR}}$ in the derivation of eq. 5.6 limits the applicability to spectral ranges around the resonance frequency.

### 5.5.3    *Derivation of the PBG Width in an Infinite Structure*

Complimentarily to the considerations above, one can derive a maximum width of the PBG for an infinite structure. Even though only small layer numbers are considered here, the consideration of the infinite structure is important, as it governs the ultimate achievable band gap width. Additionally, it provides another point of view on the problem.

The calculation is similar to the derivation of electronic band gaps in a perfect crystal structure as it was introduced by Kronig and Penney [287]. To do so, a transfer matrix $\mathcal{M}$ has to be derived for the propagation in one period. The transfer matrix is a $2 \times 2$ matrix which connects the propagating fields in period $m-1$ to those in period $m$. Using the notation of Fig. 2.6 the general form of the problem is [277]

$$
\begin{pmatrix} E_{m-1}^+ \\ E_{m-1}^- \end{pmatrix} = \mathcal{M} \begin{pmatrix} E_m^+ \\ E_m^- \end{pmatrix},
\tag{5.11}
$$

where the $E_m^\pm$ are the forward and backward field amplitudes at a certain point within one period. The matrix $\mathcal{M}$ can be decomposed into a propagation matrix for the spacer layer $\mathcal{P}$, and a reflection and transmission coefficient matrix $\mathcal{T}$ describing the resonant layer, which is assumed to be infinitely thin. To derive the elements of $\mathcal{T}$ one can express the outgoing field amplitudes as

$$
E_{m-1}^- = \mathfrak{t} E_m^- + \mathfrak{r} E_{m-1}^+ \qquad\qquad E_m^+ = \mathfrak{t} E_{m-1}^+ + \mathfrak{r} E_m^-.
$$

Rewriting these such that the left hand side (LHS) only contains the fields in layer $m-1$ and the right hand side (RHS) only those in layer $m$, the elements of the matrix are acquired and one can write the matrix $\mathcal{M}$ for a full period

$$
\mathcal{M} = \mathcal{T} \cdot \mathcal{P} = \begin{pmatrix} \frac{1}{\mathfrak{t}} & -\frac{\mathfrak{r}}{\mathfrak{t}} \\ \frac{\mathfrak{r}}{\mathfrak{t}} & \frac{\mathfrak{t}^2 - \mathfrak{r}^2}{\mathfrak{t}} \end{pmatrix} \cdot \begin{pmatrix} e^{-ikd_z} & 0 \\ 0 & e^{ikd_z} \end{pmatrix} = \begin{pmatrix} \frac{1}{\mathfrak{t}} e^{-ikd_z} & -\frac{\mathfrak{r}}{\mathfrak{t}} e^{ikd_z} \\ \frac{\mathfrak{r}}{\mathfrak{t}} e^{-ikd_z} & \frac{\mathfrak{t}^2 - \mathfrak{r}^2}{\mathfrak{t}} e^{ikd_z} \end{pmatrix}.
\tag{5.12}
$$

An explicit inclusion of the single layer reflection and transmission coefficients[viii] in eq. 5.12 yields

$$\mathcal{M} = \begin{pmatrix} \left(1 - i\chi(E)\right) e^{-ikd_z} & -i\chi(E) e^{ikd_z} \\ i\chi(E) e^{-ikd_z} & \left(1 + i\chi(E)\right) e^{ikd_z} \end{pmatrix},$$  (5.13)

where for simplicity the factor $k/(2\varepsilon_{Sp})$ is omitted as it will be included into $\chi(E)$. It is easy to evaluate $\det(\mathcal{M}) = 1$, therefore the eigenvalues of $\mathcal{M}$ can be displayed as $\lambda_{1,2} = e^{\pm i\phi}$. Using $\phi = Kd_z$, it is possible to identify $K$ to be the absolute value of an effective wave vector for the propagation in the periodic medium. Using the identity

$$\sum_{n=1}^{2} \lambda_i = \text{Tr}(\mathcal{M})$$  (5.14)

leads to the equation

$$\cos(Kd_z) = \cos(kd_z) - \chi(E)\sin(kd_z).$$  (5.15)

This equation is well known in the context of infinite periodic problems and is found in different forms. Often $\chi$ is constant, which facilitates the analysis. However, in our case $\chi$ depends on the energy and exhibits a resonant character around $E_{PPR}$.

If the RHS of eq. 5.15 takes values between $-1$ and $1$, $K$ is real-valued and thus wave propagation is possible. If it exceeds this range, $K$ becomes imaginary and no propagating solution is possible, hence leading to the emergence of a stop band. The criterion for the PBG therefore is

$$\cos(kd_z) - \chi(E)\sin(kd_z) \begin{cases} > 1 \\ < -1 \end{cases}.$$  (5.16)

A proper evaluation of these inequalities requires a case determination for different spectral regions. As before, $\chi(E)$ from eq. 2.30 is used for the modeling of the oscillators, however, it is necessary to neglect the nonradiative damping term, $\Gamma = 0$, in order to arrive at analytical expressions. Furthermore, the identities [288]

$$\tan\left(\frac{\varphi}{2}\right) = \frac{1 - \cos\varphi}{\sin\varphi} \qquad\qquad \cot\left(\frac{\varphi}{2}\right) = \frac{1 + \cos\varphi}{\sin\varphi}$$

---

viii  see eq. A.6

are applied, which yields[ix]

$$\frac{X}{G} \tan\left(\frac{kd_z}{2}\right) > 1 \tag{5.17}$$

$$-\frac{X}{G} \cot\left(\frac{kd_z}{2}\right) < -1. \tag{5.18}$$

Here, $\chi(E) = -\Gamma_o/(E - E_{PPR})$ has been expressed in terms of the scale free quantities

$$X = \frac{E - E_{PPR}}{E_{PPR}} \qquad\qquad G = \frac{\Gamma_o}{E_{PPR}}.$$

Furthermore, we can make use of

$$\cot x = -\tan\left(x - \frac{\pi}{2}\right) \qquad\qquad \tan x = -\cot\left(x - \frac{\pi}{2}\right)$$

and rewrite $\pi$ in the argument utilizing the fact, that the structures are stacked at Bragg spacing, thus [289] $k_{PPR}d_z = \pi$, so that the final form of eqs. 5.17 and 5.18 is

$$\frac{X}{G} \cot\left(\frac{\pi}{2}X\right) < -1 \tag{5.19}$$

$$\frac{X}{G} \tan\left(\frac{\pi}{2}X\right) < 1. \tag{5.20}$$

Equation 5.19 cannot be fulfilled as the LHS is positive irrespective of the value of $G$ in the considered spectral range $X = (-1, 1)$. From eq. 5.20 we can calculate the width of the PBG, approximating $\tan x \approx x$, which yields

$$E_{1,2} = E_{PPR} \pm \sqrt{\frac{2\Gamma_o \omega_{PPR}}{\pi}}$$

and thus the maximum achievable PBG width

$$\Delta E_{max} = 2\sqrt{\frac{2\Gamma_o E_{PPR}}{\pi}}. \tag{5.21}$$

---

ix  This evaluation is valid in the spectral region from $E = 0$ up to $E = 2E_{PPR}$. A special situation occurs at exactly $E = E_{PPR}$ as there the second term on the RHS of eq. 5.15 vanishes and a propagating solution with $K = \omega_{PPR}/c$ exists. This might be the reason for the small remaining peak exactly at $E_{PPR}$ in the spectra of Fig. 5.4.

Comparing eq. 5.21 to eq. 5.10 one finds, that this exceeds the maximum Lorentzian linewidth $\Gamma_{lim}$ by a factor of $\sqrt{2}$, which can also be interpreted as the maximum linewidth to be achieved for a layer number of

$$N_{max} = \sqrt{2}N_{lim} = \sqrt{\frac{2E_{PPR}\Gamma_o}{\pi}}. \tag{5.22}$$

### 5.5.4   Comparison to Numerical Data

In order to test these findings we perform SMM calculations. In these we can artificially tune the oscillator strength of the wires by changing their width $W$ and height $H$. Their spectral position is roughly preserved as long as a constant aspect ratio is maintained[x].

To avoid influences of the gold d-band absorption the calculations assume a Drude metal with $\omega_p$ = 2100 THz and $\gamma_D$ = 21 THz. The other parameters are kept fixed with respect to the previous sections. A basic wire geometry of $W \times H$ = 180 nm × 20 nm is used as a starting point. From this the wire size is successively reduced. Furthermore, a slight adjustment of the vertical spacing $d_z$ is necessary.

The resulting reflectance spectra are displayed in Fig. 5.9 for six different geometries. For each geometry the layer number $N$ is varied from one to ten layers. The bottom row ($N$ = 1) nicely displays the growth of the oscillator strength for increased wire dimensions, which results in a growing modulation depth of the spectral feature and a spectral broadening due to increased radiative damping of the oscillator.

For a quantitative analysis the full width at half maximum (FWHM) is extracted from all reflectance spectra in Fig. 5.9. The results are displayed in Fig. 5.10. For all wire geometries the FWHM increases first, then a saturation of the width sets in. Only for the very small wires a nearly linear regime of FWHM increase is observed. For larger wires the saturation is achieved already for relatively low oscillator numbers. Notably, the FWHM decreases again for large layer numbers, so that the maximum width is observed close to the onset of saturation. This decrease stems from the fact, that for large $N$ a considerable amount of metal is incorporated in the structure, and therefore the absorption at the PBG edges grows (see absorbance panel of Fig. 5.5).

---

x  Maintaining a constant aspect ratio provides a good first order approximation. However, for the calculation of Fig. 5.9 the spectral position is fine tuned by an additional height variation.
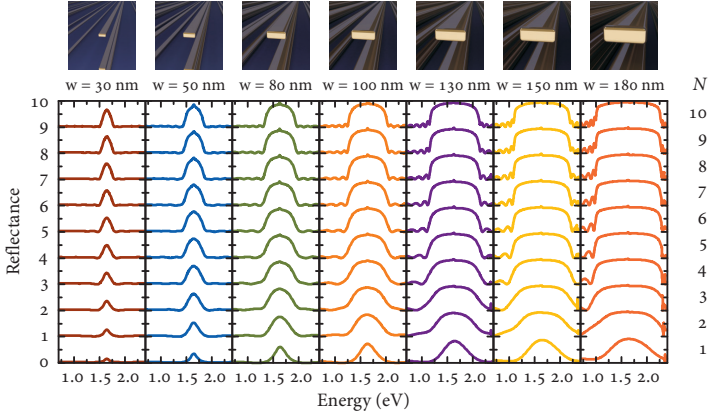
FIGURE 5.9. Calculated reflectance spectra for increasing number of layers $N$ of a Bragg stack with different wire geometries. The widths and heights of the wires are 30 nm × 2.3 nm (red), 50 nm × 4 nm (blue), 80 nm × 6.8 nm (green), 100 nm × 9 nm (orange), 130 nm × 12.8 nm (purple), 150 nm × 15.7 nm (yellow), and 180 nm × 20 nm (light red). All calculations use a Drude model for the gold in order to suppress the increasing material absorption above 2 eV. The stacking distance is slightly tuned for each geometry in order to exactly match the Bragg spacing (from left to right $d_z$ = 256 nm, 254 nm, 254 nm, 250 nm, 248 nm, 245 nm, and 241 nm).

It is possible to extract the values of $\Gamma_0$ and $\Gamma$ from the single layer spectra for the respective geometry, using eq. A.9. These values can then be used to calculate the width limit of the band gap $\Delta E_{max}$ from the Kronig-Penney calculation, eq. 5.21, as well as the maximum number of layers due to the dephasing length $N_{max}$ according to eq. 5.22. The former is displayed as horizontal, the latter as vertical dashed lines in Fig. 5.10.

Both show reasonable agreement with the numerical results. The maximum layer numbers roughly coincide with the onset of saturation. For the large wire geometries the values for $N_{max}$ seem to be slightly below the actual onset of saturation, for the small wires the correspondence is more accurate.

The values for $\Delta E_{max}$ agree well with the results for the large wires, while they overestimate the maximum width for the small wire geometries. This originates from neglecting the nonradiative width in the derivation of eq. 5.21, and hence the approximation works well for large
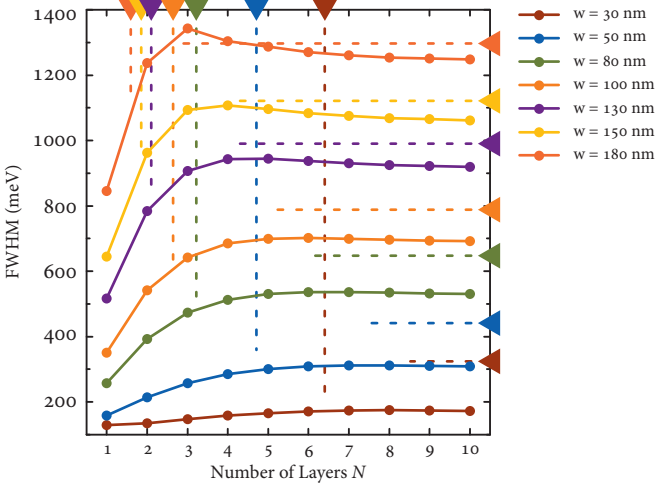
FIGURE 5.10. FWHM extracted from the spectra in Fig. 5.9. The horizontal dashed lines indicate the maximum band gap $\Delta E_{max}$ calculated from eq. 5.21, vertical dashed lines indicate the maximum number of layers that can be coupled $N_{max}$ calculated using eq. 5.22.

wires, where the nonradiative linewidth is rather low. For decreasing wire size it becomes more and more significant, so that the discrepancy between estimated and calculated width increases with decreasing wire size.

## 5.6   BRAGG-STACKED CUT-WIRE STRUCTURES

Finally, we have to address the question of transferability of the findings. Up to now all results have been based on the quasi two-dimensional nanowire geometry introduced in section 4.2. The peculiarity of these is that a transversal PPR mode (perpendicular to the long axis of the wire) is excited which leads to a relatively short PPR wavelength with concurrently high oscillator strength.

To explore the feasibility of Bragg stacked structures for other building blocks, we consider a Bragg arrangement of Au cut-wires. In the SMM calculations 250 nm long wires with a width of 50 nm and a height of 20 nm are arranged in a square lattice with 360 nm lateral spacing.
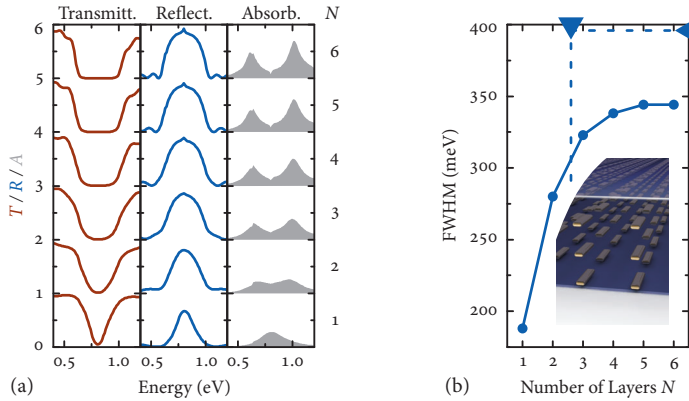
FIGURE 5.11.   (a) Calculated transmittance, reflectance and absorbance spectra for cut-wires stacked at Bragg distance for increasing number of layers $N$. The wire dimensions are 250 nm × 50 nm × 20 nm. The period is $d_x = d_y$ = 360 nm with a vertical distance of $d_z$ = 510 nm, which corresponds to the first Bragg distance for this geometry.   (b) FWHM values extracted from the reflectance spectra shown in (a). Just as in Fig. 5.10 the horizontal dashed line indicates the maximum band gap $\Delta E_{max}$ calculated from eq. 5.21, the vertical dashed line indicates the maximum layer number $N_{max}$ calculated using eq. 5.22. The inset schematically depicts the structure geometry for $N$ = 3.

Their fundamental PPR is excited by light polarized parallel to the long axis. Its spectral position is located around 0.8 eV. Even though the cut-wire length is similar to the width of the extended nanowire structure considered before, their PPR is considerably red-shifted. Therefore it is possible to include the gold permittivity values of Johnson and Christy [112] without the difficulty of approaching the d-band absorption in this case. As a further consequence, the first Bragg spacing is achieved for a vertical distance of $d_z$ = 510 nm, in contrast to 260 nm in the extended nanowires, which implies a substantial increase of the overall vertical dimensions of the structure.

Spectra for up to six layers of stacked cut-wires are displayed in Fig. 5.11 (a). The extracted values are shown in panel (b) of Fig. 5.11. Comparing these to the results of Fig. 5.10 shows an overall similar behavior, however, the absolute numbers strongly differ for both cases. For the stacked cut-wires an overall maximum width of about 0.34 eV is achieved, while the PBG width of the extended nanowire structures

exceeds 1 eV. The spectral width of a single oscillator is substantially lower for the cut-wire samples. Indeed, the FWHM of the single layer reflectance is only slightly below 0.2 eV, while the single layer spectral width achieved in Fig. 5.5 is about 0.64 eV. The situation even gets worse when considering the relative width $\Gamma_o/E_{PPR}$: due to the pronounced red shift of the cut-wire structure, the relative width is as low as $\Gamma_o/E_{PPR} = 0.1$ while it slightly exceeds 0.2 for the extended wires. Consequently, the extended wires exhibit a more than double relative width compared to the cut-wires. This is the reason for the emergence of the octave-wide PBG in the extended nanowires Bragg stack.

As a result, the Bragg scheme can be straightforwardly transferred to different plasmonic building blocks. However, large PBGs are achieved by building blocks which provide especially large oscillator strengths. In case of the cut-wires, the enhancement of oscillator strength would be possible by a length increase, which in turn would yield a further red shift of the PPR. An increase of width or height might be a better strategy in this case, as this would shift the PPR to the blue while enlarging the oscillator strength. Potentially, there also might be different building block designs to accomplish this.

## 5.7    CONCLUSION

This chapter has covered Bragg-stacked arrangements of plasmonic building blocks. In this special arrangement, the vertical spacing $d_z$ is matched to the plasmonic resonance wavelength. As a consequence, the re-emitted fields of the oscillators interfere constructively in forward direction and destructively in backward direction, which yields high reflectance and low transmittance over a broad spectral region.

We have investigated similarities as well as differences between this type of resonant structures and passive photonic crystals, which consist of a periodic refractive index modulation achieved by a multilayer dielectric arrangement. In a dielectric structure, the band gap region is limited by the refractive index contrast, which in most cases has to be kept quite low in order to avoid absorption. The plasmonic structure effectively provides an increased refractive index contrast with very low absorption.

A Bragg-stacked structure consisting of four layers of plasmonic nanowires has been experimentally realized. Upon increase of the layer number from one to four layers an increase of the spectral response of the coupled system is observed. Additionally the spectral shape changes

from a Lorentzian lineshape to a rectangular one, which is characteristic for a photonic band gap. A broad photonic band gap spanning about 0.8 eV was experimentally observed for a structure consisting of four layers, with a maximum reflectance of approximately 80 %.

The phenomena can be described analytically by using the coupled oscillator model introduced earlier. The understanding of the limitations to the photonic band gap width has been approached from two different points of view. On the on hand the coupling limitation due to the dephasing length in the particles has been examined, on the other hand, the ultimate photonic band gap width for an infinite structure has been calculated. In the former case a maximum number of layers is obtained, the latter case provides a maximum spectral width. It is noteworthy, that the dephasing length can also be understood in the (semi-)infinite structure in terms of a penetration depth which is retrieved from the imaginary part of the effective wave vector $K$.

Finally, the transferability to building blocks other than the extended nanowire structure has been studied. It is straightforward to transfer the findings to other geometries, however, the initial broad spectral width provided by the extended wires is the main reason for the observation of the very broad photonic band gaps in our Bragg stacks [290].

The effortless tunability of the oscillators in contrast to atoms or quantum well structures allows for a flexible and easy tailoring of very broad photonic band gaps.

$\sim$

# COUPLING IN THE INTERMEDIATE REGIME: THE CLASSICAL ANALOG OF ELECTROMAGNETICALLY INDUCED ABSORPTION

## 6.1 INTRODUCTION

As the previous chapters have been entirely devoted to plasmonic coupling in its limiting cases of either purely quasistatic or purely radiative interaction, this chapter will deal with an interesting case of coupling in the intermediate regime between both. Near-field interaction is characterized by the complete absence of radiative or wave effects, this means that propagation phases are meaningless. In contrast, radiative interaction is solely described by far-field effects. It is assumed that the near fields of the oscillators have decayed sufficiently to not mediate any interaction and therefore, their complete absence is assumed.

In this chapter we will discuss a structure in which both, near- as well as far-field coupling effects take place at the same time. A plasmonic dipole wire coupled to a quadrupolar wire pair will exhibit features of radiative coupling such as a retardation phase between oscillators, while at the same time excitation of the quadrupole oscillation is possible, which is a near-field effect.

This introduces the ability to manipulate the phase shift between two coupled plasmonic resonances in a controlled fashion. We theoretically and experimentally demonstrate that in the intermediate regime the coupling of a broad dipolar to a narrow dark quadrupolar plasmon resonance is possible while simultaneously allowing for a retardation-induced phase shift. The additional phase will be used to tune the interaction phase of the oscillators and change the destructive interference which is present in the plasmonic analog of electromagnetically induced transparency (EIT) [215] to constructive interference and hence increased absorption. This system exhibits similarities to the atomic physics effect of electromagnetically induced absorption (EIA) and thus will be termed the classical analog of EIA.

First, a short review of EIT in atomic and classical systems is given, then the plasmonic analog of EIT will be discussed, followed by the presentation of the classical analog of EIA.

## 6.2   EIT AND EIA IN ATOMIC SYSTEMS
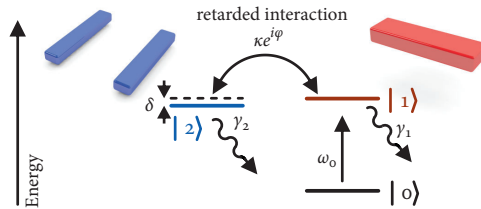


FIGURE 6.1. Three-level model scheme for the system. The energy level $|1\rangle$ can be excited from the ground level $|0\rangle$ by a bright transition with a large dipole moment and is simultaneously coupled to a dark state $|2\rangle$. In a usual EIT system the coupling parameter $\kappa$ is real. If it is possible to apply an additional phase factor $e^{i\varphi}$, for example by using a retarded coupling mechanism, the type of interference between both pathways can be changed from destructive to constructive, resulting in either EIT or EIA.

EIT is an inherently quantum mechanical effect which occurs in specifically prepared atomic three-level systems [291]. It was first proposed and experimentally realized by Harris and co workers [292, 293]. Usually, a $\Lambda$ configuration as depicted in Fig. 6.1 is used. The energy level $|1\rangle$ is coupled to the ground state $|0\rangle$ by a bright dipole-allowed transition with resonance frequency $\omega_0$. At the same time, it is coupled to a dark state $|2\rangle$ which might be detuned by a shift $\delta$. The coupling is mediated by an additional coupling field provided by an additional laser which ensures the coherence of both levels. The direct excitation $|0\rangle \rightarrow |2\rangle$ is dipole-forbidden, therefore its decay rate $\gamma_2$ is smaller than the bright transition rate $\gamma_1$. However, the coupling of the levels $|1\rangle$ and $|2\rangle$, described by the coupling parameter $\kappa \exp(i\varphi)$, allows for a population of state $|2\rangle$ which will cause a back action and an excitation of level $|1\rangle$. Overall this level scheme allows for two different excitation pathways leading to an occupation of the dipole allowed state $|1\rangle$: the direct transition $|0\rangle \rightarrow |1\rangle$ and the indirect one $|0\rangle \rightarrow |1\rangle \rightarrow |2\rangle \rightarrow |1\rangle$.

If the interference between these both pathways is destructive, the excitation $|0\rangle \rightarrow |1\rangle$ is not possible, light will not be absorbed and a narrow transmission peak opens up. As the coupling between level $|1\rangle$ and $|2\rangle$ and thus the possibility of interference is mediated by the cou-

pling laser field the effect is termed electromagnetically induced transparency (EIT).

EIT can be considered as a special case of a Fano resonance [133]. While the general Fano resonance formula describes a multitude of phenomena which can be explained by the interference of excitation pathways, and thus results in a variety of different asymmetric lineshapes, EIT is a special case for perfect destructive interference of two excitation paths and yields the typical spectral shape of a narrow transmittance window imposed onto a broad dipolar transmittance lineshape.

A complementary process to EIT would be the enhancement of absorption in an atomic system by a coherent effect. In atomic physics, this has been realized using degenerate two-level systems and has been termed electromagnetically induced absorption [294–297]. In this case two branches of the degenerate ground state form the two lower levels of the $\Lambda$ system. When driving the system with a coupling laser, a narrow, sublinewidth peak of enhanced absorbance is observed on top of the broader dipolar absorbance peak.

## 6.3 EIT IN CLASSICAL SYSTEMS AND PLASMONICS

Even though EIT is a quantum mechanical effect involving interference of probability amplitudes, EIT-like effects can be observed in classical systems such as plasmas [298, 299] and even in very fundamental systems like coupled mechanical oscillators and LC resonators [300, 301]. The realization of EIT in classical optical systems is of particular interest. There it emerges from the interference of the normal modes rather than from quantum interference of excitation probabilities. This was first realized using evanescently coupled high-$Q$ microresonators [302–307], and recently in metamaterials [155, 308, 309] and plasmonic structures [96, 134, 147, 150, 215, 216, 310, 311]. An effect similar to EIT and EIA is the so-called superscattering, where the higher modes of a structure are tuned such that their scattering amplitudes overlap with their fundamental dipolar mode and therefore substantially contribute to the total scattering of the particle. This leads to a narrow scattering peak on top of the broad dipolar scattering resonance. However, this only has been predicted theoretically up to now [312–314].

Besides the physical peculiarity of the EIT effect itself, there are numerous applications which make it very useful and therefore a realization in systems other than cold atomic gases would be very convenient. For example it can be harnessed to enhance nonlinear interaction in

optical media [291], for dispersion engineering, in particular the real-
ization of slow light [302, 305, 307] or delay lines [307, 309], reduction
of losses [308], or plasmonic sensing with narrow linewidths [96].
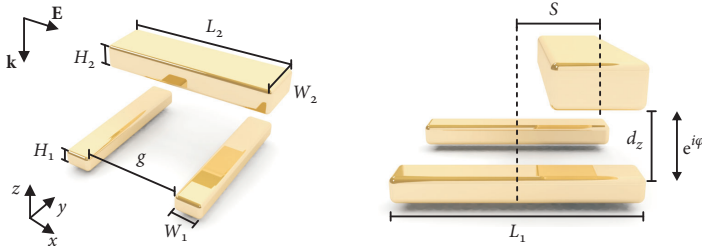


FIGURE 6.2. Geometry parameters of the structure. The phase difference be-
tween dipole and quadrupole can be tuned by changing the vertical spacing
$d_z$.

In a classical system EIT is realized by modeling bright and dark tran-
sition by oscillators with different damping constants. Particularly, in a
plasmonic system the transitions are represented by metallic cut-wires:
a quadrupolar cut-wire pair, which exhibits no net dipole moment and
therefore does not couple to the far field, is used for the dark transition
and a dipolar cut-wire is used for the bright transition. A schematic
of the stacked structure is depicted in Fig. 6.2, where also the relevant
dimensions are introduced. In contrast to EIT in atomic physics, where
a probe laser is used to monitor the spectral response of the system,
the effect can be directly observed by acquiring white light spectra of
the structure with light polarized parallel to the dipolar wire. Further-
more, the coupling between both oscillators is not mediated by the use
of a coupling laser but rather by the plasmonic near fields of the oscil-
lators themselves. Hence it is favorable to maximize the (near-field)
coupling strength between quadrupole and dipole. In contrast to a pla-
nar side-by-side arrangement [216] a stacked arrangement exhibits a
substantially higher coupling strength and therefore an increased mod-
ulation depth for the effect [215]. The coupling strength can be tuned
by varying the offset parameter $S$. For $s = 0$ nm no coupling between
dipole and quadrupole is possible due to symmetry considerations. For
increasing offset, an excitation of the quadrupole via the near field of
the dipole is possible. Therefore the near-field coupling strength, rep-

resented by $S$, is analogous to the coupling laser field strength $\Omega_c$ in atomic systems.

## 6.4 MODES OF THE EIT STRUCTURE

To investigate the basic principles of the structure Fig. 6.3 displays a set of field calculations for different frequencies of incoming light, namely at both transmittance dips (150 THz and 201 THz) and at the EIT peak (176 THz). The $z$ component of the electric field in planes slightly above the corresponding oscillators is displayed. This field component corresponds to the normal field on the respective surface, which is tightly connected to the charge distribution and therefore plasmon oscillation within the wires. As structural parameters the values of Liu et al. [215], $L_1 = 315$ nm, $L_2 = 355$ nm, $H_1 = H_2 = 40$ nm, $W_1 = W_2 = 80$ nm, $d_z = 30$ nm[i], $g = 220$ nm, and $S = 120$ nm are used. The periodicity is 700 nm in both directions.

Fig. 6.3 (a) shows the calculated transmittance spectrum which exhibits the characteristic shape of a window of high transmittance on top of the broader dipolar transmittance dip. Fig. 6.3 (b-d) shows the amplitude of the electric field $z$ component on a plane slightly above the dipole and quadrupole. Temporally, the fields are displayed at the point of maximum field intensity. For the points of minimum transmittance, i.e., at frequencies of (b) 150 THz and (d) 201 THz one can observe two of the expected modes [214, 315] in a coupled three-particle system: both quadrupole wires oscillate exactly antipodal due to symmetry and excitation mechanism. Therefore they exhibit a typical quadrupolar charge distribution which cancels in the far field and hence this mode cannot couple to far-field radiation on its own.

The polarization of the dipole wire takes two orientations with respect to the quadrupole: in case of (b) the quadrupolar and dipolar wire end which are faced towards each other exhibit opposite charges, analogous to the antisymmetric mode in wire pairs. Therefore, this mode will be referred to as the antisymmetric mode of the structure[ii]. The electrostatic energy is decreased, therefore this mode is red shifted from the single oscillator resonance positions. In case of (d) the nano-wire ends facing toward each other exhibit equal charges, which resem-

---

i  Here $d_z$ is defined as the pure spacer layer thickness, in contrast to the paper by Liu et al. [215].

ii  Unlike in the wire pair case, the modes do not exhibit real symmetry or anti-symmetry. Nevertheless, this naming is intuitive by considering the analogies to the wire pair case.
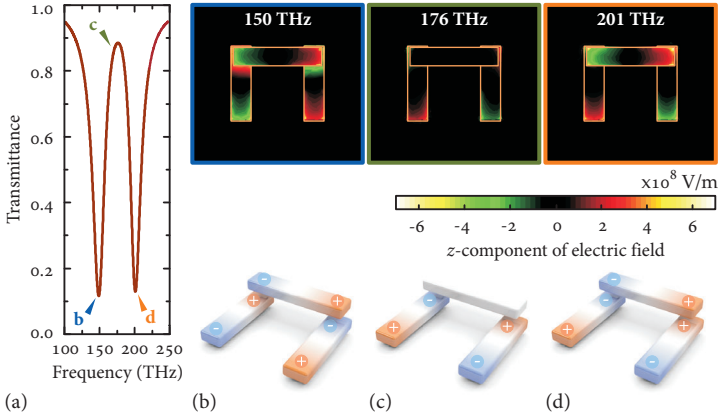
FIGURE 6.3. (a) Calculated transmittance spectrum of the EIT structure with arrows indicating the spectral positions at which electric field calculations (b-d) were performed. (b-d) Calculated $z$ component of the electric field for the EIT structure with $d_z = 30\,nm$ for different spectral positions, (b) 150 THz, (c) 176 THz and (d) 201 THz. At the transmittance minima a characteristic anti-symmetric (b) and symmetric (d) field distribution is observed. Interference between these two modes of the structure leads to the cancellation of dipole oscillation in case of (c) and hence the observation of the EIT peak. The bottom row shows a schematic of the charge distribution for the different situations.

bles the symmetric mode of a wire pair, thus the resonance position is blue-shifted and the mode will be referred to as the symmetric mode[ii]. Between these modes, namely at the transmittance peak, almost no field intensity is observed at the dipole and only the quadrupole wires exhibit a plasmonic oscillation. This is depicted in the field plot for a frequency of 176 THz. It is possible to interpret this in terms of a destructive interference of the two modes. In this picture, the cancellation of the dipole wire plasmon oscillation is a direct analog to the inhibited population of state $|1\rangle$ due to the destructive interference of probability amplitudes, thus the effect can indeed be termed the classical analog of EIT.

## 6.5 PHASE TUNING AND THE TRANSITION TO EIA

To realize EIA it is necessary to change the destructive to a constructive interference. In an atomic system special care has to be taken in order to achieve this. However, the realization for classical oscillators appears quite straightforward: one can simply tune the oscillator phases in order to change the type of interference between them. While this again is a quite challenging task for mechanical oscillators connected by springs, in an optical system retardation is present and can be harnessed for phase tuning by increasing the vertical distance of the building blocks.

Analogous to the previous chapters, the behavior of the system will be examined by calculating the spectra for different vertical distances $d_z$ between dipole and quadrupole. Fig. 6.4 (a) shows calculated transmittance, reflectance, and absorbance of the structure for the dimensions stated above. The offset is $S = 120$ nm which corresponds to maximum coupling strength between dipole and quadrupole. To display the pure effect undisturbed by nonradiative damping due to ohmic losses in the metal, the damping parameter in the Drude model for gold has been reduced to $\gamma_\mathrm{D} = 1\,\mathrm{THz}$[iii].

For small $d_z$ the transmittance graph shows the typical behavior of the EIT structure with a narrow transmittance peak imposed onto the dipolar transmittance dip. Remarkably, for very low distances the spectra looks similar to a conventional near-field splitting in a dimer structure. The increasing spectral splitting for these very low distances stems from the increased coupling strength and also is present in atomic systems where it is termed Autler-Townes-Splitting.

On increased vertical spacing the near-field coupling strength is decreased and the spectra resemble a case of badly tuned EIT, as the modulation of the transmittance peak becomes smaller. However, a pronounced difference in transmittance and reflectance can be observed: The modulation of the dip in reflectance is much stronger than that of the peak in transmittance, indicating that there is a change in absorbance. This can be seen in the absorbance spectra in the right panel which are calculated using $A = 1 - T - R$. At the quadrupole resonance position a very strong and narrow peak of increased absorbance is observed. This effect is maximum for a vertical spacing of approximately $d_z = 260$ nm, as can be seen from the cross section plot below the absorbance graph. The retardation phase at this point is matched

---

iii  See definition in section 2.3.1.

FIGURE 6.4.    (a) Color-coded calculated transmittance, reflectance and absorbance spectra for increasing vertical spacing $d_z$ between dipole and quadrupole and maximum coupling strength.    (b) Calculated transmittance (solid) and reflectance (dashed) and    (c) absorbance for the EIA structure with an increasing offset $S = 0$ nm to 120 nm and a vertical spacing of $d_z = 260$ nm. To show the effect unhampered by nonradiative damping, the damping coefficient in the Drude model is set to $\gamma_D = 1$ THz in this calculation. The two spectral shifts between 300 nm and 350 nm in (a) arise due to numerical artifacts.

to obtain constructive interference and the absorbance is increased due to the coupling between dipole and quadrupole.

For this vertical distance, calculated transmittance and reflectance for varying offset $S$ and thus coupling strength are displayed in Fig. 6.4 (b). The resulting absorbance is shown in (c). In case of symmetric arrangement ($S$ = 0 nm, bottom row) coupling between dipole and quadrupole is not possible and only the dipolar absorbance is observed. As ohmic losses have artificially been reduced, the absorbance is rather low, with a maximum peak height of only 3 %. By increasing the offset of the dipole the coupling strength increases and a sharp absorbance feature at the quadrupole resonance position emerges on top of the dipole peak. This yields a double-Lorentzian lineshape. At this peak, the absorbance is substantially enhanced to an absolute value of 49 %, which corresponds to an enhancement of more than one order of magnitude.

The spectra in Fig. 6.4 (c) correspond very well to those observed in atomic EIA systems [294–296], with a very narrow peak that is substantially increased in height, compared to the pure dipolar absorbance. To transfer this concept to plasmonics, however, it is important to note, that ohmic losses in the plasmonic system constitute an additional loss mechanism which is not present in atomic systems. This loss imposes a lower limit for the achievable linewidth in a plasmonic system [216] and therefore the appearance of the spectra substantially changes. Still, the underlying mechanism is valid for high damping values as well. Fig. 6.5 shows calculations analogous to Fig. 6.4 with a realistic damping parameter, $\gamma_D$ = 20 THz. The spectra show two distinct differences with respect to the idealized calculations of Fig. 6.4: first, the overall dipolar absorption is strongly increased. While in the former case the pure dipolar absorption was 3 % it is now around 34 %. As the maximum absorbance in the coupled case is not substantially altered and still is around 50 %, the allover change in absorption strength is less dramatic. Second, the linewidth strongly changes. The low damping spectra exhibit a nice double-Lorentzian shape due to the strong difference in linewidths ($\gamma_1/\gamma_2 \approx$ 30) which cannot be easily observed for high damping. The reason is the additional nonradiative damping which strongly broadens the quadrupolar resonance, leading to a ratio of only $\gamma_1/\gamma_2 \approx$ 2.

## 6.6 EXPERIMENTAL REALIZATION

As discussed in the previous section, an experimental observation of the EIA effect is hampered by the spectral broadening due to nonradiative ohmic losses in the gold. Consequently, to improve the observability of
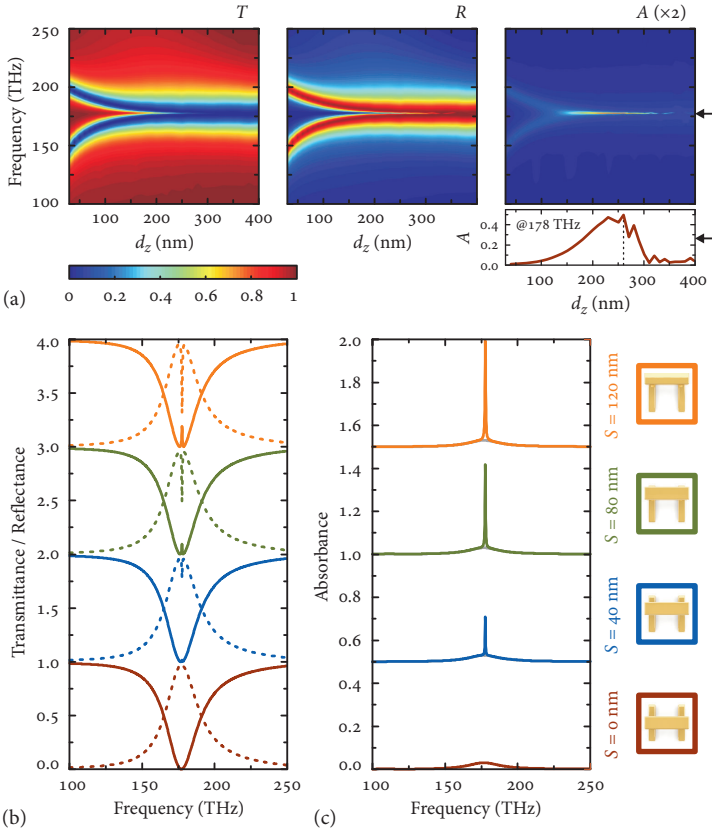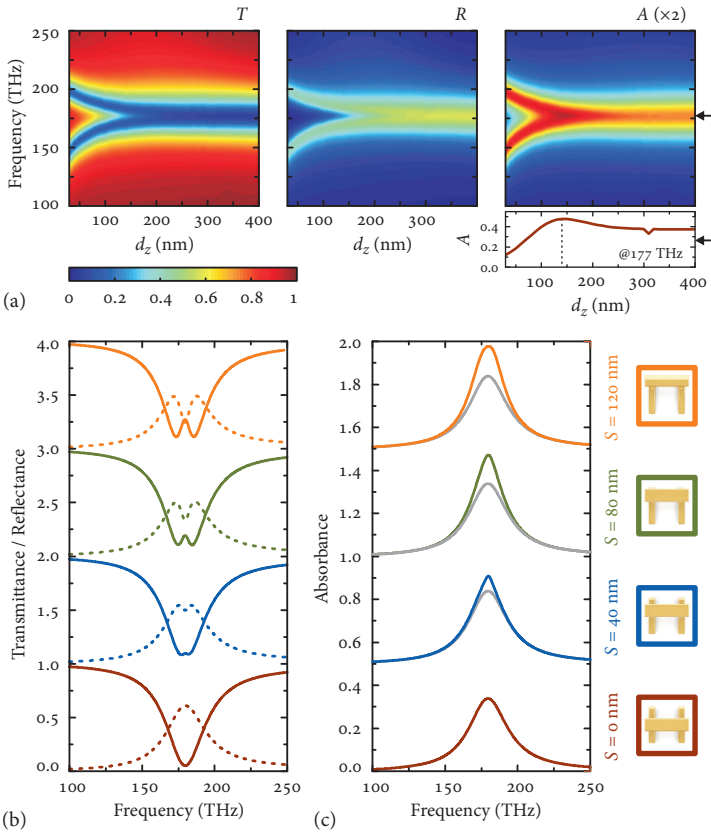
FIGURE 6.5.    (a) Color-coded calculated transmittance, reflectance and absorbance spectra for increasing vertical spacing $d_z$ between dipole and quadrupole and maximum coupling strength.   (b) Calculated transmittance (solid) and reflectance (dashed) and   (c) absorbance for the EIA structure with an increasing offset $S$ = 0 nm to 120 nm and a vertical spacing of 140 nm. In this calculation a realistic gold damping coefficient in the Drude model, $\gamma_D$ = 20 THz, is assumed. The spectral shift slightly above 300 nm in (a) arises due to a numerical artifact.

the effect, it is desirable to reduce the bare dipolar absorbance compared to that of the quadrupolar mode. This is accomplished by changing the wire geometry: we increase the width $W_2$ and height $H_2$ of the dipole wire, preserving the spectral position by tuning the length $L_2$. Doing so

leads to a change in the proportion of scattering and absorbance. This is evident by comparing the absorbance spectra in Fig. 6.5 and Fig. 6.8 for offset $S$ = 0 nm. Absorbance is reduced from 34 % in the first case to only 20 % for the structure with the larger dipole wire. Similarly, the absorbance of the quadrupole can be increased by reducing its wire cross section, still preserving the spectral position by tuning the length $L_1$. Additionally, a slight detuning $\delta$ of the spectral positions of dipolar and quadrupolar mode is desirable, as this further facilitates the observation of the double-Lorentzian lineshape.

For this new, detuned geometry with quadrupole dimensions of $L_1 \times W_1 \times H_1$ = 375 nm × 65 nm × 40 nm, $g$ = 220 nm, and dipole dimensions of $L_2 \times W_2 \times H_2$ = 420 nm × 120 nm × 40 nm, calculated transmittance, reflectance, and absorbance for full offset $S$ and increasing vertical distance are shown in Fig. 6.6. The top row shows the calculations for $\gamma_D$ = 20 THz while the bottom row displays the idealized calculations with $\gamma_D$ = 1 THz.

First, the case of high damping (top row) will be discussed. As is evident from the calculations, changing the geometry of the wires strongly alters the appearance of the spectra: these are not symmetric any more. For the dipole wire the absorbance is reduced, hence the symmetric (blue shifted) mode of the structure, i. e., the one with a huge dipole moment, is attenuated in absorbance and appears more pronounced in reflectance. The opposite holds true for the antisymmetric mode, which exhibits a more efficient coupling to the quadrupolar resonance due to its charge distribution (compare Fig. 6.3 (b)). Decreasing width and height of the quadrupolar wires here leads to a strong increase in absorbance, hence the mode shows up strongly pronounced in absorbance and rather weak in reflectance. The enhancement of absorbance shifts to significantly lower vertical spacings and the absorbance difference for $d_z$ = 30 nm and $d_z$ = 90 nm is less pronounced compared to the non-detuned situation. Still the difference in modulation depth of reflectance dip and transmittance peak is observed resulting in a sub-dipole-linewidth absorbance feature in the spectrum. The optimum vertical distance is found by comparing the absorbance peak for full ($S$ = 120 nm) to that of zero offset. It occurs around $d_z$ = 90 nm. To confirm these findings, also the low gold damping case is calculated for the detuned system. The spectra in the bottom row of Fig. 6.6 display the characteristic behavior for the system (compare Fig. 6.4 (a)), even though the asymmetry of the spectral features is also observable. Hence, as already stated before, the main obstacle in the observation of
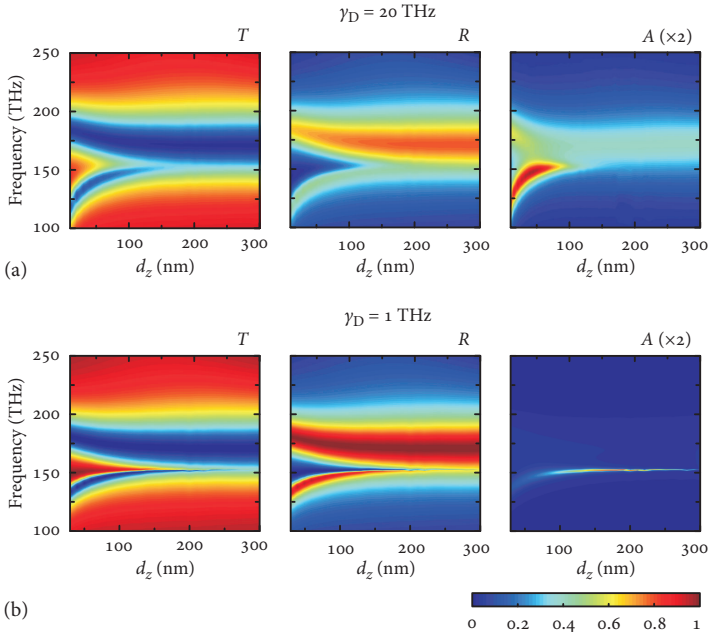
FIGURE 6.6. Calculated transmittance, reflectance, and absorbance for increasing vertical distance $d_z$ with a spectral detuning between dipole and quadrupole for a gold damping value of $\gamma_D = 20$ THz (top row) and $\gamma_D = 1$ THz (bottom row). The spectral as well as scattering strength detuning leads to strongly asymmetric spectra, especially in case of high damping. However, the EIA effect is still present, which is more pronouncedly observed in the bottom row.

the effect are the ohmic losses in the gold. But also for realistic damping values, it should be possible to observe it in the detuned structure.

To experimentally support the findings a sample with several arrays of structures was fabricated using a two-step electron beam lithography process. Quadrupole and dipole sizes are approximately matched to the dimensions of the detuned structure. The spacer layer is $d_z \approx 100$ nm thick. The array size is 90 μm × 90 μm for each field. The offset $S$ is varied from field to field in order to examine different coupling strengths. Due to limited overlay accuracy, the offsets of the fabricated structures have to be measured after fabrication. These are determined to be $S = 30$ nm, 45 nm, 60 nm, and 150 nm. A scanning electron micrograph of the fabricated structure with maximum offset is shown in Fig. 6.7.
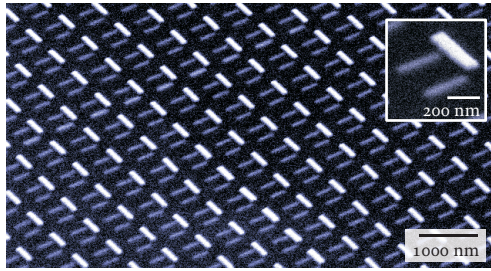
FIGURE 6.7. SEM micrograph of the fabricated structure with maximum offset *S*. The inset displays one unit cell.

This image shows the large difference in wire sizes for the dipole and the quadrupole.

Reflectance and transmittance measurements for the different offsets are performed by Fourier-transform infrared spectrometer (FTIR) measurement using a liquid nitrogen cooled Mercury Cadmium Telluride (MCT) detector. As absorbance will be calculated from the measurements of transmittance and reflectance, great care in the alignment and during the measurement has to be taken to achieve quantitatively comparable results in both measurements. The acquired spectra are shown in the left panel of Fig. 6.8 (a). For comparison, calculations are displayed in the right panel.

The resulting absorbance spectra are displayed in Fig. 6.8 (b). In these graphs the double-Lorentzian spectral shape is well pronounced. For maximum offset *S* the experimentally observed peak absorbance is 38 % compared to 28 % in the uncoupled case which corresponds to an enhancement of roughly 35 %. In the calculations, this difference is even more pronounced with a peak absorbance of 44 % versus 20 %, which corresponds to an increase by more than 100 %. However, the enhancement of the absolute value of absorbance is not the crucial point, as this always can be incorporated by introducing additional losses. In this case the spectral width of the absorbance feature is smaller than the pure dipolar absorbance peak.
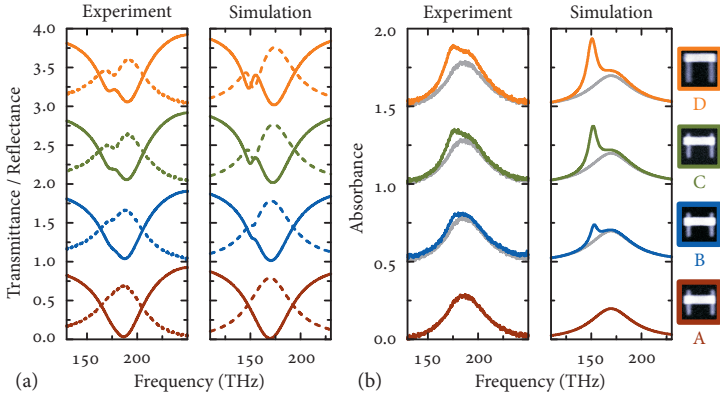
FIGURE 6.8.   (a) Measured (left) and calculated (right) transmittance spectra (solid) and reflectance spectra (dashed) for different offsets $S$.   (b) Corresponding measured (left) and calculated (right) absorbance. For increased offset $S$ and therefore increased coupling strength between dipole and quadrupole, a narrow absorbance dip originating from the excitation of the quadrupole appears. The minimum offset absorbance curve is shown in every graph in light gray for comparison. Simulated spectra are shown for offsets of 0 nm, 40 nm, 80 nm, and 120 nm.

## 6.7    ANALYTICAL MODELING

### 6.7.1    *Coupled Oscillator Model*

Analogous to the straightforward description of EIT in terms of classical oscillators [300, 316] the coupled oscillator model is also appropriate to describe EIA. The system shown in Fig. 6.9 is described by two coupled second order differential equations

$$\ddot{x}_1(t) + \gamma_1 \dot{x}_1(t) + \omega_1^2 x_1(t) - \widetilde{\kappa'} x_2(t) = f'_{\text{ext}}(t)$$
$$\ddot{x}_2(t) + \gamma_2 \dot{x}_2(t) + \omega_2^2 x_2(t) - \widetilde{\kappa'} x_1(t) = 0,$$

$$(6.1)$$

where dipole and quadrupole are represented by oscillator 1 and 2, respectively.

Only the dipole couples directly to the radiation field $f'_{\text{ext}}(t)$. Crucial to the description of EIA is the use of a complex coupling coefficient $\widetilde{\kappa'} = \kappa' \exp(i\varphi)$ which is necessary to model the phase retardation effect. Us-
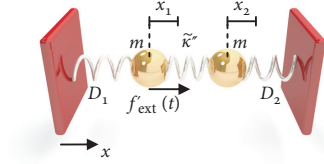
FIGURE 6.9. Mechanical schematic of the coupled oscillator model for two oscillators with damping constants $\gamma_i = D_i/m$ and $\gamma_2 \ll \gamma_1$, coupled by $\widetilde{\kappa}' = \widetilde{\kappa}''/m$. Only the left oscillator is excited by the external force. For the implementation of EIA $\widetilde{\kappa}'$ has to be complex.

ing the harmonic ansatz $x_j(t) = a_j \exp(-i\omega t)$, $f'_{\text{ext}}(t) = f' \exp(-i\omega t)$ and the approximation

$$\omega_j^2 - \omega^2 - i\omega\gamma_j \overset{\omega \approx \omega_j \approx \omega_o}{\approx} -2\omega_o\left(\omega - \omega_j + i\frac{\gamma_j}{2}\right) =: -2\omega_o\Omega_j \quad (6.2)$$

which is valid for $\omega \approx \omega_j \approx \omega_o$, the system can be simplified to

$$\begin{pmatrix} -2\omega_o\Omega_1 & -\widetilde{\kappa}' \\ -\widetilde{\kappa}' & -2\omega_o\Omega_2 \end{pmatrix}\begin{pmatrix} a_1 \\ a_2 \end{pmatrix} = \begin{pmatrix} f' \\ 0 \end{pmatrix}. \quad (6.3)$$

The solution is found by matrix inversion

$$\begin{pmatrix} a_1 \\ a_2 \end{pmatrix} = \frac{1}{\widetilde{\kappa}'^2 - 4\omega_o^2\Omega_1\Omega_2}\begin{pmatrix} 2\omega_o\Omega_2 f' \\ -\widetilde{\kappa}' f' \end{pmatrix}. \quad (6.4)$$

From this equation it is evident, that the quadrupolar oscillator is excited only via the coupling to the dipole: the second oscillator amplitude $a_2$ is proportional to the external field multiplied by the coupling coefficient. The absorbance of the system is calculated as the dissipated power, which yields

$$A(\omega) = \Im \frac{2\omega_o\Omega_2 f'}{\widetilde{\kappa}'^2 - 4\omega_o^2\Omega_1\Omega_2}. \quad (6.5)$$

Identifying $\Omega_1 = \omega - \omega_o + i\gamma_1/2$ and $\Omega_2 = \omega - \omega_o + \delta + i\gamma_2/2$ alongside with normalized values $\widetilde{\kappa} = \widetilde{\kappa}'/(2\omega_o)$ and $f = f'/(2\omega_o)$ one arrives at

$$A(\omega) = \Im \frac{f\Omega_2}{\widetilde{\kappa}^2 - \Omega_1\Omega_2}. \quad (6.6)$$

This equation is formally identical to those derived previously [215, 216, 291, 300, 315], except for the complex coupling coefficient $\widetilde{\kappa}$. The consequences of this complex coupling coefficient are discussed in Fig. 6.10. In this plot matrix, eq. 6.6 is shown for different values of $\kappa$ and $\varphi$. For $\varphi = 0$ (left column of Fig. 6.10) the spectra for a real coupling parameter are shown and therefore the typical behavior of the EIT effect—a dip emerging on the broad dipolar absorbance feature—is observed. The upper row of Fig. 6.10 shows the spectra for almost vanishing coupling strength $\kappa$, where basically only the dipolar absorbance is present. For intermediate coupling strengths ($\kappa = 0.1$), a transformation from a small dip in the absorbance for $\varphi = 0$ to a small peak on top of the absorbance for $\varphi = \pi/2$ can be observed. However, this peak does not simply emerge out of the dip, but a rather complex behavior takes place. In the next row, $\kappa = 0.2$, this effect is more pronounced. The narrow peak emerges from the right maximum next to the dip, grows and is most pronounced at exactly $\varphi = \pi/2$. At this $\varphi$ value, it is furthermore symmetric around $\omega = \omega_0$.
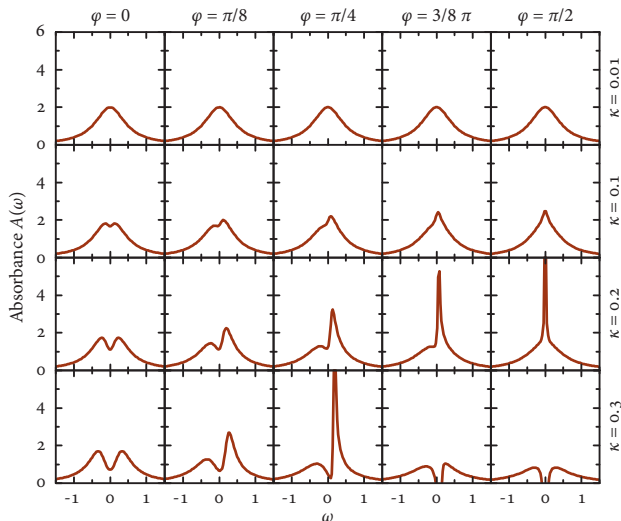


FIGURE 6.10. Numerical evaluation of the analytical coupled oscillator formula, eq. 6.6, with a complex coupling coefficient $\widetilde{\kappa} = \kappa \exp(i\varphi)$ for different combinations of $\kappa$ and $\varphi$. All quantities are dimensionless. The other parameters are $\omega_0 = \delta = 0$, $f = 1$, $\gamma_1 = 1$ and $\gamma_2 = 0.2$.

For the parameter range from $\varphi = \pi/2$ to $\pi$ the spectra look identical but mirrored about the $\omega = \omega_0$ axis. This is a characteristic Fano behavior as observed in section 2.6, where the extreme case of a symmetric dip is realized for $\varphi = 0$ and the extreme case of a symmetric peak for $\varphi = \pi/2$.

An interesting situation occurs for large coupling strengths, as can be seen in the last row of Fig. 6.10: increasing the coupling strength beyond $\kappa > \sqrt{\gamma_1 \gamma_2/4}$ leads to negative absorbance. Such a phenomenon of $A < 0$ has also been reported in atomic EIA spectra [297]. There this is not a problem, as the atomic system is usually pumped by the coupling laser and therefore gain might be possible. However, in a plasmonic system, this would break energy conservation. In the coupled harmonic oscillator model, the situation of strong coupling with $\varphi = \pi/2$ corresponds to a strong force which is exerted on the second particle *in the wrong direction*. This cannot occur in a real system. In the same manner, some mechanism in the radiatively coupled system has to ensure energy conservation, so that this situation is somehow prevented.

### 6.7.2 *Fits to Experimental and Calculated Spectra*

It is possible to fit eq. 6.6 to the experimental as well as to the calculated spectra. These are shown in Fig. 6.11. The parameters retrieved[iv] from both fits are given in table 6.1. Even though the fitting to the calculated spectra is more robust as the effect is more pronounced and can be observed unhampered by experimental difficulties such as noise and inhomogeneous broadening, there is reasonable qualitative agreement between both, the parameters extracted from the experimental and the calculated data. As expected, increasing the offset $S$ yields an increase in the coupling parameter $\kappa$. For maximum offset, $\kappa$ exceeds the dark mode linewidth in the calculated data, hence the coupling from the dipole to the quadrupole is stronger than the dissipation processes in the metallic quadrupole wires. This is less pronounced in the experimental data, still at least $\kappa$ and $\gamma_2$ are of similar magnitude. The phase parameter $\varphi$ also changes for increasing offset, starting from approximately $\pi$ for the lowest offset and going to a final value of approximately $0.7\pi$. This trend is quite exactly reproduced in both parameter sets. There is no straightforward explanation why $\varphi$ ends up at an odd value

---

iv In order to keep the fitting parameter space small for the experimental fits, the parameters $\omega_0$ and $\delta$ are determined directly from the curve and kept fixed.

instead of a more intuitive one such as a multiple of $\pi/2$ or $\pi$. However, one has to keep in mind, that the system is more complex than suggested by the model, consisting of three oscillators of which each possesses several loss channels, thus the maximum of absorption does not necessarily occur for a phase which is intuitively expected.
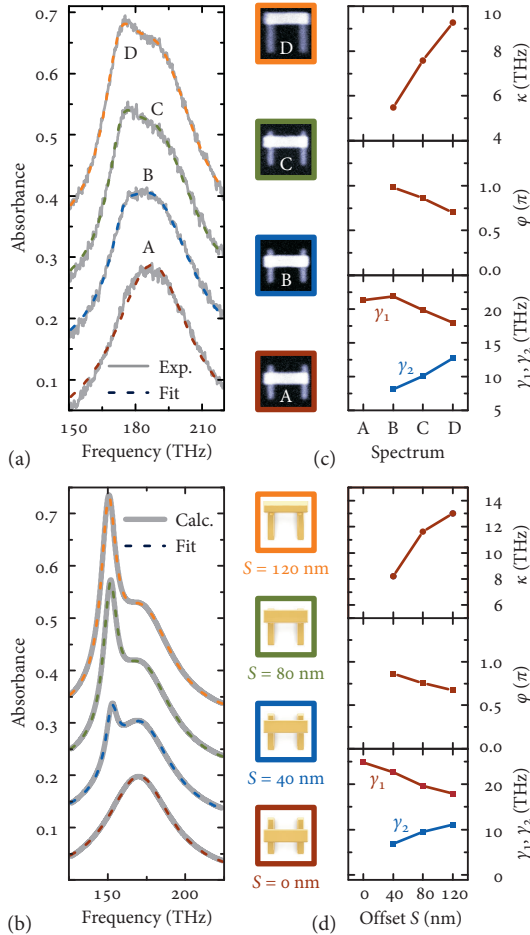


FIGURE 6.11.    (a,b) Fit curves (dashed) of the coupled oscillator model with complex coupling coefficient (eq. 6.6) to the (a) experimental and (c) calculated absorbance spectra (solid gray).    (c,d) Retrieved fit parameters $\kappa$, $\varphi$, $\gamma_1$, and $\gamma_2$.

| | EXPERIMENT | | | | THEORY | | | |
| | A | B | C | D | 0 nm | 40 nm | 80 nm | 120 nm |
|---|---|---|---|---|---|---|---|---|
| $\kappa$ | – | 5.5 | 7.6 | 9.3 | – | 8.2 | 11.6 | 13.0 |
| $\varphi$ | – | 1.0 | 0.9 | 0.7 | – | 0.9 | 0.8 | 0.7 |
| $\gamma_1$ | 21 | 22 | 20 | 18 | 25 | 23 | 20 | 18 |
| $\gamma_2$ | – | 8.2 | 10 | 13 | – | 6.8 | 9.2 | 11 |
| $f$ | 6.1 | 7.0 | 7.2 | 8.0 | 4.9 | 5.3 | 6.1 | 6.6 |
| $\omega_0$ | 188 | 188 | 188 | 188 | 170 | 170 | 168.0 | 167 |
| $\delta$ | – | 13 | 13 | 13 | – | 16 | 12 | 10 |

TABLE 6.1. Fit parameters obtained from experiment and simulation using eq. 6.6. All parameters except $\varphi$ are given in THz, $\varphi$ is given in multiples of $\pi$.

As an example, one would expect constructive interference for a phase delay of multiples of $\pi$—including 0. Still, the near-field coupled EIT system obviously exhibits destructive interference instead, which indicates that the concept of plane wave interference is not directly applicable to this system of coupled oscillators in the intermediate coupling regime, in which near-field coupling effects still play a role.

Finally, the fitting parameters show that the quadrupolar linewidth is in fact smaller than the dipolar linewidth, which is already obvious from the spectra. However, it is of interest that the dipolar linewidth consistently decreases with increasing coupling strength, while the quadrupolar linewidth increases. In the naive coupled oscillator picture these parameters should be constant as they are inherent oscillator properties and all coupling effects should be included within $\kappa$.

This indicates that the coupled harmonic oscillator system is indeed a good model system which captures the major features for the description of the effect, but the real system possesses a higher degree of complexity and therefore the model does not capture all of the details.

## 6.8   ELECTRIC FIELD DISTRIBUTION IN THE EIA STRUCTURE

To further investigate the phase behavior of the oscillators, we perform electromagnetic field calculations for the structure. In the calculation the detuned geometry with a vertical spacing of $d_z$ = 100 nm and an

offset of $S = 120$ nm is used. The field is calculated at a frequency of $f_q = 152$ THz which corresponds to the quadrupole resonance frequency of the detuned structure.

As the EIA structure intrinsically depends on retardation effects, the field has to be evaluated in different planes perpendicular to the light propagation axis, as indicated by Fig. 6.12 (a). Additionally, the field maxima at the dipole and the quadrupole do not necessarily occur at the same time due to retardation effects, hence the time-dependent fields have to be considered. Thus, four different images of the $z$ component of the calculated electric field are displayed in Fig. 6.12 (b), for different planes, $z = 211$ nm and $z = 51$ nm, as well as phases of the light field $\omega_q t = 2\pi f_q t$. The latter are chosen by determining the maximum field strength at the dipole and the quadrupole. The field amplitude at the dipole reaches its maximum value for $\omega_q t = 1.24\pi$, whereas the field amplitude at the quadrupole is maximum for $\omega_q t = 1.74\pi$. For both maxima the field at the respective other oscillator is very low, indicating an out-of-phase oscillation of dipole and quadrupole.

Comparing this field distribution to the ones obtained for the near-field-coupled EIT structure (see Fig. 6.3) the main difference between both cases can be observed: In case of EIT the dipole excitation is canceled due to interference. At the quadrupole resonance frequency no net plasmon oscillation is excited in the dipole wire, thus leading to high transmittance through the structure. In contrast, for EIA the resulting effect is an out-of-phase oscillation of quadrupole and dipole. This phase offset can be observed more clearly in Fig. 6.12 (c) where the field intensity at two distinct points (indicated by circles in Fig. 6.12 (b)), at the tip of the quadrupole (blue) and the dipole (red) are shown as a function of time. The quadrupole phase lags behind that of the dipole by $\pi/2$, therefore the amplitude at one oscillator is zero for maximum

FIGURE 6.12 *(FACING PAGE)*.    (a) Schematic for the planes, in which field calculations are shown.    (b) Calculated $z$ component of the electric field above the dipole (top row) and the quadrupole (bottom row) for $d_z = 100$ nm. Maximum field strength at dipole and quadrupole are observed at different times.  $z$ denotes the vertical position of the cross section. The dipole field is maximum for $\omega_q t = 1.24\pi$ (left column), the quadrupole field is maximum for $\omega_q t = 1.74\pi$ (right column).    (c) Calculated time evolution of the electric field strength at the dipole and quadrupole tip (indicated by blue and red circle in (b)).

(a)

(b)

(c)
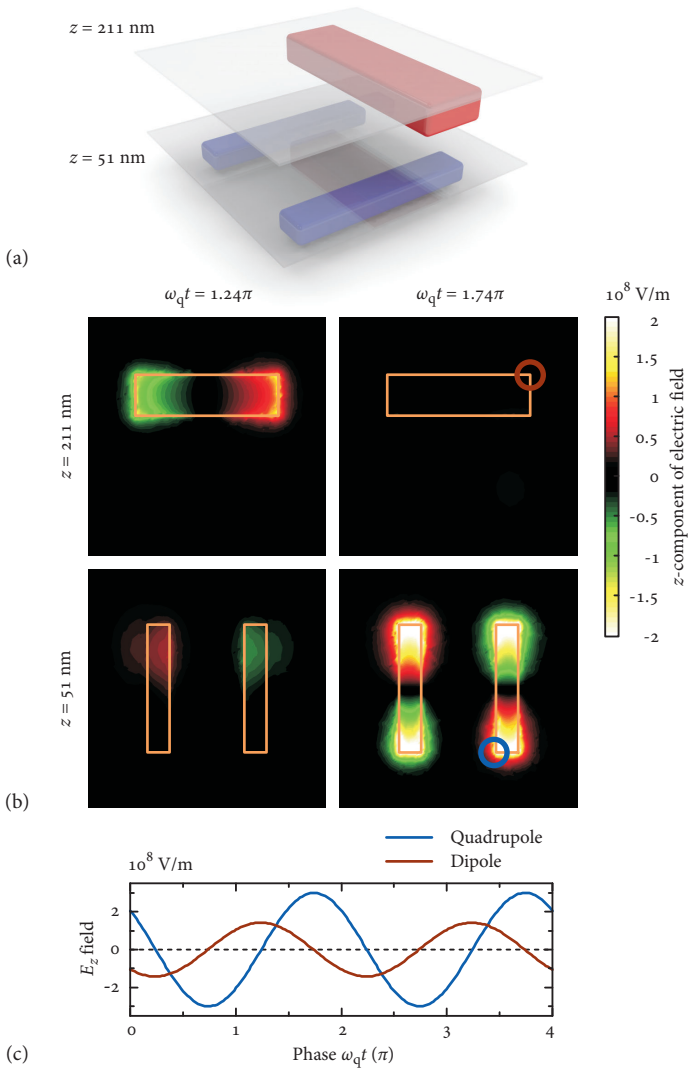
amplitude at the respective other oscillator. This yields a maximum energy dissipation and hence high absorbance in the structure.

This behavior of field maxima occuring at different times for different oscillators cannot be explained using only near-field coupling. As there are no phases in the pure near-field part, all coupled oscillators exhibit zero or $\pi$ phase delay. Thus, the field distribution shows different amplitudes at different positions, but all the maxima are achieved at the same time in an oscillation cycle, which indeed is observed in the field plots of the EIT structure. Fig. 6.12 shows, that this is not the case any more in the EIA structure, and therefore demonstrates the necessity of considering the phase in the latter.

## 6.9   CONCLUSION

In conclusion, this chapter has given an overview over the work that has been performed in connection with the plasmonic analog of electromagnetically included transmission and absorption in a plasmonic system, with a major emphasis on the structure consisting of a dipole cut-wire stacked on top of two cut-wires forming a plasmonic quadrupole. In order to be able to tune the phase between dipolar and quadrupolar oscillator, an additional phase term has been introduced. This additional phase was realized by increasing the vertical distance between the oscillators. Therefore we were able to manipulate the coupling phase of the oscillators and obtain constructive interference of the two excitations, leading to enhanced absorption. In doing so, we have demonstrated an analog system to electromagnetically induced absorption for classical oscillators.

One interesting feature of this structure is, that the vertical distance is in the intermediate regime and the coupling exhibits characteristics of both, the near- as well as the far-field regime. An excitation of the quadrupole is still possible, but phase retardation due to enlarged spacing between the oscillators is already significant. Considering only radiative coupling would render the excitation of the quadrupolar oscillator impossible, while on the other hand, considering only near-field interaction would not allow for retardation phases in the structure. This intermediate coupling regime offers new fascinating possibilities, such as phase control for the coupling of plasmonic building blocks.

It is noteworthy that, unlike the plasmonic analog of electromagnetically induced transparency, there is no straightforward implementation of electromagnetically induced absorption in a system of mechanical

masses and springs, as the coupling force is not instantaneous but inherently relying on retardation.

∼

# 7

## CONCLUSION & OUTLOOK

In conclusion, this thesis has provided an insight into the coupling of plasmonic nanoparticles with a special emphasis on the investigation of far-field coupling in three-dimensional, stacked arrangements.

Predominantly one building block, a gold nanowire, was utilized. It is infinitely extended along one axis and a particle plasmon resonance can be excited by light perpendicular to the wire. For typical geometries it is spectrally located in the visible or near-infrared wavelength range.

To understand the basic coupling mechanisms, initially only dimer arrangements were considered, and near- as well as far-field coupling were investigated. In the near-field regime the electrostatic approximation is sufficient for a qualitative description of the coupling effects. In this regime the plasmon hybridization concept is a valuable tool. The coupled dimer system supports two modes: a symmetric and an antisymmetric one. Their resonance frequencies have to be determined from the specific arrangement of the particles and are very sensitive to the specific orientation of the particles with respect to each other and the polarization of the incident light. This was particularly observed for a lateral shift of the top layer which leads to an inversion of the hybridization scheme yielding a Fano lineshape in the spectra.

In the far-field regime Fabry-Pérot modes arise due to the spatial arrangement of the oscillators. They interact with the particle plasmon modes, giving rise to new coupled modes. These can be understood in a simple model, the resonant mirror model, which is capable to predict their resonance positions from the resonance properties of the plasmonic nanowires and their spacing.

The calculations were confirmed by the experimental realization of 11 stacked dimer samples with different spacings covering a broad range from the near-field to the far-field regime. The experimental spectra agree very well with the calculations.

A peculiar situation occurs whenever the vertical spacing matches a multiple of half the single particle plasmon resonance wavelength, thus fulfilling the Bragg condition at this wavelength. The coupled mode which spectrally approaches the single particle plasmon resonance wavelength becomes very narrow and almost vanishes for exact

Bragg spacing. This results in a broad range of high reflectance and low transmittance as well as absorbance. In this special case the re-emitted oscillator fields interfere constructively in backward direction and destructively in forward direction.

Structures with increasing layer number—each stacked at Bragg distance—have been studied. These exhibit similarities to passive photonic crystals which feature a photonic band gap, however, due to the inclusion of resonant elements, new exciting properties arise. Due to the resonant response of the individual plasmonic layers and their matched arrangement a very broad photonic band gap emerges, which spans about one octave at optical frequencies.

These findings were experimentally confirmed by realizing a four layer plasmonic Bragg structure where a photonic band gap of 0.8 eV could be observed. The absorption was relatively low, yielding a reflectance around 80 %.

Besides the full calculations, a coupled oscillator model [131] which describes the interaction of stacked resonant layers was capable of describing all far-field coupling effects. This model gives an analytical description by incorporating all the oscillator polarizabilities and the propagation phases between them.

The understanding of the mechanisms which govern the achievable width of the photonic band gap can be approached from two different directions. On the one hand, a dephasing length can be introduced, which yields a maximum number of oscillators that are able to couple. On the other hand the ultimate width for an infinite structure can be calculated. Both points of view were compared to numerical results yielding a reasonable agreement.

Even though all calculations were implemented using extended nanowires, the transferability of the results to different plasmonic building blocks such as cut-wires, nanodiscs or even more complex ones is straightforward. In the far-field regime the key parameters are resonance position and spectral width. The straightforward tunability of the oscillators, which is not available for atoms, quantum wells, or quantum dots, allows for a flexible and easy tailoring of functional structures.

Finally, the intermediate regime of plasmonic coupling was examined. In this regime neither the near- nor the far-field approximation is valid. A plasmonic dipole cut-wire was stacked on top of a cut-wire pair forming a quadrupolar oscillator. This arrangement mimics the coupling of a bright (dipolar) transition to a dark (quadrupolar) transition, yielding the plasmonic analog of electromagnetically induced

transparency. By increasing the space between both oscillators an additional phase was imposed onto the system which changes the relative phases between the oscillators from a destructive to a constructive interference, thus yielding an enhanced absorption instead of transmission. Consequently, the effect is termed the classical analog of electromagnetically induced absorption. Both, near- as well as far-field effects have to be present to achieve this: In the near-field regime the quasistatic fields would not be able to mediate a retarded interaction, in the far-field regime a coupling between dipolar and quadrupolar oscillator would not be possible, as the quadrupolar oscillator does not couple to the radiation field.

Beyond the work presented here, several perspectives open up: First of all, future work has to address the extension from coupling in purely plasmonic to coupling in hybrid systems incorporating emitters of different types. In these terms, the coupling to quantum emitters such as quantum wells and quantum dots or dye molecules [317] would yield a multitude of possibilities. The far-field coupling scheme might be feasible to mediate, and thus enhance the coupling of quantum emitters to the radiation field [318]. Defects in Bragg stacks could be utilized to obtain high-$Q$ localized modes within the photonic band gap region [319]. In combination with the effortless tunability of the oscillators this potentially might be useful for novel filters, resonant cavities [221, 258, 259, 320], plasmonic distributed gain schemes [321], or spaser concepts [322]. To do so, a deeper understanding of the dispersion characteristics of the Bragg stacked multilayer structure would prove useful. A first step towards this would be the investigation of the response under oblique incidence illumination and the generalization to a three-dimensional photonic band gap.

Using plasmonic far-field coupling of *optical nanoantennas* for the realization of optical interconnects as described by Alù and Engheta [98] is tempting. Optimized building blocks such as Yagi-Uda antennas [10, 77] on the emitter and receiver side would greatly improve the coupling efficiency. A prerequisite for this, however, is the availability of schemes for the local excitation and detection of radiation in single structures. A final long-term objective would be the coupling between two quantum emitters mediated via plasmonic nanoantennas on the emitter as well as receiver side.

The research area of *metamaterials* has undergone a paradigm shift from subwavelength effective media towards tailored structures with

specific functionalities [323]. While in the former far-field coupling was not possible by definition, the latter would allow for incorporation of far-field coupling effects for the design of functional structures.

The dimer structure with lateral shift could be useful for *plasmonic sensing*, as it features a Fano resonance with steep slope. The implementation would demand for a reliable fabrication technique for very small stacking distances. Besides this, a further optimization of the structure could improve the sensitivity.

The concept of coupling in the intermediate regime introduces an additional tuning parameter into the design of structures. This could prove useful to achieve tailored phase relations between oscillators. While several schemes have been proposed which make use of a strong detuning of the oscillators to harness the excitation phase change across the resonance [185, 324], in the intermediate coupling regime this can be achieved for non-detuned oscillators.

Finally, still one uncharted territory remains in the field of plasmonic coupling: For ever decreasing distance between particles, at some point classical electrodynamics should become invalid due to the occurrence of quantum effects. Down to approximately 1 nm surface-to-surface distance, no quantum effects could be observed [14]. The exploration of this region requires a strong improvement of both, experimental techniques as well as theoretical concepts which is an exciting challenge for the years ahead.

$\sim$

# A

## A.1 SPHERICAL BESSEL AND HANKEL FUNCTIONS, ASSOCIATED LEGENDRE FUNCTIONS

The spherical Bessel and Hankel functions are defined as [325]:

$$j_n(x) = \sqrt{\frac{\pi}{2x}} J_{n+1/2}(x) \tag{A.1a}$$

$$y_n(x) = \sqrt{\frac{\pi}{2x}} J_{-n-1/2}(x) \tag{A.1b}$$

$$h_n^{(1)}(x) = j_n(x) + i y_n(x) \tag{A.1c}$$

$$h_n^{(2)}(x) = j_n(x) - i y_n(x). \tag{A.1d}$$

Here $J_n(x)$ denotes the Bessel function of the first kind which is given by

$$J_n(x) = \sum_{s=0}^{\infty} \frac{(-1)^s}{s!(n+s)!} \left(\frac{x}{2}\right)^{n+2s}. \tag{A.2}$$

The associated Legendre functions are defined as [325]:

$$P_n^m(x) = (1 - x^2)^{m/2} \frac{\partial^m}{\partial x^m} P_n(x), \tag{A.3}$$

where the $P_n(x)$ are the Legendre polynomials [288]

$$P_n(x) = \frac{1}{2^n n!} \frac{\partial^n}{\partial x^n} (x^2 - 1)^n. \tag{A.4}$$

## A.2 DISCUSSION OF THE ARCTANGENT FUNCTION

As the tangent is a $\pi$-periodic function with a range of $(-\infty, \infty)$, its inverse, the arc tangent, is defined for all real values with a range of $(-\pi/2, \pi/2)$. It is antisymmetric, $\arctan(-x) = -\arctan(x)$, and continuous over the whole domain.

It is a peculiarity of the arc tangent function that inverting its argument only yields a sign flip and a constant offset, i. e.,

$$\arctan(x) = -\arctan\left(\frac{1}{x}\right) + C.$$

This can be immediately conferred from the derivatives:

$$\frac{\partial}{\partial x}\left(-\arctan\left(\frac{1}{x}\right)\right) = -\frac{\left(-\frac{1}{x^2}\right)}{1 + \left(\frac{1}{x}\right)^2} = \frac{1}{1 + x^2} = \frac{\partial}{\partial x}\arctan(x).$$

As these are identical, on each domain the functions can differ only by a constant $C$, which is obtained by direct evaluation, setting $x = \pm 1$:

$$C - \arctan(1) = \arctan(1) \quad \Rightarrow C = 2\arctan(1) = \frac{\pi}{2}$$

$$C - \arctan(-1) = \arctan(-1) \quad \Rightarrow C = 2\arctan(-1) = -\frac{\pi}{2}.$$

Thus, we can write

$$\arctan(x) = \begin{cases} \dfrac{\pi}{2} - \arctan\left(\dfrac{1}{x}\right) & x > 0 \\[3mm] -\dfrac{\pi}{2} - \arctan\left(\dfrac{1}{x}\right) & x < 0. \end{cases} \tag{A.5}$$

As the situation in section 4.7 is $\pi$-periodic anyway, the differing $C$ for different signs of $x$ is incorporated into the mode number $M$ and therefore does not matter.

A.3    DISCUSSION OF SINGLE LAYER REFLECTANCE IN THE ANALYTICAL COUPLING MODEL

From the analytical model introduced by eqs. 2.66 and 2.67 the reflection amplitude for a single layer located at $z = 0$ is obtained as[i]

$$\mathfrak{r}(E) = \frac{i\chi(E)}{1 - i\chi(E)} \tag{A.6}$$

$$\mathfrak{t}(E) = 1 + \mathfrak{r}(E).$$

---

i  The factor $k/(2\varepsilon_{\mathrm{Sp}})$ is omitted and included into $\chi(E)$.

This can be evaluated using the susceptibility of the harmonic oscillator model given in eq. 2.30, yielding

$$\mathfrak{r}(\omega) = -\frac{i\Gamma_{\mathrm{o}}}{\omega - \omega_{\mathrm{PPR}} + i(\Gamma_{\mathrm{o}} + \Gamma)}, \tag{A.7}$$

which shows, that the linewidth of the acquired reflectance is increased by the radiative coupling strength $\Gamma_{\mathrm{o}}$. Calculation of the reflectance $R = |\mathfrak{r}|^2$ from this yields

$$R(\omega) = \frac{\Gamma_{\mathrm{o}}^2}{(\omega - \omega_{\mathrm{PPR}})^2 + (\Gamma_{\mathrm{o}} + \Gamma)^2}. \tag{A.8}$$

This allows to retrieve the oscillator parameters $\omega_{\mathrm{PPR}}$, $\Gamma_{\mathrm{o}}$, and $\Gamma$ from a reflectance measurement. Obviously, the maximum reflectance occurs for $\omega = \omega_{\mathrm{PPR}}$. Its absolute value $R_{\mathrm{max}}$ is

$$R_{\mathrm{max}} = R(\omega_{\mathrm{PPR}}) = \left(\frac{\Gamma_{\mathrm{o}}}{\Gamma_{\mathrm{o}} + \Gamma}\right)^2.$$

Furthermore, the condition $R(\omega) = R_{\mathrm{max}}/2$ is found for $\omega = \omega_{\mathrm{PPR}} \pm (\Gamma_{\mathrm{o}} + \Gamma)$, therefore the full width at half maximum is FWHM $= 2(\Gamma_{\mathrm{o}} + \Gamma)$. Both values, can be retrieved from the reflectance data which yields the parameters

$$\begin{aligned} \Gamma_{\mathrm{o}} &= \frac{\mathrm{FWHM}}{2}\sqrt{R_{\mathrm{max}}} \\ \Gamma &= \frac{\mathrm{FWHM}}{2}\left(1 - \sqrt{R_{\mathrm{max}}}\right). \end{aligned} \tag{A.9}$$

## A.4 CALCULATION OF THE INVERSE COUPLING MATRIX

Here, the inverse of the $N \times N$ dimensional matrix introduced in section 5.5.1 with elements

$$\mathcal{A}_{mn} = \delta_{mn} - (-1)^{m+n}\eta$$

is calculated for arbitrary $N$. To calculate the inverse, Gauss-Jordan elimination is applied to the matrix $(\mathcal{A}|\mathcal{I})$ with the $N \times N$ dimensional unit matrix $\mathcal{I}$, as

$$(\mathcal{A}|\mathcal{I}) \cdot \mathcal{A}^{-1} = (\mathcal{I}|\mathcal{A}^{-1}).$$

The initial scheme reads

| $1-\eta$ | $\eta$ | $-\eta$ | $\eta$ | $\cdots$ | $\mp\eta$ | $\pm\eta$ | 1 | 0 | 0 | 0 | $\cdots$ | 0 | 0 |
|---|---|---|---|---|---|---|---|---|---|---|---|---|---|
| $\eta$ | $1-\eta$ | $\eta$ | $-\eta$ | $\cdots$ | $\pm\eta$ | $\mp\eta$ | 0 | 1 | 0 | 0 | $\cdots$ | 0 | 0 |
| $-\eta$ | $\eta$ | $1-\eta$ | $\eta$ | $\cdots$ | $\mp\eta$ | $\pm\eta$ | 0 | 0 | 1 | 0 | $\cdots$ | 0 | 0 |
| $\vdots$ | $\vdots$ | $\vdots$ | $\vdots$ | $\ddots$ | $\vdots$ | $\vdots$ | $\vdots$ | $\vdots$ | $\vdots$ | $\vdots$ | $\ddots$ | $\vdots$ | $\vdots$ |
| $\mp\eta$ | $\pm\eta$ | $\mp\eta$ | $\pm\eta$ | $\cdots$ | $1-\eta$ | $\eta$ | 0 | 0 | 0 | 0 | $\cdots$ | 1 | 0 |
| $\pm\eta$ | $\mp\eta$ | $\pm\eta$ | $\mp\eta$ | $\cdots$ | $\eta$ | $1-\eta$ | 0 | 0 | 0 | 0 | $\cdots$ | 0 | 1 |

Due to the special values of the components, it is possible to obtain a triangular matrix, where only the diagonal elements and the last column are non-zero for the first $N-1$ rows by subsequent addition and subtraction of row $m+1$ to row $m$, whereas the last, $N$th row is kept unchanged. This yields

| 1 | 0 | 0 | 0 | $\cdots$ | 0 | $\pm1$ | 1 | 0 | 0 | 0 | $\cdots$ | 0 | $\pm1$ |
|---|---|---|---|---|---|---|---|---|---|---|---|---|---|
| 0 | 1 | 0 | 0 | $\cdots$ | 0 | $\mp1$ | 0 | 1 | 0 | 0 | $\cdots$ | 0 | $\mp1$ |
| 0 | 0 | 1 | 0 | $\cdots$ | 0 | $\pm1$ | 0 | 0 | 1 | 0 | $\cdots$ | 0 | $\pm1$ |
| $\vdots$ | $\vdots$ | $\vdots$ | $\vdots$ | $\ddots$ | $\vdots$ | $\vdots$ | $\vdots$ | $\vdots$ | $\vdots$ | $\vdots$ | $\ddots$ | $\vdots$ | $\vdots$ |
| 0 | 0 | 0 | 0 | $\cdots$ | 1 | 1 | 0 | 0 | 0 | 0 | $\cdots$ | 1 | 1 |
| $\pm\eta$ | $\mp\eta$ | $\pm\eta$ | $\mp\eta$ | $\cdots$ | $\eta$ | $1-\eta$ | 0 | 0 | 0 | 0 | $\cdots$ | 0 | 1 |

To eliminate the last line, all but the last row have to be multiplied by $\mp\eta$ and added to the last line. The last column deserves special attention. The signs in row $m$ of this column exactly correspond to those of $\eta$ in the $m$th column of the last row. This leads to the appearance of the factor $N$ in the bottom right entry.

| $\vdots$ | $\vdots$ | $\vdots$ | $\vdots$ | $\ddots$ | $\vdots$ | $\vdots$ | $\vdots$ | $\vdots$ | $\vdots$ | $\vdots$ | $\ddots$ | $\vdots$ | $\vdots$ |
|---|---|---|---|---|---|---|---|---|---|---|---|---|---|
| 0 | 0 | 0 | 0 | $\cdots$ | 0 | $1-N\eta$ | $\mp\eta$ | $\pm\eta$ | $\mp\eta$ | $\pm\eta$ | $\cdots$ | $\eta$ | $1-(N-1)\eta$ |

To obtain the unity matrix on the left side, the last row has to be divided by $1-N\eta$ and added to all rows above in order to eliminate the last column. This yields the final inverse matrix on the right side:

$$
\left(
\begin{array}{cccc}
1 & 0 & 0 & \cdots \\
0 & 1 & 0 & \cdots \\
0 & 0 & 1 & \cdots \\
\vdots & \vdots & \vdots & \ddots
\end{array}
\right|
\left.
\begin{array}{cccccc}
1 + \frac{\eta}{1-N\eta} & -\frac{\eta}{1-N\eta} & +\frac{\eta}{1-N\eta} & \cdots & \pm\frac{\eta}{1-N\eta} & \mp\frac{\eta}{1-N\eta} \\
-\frac{\eta}{1-N\eta} & 1+\frac{\eta}{1-N\eta} & -\frac{\eta}{1-N\eta} & \cdots & \mp\frac{\eta}{1-N\eta} & \pm\frac{\eta}{1-N\eta} \\
+\frac{\eta}{1-N\eta} & -\frac{\eta}{1-N\eta} & 1+\frac{\eta}{1-N\eta} & \cdots & \pm\frac{\eta}{1-N\eta} & \mp\frac{\eta}{1-N\eta} \\
\vdots & \vdots & \vdots & \ddots & \vdots & \vdots \\
\pm\frac{\eta}{1-N\eta} & \mp\frac{\eta}{1-N\eta} & \pm\frac{\eta}{1-N\eta} & \cdots & 1+\frac{\eta}{1-N\eta} & -\frac{\eta}{1-N\eta} \\
\mp\frac{\eta}{1-N\eta} & \pm\frac{\eta}{1-N\eta} & \mp\frac{\eta}{1-N\eta} & \cdots & -\frac{\eta}{1-N\eta} & \frac{1-(N-1)\eta}{1-N\eta}
\end{array}
\right)
$$

The final inverse matrix can straightforwardly be expressed component-wise, which yields

$$
\mathcal{A}_{mn}^{-1} = \delta_{mn} + (-1)^{m+n}\frac{\eta}{1-N\eta}. \tag{A.10}
$$

## A.5   MANIPULATABLE PLOT OF EIA OSCILLATOR MODEL

To investigate the properties of the EIA oscillator model, the differential equations can be solved in Mathematica by using the following input:

```
Exit []

f[kappa_,phi_] := x1 /. Solve[{
     - omega^2 x1 - I omega gamma1 x1
     + omega1^2 x1 + kappa Exp[I*phi] x2 == Eext,
     - omega^2 x2 - I omega gamma2 x2
     + omega2^2 x2 + kappa Exp[I*phi] x1 == 0
   }, x1, {x2 }][[1]]

omega2 = omega1 = 1;
Eext = 1;
gamma2 = 0.03;
gamma1 = 0.1;

Manipulate[
     Plot[Im[f[kappa,phi ]],{ omega ,0,2}, PlotRange -> All ],
     {{kappa ,0.07},0,0.5},{ phi ,0,3.141}]
```

$\sim$

[14]     H. Duan, A. I. Fernández-Domínguez, M. Bosman,
         S. A. Maier, and J. K. W. Yang: *Nanoplasmonics: Classical
         down to the nanometer scale*, Nano Lett. **12**, 1683–1689, (2012),
         DOI 10.1021/nl3001309, (cit. on pp. 1, 47, 144).

[15]     U. Kreibig and M. Vollmer: *Optical properties of metal clusters*,
         1st ed., Berlin, Heidelberg, New York: Springer, 1995, (cit. on
         pp. 1, 17).

[16]     I. Freestone, N. Meeks, M. Sax, and C. Higgitt: *The Lycurgus
         cup – A Roman nanotechnology*, Gold Bull. **40**, 270–277,
         (2007), DOI 10.1007/BF03215599, (cit. on p. 1).

[17]     M. Faraday: *The Bakerian lecture: Experimental relations of
         gold (and other metals) to light*, Phil. Trans. R. Soc. London **147**,
         145–181, (1857), http://www.jstor.org/stable/108616, (cit. on p. 1).

[18]     R. W. Wood: *On a remarkable case of uneven distribution of
         light in a diffraction grating spectrum*, P. R. Soc. London **18**,
         269–275, (1902), DOI 10.1088/1478-7814/18/1/325, (cit. on pp. 1, 57).

[19]     J. W. Strutt: *XV. On the light from the sky, its polarization and
         colour*, Philos. Mag. 4 **41**, 107–120, (1871),
         http://www.tandfonline.com/doi/abs/10.1080/14786447108640452, (cit. on
         pp. 1, 26).

[20]     J. W. Strutt: *XXXVI. On the light from the sky, its polarization
         and colour*, Philos. Mag. 4 **41**, 274–279, (1871),
         http://www.tandfonline.com/doi/abs/10.1080/14786447108640479, (cit. on
         pp. 1, 26).

[21]     L. Rayleigh: *On the dynamical theory of gratings*, P. R. Soc.
         London A **79**, 399–416, (1907), DOI 10.1098/rspa.1907.0051, (cit. on
         pp. 1, 57).

[22]     G. Mie: *Beiträge zur Optik trüber Medien, speziell kolloidaler
         Metalllösungen*, Ann. Phys. **330**, 377–445, (1908),
         DOI 10.1002/andp.19083300302, (cit. on pp. 1, 22).

[23]     D. Bohm and D. Pines: *A collective description of electron
         interactions. I. Magnetic interactions*, Phys. Rev. **82**, 625–634,
         (1951), DOI 10.1103/PhysRev.82.625, (cit. on p. 1).

[24]    D. Pines and D. Bohm: *A collective description of electron interactions: II. Collective vs. individual particle aspects of the interactions*, Phys. Rev. **85**, 338–353, (1952), DOI 10.1103/PhysRev.85.338, (cit. on p. 1).

[25]    D. Bohm and D. Pines: *A collective description of electron interactions: III. Coulomb interactions in a degenerate electron gas*, Phys. Rev. **92**, 609–625, (1953), DOI 10.1103/PhysRev.92.609, (cit. on p. 1).

[26]    R. H. Ritchie: *Plasma losses by fast electrons in thin films*, Phys. Rev. **106**, 874–881, (1957), DOI 10.1103/PhysRev.106.874, (cit. on pp. 1, 21).

[27]    A. Sommerfeld: *Über die Fortpflanzung elektrodynamischer Wellen längs eines Drahtes*, Ann. Phys. **303**, 233–290, (1899), DOI 10.1002/andp.18993030202, (cit. on p. 2).

[28]    J. Zenneck: *Über die Fortpflanzung ebener elektromagnetischer Wellen längs einer ebenen Leiterfläche und ihre Beziehung zur drahtlosen Telegraphie*, Ann. Phys. **328**, 846–866, (1907), DOI 10.1002/andp.19073281003, (cit. on p. 2).

[29]    A. Otto: *Excitation of nonradiative surface plasma waves in silver by the method of frustrated total reflection*, Z. Phys. A **216**, 398–410, (1968), DOI 10.1007/BF01391532, (cit. on pp. 2, 21).

[30]    E. Kretschmann and H. Raether: *Radiative decay of non radiative surface plasmons excited by light*, Z. Phys. A **23**, 2135–2136, (1968), (cit. on pp. 2, 21).

[31]    Y.-H. Liau, A. N. Unterreiner, Q. Chang, and N. F. Scherer: *Ultrafast dephasing of single nanoparticles studied by two-pulse second-order interferometry*, J. Phys. Chem. B **105**, 2135–2142, (2001), DOI 10.1021/jp002831x, (cit. on p. 2).

[32]    J. R. Krenn, G. Schider, W. Rechberger, B. Lamprecht, A. Leitner, F. R. Aussenegg, and J. C. Weeber: *Design of multipolar plasmon excitations in silver nanoparticles*, Appl. Phys. Lett. **77**, 3379–3381, (2000), DOI 10.1063/1.1327615, (cit. on p. 2).

[33]  C. Sönnichsen, S. Geier, N. E. Hecker, G. von Plessen,
      J. Feldmann, H. Ditlbacher, B. Lamprecht, J. R. Krenn,
      F. R. Aussenegg, V. Z.-H. Chan, J. P. Spatz, and M. Möller:
      *Spectroscopy of single metallic nanoparticles using total internal
      reflection microscopy*, Appl. Phys. Lett. **77**, 2949–2951, (2000),
      DOI 10.1063/1.1323553, (cit. on p. 2).

[34]  F. Stietz, J. Bosbach, T. Wenzel, T. Vartanyan, A. Goldmann,
      and F. Träger: *Decay times of surface plasmon excitation in
      metal nanoparticles by persistent spectral hole burning*, Phys.
      Rev. Lett. **84**, 5644–5647, (2000), DOI 10.1103/PhysRevLett.84.5644,
      (cit. on p. 2).

[35]  M. Perner, S. Gresillon, J. März, G. von Plessen, J. Feldmann,
      J. Porstendorfer, K.-J. Berg, and G. Berg: *Observation of
      hot-electron pressure in the vibration dynamics of metal
      nanoparticles*, Phys. Rev. Lett. **85**, 792–795, (2000),
      DOI 10.1103/PhysRevLett.85.792, (cit. on p. 2).

[36]  S. Grésillon, L. Aigouy, A. C. Boccara, J. C. Rivoal, X. Quelin,
      C. Desmarest, P. Gadenne, V. Shubin, A. K. Sarychev, and
      V. M. Shalaev: *Experimental observation of localized optical
      excitations in random metal-dielectric films*, Phys. Rev. Lett. **82**,
      4520–4523, (1999), DOI 10.1103/PhysRevLett.82.4520, (cit. on p. 2).

[37]  B. Lamprecht, J. R. Krenn, A. Leitner, and F. R. Aussenegg:
      *Resonant and off-resonant light-driven plasmons in metal
      nanoparticles studied by femtosecond-resolution
      third-harmonic generation*, Phys. Rev. Lett. **83**, 4421–4424,
      (1999), DOI 10.1103/PhysRevLett.83.4421, (cit. on p. 2).

[38]  T. Klar, M. Perner, S. Grosse, G. von Plessen, W. Spirkl, and
      J. Feldmann: *Surface-plasmon resonances in single metallic
      nanoparticles*, Phys. Rev. Lett. **80**, 4249–4252, (1998),
      DOI 10.1103/PhysRevLett.80.4249, (cit. on p. 2).

[39]  A. F. Koenderink, R. de Waele, J. C. Prangsma, and A. Polman:
      *Experimental evidence for large dynamic effects on the plasmon
      dispersion of subwavelength metal nanoparticle waveguides*,
      Phys. Rev. B **76**, 201403(R)–4, (2007),
      DOI 10.1103/PhysRevB.76.201403, (cit. on p. 2).

[40]  R. de Waele, A. F. Koenderink, and A. Polman: *Tunable nanoscale localization of energy on plasmon particle arrays*, Nano Lett. **7**, 2004–2008, (2007), DOI 10.1021/nl070807q, (cit. on p. 2).

[41]  A. F. Koenderink and A. Polman: *Complex response and polariton-like dispersion splitting in periodic metal nanoparticle chains*, Phys. Rev. B **74**, 033402–4, (2006), DOI 10.1103/PhysRevB.74.033402, (cit. on p. 2).

[42]  M. Salerno, J. R. Krenn, A. Hohenau, H. Ditlbacher, G. Schider, A. Leitner, and F. R. Aussenegg: *The optical near-field of gold nanoparticle chains*, Opt. Commun. **248**, 543–549, (2005), DOI 10.1016/j.optcom.2004.12.023, (cit. on p. 2).

[43]  Q.-H. Wei, K.-H. Su, S. Durant, and X. Zhang: *Plasmon resonance of finite one-dimensional Au nanoparticle chains*, Nano Lett. **4**, 1067–1071, (2004), DOI 10.1021/nl049604h, (cit. on p. 2).

[44]  S. A. Maier, P. G. Kik, H. A. Atwater, S. Meltzer, E. Harel, B. E. Koel, and A. A. G. Requicha: *Local detection of electromagnetic energy transport below the diffraction limit in metal nanoparticle plasmon waveguides*, Nat. Mater. **2**, 229–232, (2003), DOI 10.1038/nmat852, (cit. on p. 2).

[45]  S. A. Maier, M. L. Brongersma, P. G. Kik, and H. A. Atwater: *Observation of near-field coupling in metal nanoparticle chains using far-field polarization spectroscopy*, Phys. Rev. B **65**, 193408–4, (2002), DOI 10.1103/PhysRevB.65.193408, (cit. on p. 2).

[46]  S. A. Maier, P. G. Kik, and H. A. Atwater: *Observation of coupled plasmon-polariton modes in Au nanoparticle chain waveguides of different lengths: Estimation of waveguide loss*, Appl. Phys. Lett. **81**, 1714–1716, (2002), DOI 10.1063/1.1503870, (cit. on p. 2).

[47]  M. L. Brongersma, J. W. Hartman, and H. A. Atwater: *Electromagnetic energy transfer and switching in nanoparticle chain arrays below the diffraction limit*, Phys. Rev. B **62**, R16356–R16359, (2000), DOI 10.1103/PhysRevB.62.R16356, (cit. on p. 2).

[48]  J. Krenn, A. Dereux, J. C. Weeber, E. Bourillot, Y. Lacroute,
      J. P. Goudonnet, G. Schider, W. Gotschy, A. Leitner,
      F. R. Aussenegg, and C. Girard: *Squeezing the optical near-field
      zone by plasmon coupling of metallic nanoparticles*, Phys. Rev.
      Lett. **82**, 2590–2593, (1999), DOI 10.1103/PhysRevLett.82.2590, (cit. on
      p. 2).

[49]  M. Quinten, A. Leitner, J. R. Krenn, and F. R. Aussenegg:
      *Electromagnetic energy transport via linear chains of silver
      nanoparticles*, Opt. Lett. **23**, 1331–1333, (1998),
      DOI 10.1364/OL.23.001331, (cit. on p. 2).

[50]  E. Ozbay: *Plasmonics: Merging photonics and electronics at
      nanoscale dimensions*, Science **311**, 189–193, (2006),
      DOI 10.1126/science.1114849, (cit. on p. 2).

[51]  V. G. Veselago: *The electrodynamics of substances with
      simultaneously negative values of ε and μ*, Sov. Phys.
      Uspekhi **10**, 509–514, (1968),
      DOI 10.1070/PU1968v010n04ABEH003699, (cit. on p. 2).

[52]  J. B. Pendry: *Negative refraction makes a perfect lens*, Phys.
      Rev. Lett. **85**, 3966–3969, (2000), DOI 10.1103/PhysRevLett.85.3966,
      (cit. on p. 2).

[53]  J. B. Pendry, D. Schurig, and D. R. Smith: *Controlling
      electromagnetic fields*, Science **312**, 1780–1782, (2006),
      DOI 10.1126/science.1125907, (cit. on p. 2).

[54]  U. Leonhardt: *Optical conformal mapping*, Science **312**,
      1777–1780, (2006), DOI 10.1126/science.1126493, (cit. on p. 2).

[55]  D. Schurig, J. J. Mock, B. J. Justice, S. A. Cummer, J. B. Pendry,
      A. F. Starr, and D. R. Smith: *Metamaterial electromagnetic
      cloak at microwave frequencies*, Science **314**, 977–980, (2006),
      DOI 10.1126/science.1133628, (cit. on p. 2).

[56]  D. R. Smith, J. B. Pendry, and M. C. K. Wiltshire:
      *Metamaterials and negative refractive index*, Science **305**,
      788–792, (2004), DOI 10.1126/science.1096796, (cit. on p. 2).

[57]  R. A. Shelby, D. R. Smith, and S. Schultz: *Experimental
      verification of a negative index of refraction*, Science **292**,
      77–79, (2001), DOI 10.1126/science.1058847, (cit. on p. 2).

[58]   D. R. Smith, W. J. Padilla, D. C. Vier, S. C. Nemat-Nasser, and
       S. Schultz: *Composite medium with simultaneously negative
       permeability and permittivity*, Phys. Rev. Lett. **84**, 4184–4187,
       (2000), DOI 10.1103/PhysRevLett.84.4184, (cit. on p. 2).

[59]   C. Rockstuhl, F. Lederer, C. Etrich, T. Zentgraf, J. Kuhl, and
       H. Giessen: *On the reinterpretation of resonances in
       split-ring-resonators at normal incidence*, Opt. Express **14**,
       8827–8836, (2006), DOI 10.1364/OE.14.008827, (cit. on p. 2).

[60]   T. Ergin, N. Stenger, P. Brenner, J. B. Pendry, and M. Wegener:
       *Three-dimensional invisibility cloak at optical wavelengths*,
       Science **328**, 337–339, (2010), DOI 10.1126/science.1186351, (cit. on
       p. 2).

[61]   J. Valentine, S. Zhang, T. Zentgraf, E. Ulin-Avila, D. A. Genov,
       G. Bartal, and X. Zhang: *Three-dimensional optical
       metamaterial with a negative refractive index*, Nature **455**,
       376–379, (2008), DOI 10.1038/nature07247, (cit. on p. 2).

[62]   G. Dolling, M. Wegener, C. M. Soukoulis, and S. Linden:
       *Negative-index metamaterial at 780 nm wavelength*, Opt.
       Lett. **32**, 53–55, (2007), DOI 10.1364/OL.32.000053, (cit. on p. 2).

[63]   G. Shvets and Y. A. Urzhumov: *Negative index meta-materials
       based on two-dimensional metallic structures*, J. Opt. A **8**,
       S122–S130, (2006), DOI 10.1088/1464-4258/8/4/S11, (cit. on p. 2).

[64]   C. Enrich, M. Wegener, S. Linden, S. Burger, L. Zschiedrich,
       F. Schmidt, J. F. Zhou, T. Koschny, and C. M. Soukoulis:
       *Magnetic metamaterials at telecommunication and visible
       frequencies*, Phys. Rev. Lett. **95**, 203901–4, (2005),
       DOI 10.1103/PhysRevLett.95.203901, (cit. on p. 2).

[65]   S. Zhang, W. Fan, K. J. Malloy, S. R. Brueck, N. C. Panoiu, and
       R. M. Osgood: *Near-infrared double negative metamaterials*,
       Opt. Express **13**, 4922–4930, (2005), DOI 10.1364/OPEX.13.004922,
       (cit. on p. 2).

[66]   S. Linden, C. Enrich, M. Wegener, J. F. Zhou, T. Koschny,
       and C. M. Soukoulis: *Magnetic response of metamaterials at
       100 Terahertz*, Science **306**, 1351–1353, (2004),
       DOI 10.1126/science.1105371, (cit. on p. 2).

[67]    T. J. Yen, W. J. Padilla, N. Fang, D. C. Vier, D. R. Smith,
        J. B. Pendry, D. N. Basov, and X. Zhang: *Terahertz magnetic
        response from artificial materials*, Science **303**, 1494–1496,
        (2004), DOI 10.1126/science.1094025, (cit. on p. 2).

[68]    C. M. Soukoulis, S. Linden, and M. Wegener: *Negative
        refractive index at optical wavelengths*, Science **315**, 47–49,
        (2007), DOI 10.1126/science.1136481, (cit. on pp. 3, 60).

[69]    P. Ghenuche, S. Cherukulappurath, T. H. Taminiau,
        N. F. van Hulst, and R. Quidant: *Spectroscopic mode mapping
        of resonant plasmon nanoantennas*, Phys. Rev. Lett. **101**,
        116805–4, (2008), DOI 10.1103/PhysRevLett.101.116805, (cit. on p. 3).

[70]    L. Novotny: *Effective wavelength scaling for optical antennas*,
        Phys. Rev. Lett. **98**, 266802–4, (2007),
        DOI 10.1103/PhysRevLett.98.266802, (cit. on p. 3).

[71]    P. Mühlschlegel, H.-J. Eisler, O. J. F. Martin, B. Hecht, and
        D. W. Pohl: *Resonant optical antennas*, Science **308**, 1607–1609,
        (2005), DOI 10.1126/science.1111886, (cit. on p. 3).

[72]    V. Giannini, A. I. Fernández-Domínguez, S. C. Heck, and
        S. A. Maier: *Plasmonic nanoantennas: Fundamentals and their
        use in controlling the radiative properties of nanoemitters*,
        Chem. Rev. **111**, 3888–3912, (2011), DOI 10.1021/cr1002672, (cit. on
        p. 3).

[73]    P. J. Schuck, D. P. Fromm, A. Sundaramurthy, G. S. Kino, and
        W. E. Moerner: *Improving the mismatch between light and
        nanoscale objects with gold bowtie nanoantennas*, Phys. Rev.
        Lett. **94**, 017402–4, (2005), DOI 10.1103/PhysRevLett.94.017402,
        (cit. on p. 3).

[74]    P. Anger, P. Bharadwaj, and L. Novotny: *Enhancement and
        quenching of single-molecule fluorescence*, Phys. Rev. Lett. **96**,
        113002–4, (2006), DOI 10.1103/PhysRevLett.96.113002, (cit. on p. 3).

[75]    S. Kühn, U. Håkanson, L. Rogobete, and V. Sandoghdar:
        *Enhancement of single-molecule fluorescence using a gold
        nanoparticle as an optical nanoantenna*, Phys. Rev. Lett. **97**,
        017402–4, (2006), DOI 10.1103/PhysRevLett.97.017402, (cit. on p. 3).

[76]    E. M. Purcell: *Spontaneous emission probabilities at radio
        frequencies*, Phys. Rev. **69**, 681, (1946), (cit. on p. 3).

[77]    T. Kosako, Y. Kadoya, and H. F. Hofmann: *Directional control of light by a nano-optical Yagi-Uda antenna*, Nat. Photonics **4**, 312–315, (2010), DOI 10.1038/nphoton.2010.34, (cit. on pp. 3, 143).

[78]    T. H. Taminiau, F. D. Stefani, F. B. Segerink, and N. F. van Hulst: *Optical antennas direct single-molecule emission*, Nat. Photonics **2**, 234–237, (2008), DOI 10.1038/nphoton.2008.32, (cit. on p. 3).

[79]    A. G. Curto, G. Volpe, T. H. Taminiau, M. P. Kreuzer, R. Quidant, and N. F. van Hulst: *Unidirectional emission of a quantum dot coupled to a nanoantenna*, Science **329**, 930–933, (2010), DOI 10.1126/science.1191922, (cit. on p. 3).

[80]    M. Liu, T.-W. Lee, S. K. Gray, P. Guyot-Sionnest, and M. Pelton: *Excitation of dark plasmons in metal nanoparticles by a localized emitter*, Phys. Rev. Lett. **102**, 107401–4, (2009), DOI 10.1103/PhysRevLett.102.107401, (cit. on p. 3).

[81]    E. Hendry, T. Carpy, J. Johnston, M. Popland, R. V. Mikhaylovskiy, A. J. Lapthorn, S. M. Kelly, L. D. Barron, N. Gadegaard, and M. Kadodwala: *Ultrasensitive detection and characterization of biomolecules using superchiral fields.* Nat. Nanotechnol. **5**, 783–787, (2010), DOI 10.1038/nnano.2010.209, (cit. on p. 3).

[82]    J. N. Anker, W. P. Hall, O. Lyandres, N. C. Shah, J. Zhao, and R. P. Van Duyne: *Biosensing with plasmonic nanosensors*, Nat. Mater. **7**, 442–453, (2008), DOI 10.1038/nmat2162, (cit. on p. 3).

[83]    S. Lal, S. Link, and N. J. Halas: *Nano-optics from sensing to waveguiding*, Nat. Photonics **1**, 641–648, (2007), DOI 10.1038/nphoton.2007.223, (cit. on p. 3).

[84]    F. Neubrech, A. Pucci, T. W. Cornelius, S. Karim, A. García-Etxarri, and J. Aizpurua: *Resonant plasmonic and vibrational coupling in a tailored nanoantenna for infrared detection*, Phys. Rev. Lett. **101**, 157403–4, (2008), DOI 10.1103/PhysRevLett.101.157403, (cit. on p. 3).

[85]    K. Kneipp, Y. Wang, H. Kneipp, L. T. Perelman, I. Itzkan, R. R. Dasari, and M. S. Feld: *Single molecule detection using surface-enhanced raman scattering (SERS)*, Phys. Rev. Lett. **78**, 1667–1670, (1997), DOI 10.1103/PhysRevLett.78.1667, (cit. on p. 3).

[86] M. Moskovits: *Surface-enhanced spectroscopy*, Rev. Mod. Phys. **57**, 783–826, (1985), DOI 10.1103/RevModPhys.57.783, (cit. on p. 3).

[87] N. Liu, M. L. Tang, M. Hentschel, H. Giessen, and A. P. Alivisatos: *Nanoantenna-enhanced gas sensing in a single tailored nanofocus*, Nat. Mater. **10**, 631–636, (2011), DOI 10.1038/NMAT3029, (cit. on p. 3).

[88] I. Ament, J. Prasad, A. Henkel, S. Schmachtel, and C. Sönnichsen: *Single unlabeled protein detection on individual plasmonic nanoparticles*, Nano Lett. **12**, 1092–1095, (2012), DOI 10.1021/nl204496g, (cit. on p. 3).

[89] P. Zijlstra, P. M. R. Paulo, and M. Orrit: *Optical detection of single non-absorbing molecules using the surface plasmon resonance of a gold nanorod*, Nat. Nanotechnol. AOP 2012/04/15, (2012), DOI 10.1038/nnano.2012.51, (cit. on p. 3).

[90] B. K. Canfield, H. Husu, J. Laukkanen, B. Bai, M. Kuittinen, J. Turunen, and M. Kauranen: *Local field asymmetry drives second-harmonic generation in noncentrosymmetric nanodimers*, Nano Lett. **7**, 1251–1255, (2007), DOI 10.1021/nl0701253, (cit. on p. 3).

[91] M. W. Klein, C. Enkrich, M. Wegener, and S. Linden: *Second-harmonic generation from magnetic metamaterials*, Science **313**, 502–504, (2006), DOI 10.1126/science.1129198, (cit. on p. 3).

[92] S. Kim, J. Jin, Y.-J. Kim, I.-Y. Park, Y. Kim, and S.-W. Kim: *Kim et al. reply*, Nature **485**, E1–E3, (2012), DOI 10.1038/nature10979, (cit. on p. 3).

[93] M. Sivis, M. Duwe, B. Abel, and C. Ropers: *Nanostructure-enhanced atomic line emission*, Nature **485**, E1–E3, (2012), DOI 10.1038/nature10978, (cit. on p. 3).

[94] S. Kim, J. Jin, Y.-J. Kim, I.-Y. Park, Y. Kim, and S.-W. Kim: *High-harmonic generation by resonant plasmon field enhancement*, Nature **453**, 757–760, (2008), DOI 10.1038/nature07012, (cit. on p. 3).

[95]    J. B. Lassiter, H. Sobhani, J. A. Fan, J. Kundu, F. Capasso, P. Nordlander, and N. J. Halas: *Fano resonances in plasmonic nanoclusters: Geometrical and chemical tunability*, Nano Lett. **10**, 3184–3189, (2010), DOI 10.1021/nl102108u, (cit. on pp. 3, 36, 48, 54).

[96]    N. Liu, T. Weiss, M. Mesch, L. Langguth, U. Eigenthaler, M. Hirscher, C. Sönnichsen, and H. Giessen: *Planar metamaterial analogue of electromagnetically induced transparency for plasmonic sensing*, Nano Lett. **10**, 1103–1107, (2010), DOI 10.1021/nl902621d, (cit. on pp. 3, 119–120).

[97]    M. Meier, A. Wokaun, and P. F. Liao: *Enhanced fields on rough surfaces: Dipolar interactions among particles of sizes exceeding the rayleigh limit*, J. Opt. Soc. Am. B **2**, 931–949, (1985), DOI 10.1364/JOSAB.2.000931, (cit. on p. 4).

[98]    A. Alù and N. Engheta: *Wireless at the nanoscale: Optical interconnects using matched nanoantennas*, Phys. Rev. Lett. **104**, 213902–4, (2010), DOI 10.1103/PhysRevLett.104.213902, (cit. on pp. 4, 143).

[99]    A. Christ: *Optical properties of metallic photonic crystal structures*, PhD thesis, Philipps-Universität Marburg, 2005, http://archiv.ub.uni-marburg.de/diss/z2005/0527//view.html, (cit. on pp. 4, 48).

[100]   E. Yablonovitch: *Inhibited spontaneous emission in solid-state physics and electronics*, Phys. Rev. Lett. **58**, 2059–2062, (1987), DOI 10.1103/PhysRevLett.58.2059, (cit. on pp. 4, 94).

[101]   J. D. Jackson: *Classical electrodynamics*, 3rd ed., Hoboken: John Wiley & Sons, 1999, (cit. on pp. 7, 9–11, 27, 55).

[102]   X. Chen, B. I. Wu, J. A. Kong, and T. M. Grzegorczyk: *Retrieval of the effective constitutive parameters of bianisotropic metamaterials*, Phys. Rev. E **71**, 046610–9, (2005), DOI 10.1103/PhysRevE.71.046610, (cit. on p. 7).

[103]   H. Haug and S. W. Koch: *Quantum theory of the optical and electronic properties of semiconductors*, 2nd ed., Singapore: World Scientific, 1993, (cit. on p. 14).

[104]   C. F. Klingshirn: *Semiconductor optics*, 3rd ed., Berlin, Heidelberg: Springer, 2007, (cit. on p. 14).

[105]   L. G. Schulz: *An experimental confirmation of the Drude free electron theory of the optical properties of metals for silver, gold, and copper in the near infrared*, J. Opt. Soc. Am. **44**, 540–545, (1954), DOI 10.1364/JOSA.44.000540, (cit. on pp. 17–18).

[106]   V. G. Padalka and I. N. Shklyarevskii, Opt. Spectroscop. **11**, 285, (1961), (cit. on pp. 17–19).

[107]   G. A. Bolotin, A. N. Voloshinskii, M. M. Kirilbra, M. M. Neskov, A. V. Sokolov, and B. A. Charikov, Fiz. Met. Metalloved. **13**, 823, (1962), (cit. on pp. 17–19).

[108]   B. Dold and R. Mecke: *Optical properties of noble metals, transition metals, and their alloys in the infrared*, Optik **22**, 435, (1965), (cit. on pp. 17–19).

[109]   G. P. Motulevich and A. A. Shubin, Sov. Phys. JETP-USSR **20**, 560, (1965), (cit. on pp. 17–19).

[110]   H. E. Bennett and J. M. Bennett: "Validity of the Drude theory for silver, gold and aluminum in the infrared", in: *Optical Properties and Electronic Structure of Metals and Alloys*, ed. by F. Abelès, Amsterdam: North Holland, 1966, p. 75, (cit. on pp. 17, 19).

[111]   M.-L. Thèye: *Investigation of the optical properties of Au by means of thin semitransparent films*, Phys. Rev. B **2**, 3060–3078, (1970), DOI 10.1103/PhysRevB.2.3060, (cit. on pp. 17–20).

[112]   P. B. Johnson and R. W. Christy: *Optical constants of the noble metals*, Phys. Rev. B **6**, 4370–4379, (1972), DOI 10.1103/PhysRevB.6.4370, (cit. on pp. 17–20, 46, 49, 114).

[113]   H. J. Hagemann, W. Gudat, and C. Kunz: *Optical constants from the far infrared to the x-ray region: Mg, Al, Cu, Ag, Au, Bi, C, and $Al_2O_3$*, J. Opt. Soc. Am. **65**, 742–744, (1975), DOI 10.1364/JOSA.65.000742, (cit. on pp. 17–19).

[114]   J. H. Weaver, C. Krafka, D. W. Lynch, and E. E. Koch, eds.: *Physics data, opt. properties of metals, part 2*, Karlsruhe: Fachinformationszentrum, 1981, (cit. on pp. 17–19).

[115]   R. A. Innes and J. R. Sambles: *Optical characterization of gold using surface plasmon-polaritons*, J. Phys. F **17**, 277–287, (1987), DOI 10.1088/0305-4608/17/1/031, (cit. on pp. 17–19).

[116]   D. W. Lynch and W. R. Hunter: "Handbook of Optical Constants of Solids", in: ed. by E. D. Palik, London: Academic Press, 1985, chap. Subpart 1 - Metals, Comments on the optical constants of metals and an introduction ot the data for several metals, pp. 286–295, (cit. on p. 17).

[117]   M. A. Ordal, L. L. Long, R. J. Bell, S. E. Bell, R. R. Bell, R. W. Alexander, and C. A. Ward: *Optical properties of the metals Al, Co, Cu, Au, Fe, Pb, Ni, Pd, Pt, Ag, Ti, and W in the infrared and far infrared*, Appl. Opt. **22**, 1099–1119, (1983), DOI 10.1364/AO.22.001099, (cit. on pp. 17, 20).

[118]   G. R. Parkins, W. E. Lawrence, and R. W. Christy: *Intraband optical conductivity $\sigma(\omega, T)$ of Cu, Ag, and Au: Contribution from electron-electron scattering*, Phys. Rev. B **23**, 6408–6416, (1981), DOI 10.1103/PhysRevB.23.6408, (cit. on p. 20).

[119]   P. G. Etchegoin, E. C. Le Ru, and M. Meyer: *An analytic model for the optical properties of gold*, J. Chem. Phys. **125**, 164705–3, (2006), DOI 10.1063/1.2360270, (cit. on p. 20).

[120]   A. D. Rakic, A. B. Djurišic, J. M. Elazar, and M. L. Majewski: *Optical properties of metallic films for vertical-cavity optoelectronic devices*, Appl. Opt. **37**, 5271–5283, (1998), DOI 10.1364/AO.37.005271, (cit. on p. 20).

[121]   W. L. Barnes, A. Dereux, and T. W. Ebbesen: *Surface plasmon subwavelength optics*, Nature **424**, 824–830, (2003), DOI 10.1038/nature01937, (cit. on p. 21).

[122]   J. Homola, S. S. Yee, and G. Gauglitz: *Surface plasmon resonance sensors: Review*, Sens. Actuators, B **54**, 3–15, (1999), DOI 10.1016/S0925-4005(98)00321-9, (cit. on p. 21).

[123]   R. Gans: *Über die Form ultramikroskopischer Goldteilchen*, Ann. Phys. **342**, 881–900, (1912), DOI 10.1002/andp.19123420503, (cit. on p. 22).

[124]   C. F. Bohren and D. R. Huffman: *Absorption and scattering of light by small particles*, 1998th ed., Weinheim: John Wiley & Sons, 1983, (cit. on pp. 23, 25).

[125]   S. A. Maier: *Plasmonics: Fundamentals and applications*, New York: Springer, 2007, (cit. on p. 28).

[126]    K. L. Kelly, E. Coronado, L. L. Zhao, and G. C. Schatz: *The optical properties of metal nanoparticles: the influence of size, shape, and dielectric environment*, J. Phys. Chem. B **107**, 668–677, (2003), DOI 10.1021/jp026731y, (cit. on p. 29).

[127]    H. Ditlbacher, A. Hohenau, D. Wagner, U. Kreibig, M. Rogers, F. Hofer, F. R. Aussenegg, and J. R. Krenn: *Silver nanowires as surface plasmon resonators*, Phys. Rev. Lett. **95**, 257403–4, (2005), DOI 10.1103/PhysRevLett.95.257403, (cit. on p. 31).

[128]    J. Dorfmüller, R. Vogelgesang, R. T. Weitz, C. Rockstuhl, C. Etrich, T. Pertsch, F. Lederer, and K. Kern: *Fabry-Pérot resonances in one-dimensional plasmonic nanostructures*, Nano Lett. **9**, 2372–2377, (2009), DOI 10.1021/nl900900r, (cit. on p. 31).

[129]    J. Dorfmüller, R. Vogelgesang, W. Khunsin, C. Rockstuhl, C. Etrich, and K. Kern: *Plasmonic nanowire antennas: Experiment, simulation, and theory*, Nano Lett. **10**, 3596–3603, (2010), DOI 10.1021/nl101921y, (cit. on p. 31).

[130]    T. Warncke: *Coherent dynamics of radiatively coupled quantum well excitons*, PhD thesis, Philipps-Universität Marburg, 1996, (cit. on p. 32).

[131]    T. Stroucken, A. Knorr, P. Thomas, and S. W. Koch: *Coherent dynamics of radiatively coupled quantum-well excitons*, Phys. Rev. B **53**, 2026–2033, (1996), DOI 10.1103/PhysRevB.53.2026, (cit. on pp. 32, 94, 103–104, 106, 142).

[132]    A. E. Miroshnichenko, S. Flach, and Y. S. Kivshar: *Fano resonances in nanoscale structures*, Rev. Mod. Phys. **82**, 2257–2298, (2010), DOI 10.1103/RevModPhys.82.2257, (cit. on p. 35).

[133]    U. Fano: *Effects of configuration interaction on intensities and phase shifts*, Phys. Rev. **124**, 1866–1878, (1961), DOI 10.1103/PhysRev.124.1866, (cit. on pp. 35, 119).

[134]    B. Luk'yanchuck, N. I. Zheludev, S. A. Maier, N. J. Halas, P. Nordlander, H. Giessen, and C. T. Chong: *The Fano resonance in plasmonic nanostructures and metamaterials*, Nat. Mater. **9**, 707–715, (2010), DOI 10.1038/nmat2810, (cit. on pp. 36, 48, 119).

[135]   A. Christ, O. J. F. Martin, Y. Ekinci, N. A. Gippius, and
        S. G. Tikhodeev: *Symmetry breaking in a plasmonic
        metamaterial at optical wavelength*, Nano Lett. **8**, 2171–2175,
        (2008), DOI 10.1021/nl0805559, (cit. on pp. 36, 48, 63, 66).

[136]   A. Christ, Y. Ekinci, H. H. Solak, N. A. Gippius,
        S. G. Tikhodeev, and O. J. F. Martin: *Controlling the Fano
        interference in a plasmonic lattice*, Phys. Rev. B **76**,
        201405(R)–4, (2007), DOI 10.1103/PhysRevB.76.201405, (cit. on
        pp. 36, 48, 63).

[137]   B. Kanté, S. N. Burokur, A. Sellier, A. de Lustrac, and
        J.-M. Lourtioz: *Controlling plasmon hybridization for negative
        refraction metamaterials*, Phys. Rev. B **79**, 075121–4, (2009),
        DOI 10.1103/PhysRevB.79.075121, (cit. on pp. 36, 63).

[138]   Y. Sonnefraud, N. Verellen, H. Sobhani, G. A. E. Vandenbosch,
        V. V. Moshchalkov, P. Van Dorpe, P. Nordlander, and
        S. A. Maier: *Experimental realization of subradiant,
        superradiant, and Fano resonances in ring/disk plasmonic
        nanocavities*, ACS nano **4**, 1664–1670, (2010),
        DOI 10.1021/nn901580r, (cit. on pp. 36, 48).

[139]   F. Hao, P. Nordlander, Y. Sonnefraud, P. Van Dorpe, and
        S. A. Maier: *Tunability of subradiant dipolar and Fano-type
        plasmon resonances in metallic ring/disk cavities: Implications
        for nanoscale optical sensing*, ACS nano **3**, 643–652, (2009),
        DOI 10.1021/nn900012r, (cit. on pp. 36, 48).

[140]   F. Hao, Y. Sonnefraud, P. Van Dorpe, S. A. Maier, N. J. Halas,
        and P. Nordlander: *Symmetry breaking in plasmonic
        nanocavities: Subradiant lspr sensing and a tunable Fano
        resonance*, Nano Lett. **8**, 3983–3988, (2008), DOI 10.1021/nl802509r,
        (cit. on pp. 36, 48).

[141]   M. Frimmer, T. Coenen, and A. F. Koenderink: *Signature of a
        Fano resonance in a plasmonic metamolecule's local density of
        optical states*, Phys. Rev. Lett. **108**, 077404–5, (2012),
        DOI 10.1103/PhysRevLett.108.077404, (cit. on pp. 36, 48).

[142]   D. Dregely, M. Hentschel, and H. Giessen: *Excitation and
        tuning of higher-order Fano resonances in plasmonic oligomer
        clusters*, ACS nano **5**, 8202–8211, (2011), DOI 10.1021/nn202876k,
        (cit. on pp. 36, 48, 54).

[143]  M. Hentschel, D. Dregely, R. Vogelgesang, H. Giessen, and
N. Liu: *Plasmonic oligomers: The role of individual particles in
collective behavior*, ACS nano **5**, 2042–2050, (2011),
DOI 10.1021/nn103172t, (cit. on pp. 36, 48, 54).

[144]  M. Hentschel, M. Saliba, R. Vogelgesang, H. Giessen,
A. P. Alivisatos, and N. Liu: *Transition from isolated to
collective modes in plasmonic oligomers*, Nano Lett. **10**,
2721–2726, (2010), DOI 10.1021/nl101938p, (cit. on pp. 36, 48, 54).

[145]  J. A. Fan, C. Wu, K. Bao, J. Bao, R. Bardhan, N. J. Halas,
V. N. Manoharan, P. Nordlander, G. Shvets, and F. Capasso:
*Self-assembled plasmonic nanoparticle clusters*, Science **328**,
1135–1138, (2010), DOI 10.1126/science.1187949, (cit. on pp. 36, 48,
54).

[146]  G. Bachelier, I. Russier-Antoine, E. Benichou, C. Jonin, N. Del
Fatti, F. Vallée, and P.-F. Brevet: *Fano profiles induced by
near-field coupling in heterogeneous dimers of gold and silver
nanoparticles*, Phys. Rev. Lett. **101**, 197401–4, (2008),
DOI 10.1103/PhysRevLett.101.197401, (cit. on pp. 36, 47).

[147]  C. Wu, A. B. Khanikaev, R. Adato, N. Arju, A. A. Yanik,
H. Altug, and G. Shvets: *Fano-resonant asymmetric
metamaterials for ultrasensitive spectroscopy and identification
of molecular monolayers*, Nat. Mater. **11**, 69–75, (2012),
DOI 10.1038/nmat3161, (cit. on pp. 36, 48, 119).

[148]  N. Verellen, P. Van Dorpe, C. Huang, K. Lodewijks,
G. A. E. Vandenbosch, L. Lagae, and V. V. Moshchalkov:
*Plasmon line shaping using nanocrosses for high sensitivity
localized surface plasmon resonance sensing*, Nano Lett. **11**,
391–397, (2011), DOI 10.1021/nl102991v, (cit. on pp. 36, 48).

[149]  S. N. Sheikholeslami, A. García-Etxarri, and J. A. Dionne:
*Controlling the interplay of electric and magnetic modes via
Fano-like plasmon resonances*, Nano Lett. **11**, 3927–3934, (2011),
DOI 10.1021/nl202143j, (cit. on pp. 36, 48).

[150]  A. Artar, A. A. Yanik, and H. Altug: *Directional double Fano
resonances in plasmonic hetero-oligomers*, Nano Lett. **11**,
3694–3700, (2011), DOI 10.1021/nl201677h, (cit. on pp. 36, 48, 63,
119).

[151]  V. A. Fedotov, M. Rose, S. L. Prosvirnin, N. Papasimakis, and
N. I. Zheludev: *Sharp trapped-mode resonances in planar
metamaterials with a broken structural symmetry*, Phys. Rev.
Lett. **99**, 147401–4, (2007), DOI 10.1103/PhysRevLett.99.147401,
(cit. on pp. 36, 48).

[152]  B. Gallinet and O. J. F. Martin: *Influence of electromagnetic
interactions on the lineshape of plasmonic Fano resonances*,
ACS nano **5**, 8999–9008, (2011), DOI 10.1021/nn203173r, (cit. on
p. 36).

[153]  B. Gallinet and O. J. F. Martin: *Ab initio theory of Fano
resonances in plasmonic nanostructures and metamaterials*,
Phys. Rev. B **83**, 235427–6, (2011), DOI 10.1103/PhysRevB.83.235427,
(cit. on p. 36).

[154]  B. Gallinet and O. J. F. Martin: *Relation between near-field and
far-field properties of plasmonic Fano resonances*, Opt.
Express **19**, 22167–22175, (2011), DOI 10.1364/OE.19.022167, (cit. on
p. 36).

[155]  C. Wu, A. B. Khanikaev, and G. Shvets: *Broadband slow light
metamaterial based on a double-continuum Fano resonance*,
Phys. Rev. Lett. **106**, 107403–4, (2011),
DOI 10.1103/PhysRevLett.106.107403, (cit. on pp. 36, 119).

[156]  N. A. Mirin, K. Bao, and P. Nordlander: *Fano resonances in
plasmonic nanoparticle aggregates*, J. Phys. Chem. A **113**,
4028–4034, (2009), DOI 10.1021/jp810411q, (cit. on p. 36).

[157]  *Lithografie - Theorie und Anwendung von Fotolacken,
Entwicklern, Ätzchemikalien und Lösemitteln*,
MicroChemicals GmbH, Ulm, 2008/2009, (cit. on p. 37).

[158]  N. Liu, H. Guo, L. Fu, S. Kaiser, H. Schweizer, and H. Giessen:
*Three-dimensional photonic metamaterials at optical
frequencies*, Nat. Mater. **7**, 31–37, (2008), DOI 10.1038/nmat2072,
(cit. on pp. 40, 60).

[159]  G. Subramania and S. Y. Lin: *Fabrication of three-dimensional
photonic crystal with alignment based on electron beam
lithography*, Appl. Phys. Lett. **85**, 5037–5039, (2004),
DOI 10.1063/1.1825623, (cit. on p. 40).

[160]  D. Meyerhofer: *Characteristics of resist films produced by
spinning*, J. Appl. Phys. **49**, 3993–3997, (1978), DOI 10.1063/1.325357,
(cit. on p. 41).

[161]   D. M. Whittaker and I. S. Culshaw: *Scattering-matrix treatment of patterned multilayer photonic structures*, Phys. Rev. B **60**, 2610–2618, (1999), DOI 10.1103/PhysRevB.60.2610, (cit. on pp. 44–45).

[162]   *CST Microwave Studio Documentation*, 2012, (cit. on p. 44).

[163]   S. G. Tikhodeev, A. L. Yablonskii, E. A. Muljarov, N. A. Gippius, and T. Ishihara: *Quasiguided modes and optical properties of photonic crystal slabs*, Phys. Rev. B **66**, 045102–17, (2002), DOI 10.1103/PhysRevB.66.045102, (cit. on p. 45).

[164]   T. Weiss, G. Granet, N. A. Gippius, S. G. Tikhodeev, and H. Giessen: *Matched coordinates and adaptive spatial resolution in the fourier modal method*, Opt. Express **17**, 8051–8061, (2009), DOI 10.1364/OE.17.008051, (cit. on p. 45).

[165]   C. L. Haynes, A. D. McFarland, L. Zhao, R. P. Van Duyne, G. C. Schatz, L. Gunnarsson, J. Prikulis, B. Kasemo, and M. Käll: *Nanoparticle optics: The importance of radiative dipole coupling in two-dimensional nanoparticle arrays*, J. Phys. Chem. B **107**, 7337–7342, (2003), DOI 10.1021/jp034234r, (cit. on pp. 47, 58).

[166]   W. Rechberger, A. Hohenau, A. Leitner, J. R. Krenn, B. Lamprecht, and F. R. Aussenegg: *Optical properties of two interacting gold nanoparticles*, Opt. Commun. **220**, 137–141, (2003), DOI 10.1016/S0030-4018(03)01357-9, (cit. on pp. 47, 55).

[167]   K.-H. Su, Q.-H. Wei, X. Zhang, J. J. Mock, D. R. Smith, and S. Schultz: *Interparticle coupling effects on plasmon resonances of nanogold particles*, Nano Lett. **3**, 1087–1090, (2003), DOI 10.1021/nl034197f, (cit. on p. 47).

[168]   J. P. Kottmann and O. J. F. Martin: *Retardation-induced plasmon resonances in coupled nanoparticles*, Opt. Lett. **26**, 1096–1098, (2001), DOI 10.1364/OL.26.001096, (cit. on p. 47).

[169]   G. Schider, J. R. Krenn, W. Gotschy, B. Lamprecht, H. Ditlbacher, A. Leitner, and F. R. Aussenegg: *Optical properties of Ag and Au nanowire gratings*, J. Appl. Phys. **90**, 3825–3830, (2001), DOI 10.1063/1.1404425, (cit. on p. 47).

[170]  B. Lamprecht, G. Schider, R. T. Lechner, H. Ditlbacher, J. R. Krenn, A. Leitner, and F. R. Aussenegg: *Metal nanoparticle gratings: Influence of dipolar particle interaction on the plasmon resonance*, Phys. Rev. Lett. **84**, 4721–4724, (2000), DOI 10.1103/PhysRevLett.84.4721, (cit. on p. 47).

[171]  T. J. Davis, K. C. Vernon, and D. Gómez: *Designing plasmonic systems using optical coupling between nanoparticles*, Phys. Rev. B **79**, 155423–10, (2009), DOI 10.1103/PhysRevB.79.155423, (cit. on p. 47).

[172]  C. Dahmen, B. Schmidt, and G. von Plessen: *Radiation damping in metal nanoparticle pairs*, Nano Lett. **7**, 318–322, (2007), DOI 10.1021/nl062377u, (cit. on p. 47).

[173]  M. Quinten, U. Kreibig, D. Schönauer, and L. Genzel: *Optical absorption spectra of pairs of small metal particles*, Surface Science **156**, 741–750, (1985), DOI 10.1016/0039-6028(85)90244-4, (cit. on p. 47).

[174]  P. K. Jain, W. Huang, and M. A. El-Sayed: *On the universal scaling behavior of the distance decay of plasmon coupling in metal nanoparticle pairs: A plasmon ruler equation*, Nano Lett. **7**, 2080–2088, (2007), DOI 10.1021/nl071008a, (cit. on pp. 47, 55).

[175]  A. N. Grigorenko, A. K. Geim, H. F. Gleeson, Y. Zhang, A. A. Firsov, I. Y. Khrushchev, and J. Petrovic: *Nanofabricated media with negative permeability at visible frequencies*, Nature **438**, 335–338, (2005), DOI 10.1038/nature04242, (cit. on p. 47).

[176]  L. Gunnarsson, T. Rindzevicius, J. Prikulis, B. Kasemo, M. Käll, S. Zou, and G. C. Schatz: *Confined plasmons in nanofabricated single silver particle pairs: Experimental observations of strong interparticle interactions*, J. Phys. Chem. B **109**, 1079–1087, (2005), DOI 10.1021/jp049084e, (cit. on pp. 47, 55).

[177]  K. Aydin, I. M. Pryce, and H. A. Atwater: *Symmetry breaking and strong coupling in planar optical metamaterials*, Opt. Express **18**, 13407–13417, (2010), DOI 10.1364/OE.18.013407, (cit. on p. 47).

[178]  N. Liu, H. Liu, S. Zhu, and H. Giessen: *Stereometamaterials*, Nat. Photonics **3**, 157–162, (2009), DOI 10.1038/NPHOTON.2009.4, (cit. on p. 47).

[179]   C.-Y. Tsai, J.-W. Lin, C.-Y. Wu, P.-T. Lin, T.-W. Lu, and P.-T. Lee: *Plasmonic coupling in gold nanoring dimers: Observation of coupled bonding mode*, Nano Lett. **12**, 1648–1654, (2012), DOI 10.1021/nl300012m, (cit. on p. 47).

[180]   A. M. Funston, C. Novo, T. J. Davis, and P. Mulvaney: *Plasmon coupling of gold nanorods at short distances and in different geometries*, Nano Lett. **9**, 1651–1658, (2009), DOI 10.1021/nl900034v, (cit. on p. 47).

[181]   M. Decker, M. Ruther, C. E. Kriegler, J. Zhou, C. M. Soukoulis, S. Linden, and M. Wegener: *Strong optical activity from twisted-cross photonic metamaterials*, Opt. Lett. **34**, 2501–2503, (2009), DOI 10.1364/OL.34.002501, (cit. on p. 47).

[182]   S.-C. Yang, H. Kobori, C.-L. He, M.-H. Lin, H.-Y. Chen, C. Li, M. Kanehara, T. Teranishi, and S. Gwo: *Plasmon hybridization in individual gold nanocrystal dimers: Direct observation of bright and dark modes*, Nano Lett. **10**, 632–637, (2010), DOI 10.1021/nl903693v, (cit. on p. 47).

[183]   H. Fischer and O. J. F. Martin: *Retardation-induced plasmonic blinking in coupled nanoparticles*, Opt. Lett. **34**, 368–370, (2009), DOI 10.1364/OL.34.000368, (cit. on pp. 47, 59).

[184]   P. Olk, J. Renger, M. T. Wenzel, and L. M. Eng: *Distance dependent spectral tuning of two coupled metal nanoparticles*, Nano Lett. **8**, 1174–1178, (2008), DOI 10.1021/nl080044m, (cit. on p. 47).

[185]   T. Shegai, S. Chen, V. D. Miljković, G. Zengin, P. Johansson, and M. Käll: *A bimetallic nanoantenna for directional colour routing*, Nat. Commun. **2**, 481, (2011), DOI 10.1038/ncomms1490, (cit. on pp. 47, 144).

[186]   S. Sheikholeslami, Y.-w. Jun, P. K. Jain, and A. P. Alivisatos: *Coupling of optical resonances in a compositionally asymmetric plasmonic nanoparticle dimer*, Nano Lett. **10**, 2655–2660, (2010), DOI 10.1021/nl101380f, (cit. on p. 47).

[187]   L. Shao, C. Fang, H. Chen, Y. C. Man, J. Wang, and H.-Q. Lin: *Distinct plasmonic manifestation on gold nanorods induced by the spatial perturbation of small gold nanospheres*, Nano Lett. **12**, 1424–1430, (2012), DOI 10.1021/nl2041063, (cit. on p. 47).

[188]   C. Menzel, C. Helgert, C. Rockstuhl, E.-B. Kley,
        A. Tünnermann, T. Pertsch, and F. Lederer: *Asymmetric
        transmission of linearly polarized light at optical metamaterials*,
        Phys. Rev. Lett. **104**, 253902–4, (2010),
        DOI 10.1103/PhysRevLett.104.253902, (cit. on p. 47).

[189]   Z.-G. Dong, H. Liu, M.-X. Xu, T. Li, S.-M. Wang, S.-N. Zhu,
        and X. Zhang: *Plasmonically induced transparent magnetic
        resonance in a metallic metamaterial composed of asymmetric
        double bars*, Opt. Express **18**, 18229–18234, (2010),
        DOI 10.1364/OE.18.018229, (cit. on p. 47).

[190]   H. Guo, N. Liu, L. Fu, T. P. Meyrath, T. Zentgraf, H. Schweizer,
        and H. Giessen: *Resonance hybridization in double split-ring
        resonator metamaterials*, Opt. Express **15**, 12095–12101, (2007),
        DOI 10.1364/OE.15.012095, (cit. on p. 47).

[191]   V. Giannini, G. Vecchi, and J. Gómez Rivas: *Lighting up
        multipolar surface plasmon polaritons by collective resonances
        in arrays of nanoantennas*, Phys. Rev. Lett. **105**, 266801–4,
        (2010), DOI 10.1103/PhysRevLett.105.266801, (cit. on p. 47).

[192]   J. Sung, E. M. Hicks, R. P. Van Duyne, and K. G. Spears:
        *Nanoparticle spectroscopy: Plasmon coupling in finite-sized
        two-dimensional arrays of cylindrical silver nanoparticles*, J.
        Phys. Chem. C **112**, 4091–4096, (2008), DOI 10.1021/jp077332b,
        (cit. on p. 47).

[193]   R. Adato, A. A. Yanik, C.-H. Wu, G. Shvets, and H. Altug:
        *Radiative engineering of plasmon lifetimes in embedded
        nanoantenna arrays*, Opt. Express **18**, 4526–4537, (2010),
        DOI 10.1364/OE.18.004526, (cit. on p. 47).

[194]   B. Auguié and W. L. Barnes: *Collective resonances in gold
        nanoparticle arrays*, Phys. Rev. Lett. **101**, 143902–4, (2008),
        DOI 10.1103/PhysRevLett.101.143902, (cit. on pp. 47, 58).

[195]   E. M. Hicks, S. Zou, G. C. Schatz, K. G. Spears, R. P. Van
        Duyne, L. Gunnarsson, T. Rindzevicius, B. Kasemo, and
        M. Käll: *Controlling plasmon line shapes through diffractive
        coupling in linear arrays of cylindrical nanoparticles fabricated
        by electron beam lithography*, Nano Lett. **5**, 1065–1070, (2005),
        DOI 10.1021/nl0505492, (cit. on pp. 47, 58).

[196]   V. G. Kravets, F. Schedin, and A. N. Grigorenko: *Extremely narrow plasmon resonances based on diffraction coupling of localized plasmons in arrays of metallic nanoparticles*, Phys. Rev. Lett. **101**, 087403–4, (2008), DOI 10.1103/PhysRevLett.101.087403, (cit. on pp. 47, 58).

[197]   V. A. Markel: *Divergence of dipole sums and the nature of non-lorentzian exponentially narrow resonances in one-dimensional periodic arrays of nanospheres*, J. Phys. B **38**, L115–L121, (2005), DOI 10.1088/0953-4075/38/7/L02, (cit. on p. 48).

[198]   S. Zou, N. Janel, and G. C. Schatz: *Silver nanoparticle array structures that produce remarkably narrow plasmon lineshapes*, J. Chem. Phys. **120**, 10871–10875, (2004), DOI 10.1063/1.1760740, (cit. on pp. 48, 58).

[199]   L. Zhao, K. L. Kelly, and G. C. Schatz: *The extinction spectra of silver nanoparticle arrays: Influence of array structure on plasmon resonance wavelength and width*, J. Phys. Chem. B **107**, 7343–7350, (2003), DOI 10.1021/jp034235j, (cit. on pp. 48, 58).

[200]   V. A. Markel: *Coupled-dipole approach to scattering of light from a one-dimensional periodic dipole structure*, J. Mod. Opt. **40**, 2281–2291, (1993), DOI 10.1080/09500349314552291, (cit. on p. 48).

[201]   M. Decker, N. Feth, C. M. Soukoulis, S. Linden, and M. Wegener: *Retarded long-range interaction in split-ring-resonator square arrays*, Phys. Rev. B **84**, 085416–7, (2011), DOI 10.1103/PhysRevB.84.085416, (cit. on pp. 48, 58).

[202]   A. Bitzer, J. Wallauer, H. Merbold, H. Helm, T. Feurer, and M. Walther: *Lattice modes mediate radiative coupling in metamaterial arrays*, Opt. Express **17**, 22108–22113, (2009), DOI 10.1364/OE.17.022108, (cit. on pp. 48, 58).

[203]   T. Utikal, T. Zentgraf, T. Paul, C. Rockstuhl, F. Lederer, M. Lippitz, and H. Giessen: *Towards the origin of the nonlinear response in hybrid plasmonic systems*, Phys. Rev. Lett. **106**, 133901–4, (2011), DOI 10.1103/PhysRevLett.106.133901, (cit. on p. 48).

[204]   D. Nau, A. Schönhardt, C. Bauer, A. Christ, T. Zentgraf, J. Kuhl, M. W. Klein, and H. Giessen: *Correlation effects in disordered metallic photonic crystal slabs*, Phys. Rev. Lett. **98**, 133902–4, (2007), DOI 10.1103/PhysRevLett.98.133902, (cit. on p. 48).

[205]  D. Nau: *The influence of disorder in metallic photonic crystals*, PhD thesis, Rheinische Friedrich-Wilhelms-Universität Bonn, 2006, http://nbn-resolving.de/urn:nbn:de:hbz:5N-07859, (cit. on p. 48).

[206]  A. Christ, T. Zentgraf, J. Kuhl, S. G. Tikhodeev, N. A. Gippius, and H. Giessen: *Optical properties of planar metallic photonic crystal structures: Experiment and theory*, Phys. Rev. B **70**, 125113–15, (2004), DOI 10.1103/PhysRevB.70.125113, (cit. on pp. 48, 58).

[207]  A. Christ, S. G. Tikhodeev, N. A. Gippius, J. Kuhl, and H. Giessen: *Waveguide-plasmon polaritons: Strong coupling of photonic and electronic resonances in a metallic photonic crystal slab*, Phys. Rev. Lett. **91**, 183901–4, (2003), DOI 10.1103/PhysRevLett.91.183901, (cit. on p. 48).

[208]  S. Linden, J. Kuhl, and H. Giessen: *Controlling the interaction between light and gold nanoparticles: Selective suppression of extinction*, Phys. Rev. Lett. **86**, 4688–4691, (2001), DOI 10.1103/PhysRevLett.86.4688, (cit. on p. 48).

[209]  S. Linden: *Kontrolle der Wechselwirkung zwischen Licht und Partikelplasmonen durch selektive Unterdrückung der Extinktion*, PhD thesis, Philipps-Universität Marburg, 2001, (cit. on p. 48).

[210]  T. J. Davis: "Evanescent Coupling Between Resonant Plasmonic Nanoparticles and the Design of Nanoparticle Systems", in: *Plasmons: Theory and Applications*, ed. by K. N. Helsey, 1st ed., Nova Publishers, 2011, chap. 4, pp. 111–141, (cit. on p. 48).

[211]  F. Hao, P. Nordlander, M. T. Burnett, and S. A. Maier: *Enhanced tunability and linewidth sharpening of plasmon resonances in hybridized metallic ring/disk nanocavities*, Phys. Rev. B **76**, 245417–6, (2007), DOI 10.1103/PhysRevB.76.245417, (cit. on p. 48).

[212]  T. J. Davis, M. Hentschel, N. Liu, and H. Giessen: *Analytical model of the three-dimensional plasmonic ruler*, ACS nano **6**, 1291–1298, (2012), DOI 10.1021/nn204029p, (cit. on p. 48).

[213]  N. Liu, M. Hentschel, T. Weiss, A. P. Alivisatos, and H. Giessen: *Three-dimensional plasmon rulers*, Science **332**, 1407–1410, (2011), DOI 10.1126/science.1199958, (cit. on p. 48).

[214]   N. Verellen, Y. Sonnefraud, H. Sobhani, F. Hao,
        V. V. Moshchalkov, P. Van Dorpe, P. Nordlander, and
        S. A. Maier: *Fano resonances in individual coherent plasmonic
        nanocavities*, Nano Lett. **9**, 1663–1667, (2009),
        DOI 10.1021/nl9001876, (cit. on pp. 48, 121).

[215]   N. Liu, L. Langguth, T. Weiss, J. Kästel, M. Fleischhauer,
        T. Pfau, and H. Giessen: *Plasmonic analogue of
        electromagnetically induced transparency at the Drude
        damping limit*, Nat. Mater. **8**, 758–762, (2009),
        DOI 10.1038/nmat2495, (cit. on pp. 48, 117, 119–121, 132).

[216]   S. Zhang, D. A. Genov, Y. Wang, M. Liu, and X. Zhang:
        *Plasmon-induced transparency in metamaterials*, Phys. Rev.
        Lett. **101**, 047401–4, (2008), DOI 10.1103/PhysRevLett.101.047401,
        (cit. on pp. 48, 119–120, 125, 132).

[217]   L. Chuntonov and G. Haran: *Trimeric plasmonic molecules:
        The role of symmetry*, Nano Lett. **11**, 2440–2445, (2011),
        DOI 10.1021/nl2008532, (cit. on p. 48).

[218]   L. Chuntonov and G. Haran: *Effect of symmetry breaking on
        the mode structure of trimeric plasmonic molecules*, J. Phys.
        Chem. C **115**, 19488–19495, (2011), DOI 10.1021/jp2045433, (cit. on
        p. 48).

[219]   J. Alegret, T. Rindzevicius, T. Pakizeh, Y. Alaverdyan,
        L. Gunnarsson, and M. Käll: *Plasmonic properties of silver
        trimers with trigonal symmetry fabricated by electron-beam
        lithography*, J. Phys. Chem. C **112**, 14313–14317, (2008),
        DOI 10.1021/jp804505k, (cit. on p. 48).

[220]   S. J. Barrow, A. M. Funston, D. E. Gómez, T. J. Davis, and
        P. Mulvaney: *Surface plasmon resonances in strongly coupled
        gold nanosphere chains from monomer to hexamer*, Nano
        Lett. **11**, 4180–4187, (2011), DOI 10.1021/nl202080a, (cit. on p. 48).

[221]   R. Ameling, D. Dregely, and H. Giessen: *Strong coupling of
        localized and surface plasmons to microcavity modes*, Opt.
        Lett. **36**, 2218–2220, (2011), DOI 10.1364/OL.36.002218, (cit. on
        pp. 48, 87, 143).

[222]   T. Utikal, T. Zentgraf, S. G. Tikhodeev, M. Lippitz, and
        H. Giessen: *Tailoring the photonic band splitting in
        metallodielectric photonic crystal superlattices*, Phys. Rev. B **84**,
        075101–5, (2011), DOI 10.1103/PhysRevB.84.075101, (cit. on p. 48).

[223]   T. Utikal: *Ultrafast nonlinear spectroscopy of hybrid plasmonic systems*, PhD thesis, Universität Stuttgart, 2011, http://elib.uni-stuttgart.de/opus/volltexte/2011/6130, (cit. on p. 48).

[224]   M. Geiselmann, T. Utikal, M. Lippitz, and H. Giessen: *Tailoring the ultrafast dynamics of the magnetic mode in magnetic photonic crystals*, Phys. Rev. B **81**, 235101–6, (2010), DOI 10.1103/PhysRevB.81.235101, (cit. on p. 48).

[225]   T. Utikal, M. I. Stockman, A. P. Heberle, M. Lippitz, and H. Giessen: *All-optical control of the ultrafast dynamics of a hybrid plasmonic system*, Phys. Rev. Lett. **104**, 113903–4, (2010), DOI 10.1103/PhysRevLett.104.113903, (cit. on p. 48).

[226]   T. Zentgraf, S. Zhang, R. F. Oulton, and X. Zhang: *Ultranarrow coupling-induced transparency bands in hybrid plasmonic systems*, Phys. Rev. B **80**, 195415–6, (2009), DOI 10.1103/PhysRevB.80.195415, (cit. on p. 48).

[227]   T. Utikal, T. Zentgraf, J. Kuhl, and H. Giessen: *Dynamics and dephasing of plasmon polaritons in metallic photonic crystal superlattices: Time- and frequency-resolved nonlinear autocorrelation measurements and simulations*, Phys. Rev. B **76**, 245107–6, (2007), DOI 10.1103/PhysRevB.76.245107, (cit. on p. 48).

[228]   A. Christ, T. Zentgraf, S. G. Tikhodeev, N. A. Gippius, J. Kuhl, and H. Giessen: *Controlling the interaction between localized and delocalized surface plasmon modes: Experiment and numerical calculations*, Phys. Rev. B **74**, 155435–8, (2006), DOI 10.1103/PhysRevB.74.155435, (cit. on p. 48).

[229]   S. Linden, M. Decker, and M. Wegener: *Model system for a one-dimensional magnetic photonic crystal*, Phys. Rev. Lett. **97**, 083902–4, (2006), DOI 10.1103/PhysRevLett.97.083902, (cit. on p. 48).

[230]   T. Zentgraf, A. Christ, J. Kuhl, N. A. Gippius, S. G. Tikhodeev, D. Nau, and H. Giessen: *Metallodielectric photonic crystal superlattices: Influence of periodic defects on transmission properties*, Phys. Rev. B **73**, 115103–9, (2006), DOI 10.1103/PhysRevB.73.115103, (cit. on p. 48).

[231]   X. Zhang, B. Sun, R. H. Friend, H. Guo, D. Nau, and H. Giessen: *Metallic photonic crystals based on solution-processible gold nanoparticles*, Nano Lett. **6**, 651–655, (2006), DOI 10.1021/nl0523610, (cit. on p. 48).

[232]   T. Zentgraf, A. Christ, J. Kuhl, and H. Giessen: *Tailoring the ultrafast dephasing of quasiparticles in metallic photonic crystals*, Phys. Rev. Lett. **93**, 243901–4, (2004), DOI 10.1103/PhysRevLett.93.243901, (cit. on p. 48).

[233]   E. Prodan, C. Radloff, N. J. Halas, and P. Nordlander: *A hybridization model for the plasmon response of complex nanostructures*, Science **302**, 419–422, (2003), DOI 10.1126/science.1089171, (cit. on p. 53).

[234]   N. J. Halas, S. Lal, W.-S. Chang, S. Link, and P. Nordlander: *Plasmons in strongly coupled metallic nanostructures*, Chem. Rev. **111**, 3913–3961, (2011), DOI 10.1021/cr200061k, (cit. on p. 53).

[235]   P. Nordlander and E. Prodan: *Plasmon hybridization in nanoparticles near metallic surfaces*, Nano Lett. **4**, 2209–2213, (2004), DOI 10.1021/nl0486160, (cit. on p. 53).

[236]   F. Le, N. Z. Lwin, J. M. Steele, M. Käll, N. J. Halas, and P. Nordlander: *Plasmons in the metallic nanoparticle-film system as a tunable impurity problem*, Nano Lett. **5**, 2009–2013, (2005), DOI 10.1021/nl0515100, (cit. on p. 53).

[237]   E. Prodan and P. Nordlander: *Plasmon hybridization in spherical nanoparticles*, J. Chem. Phys. **120**, 5444–5454, (2004), DOI 10.1063/1.1647518, (cit. on p. 54).

[238]   P. Nordlander, C. Oubre, E. Prodan, K. Li, and M. I. Stockman: *Plasmon hybridization in nanoparticle dimers*, Nano Lett. **4**, 899–903, (2004), DOI 10.1021/nl049681c, (cit. on p. 54).

[239]   B. Willingham, D. W. Brandl, and P. Nordlander: *Plasmon hybridization in nanorod dimers*, Appl. Phys. B **93**, 209–216, (2008), DOI 10.1007/s00340-008-3157-5, (cit. on p. 54).

[240]   M. Schmeits and L. Dambly: *Fast-electron scattering by bispherical surface-plasmon modes*, Phys. Rev. B **44**, 12706–12712, (1991), DOI 10.1103/PhysRevB.44.12706, (cit. on p. 55).

[241]   E. Hecht: *Optik*, 5th ed., München: Oldenbourg, 2009, (cit. on p. 58).

[242]   A. Hessel and A. A. Oliner: *A new theory of Wood's anomalies on optical gratings*, Appl. Opt. **4**, 1275–1297, (1965), DOI 10.1364/AO.4.001275, (cit. on p. 58).

[243]   U. Fano: *The theory of anomalous diffraction gratings and of quasi-stationary waves on metallic surfaces (Sommerfeld's waves)*, J. Opt. Soc. Am. **31**, 213–222, (1941), DOI 10.1364/JOSA.31.000213, (cit. on p. 58).

[244]   U. Fano: *Zur Theorie der Intensitätsanomalien der Beugung*, Ann. Phys. **424**, 393–443, (1938), DOI 10.1002/andp.19384240502, (cit. on p. 58).

[245]   U. Fano: *Some theoretical considerations on anomalous diffraction gratings*, Phys. Rev. **50**, 573, (1936), DOI 10.1103/PhysRev.50.573, (cit. on p. 58).

[246]   M. Sarrazin, J.-P. Vigneron, and J.-M. Vigoureux: *Role of Wood anomalies in optical properties of thin metallic films with a bidimensional array of subwavelength holes*, Phys. Rev. B **67**, 085415–8, (2003), DOI 10.1103/PhysRevB.67.085415, (cit. on p. 58).

[247]   W. Zhou and T. W. Odom: *Tunable subradiant lattice plasmons by out-of-plane dipolar interactions*, Nat. Nanotechnol. **6**, 423–427, (2011), DOI 10.1038/nnano.2011.72, (cit. on p. 58).

[248]   N. Liu, H. Guo, L. Fu, S. Kaiser, H. Schweizer, and H. Giessen: *Plasmon hybridization in stacked cut-wire metamaterials*, Adv. Mater. **19**, 3628–3632, (2007), DOI 10.1002/adma.200700123, (cit. on p. 60).

[249]   H.-K. Yuan, U. K. Chettiar, W. Cai, A. V. Kildishev, A. Boltasseva, V. P. Drachev, and V. M. Shalaev: *A negative permeability material at red light*, Opt. Express **15**, 1076–1083, (2007), DOI 10.1364/OE.15.001076, (cit. on p. 60).

[250]   G. Dolling, C. Enrich, M. Wegener, J. F. Zhou, C. M. Soukoulis, and S. Linden: *Cut-wire pairs and plate pairs as magnetic atoms for optical metamaterials*, Opt. Lett. **30**, 3198–200, (2005), DOI 10.1364/OL.30.003198, (cit. on p. 60).

[251]   V. M. Shalaev, W. Cai, U. K. Chettiar, H.-K. Yuan, A. K. Sarychev, V. P. Drachev, and A. V. Kildishev: *Negative index of refraction in optical metamaterials*, Opt. Lett. **30**, 3356–3358, (2005), DOI 10.1364/OL.30.003356, (cit. on p. 60).

[252]   F. Ma and X. Liu: *Phase shift and penetration depth of metal mirrors in a microcavity structure*, Appl. Opt. **46**, 6247–6250, (2007), DOI 10.1364/AO.46.006247, (cit. on p. 71).

[253]    Y. Merle d'Aubigné, A. Wasiela, H. Mariette, and T. Dietl: *Polariton effects in multiple-quantum-well structures of $CdTe/Cd_{1-x}Zn_xTe$*, Phys. Rev. B **54**, 14003–14011, (1996), DOI 10.1103/PhysRevB.54.14003, (cit. on pp. 76, 78).

[254]    D. S. Citrin: *Exciton radiative decay and polaritons in multiquantum wells: Quantum-well-to-superlattice crossover*, Solid State Commun. **89**, 139–143, (1994), DOI 10.1016/0038-1098(94)90394-8, (cit. on p. 76).

[255]    D. S. Citrin: *Exciton polaritons in double versus single quantum wells: Mechanism for increased luminescence linewidths in double quantum wells*, Phys. Rev. B **49**, 1943–1946, (1994), DOI 10.1103/PhysRevB.49.1943, (cit. on p. 76).

[256]    N. A. Gippius, T. Weiss, S. G. Tikhodeev, and H. Giessen: *Resonant mode coupling of optical resonances in stacked nanostructures*, Opt. Express **18**, 7569–7574, (2010), DOI 10.1364/OE.18.007569, (cit. on p. 79).

[257]    R. Ameling: *Microcavity plasmonics*, PhD thesis, Universität Stuttgart, 2011, http://elib.uni-stuttgart.de/opus/volltexte/2011/6510, (cit. on p. 79).

[258]    R. Ameling, L. Langguth, M. Hentschel, M. Mesch, P. V. Braun, and H. Giessen: *Cavity-enhanced localized plasmon resonance sensing*, Appl. Phys. Lett. **97**, 253116–3, (2010), DOI 10.1063/1.3530795, (cit. on pp. 79, 143).

[259]    R. Ameling and H. Giessen: *Cavity plasmonics: Large normal mode splitting of electric and magnetic particle plasmons induced by a photonic microcavity*, Nano Lett. **10**, 4394–4398, (2010), DOI 10.1021/nl1019408, (cit. on pp. 79, 87, 90, 143).

[260]    N. E. Rehler and J. H. Eberly: *Superradiance*, Phys. Rev. A **3**, 1735–1751, (1971), DOI 10.1103/PhysRevA.3.1735, (cit. on pp. 87, 106).

[261]    M. G. Raizen, R. J. Thompson, R. J. Brecha, H. J. Kimble, and H. J. Carmichael: *Normal-mode splitting and linewidth averaging for two-state atoms in an optical cavity*, Phys. Rev. Lett. **63**, 240–243, (1989), DOI 10.1103/PhysRevLett.63.240, (cit. on p. 87).

[262]   Y. Kaluzny, P. Goy, M. Gross, J. M. Raimond, and S. Haroche: *Observation of self-induced Rabi oscillations in two-level atoms excited inside a resonant cavity: The ringing regime of superradiance*, Phys. Rev. Lett. **51**, 1175–1178, (1983), DOI 10.1103/PhysRevLett.51.1175, (cit. on p. 87).

[263]   R. J. Thompson, G. Rempe, and H. J. Kimble: *Observation of normal-mode splitting for an atom in an optical cavity*, Phys. Rev. Lett. **68**, 1132–1135, (1992), DOI 10.1103/PhysRevLett.68.1132, (cit. on p. 87).

[264]   C. Weisbuch, M. Nishioka, A. Ishikawa, and Y. Arakawa: *Observation of the coupled exciton-photon mode splitting in a semiconductor quantum microcavity*, Phys. Rev. Lett. **69**, 3314–3317, (1992), DOI 10.1103/PhysRevLett.69.3314, (cit. on p. 87).

[265]   Y. Zhu, J. Gauthier, S. E. Morin, Q. Wu, H. J. Carmichael, and T. W. Mossberg: *Vacuum Rabi splitting as a feature of linear-dispersion theory: Analysis and experimental observations*, Phys. Rev. Lett. **64**, 2499–2502, (1990), DOI 10.1103/PhysRevLett.64.2499, (cit. on p. 87).

[266]   H. M. Gibbs, G. Khitrova, and S. W. Koch: *Exciton-polariton light-semiconductor coupling effects*, Nat. Photonics **5**, 275–282, (2011), DOI 10.1038/nphoton.2011.15, (cit. on p. 94).

[267]   D. Goldberg, L. I. Deych, A. A. Lisyansky, Z. Shi, V. M. Menon, V. Tokranov, M. Yakimov, and S. Oktyabrsky: *Exciton-lattice polaritons in multiple-quantum-well-based photonic crystals*, Nat. Photonics **3**, 662–666, (2009), DOI 10.1038/NPHOTON.2009.190, (cit. on p. 94).

[268]   M. V. Erementchouk, L. I. Deych, and A. A. Lisyansky: *Optical properties of one-dimensional photonic crystals based on multiple-quantum-well structures*, Phys. Rev. B **71**, 235335–11, (2005), DOI 10.1103/PhysRevB.71.235335, (cit. on p. 94).

[269]   E. L. Ivchenko, M. M. Voronov, M. V. Erementchouk, L. I. Deych, and A. A. Lisyansky: *Multiple-quantum-well-based photonic crystals with simple and compound elementary supercells*, Phys. Rev. B **70**, 195106–10, (2004), DOI 10.1103/PhysRevB.70.195106, (cit. on p. 94).

[270]  J. P. Prineas, C. Ell, E. S. Lee, G. Khitrova, H. M. Gibbs, and S. W. Koch: *Exciton-polariton eigenmodes in light-coupled $In_{0.04}Ga_{0.96}As/GaAs$ semiconductor multiple-quantum-well periodic structures*, Phys. Rev. B **61**, 13863–13872, (2000), DOI 10.1103/PhysRevB.61.13863, (cit. on pp. 94, 106).

[271]  M. Hübner, J. Kuhl, T. Stroucken, A. Knorr, S. W. Koch, R. Hey, and K. Ploog: *Collective effects of excitons in multiple-quantum-well Bragg and anti-Bragg structures*, Phys. Rev. Lett. **76**, 4199–4202, (1996), DOI 10.1103/PhysRevLett.76.4199, (cit. on pp. 94, 106).

[272]  M. Hübner, J. P. Prineas, C. Ell, P. Brick, E. S. Lee, G. Khitrova, H. M. Gibbs, and S. W. Koch: *Optical lattices achieved by excitons in periodic quantum well structures*, Phys. Rev. Lett. **83**, 2841–2844, (1999), DOI 10.1103/PhysRevLett.83.2841, (cit. on pp. 94, 106).

[273]  E. L. Ivchenko, A. I. Nesvizhskii, and S. Jorda: *Resonant Bragg reflection from quantum-well structures*, Superlatt. Microstruct. **16**, 17–20, (1994), (cit. on pp. 94, 106).

[274]  A. Schilke, C. Zimmermann, P. W. Courteille, and W. Guerin: *Photonic band gaps in one-dimensionally ordered cold atomic vapors*, Phys. Rev. Lett. **106**, 223903–4, (2011), DOI 10.1103/PhysRevLett.106.223903, (cit. on p. 94).

[275]  M. Weidemüller, A. Hemmerich, A. Görlitz, T. Esslinger, and T. W. Hänsch: *Bragg diffraction in an atomic lattice bound by light*, Phys. Rev. Lett. **75**, 4583–4586, (1995), DOI 10.1103/PhysRevLett.75.4583, (cit. on p. 94).

[276]  G. Birkl, M. Gatzke, I. H. Deutsch, S. L. Rolston, and W. D. Phillips: *Bragg scattering from atoms in optical lattices*, Phys. Rev. Lett. **75**, 2823–2826, (1995), DOI 10.1103/PhysRevLett.75.2823, (cit. on p. 94).

[277]  I. H. Deutsch, R. J. C. Spreeuw, S. L. Rolston, and W. D. Phillips: *Photonic band gaps in optical lattices*, Phys. Rev. A **52**, 1394–1410, (1995), DOI 10.1103/PhysRevA.52.1394, (cit. on pp. 94, 108).

[278]   D. F. Sievenpiper, E. Yablonovitch, J. N. Winn, S. Fan,
        P. R. Villeneuve, and J. D. Joannopoulos: *3D metallo-dielectric
        photonic crystals with strong capacitive coupling between
        metallic islands*, Phys. Rev. Lett. **80**, 2829–2832, (1998),
        DOI 10.1103/PhysRevLett.80.2829, (cit. on p. 94).

[279]   E. R. Brown and O. B. McMahon: *Large electromagnetic stop
        bands in metallodielectric photonic crystals*, Appl. Phys.
        Lett. **67**, 2138–2140, (1995), DOI 10.1063/1.114745, (cit. on p. 94).

[280]   J. D. Joannopoulos, P. R. Villeneuve, and S. Fan: *Photonic
        crystals: Putting a new twist on light*, Nature **386**, 143–149,
        (1997), DOI 10.1038/386143a0, (cit. on p. 94).

[281]   J. D. Joannopoulos, S. G. Johnson, J. N. Winn, and
        R. D. Meade: *Photonic crystals: Molding the flow of light*, ed. by
        J. D. Joannopoulos, 2nd ed., Princeton: Princeton University
        Press, 2008, (cit. on p. 94).

[282]   K. Busch, G. von Freymann, S. Linden, S. Mingaleev,
        L. Tkeshelashvili, and M. Wegener: *Periodic nanostructures for
        photonics*, Phys. Reports **444**, 101–202, (2007),
        DOI 10.1016/j.physrep.2007.02.011, (cit. on p. 94).

[283]   M. J. Bloemer and M. Scalora: *Transmissive properties of
        $Ag/MgF_2$ photonic band gaps*, Appl. Phys. Lett. **72**, 1676–1678,
        (1998), DOI 10.1063/1.121150, (cit. on p. 95).

[284]   T. Ergin, T. Benkert, H. Giessen, and M. Lippitz: *Ultrafast
        time-resolved spectroscopy of one-dimensional metal-dielectric
        photonic crystals*, Phys. Rev. B **79**, 245134–6, (2009),
        DOI 10.1103/PhysRevB.79.245134, (cit. on pp. 95–96).

[285]   M. Scalora, M. J. Bloemer, A. S. Pethel, J. P. Dowling,
        C. M. Bowden, and A. S. Manka: *Transparent,
        metallo-dielectric, one-dimensional, photonic band-gap
        structures*, J. Appl. Phys. **83**, 2377–2383, (1998),
        DOI 10.1063/1.366996, (cit. on p. 95).

[286]   R. H. Dicke: *Coherence in spontaneous radiation processes*,
        Phys. Rev. **93**, 99–110, (1954), DOI 10.1103/PhysRev.93.99, (cit. on
        p. 106).

[287]   R. de L. Kronig and W. G. Penney: *Quantum mechanics of
        electrons in crystal lattices*, P. R. Soc. London A **130**, 499–513,
        (1931), DOI 10.1098/rspa.1931.0019, (cit. on p. 108).

[288]   I. N. Bronstein, K. A. Semendjajew, G. Musiol, and H. Mühlig:
        *Taschenbuch der Mathematik*, 5th ed., Thun, Frankfurt
        (Main): Verlag Harri Deutsch, 2001, (cit. on pp. 109, 145).

[289]   L. I. Deych and A. A. Lisyansky: *Polariton dispersion law in
        periodic-Bragg and near-Bragg multiple quantum well
        structures*, Phys. Rev. B **62**, 4242–4244, (2000),
        DOI 10.1103/PhysRevB.62.4242, (cit. on p. 110).

[290]   S. Husaini, L. Deych, and V. M. Menon:
        *Plasmon-resonance-induced enhancement of the reflection
        band in a one-dimensional metal nanocomposite photonic
        crystal*, Opt. Lett. **36**, 1368–1370, (2011), DOI 10.1364/OL.36.001368,
        (cit. on p. 116).

[291]   M. Fleischhauer, A. Imamoglu, and J. P. Marangos:
        *Electromagnetically induced transparency: Optics in coherent
        media*, Rev. Mod. Phys. **77**, 633–673, (2005),
        DOI 10.1103/RevModPhys.77.633, (cit. on pp. 118, 120, 132).

[292]   S. E. Harris, J. E. Field, and A. Imamoglu: *Nonlinear optical
        processes using electromagnetically induced transparency*, Phys.
        Rev. Lett. **64**, 1107–1110, (1990), DOI 10.1103/PhysRevLett.64.1107,
        (cit. on p. 118).

[293]   K. J. Boller, A. Imamoglu, and S. E. Harris: *Observation of
        electromagnetically induced transparency*, Phys. Rev. Lett. **66**,
        2593–2596, (1991), DOI 10.1103/PhysRevLett.66.2593, (cit. on p. 118).

[294]   A. M. Akulshin, S. Barreiro, and A. Lezama:
        *Electromagnetically induced absorption and transparency due
        to resonant two-field excitation of quasidegenerate levels in Rb
        vapor*, Phys. Rev. A **57**, 2996–3002, (1998),
        DOI 10.1103/PhysRevA.57.2996, (cit. on pp. 119, 125).

[295]   A. Lezama, S. Barreiro, and A. M. Akulshin:
        *Electromagnetically induced absorption*, Phys. Rev. A **59**,
        4732–4735, (1999), DOI 10.1103/PhysRevA.59.4732, (cit. on pp. 119,
        125).

[296]   A. V. Taichenachev, A. M. Tumaikin, and V. I. Yudin:
        *Electromagnetically induced absorption in a four-state system*,
        Phys. Rev. A **61**, 011802(R)–4, (1999),
        DOI 10.1103/PhysRevA.61.011802, (cit. on pp. 119, 125).

[297]   A. Lipsich, S. Barreiro, A. M. Akulshin, and A. Lezama: *Absorption spectra of driven degenerate two-level atomic systems*, Phys. Rev. A **61**, 053803–10, (2000), DOI 10.1103/PhysRevA.61.053803, (cit. on pp. 119, 133).

[298]   S. E. Harris: *Electromagnetically induced transparency in an ideal plasma*, Phys. Rev. Lett. **77**, 5357–5360, (1996), DOI 10.1103/PhysRevLett.77.5357, (cit. on p. 119).

[299]   G. Shvets and J. S. Wurtele: *Transparency of magnetized plasma at the cyclotron frequency*, Phys. Rev. Lett. **89**, 115003–4, (2002), DOI 10.1103/PhysRevLett.89.115003, (cit. on p. 119).

[300]   C. L. Garrido Alzar, M. A. G. Martinez, and P. Nussenzveig: *Classical analog of electromagnetically induced transparency*, Am. J. Phys. **70**, 37–41, (2002), DOI 10.1119/1.1412644, (cit. on pp. 119, 130, 132).

[301]   A. G. Litvak and M. D. Tokman: *Electromagnetically induced transparency in ensembles of classical oscillators*, Phys. Rev. Lett. **88**, 095003–4, (2002), DOI 10.1103/PhysRevLett.88.095003, (cit. on p. 119).

[302]   K. Totsuka, N. Kobayashi, and M. Tomita: *Slow light in coupled-resonator-induced transparency*, Phys. Rev. Lett. **98**, 213904–4, (2007), DOI 10.1103/PhysRevLett.98.213904, (cit. on pp. 119–120).

[303]   Q. Xu, S. Sandhu, M. L. Povinelli, J. Shakya, S. Fan, and M. Lipson: *Experimental realization of an on-chip all-optical analogue to electromagnetically induced transparency*, Phys. Rev. Lett. **96**, 123901–4, (2006), DOI 10.1103/PhysRevLett.96.123901, (cit. on p. 119).

[304]   A. Naweed, G. Farca, S. I. Shopova, and A. T. Rosenberger: *Induced transparency and absorption in coupled whispering-gallery microresonators*, Phys. Rev. A **71**, 043804–4, (2005), DOI 10.1103/PhysRevA.71.043804, (cit. on p. 119).

[305]   M. F. Yanik, W. Suh, Z. Wang, and S. Fan: *Stopping light in a waveguide with an all-optical analog of electromagnetically induced transparency*, Phys. Rev. Lett. **93**, 233903–4, (2004), DOI 10.1103/PhysRevLett.93.233903, (cit. on pp. 119–120).

[306]  D. D. Smith, H. Chang, K. A. Fuller, A. T. Rosenberger, and R. W. Boyd: *Coupled-resonator-induced transparency*, Phys. Rev. A **69**, 063804–6, (2004), DOI 10.1103/PhysRevA.69.063804, (cit. on p. 119).

[307]  L. Maleki, A. B. Matsko, A. A. Savchenkov, and V. S. Ilchenko: *Tunable delay line with interacting whispering-gallery-mode resonators*, Opt. Lett. **29**, 626–628, (2004), DOI 10.1364/OL.29.000626, (cit. on pp. 119–120).

[308]  P. Tassin, L. Zhang, T. Koschny, E. N. Economou, and C. M. Soukoulis: *Low-loss metamaterials based on classical electromagnetically induced transparency*, Phys. Rev. Lett. **102**, 053901–4, (2009), DOI 10.1103/PhysRevLett.102.053901, (cit. on pp. 119–120).

[309]  N. Papasimakis, V. A. Fedotov, N. I. Zheludev, and S. L. Prosvirnin: *Metamaterial analog of electromagnetically induced transparency*, Phys. Rev. Lett. **101**, 253903–4, (2008), DOI 10.1103/PhysRevLett.101.253903, (cit. on pp. 119–120).

[310]  A. Artar, A. A. Yanik, and H. Altug: *Multispectral plasmon induced transparency in coupled meta-atoms*, Nano Lett. **11**, 1685–1689, (2011), DOI 10.1021/nl200197j, (cit. on p. 119).

[311]  R. D. Kekatpure, E. S. Barnard, W. Cai, and M. L. Brongersma: *Phase-coupled plasmon-induced transparency*, Phys. Rev. Lett. **104**, 243902–4, (2010), DOI 10.1103/PhysRevLett.104.243902, (cit. on p. 119).

[312]  L. Verslegers, Z. Yu, Z. Ruan, P. Catrysse, and S. Fan: *From electromagnetically induced transparency to superscattering with a single structure: A coupled-mode theory for doubly resonant structures*, Phys. Rev. Lett. **108**, 083903–5, (2012), DOI 10.1103/PhysRevLett.108.083902, (cit. on p. 119).

[313]  Z. Ruan and S. Fan: *Design of subwavelength superscattering nanospheres*, Appl. Phys. Lett. **98**, 043101–3, (2011), DOI 10.1063/1.3536475, (cit. on p. 119).

[314]  Z. Ruan and S. Fan: *Superscattering of light from subwavelength nanostructures*, Phys. Rev. Lett. **105**, 013901–4, (2010), DOI 10.1103/PhysRevLett.105.013901, (cit. on p. 119).

[315]   T. J. Davis, D. E. Gómez, and K. C. Vernon: *Simple model for the hybridization of surface plasmon resonances in metallic nanoparticles*, Nano Lett. **10**, 2618–2625, (2010), DOI 10.1021/nl101335z, (cit. on pp. 121, 132).

[316]   P. R. Hemmer and M. G. Prentiss: *Coupled-pendulum model of the stimulated resonance Raman effect*, J. Opt. Soc. Am. B **5**, 1613–1623, (1988), DOI 10.1364/JOSAB.5.001613, (cit. on p. 130).

[317]   N. T. Fofang, T.-H. Park, O. Neumann, N. A. Mirin, P. Nordlander, and N. J. Halas: *Plexcitonic nanoparticles: Plasmon-exciton coupling in nanoshell-J-aggregate complexes*, Nano Lett. **8**, 3481–3487, (2008), DOI 10.1021/nl8024278, (cit. on p. 143).

[318]   G. Sun, J. B. Khurgin, and R. A. Soref: *Plasmonic light-emission enhancement with isolated metal nanoparticles and their coupled arrays*, J. Opt. Soc. Am. B **25**, 1748–1755, (2008), DOI 10.1364/JOSAB.25.001748, (cit. on p. 143).

[319]   L. I. Deych, M. V. Erementchouk, and A. A. Lisyansky: *Spectral engineering with defect multiple-quantum-well structures*, Appl. Phys. Lett. **83**, 4562–4564, (2003), DOI 10.1063/1.1630852, (cit. on p. 143).

[320]   D. Chanda, K. Shigeta, T. Truong, E. Lui, A. Mihi, M. Schulmerich, P. V. Braun, R. Bhargava, and J. A. Rogers: *Coupling of plasmonic and optical cavity modes in quasi-three-dimensional plasmonic crystals*, Nat. Commun. **2**, 479, (2011), DOI 10.1038/ncomms1487, (cit. on p. 143).

[321]   M. A. Noginov, G. Zhu, A. M. Belgrave, R. Bakker, V. M. Shalaev, E. E. Narimanov, S. Stout, E. Herz, T. Suteewong, and U. Wiesner: *Demonstration of a spaser-based nanolaser*, Nature **460**, 1110–1112, (2009), DOI 10.1038/nature08318, (cit. on p. 143).

[322]   D. J. Bergman and M. I. Stockman: *Surface plasmon amplification by stimulated emission of radiation: Quantum generation of coherent surface plasmons in nanosystems*, Phys. Rev. Lett. **90**, 027402–4, (2003), DOI 10.1103/PhysRevLett.90.027402, (cit. on p. 143).

[323]   N. I. Zheludev: *The road ahead for metamaterials*, Science **328**, 582–583, (2010), DOI 10.1126/science.1186756, (cit. on p. 144).

[324]  T. Pakizeh and M. Käll: *Unidirectional ultracompact optical nanoantennas*, Nano Lett. **9**, 2343–2349, (2009), DOI 10.1021/nl900786u, (cit. on p. 144).

[325]  G. B. Arfken and H. J. Weber: *Mathematical methods for physicists*, 6th ed., Amsterdam, Heidelberg: Elsevier Academic Press, 2005, (cit. on p. 145).

∼

∿

# CURRICULUM VITÆ

| | |
|---|---|
| NAME | Richard Taubert, |
| BORN | 1981-07-31 in Singen (Htwl.), |
| CITIZENSHIP | german |
| CIVIL STATUS | married |
| ADDRESS | Kanalstr. 6/3, 70771 Leinfelden-Echterdingen, Germany |
| PHONE | +49 711 91271177 |
| MAIL | richard.taubert ⓖ gmx.de |

| | |
|---|---|
| 1987–1991 | primary school: Hardbergschule Rielasingen-Worblingen |
| 1991–2000 | Friedrich-Wöhler-Gymnasium Singen |
| 2000–2001 | civil service: Ev. Jugendhaus Konstanz |
| 2001–2002 | studies of theology: BibelSeminar Königsfeld |
| 2002–2007 | studies of physics: University of Konstanz |
| 2006–2007 | diploma thesis: "Laser-based time-resolved study of acoustic phonons in nanostructures", University of Konstanz, advisor: Prof. Dr. Thomas Dekorsy |
| 2008–2012 | Ph.D. thesis: "From near-field to far-field: Plasmonic coupling in three-dimensional nanostructures", University of Stuttgart, advisor: Prof. Dr. Harald Giessen |

$\sim$